Evaluating Targeting of Mouse Cone Photoreceptors for CRISPR-Based Therapies for Inherited Retinal Diseases

Thesis submitted for MSc (Res) in Clinical Neurosciences

Ellie Rhodes, MD

Merton College

Supervisors:
Professor Robert E. MacLaren
Dr. Ahmed Salman

Michaelmas Term 2024

Declaration

The work presented in this thesis was undertaken in the lab of Professor MacLaren between 2021 and 2023. This thesis is entirely my own original work, unless stated otherwise. No material contained in this thesis has been submitted to the University of Oxford, or any other academic institution, for another degree or qualification.

Approximate Word Count: 29964

Acknowledgements

I would first and foremost like to thank my primary supervisor, Professor Robert MacLaren. His enthusiasm for research and its potential is unmatched and I am immensely grateful to have trained under him. He fosters a talented and unique group of scientists and clinicians and I feel very fortunate to have been part of this.

Words don't feel enough to thank my secondary supervisor, Dr. Ahmed Salman. He truly taught me from the ground up. This thesis would not have been possible without his endless support, patience, and guidance.

A special thank you to Dr. Michelle McClements. Whenever I felt stuck her passion for science, quick ideas, and encouragement kept me going.

Thank you to all members of the MacLaren lab and beyond. To Federica Staurenghi, Dr. Connie Han, Dr. Sophia Bellingrath, Elena Piotter, Lauren Major, Dr. Ariel Kantor, Monica Hu, Joel Quinn, Molly John – thank you for being the best lab mates I could have imagined. I will carry the memories of ARVOs, lab dinners, trips to Pret, cabinet snacks, sharing meals on level 5, and pies at the pub with me fondly. Thank you to Dr. Kanmin Xue, Dr. Jasmina Kapetanovic, and Dr. Imran Yusuf for your encouragement and impressive clinical knowledge. Thank you to our postdocs, Dr. Maria Kaukonen and Dr. Hoda Shamsnajafabadi.

To staff at the BMS and JR – thank you for helping keep things in order and for the care of the laboratory and animal spaces.

I would like to express my sincere thanks and gratitude to Rotary International for funding my studies in Oxford. To University of Colorado SOM for working with me to make this MSc happen while in medical school. And to my mentor and friend, Dr. Geeta Lalwani, for believing and supporting me in my pursuits since we first met.

Finally, thank you to my incredible friends and family. A special shout to Dr. Tessa Henessey and Dr. Kelsey Kines – thank you both for always being there for me. To my family, thank you for all your love and understanding as I have pursued my many years of education. I wouldn't be here without you all – I love you.

Abstract

Inherited retinal diseases (IRDs) are a heterogenous group of disorders affecting cells of the outer retina. They represent a large socioeconomic burden and are the leading cause of inherited blindness in the world. Cone photoreceptor dysfunction is implicated in many IRDs and several mutations specific to cone cells have been identified. Great strides have been made via gene supplementation for the treatment of recessively inherited IRDs, however, this strategy is insufficient to treat disorders which cause a gain of function or dominant negative effect, including some of the mutations identified in cone related genes. This thesis broadly explores targeting of cone photoreceptors of mice for development of gene editing applications.

In this thesis I first investigate dosing limitations and broad transduction patterns of AAV5 in combination with a ubiquitous (CAG) vs. photoreceptor-specific (hGRK1) promoter within a transgenic mouse line (CGFP) which expresses enhanced green fluorescent protein (EGFP) in a subset of cone cells. Expression of a red fluorescent protein, DsRed, was driven by either CAG or the hGRK1 promoter. CAG-DsRed and hGRK1-DsRed plasmids were packaged into AAV5 and subretinally injected into eyes of CGFP mice. Both vectors demonstrate *in-vivo* transduction of photoreceptors of the CGFP mouse, with evidence of toxicity with the ubiquitous CAG promoter.

Next, activity of CRISPR-Cas9 was assessed *in-vivo* in the CGFP mouse. To test Cas9 expression, hGRK1-SaCas9 with an EGFP targeting sgRNA, F10, was packaged into AAV5 and subretinally injected into eyes of 6-week old CGFP mice. A dose study was conducted, with viral doses of

$5x10^{11}$ gc/mL, $5x10^{12}$ gc/mL, and $1x10^{13}$ gc/mL. Some evidence of EGFP disruption was seen at the mid dose, however, attempts to detect DNA editing in pooled retinal cells were unsuccessful.

Finally, several sgRNA candidates targeting the opsin locus control region (OPSIN-LCR) of the CGFP mouse were screened *in-vitro* for use in CRIPSR interference applications. Multiple sgRNA candidates were identified which produced gene repression in a dual-luciferase assay. A novel fibroblast line derived from the CGFP mouse was also used and a preliminary protocol for electroporation was established, demonstrating activity of three ubiquitous promoters in the cell line.

Abbreviations

AAV	Adeno-associated virus
ABC	ATP-binding cassette
ABE	Adenine base editor
AD	Autosomal dominant
AMD	Age-related macular degeneration
ANOVA	Analysis of variance
AR	Autosomal recessive
ASO	Antisense oligonucleotide
BAF	Blue autofluorescence
BCM	Blue cone monochromatism
BCVA	Best corrected visual acuity
BED	Bornholm eye disease
CA	Cone-Arrestin
CAG	Cytomegalovirus (CMV) enhancer fused to the chicken beta-actin promoter
Cas	CRISPR-associated nuclease
CBE	Cytosine base editor
CDS	Cone dysfunction syndrome
CGFP	Cone green fluorescent protein mouse line
CMV	Cytomegalovirus
COD	Cone dystrophy
CORD	Cone-rod dystrophy
CRISPR	Clustered regularly interspersed palindromic repeats
CRISPRa	CRISPR activation
CRISPRi	CRISPR interference
crRNA	CRISPR RNA
cSLO	Confocal scanner laser ophthalmoscope
DAPI	4', 6-diamidino-2-phenylindole
dCas9	Deactivated Cas9
ddPCR	Digital droplet PCR
DLA	Dual luciferase assay
DSB	Double stranded break
EFS	Elongation factor 1-alpha 1 short intron-less promoter
EGFP	Enhanced green fluorescent protein
eVLP	Engineered virus-like particle
FA	Fluoresceine angiography
FACS	Fluorescence activated cell sorting
FAF	Fundus autofluorescence

GAF	Green autofluorescence
GCAP1	Guanylate cyclase activating protein 1
gDNA	Genomic DNA
GFP	Green fluorescent protein
HA	Hemagglutinin
HDR	Homology directed repair
HEK293T	Human Embryonic Kidney 293 cells expressing mutant SV40 T antigen
hGRK1	Human G-protein coupled receptor kinase 1 / Human rhodopsin kinase promoter
HSPCs	Hematopoietic stem cells and progenitor cells
ICE	Interference of CRISPR edits
ICGA	Indocyanine green angiography
IHC	Immunohistochemistry
Indel	Insertion and deletion
INL	Inner nuclear layer
IPL	Inner plexiform layer
iPSCs	Human induced pluripotent stem cells
IR	Infrared
IRAF	Infrared autofluorescence
IRD	Inherited retinal disease
ITR	Inverted terminal repeat
KRAB	Kruppel-associated box
LAL Assay	Limulus amebocyte lysate assay
LCA	Leber congenital amarousis
LPS	Lipopolysaccharide
MD	Macular dystrophy
MeCP2	Methyl-CpG binding protein 2
MGF	Mean grey fluorescence
MMP	Matrix metalloproteinase
MWS	Medium-wave sensitive
nCas9	Cas9 nickase
NGS	Next generation sequencing
NHEJ	Non-homologous end joining
NHP	Non-human primate
OCT	Optical coherence tomography
ONL	Outer nuclear layer
OPL	Outer plexiform layer
OPN1LW	Opsin-1, long-wave sensitive, red opsin gene
OPN1MW	Opsin-1, medium-wave sensitive, green opsin gene
ORF	Open reading frame
OS	Outer segment

PAM	Protospacer adjacent motif
PCR	Polmyerase chain reaction
pegRNA	Prime editing guide RNA
PR2.1	L-opsin promoter
PRL	Photoreceptor layer
qPCR	Quantitative PCR
RCD	Rode-cone dystrophy
RCD	Rod cone dystrophy
RetGC1	Retinal guanylate cyclase
RGFP	Rod green fluorescent protein mouse line
RNFL	Retinal nerve fiber layer
RNP	Ribonucleic protein
RO	Retinal organoid
RP	Retinitis pigmentosa
RPE	Retinal pigment epithelium
RT	Reverse transcriptase
SaCas9	Staphylococcus Aureus Cas9
SCD	Sickle cell disease
SD-OCT	Spectral domain optical coherence tomography
SDS-PAGE	Sodium dodecyl sulfate-polyacrylamide gel electrophoresis
SEM	Scanning electron microscopy
sgRNA	Single guide RNA
STGD1	Stargardt disease type 1
TDT	Transfusion dependent beta-thalassemia
TIDE	Tracking of indels by decomposition
tracrRNA	Transactivating RNA
TSS	Transcriptional start site
WGS	Whole genome sequencing
XLRP	X-linked retinitis pigmentosa

Table of Contents

DECLARATION **2**

ACKNOWLEDGEMENTS **3**

ABSTRACT **5**

ABBREVIATIONS **7**

CHAPTER 1: INTRODUCTION **14**

1.1 Inherited Retinal Diseases 14
1.1.1 – Cone Dysfunction Syndromes *15*
1.1.2 – Cone Dystrophies and Cone-Rod Dystrophies *16*
1.1.3 – Rod-Cone Dystrophies *21*
1.2 Retinal Morphology Through Imaging 24
1.2.1 – Optical Coherence Tomography *24*
1.2.2 – Confocal Scanning Laser Ophthalmoscopy *26*
1.3 CRISPR Biology 29
1.3.1 – Basic Principles of CRISPR-Cas9 ..... *29*
1.3.2 – Base Editing and Prime Editing *31*
1.3.2.1 - Base Editing 31
1.3.2.2 - Prime Editing 33
1.3.3 – Epigenetic editing: CRISPRi and CRISPRa *34*
1.3.3.1 - CRISPR interference 35
1.3.3.2 - CRISPR activation 36
1.4 Clinical Trials in Ophthalmology 37
1.4.1 – Gene Therapy for IRDs *37*
1.4.2 – Gene Therapy Beyond the Eye *44*
1.5 Thesis Aims 46

CHAPTER 2: METHODS & MATERIALS **47**

2.1 Molecular 47
2.1.1 – PCR *47*
2.1.2 – PCR Purification *47*
2.1.3 – Gel Electrophoresis *48*
2.1.4 – Gel Extraction *48*
2.1.5 – Genomic DNA Extraction *49*
2.1.6 – Restriction Enzyme Digest *49*
2.1.7 – sgRNA Annealing and Phosphorylation *50*
2.1.8 – Plasmid Ligation *50*
2.1.9 – Plasmid Amplification and Isolation *50*
2.1.10 – PCR Cloning *51*
2.1.11 – Cloning sgRNAs into plasmids *52*
2.1.12 – Sanger Sequencing *53*
2.2 Cell and Tissue Culture 54
2.2.1 – Subculturing HEK293T Cell Line *54*
2.2.2 – Plasmid Transfection of Cultured Cells *54*
2.2.3 – HEK293T Cell Pelleting *54*
2.2.4 – Subculturing CGFP Fibroblasts *55*
2.2.5 – Electroporation of Mouse Fibroblast Cells *55*
2.2.6 – Fibroblast Cell Pelleting *56*
2.2.7 – EVOS Imaging *56*
2.2.8 – Dual Luciferase Assay *57*

2.2.9 – Tracking of Indels via Decomposition (TIDE) Analysis *59*
2.2.9.1 - Neural Retina Harvesting 59
2.2.9.2 - HEK293T Transfection 59
2.2.9.3 - CGFP Fibroblast Electroporation 60
2.2.10 – Interference of CRISPR Edits (ICE) Analysis *60*
2.3 AAV5 PRODUCTION 61
2.3.1 – Transfection *61*
2.3.2 – Harvesting and Lysing *62*
2.3.3 – Isolation of AAV Particles *62*
2.3.4 – AAV Purification and Concentration *64*
2.3.5 – Viral Titer *65*
2.3.6 Sodium Dodecyl Sulfate-Polyacrylamide Gel Electrophoresis (SDS-PAGE) *66*
2.4 IN VIVO 68
2.4.1 – Genotyping *68*
2.4.2 – Anesthesia *68*
2.4.3 – Pupil Dilation *69*
2.4.4 – Subretinal Injections *69*
2.4.5 – Confocal-Scanning-Laser Ophthalmoscopy and Optical Coherence Tomography *70*
Confocal Scanning Laser Ophthalmoscopy (cSLO) 71
Optical Coherence Tomography (OCT) 71
2.4.6 – Mean Grey Fluorescence Measurements of cSLO Images *72*
2.5 TISSUE ANALYSIS 74
2.5.1 – Enucleation and Tissue Collection *74*
2.5.2 – DNA Extraction *75*
2.5.3 – Tracking of Indels via Decomposition (TIDE) Analysis *75*
2.5.4 – Immunohistochemistry *75*
2.5.5 – Confocal Microscopy *76*
2.6 STATISTICS 77

CHAPTER 3: PILOT *IN-VIVO* STUDY OF AAV5 PACKAGED DELIVERY TO THE CGFP MOUSE RETINA 78

3.1 INTRODUCTION 78
3.2 MATERIALS AND METHODS 80
3.2.1 – Plasmid Cloning *80*
3.2.2 – Cell Culture and AAV Production *80*
3.2.3 – In-Vivo Analysis *80*
3.2.4 – Tissue Analysis *81*
3.2.5 – Statistical Analysis *82*
3.3 RESULTS 83
3.3.1 – Cloning and AAV Production *83*
3.3.2 – Subretinal injections of AAV5-CAG-DsRed and AAV5-hGRK1-DsRed at $5x10^{11}$ gc/mL in CGFP mice *85*
3.3.3 – Dose escalation response of subretinal injections of AAV5-hGRK1-DsRed at $1x10^{12}$ gc/mL *96*
3.4 DISCUSSION 99
3.4.1 – CAG and hGRK1 promoters drive DsRed expression in photoreceptors *99*
3.4.2 – Retinal Damage and Toxicity *100*
3.4.3 – Dose Response *103*
3.5 CONCLUSIONS 105

CHAPTER 4: *IN-VIVO* DISRUPTION OF CONE-SPECIFIC EGFP WITH A CRISPR-SACAS9 SYSTEM 106

4.1 INTRODUCTION 106

4.2 MATERIALS AND METHODS 108

4.2.1 – Plasmid Cloning *108*
4.2.2 – Cell Culture and AAV Production *108*

4.2.3 – TIDE Analysis ... *109*
4.2.4 – Sequencing the opsin locus control region and EGFP ... *109*
4.2.5 – In-Vivo Analysis ... *109*
4.2.6 – Tissue Analysis with Immunohistochemistry ... *110*
4.2.7 – Statistical Analysis ... *111*
Mean Grey Fluorescence ... 111
Immunohistochemistry Analysis ... 111
4.3 Results ... 112
4.3.1 – Sequencing the CGFP mouse ... *112*
4.3.2 – Cloning and AAV production ... *113*
4.3.3 – Retinal toxicity with increasing AAV dose ... *114*
Low Dose ... 115
Mid Dose ... 117
High Dose ... 119
4.3.4 – Active SaCas9 system disrupts EGFP in-vivo ... *121*
Low Dose ... 121
Mid Dose ... 126
High Dose ... 129
4.3.5 – Dose Response ... *132*
4.3.6 – Assessing DNA Editing ... *137*
4.4 Discussion ... 138
4.4.1 – EGFP Disruption ... *138*
4.4.2 – DNA Editing ... *140*
4.4.3 – Dose Response ... *145*
4.4.4 – Improving Cone Targeting ... *147*
4.5 Conclusions ... 149

CHAPTER 5: *IN-VITRO* SGRNA SCREENING FOR EPIGENETIC DSACAS9 REPRESSION ... 150

5.1 Introduction ... 150
5.2 Materials and Methods ... 152
5.2.1 – Plasmid Cloning ... *152*
5.2.2 – Cell Culture ... *152*
5.2.3 – CGFP Fibroblast Electroporation ... *152*
5.2.4 – HEK293T Transfections for TIDE Analysis ... *153*
5.2.5 – TIDE Analysis ... *153*
5.2.6 – ICE Analysis ... *153*
5.2.7 – Subcloning Analysis ... *154*
5.2.8 – Dual Luciferase Assay ... *154*
5.2.9 – EVOS Imaging ... *155*
5.2.10 – Statistical Analysis ... *155*
5.3 Results ... 156
5.3.1 – OPN1LW sgRNA screening with dual luciferase assay ... *156*
5.3.2 – Universal promoters drive expression of EGFP in CGFP fibroblast cell line ... *157*
5.3.3 – Evaluating on-target sgRNA efficiency in-vitro ... *162*
5.4 Discussion ... 165
5.4.1 – Screening OPN1LW sgRNA candidates using the DLA ... *165*
5.4.2 – Use of the CGFP fibroblast cell line ... *167*
5.4.3 – Optimizing electroporation of CGFP fibroblasts ... *172*
5.5 Conclusions ... 174

CHAPTER 6: GENERAL DISCUSSION ... 175

6.1 Summary of Thesis Aims and Outcomes ... 175
6.2 Improving Cone Photoreceptor Targeting ... 178

6.2.1 – Promoter and Delivery *178*
6.2.2 – Dose and Toxicity *180*
6.2.3 – Measuring Editing Rates *182*
6.3 Clinical Applications and Considerations 184
6.3.1 – Off Target Effects *185*
6.3.2 – Immune Response *187*
6.3.3 – Future Directions *189*
6.3.4 – Final Considerations *190*
6.4 Concluding Thoughts 193
CHAPTER 7: REFERENCES 194
CHAPTER 8: APPENDIX 206

Chapter 1: Introduction

1.1 Inherited Retinal Diseases

Inherited retinal diseases (IRDs) are the leading cause of blindness in working-age adults in the United Kingdom and present a large socioeconomic burden[1]. IRDs represent both a clinical and genetically heterogenous group of conditions which lead to degeneration of the retina. Due to recent advances in genetic diagnostic techniques such as next generation sequencing (NGS), over 300 genes/loci have been described in IRDs, helping to provide a molecular diagnosis or identification of pathogenic variants[2,3]. Genes identified include those involved in phototransduction, the process by which light is converted into visual information and sent from the eye to the cortex, where the light signal is interpreted into visual objects[4]. The majority of known mutations occur in photoreceptor cells or retinal pigment epithelium (RPE) cells, with some affecting the choroid. In all cases, visual impairment in IRDs is due to loss of photoreceptor function – either primary photoreceptor degeneration, or secondary following degeneration of the RPE or choroid.

With varied genetic origin, a wide range of phenotypes are seen within IRDs. Symptoms of IRDs can present from birth to adulthood with varied severity and progression. In all forms, management includes correction of refractive errors, use of low-vision aids, education, and support throughout education and work[5]. IRDs are historically divided into stationary vs. progressive, with the latter further subdivided into cone dystrophies (COD), cone-rod dystrophies (CORD), macular dystrophies (MD), and rod-cone dystrophies (RCD). Stationary subtypes include rod dysfunction syndromes and cone dysfunction syndromes (CDS) and typically present

congenitally. Since this thesis focuses primarily on cone photoreceptors, cone dysfunction syndromes, cone dystrophies, and cone-rod dystrophies will be further described.

1.1.1 – Cone Dysfunction Syndromes

Cone dysfunction syndromes (CDS) are stationary disorders with classic cone visual disturbances of reduced central visual acuity, photophobia, and color vision abnormalities.

The most common CDS is achromatopsia, which presents at birth or early-infancy and can cause complete or incomplete obliteration of cone function. Clinical variants in *CNGB3* and *CNGA3* account for most cases[6,7] as functional copies of *CNGB3* and *CNGA3* are responsible for encoding subunits of a cyclic nucleotide-gated ion channel necessary for cone phototransduction. Mutations in *ATF6, GNAT2, PDE6C*, and *PDE6H* account for a small amount of achromatopsia cases, with the remaining 10-25% of cases presenting without specific variant identification[6,7]. To date, most efforts have focused on gene replacement treatments for *CNGB3* and *CNGA3* achromatopsia, where functional copies of the mutated gene are delivered.

A study demonstrated restoration of cone function in a canine model of *CNGB3* achromatopsia using adeno-associated virus serotype 5 (AAV5) packaged gene replacement therapy[8]. Similarly, AAV5 packaged *CNGA3* replacement in a mouse model showed promising results, with restored cone ERG response, prevention of cone degeneration, and improved visual acuity[9]. A study in *CNGA3*$^{-/-}$ sheep with gene supplementation also showed improved cone ERG function[10]. Building on preclinical data, early phase clinical trials for achromatopsia have also focused on gene supplementation of *CNGB3*[11] and *CNGA3*[12] via AAV8 delivery. Both trials have concluded Phase

I/II enrollment, each demonstrating an acceptable safety profile with some evidence of functional improvement. Development of these therapies has been paused; however, results of trial follow-up will inform the possible effect of gene supplementation strategies and are discussed in more detail in section 1.4.

Mutations in *OPN1LW* and *OPN1MW*, which code for red (L) and green (M) cone opsins are implicated in the X-linked disorders, blue cone monochromatism (BCM) and Bornholm eye disease (BED)[13,14]. BCM presents similar to achromatopsia, although when patients are older, they retain some color discrimination as blue (S) cone opsin is unaffected[15]. Gene replacement of *OPN1LW, OPN1MW*, or a combination, has been shown to rescue M-cone function in *OPN1MW*$^{-/-}$ mice [16,17] and provides a proof of concept for treatment of BCM. BED was first described in a large Danish family and is also known as X-linked CDS associated with myopia and dichromacy [18]. BED remains a rare disorder and as of April 2024, no *in-vivo* studies were found and may remain so due to the high economic cost associated with treatment development.

1.1.2 – Cone Dystrophies and Cone-Rod Dystrophies

Cone dystrophies (COD) and cone-rod dystrophies (CORD) are progressive diseases with cone photoreceptor degeneration, often followed by rod involvement[4]. They are clinically characterized by progressive worsening of central vision, photophobia, and disturbances in color vision. Disease causing variants have been identified in over 30 genes, most often affecting structural proteins or those involved in the phototransduction cascade[4]. A summary of implicated genes affecting cone photoreceptors and their role in phototransduction can be found in Figure

1.1 while some of the most common mutations or those amenable to gene editing will be discussed below.

Mutations in *ABCA4* are the most common cause of autosomal recessive (AR) COD/CORD. *ABCA4* encodes a retina-specific ATP-binding cassette (ABC) transporter and mutations in the gene have been implicated in a variety of IRDs, including the most common cause of Stargardt disease (STGD1), a form of macular dystrophy[19–21]. The function of ABCA4 is vital to the retinoid cycle and mutations in the gene lead to buildup of toxic byproducts in the retina, leading to RPE degeneration followed by photoreceptor degeneration and loss[22]. *ABCA4* is a large gene (6.8kb) and due to the ~4.7kb packaging capacity of AAV, typical gene replacement strategies are unsuitable[23]. In one study, nonviral DNA nanoparticles were used to deliver a working copy of the *ABCA4* gene to *ABCA4* deficient mice[24]. Treated subjects demonstrated sustained transgene expression and improvement in retinal function and phenotype, suggesting use of nonviral NPs as an alternative gene delivery method, particularly for genes over the cargo capacity of AAV[24]. While gene supplementation is currently limited by delivery methods, alternative CRISPR-based editing strategies could be used to correct the specific *ABCA4* mutations implicated in AR COD/CORD or STGD1[25]. Additionally, based on the accumulation of phototransduction byproducts and associated inflammatory response caused by *ABCA4* mutations, various clinical trials are ongoing which target other components of the visual cycle or complement system[25].

Other genes implicated in AR COD/CORDs include *CDHR1, PDE6C,* and *PDE6H,* which go beyond the scope of this thesis and are summarized nicely elsewhere[4,26]. Recently in the MacLaren lab,

Yusuf et. al. developed an *in-vivo* gene supplementation strategy for *CDHR1* which demonstrated sustained structural, functional, and behavioral rescue of photoreceptors[27]. This exciting preclinical work will inform clinical trials aimed to treat *CDHR1* related CORD. No *in-vivo* studies were found focused on the COD/CORD causing mutations in *PDE6C* or *PDE6H*, however, these genes are also implicated in achromatopsia, and gene replacement strategies are being investigated. This highlights the overlap in genes implicated in IRDs which lead to a range of phenotypes depending on the specific mutation pattern.

Due to gain of function or dominant negative effects, mutations inherited in an autosomal dominant (AD) pattern are typically unable to be treated with gene supplementation, as is the case in autosomal recessive (AR) and X-linked IRDs. Some genetic causes of COD/CORD amenable to gene editing include mutations in *GUCY2D* and *GUCA1A* which are both involved in phototransduction and lead to gain of function. Mutations in *GUCY2D* are the most common cause of autosomal dominant (AD) CORD while mutations in *GUCA1A* are implicated in CODs and CORDs [28]. *GUCY2D* encodes retinal guanylate cyclase (RetGC1) which is responsible for replenishing intracellular cGMP to mediate membrane depolarization[29]. The activity of RetGC1 is influenced by guanylate cyclase activating protein 1 (GCAP1), an enzyme encoded by *GUCA1A*[30]. When engineering gene editing strategies for gain of function mutations, it is necessary to knockout the mutated gene while maintaining or restoring normal protein levels and function. One strategy to do this, in the absence of haploinsufficiency, involves allele specific silencing, where the mutated allele is targeted via the CRISPR-Cas9 system and disrupted, while the wildtype allele is untouched. This strategy relies of the presence of a specific sequence just

downstream of the disease-causing mutation, limiting the numbers of mutations amenable to allele-specific targeting. Alternatively, a sequence present in both alleles can be targeted for gene silencing, followed by supplementation of the healthy gene. Using this strategy, coined “ablate and replace”, the Boye group first demonstrated gene silencing of *GUCY2D* via a CRISPR-SaCas9 system causing decreased RetGC1 levels with associated loss of retinal function/structure in mice and NHP[31]. Next, the same CRISPR-Cas9 system was used to disrupt *GUCY2D* but a functional, CRISPR-Cas9 resistant *GUCY2D* copy was subsequently delivered to treated eyes, replacing the mutated gene[32]. In this manner, the authors demonstrated preserved retinal function and structure with the ablate and replace technique for *GUCY2D*. Both allele-specific targeting and gene disruption followed by supplementation could be implored for AD inherited IRDs and other AD conditions.

Additional COD/CORD associated targets for gene disruption include *PRPH2, TIMP3,* and *PROM1.* Over 90 mutations have been identified within *PRPH2* including those associated with pattern dystrophy or other dystrophies involving the macula[26,33]. *PRPH2* encodes peripherin-2, a protein involved in rod and cone outer segment morphogenesis. While there are a wide range of phenotypes caused by *PRPH2* mutations, most are inherited in an AD pattern. Once again, in the case of gain of function or dominant negative alleles, gene disruption and supplementation may be a therapeutic option. As of April 2024, no *in-vivo* studies were found targeting *PRPH2* with an active Cas9 gene editing system and challenges of targeting *PRPH2* are discussed in the review by Conley et. al[34]. Mutations in *TIMP3* are associated with Sorsby fundus dystrophy, a type of AD macular dystrophy[35]. *TIMP3* encodes an inhibitor of matrix metalloproteinases (MMP), which are

involved in extracellular matrix turnover and angiogenesis[36]. Mutations in TIMP3 lead to protein accumulation in Bruch's membrane and the role of *TIMP3* in angiogenesis leads to neovascularization classically seen in SFD[36]. The role of base editing for treatment of SFD was recently discussed by our lab, and some mutations may additionally be amenable to gene knockout and replacement[37]. Variants in PROM1 are associated with AR and AD CORD, with the AD phenotype leading to a dominant negative effect[38]. In the retina, PROM1 encodes a glycoprotein important to photoreceptor disc morphogenesis and autophagy within the RPE[39,40]. For AD forms of *PROM1* associated CORD, gene silencing followed by supplementation could be of therapeutic interest.

Finally, mutations in the exon open reading frame 15 (ORF15) of *RPGR* typically result in X-linked retinitis pigmentosa (XLRP) with a rod-dominant phenotype. However, mutations in the 3' C terminus of ORF15 also cause most cases of X-linked COD/CORD with typical symptoms including poor central vision, photophobia, and abnormal color vision[41]. *RPGR* has several splicing isoforms with ORF15 being implicated in IRDs. The RPGR encoded protein localizes to the outer segment of rods and is involved with ciliary processes, however, the function of each isoform has not been fully elucidated. Despite this, research has recently implicated distal truncating mutations in leading to a cone-predominant phenotype[42,43]. Importantly, it was shown these mutations cause disruption of RGPR glutamylation via interaction with TTLL5, pushing the retina to a cone-dominant phenotype[42]. Mutations in *TTLL5* have previously been shown to cause retinal dystrophy with a cone phenotype, so it is not surprising that impaired TTLL5-RPGR interaction causes a cone dystrophy. Currently, no *in-vivo* studies have specifically looked at treatment for

X-linked COD/CORD caused by *RPGR* mutations, however, many gene augmentation strategies focused on XLRP are underway and discussed in section 1.4.

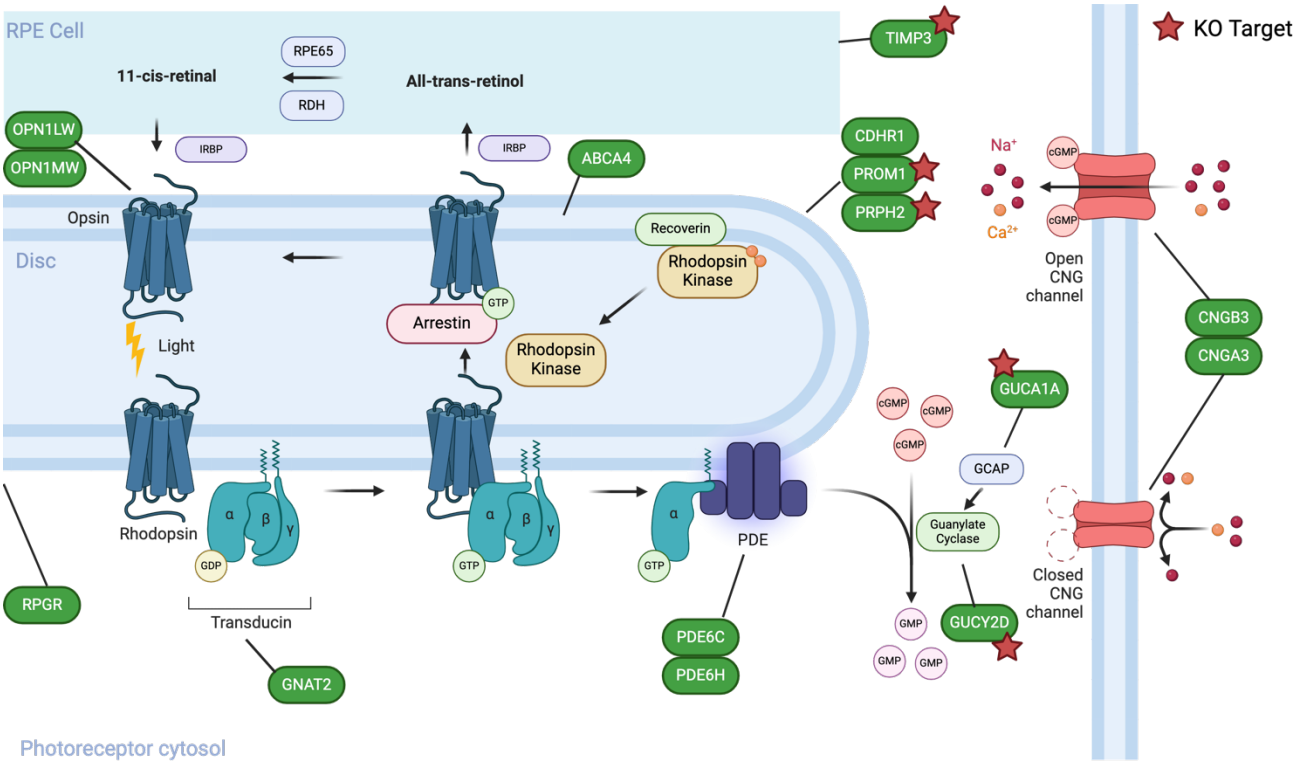


Figure 1.1 Phototransduction and associated COD/CORD genes

Summary of the phototransduction cascade with some of the COD/CORD causing genes highlighted in green. Genes with mutations amenable to gene silencing noted with a red star. Figure created in BioRender.

1.1.3 – Rod-Cone Dystrophies

As this thesis focuses on cone photoreceptors, only a brief portion will be dedicated to rod-cone dystrophies (RCDs). RCDs typically result from a primary insult in rod photoreceptors with degeneration, often followed by cone dysfunction. Retinitis pigmentosa (RP) is the most common

form of IRD, with an estimated prevalence of 1:4,000 individuals[44]. There are a variety of genetic causes, with over 50 genes implicated, as well as multiple inheritance patterns and phenotypes.

A great amount of research has been conducted on *in-vivo* CRISPR-based therapies in various models of RP, providing important preclinical data for clinical trial development and framework for future COD/CORD studies. CRISPR-SpCas9 was used in a mouse model carrying the S334ter *Rho* mutation to disrupt the mutated region, preventing photoreceptor degeneration, and improving retinal function in a rat model of AD RP[45]. Similarly, the AD RP causing P23H *Rho* mutation was targeted in a mouse model harboring the mutation with SpCas9, with intravitreal AAV9 injection slowing degeneration of photoreceptors and improving retinal function[46]. Mutations in *RPGR* are implicated in XLRP, casing frameshift mutations, and have also been the target of Cas9 therapies[47]. In their study, Gumerson et. al. injected AAV2/8 carrying a SpCas9 construct targeted to *RPGR* into retinae of rd9 mice, showing restoration of the reading frame and RPGR expression[47]. Finally, mutations in *PDE6B* are implicated in cases of AR RP. The newer prime editing strategy was delivered to mice retinae via AAV to correct a point mutation in *PDE6B*, producing up to 76% editing in retinal cells with improved visual performance[48]. More broadly, within RP, preservation of cone function is a major therapeutic goal, as cone loss is thought to be mediated by primary rod degeneration. By knocking down *Nrl*, a gene vital to rod determination, via CRISPR-SpCas9, cone function was preserved with rods adopting a more cone-like state had increased survival in mice[49]. With a broad range of targetable mutations, *in-vivo* models of RP amenable to CRISPR-based therapies, have greatly increased knowledge regarding gene editing treatment strategies for IRDs.

Despite the large interest in therapeutic development for IRDs, currently treatment options are severely limited, with most treatments being symptom driven. The value of targeted gene knockout and other gene editing methods have already demonstrated their value in treating preclinical models of these devastating disorders. Continued efforts to develop safe and effective treatments alongside advances in diagnosis, NGS, and the gene engineering toolbox provide an exciting opportunity to continue developing targeted treatments for IRDs. Throughout this thesis, I focus specifically on cone photoreceptor targeting, with future applications aimed at treating disorders involving cones as discussed above.

1.2 Retinal Morphology Through Imaging

Imaging within the field of ophthalmology has become vital to clinical practice and basic science. The ability to visualize anatomic structures, including individual retinal layers, has allowed clinicians and researchers to make significant progress in understanding physiology and disease states. Within IRDs, the heterogenous nature can cause difficulty in diagnosis, but multimodal imaging has played a large role in identifying distinct imaging findings of groups of IRDs and understanding disease mechanisms[50]. More immediate to this thesis, adaptation of imaging devices for *in-vivo* animal work has allowed continued scientific discovery and testing of novel treatments.

1.2.1 – Optical Coherence Tomography

Optical coherence tomography (OCT) is an optical imaging modality which performs high-resolution, cross-sectioning tomographic imaging of internal microstructures of tissue by measuring backscattered or back reflected light[51]. It was first described in 1991 and improvements to the technology have been rapid. OCT has become a staple within ophthalmology as it provides quick *in-vivo* visualization and quantification of individual retinal layers and the optic nerve. Current clinical technology now allows imaging with an axial resolution of 1.3 uM[52]. This is incredible considering the average foveal thickness of a healthy human retina is between 215-230uM[53,54]. The mouse retina does not have a fovea but does follow the same organization of a human retina, with an average retinal thickness around 200uM[55]. While this is comparable to human retinal thickness, it is important to note that in

transgenic mouse strains, especially those mimicking degenerative states, the retina is often thinner[56]. An example of the individual retinal layers of the mouse model used throughout this thesis, CGFP, as imaged by spectral domain OCT (SD-OCT) can be seen in Figure 1.2. Layers are identified according to data published by Staurenghi et. al, which developed a consensus nomenclature for retinal layers as imaged by SD-OCT[57].

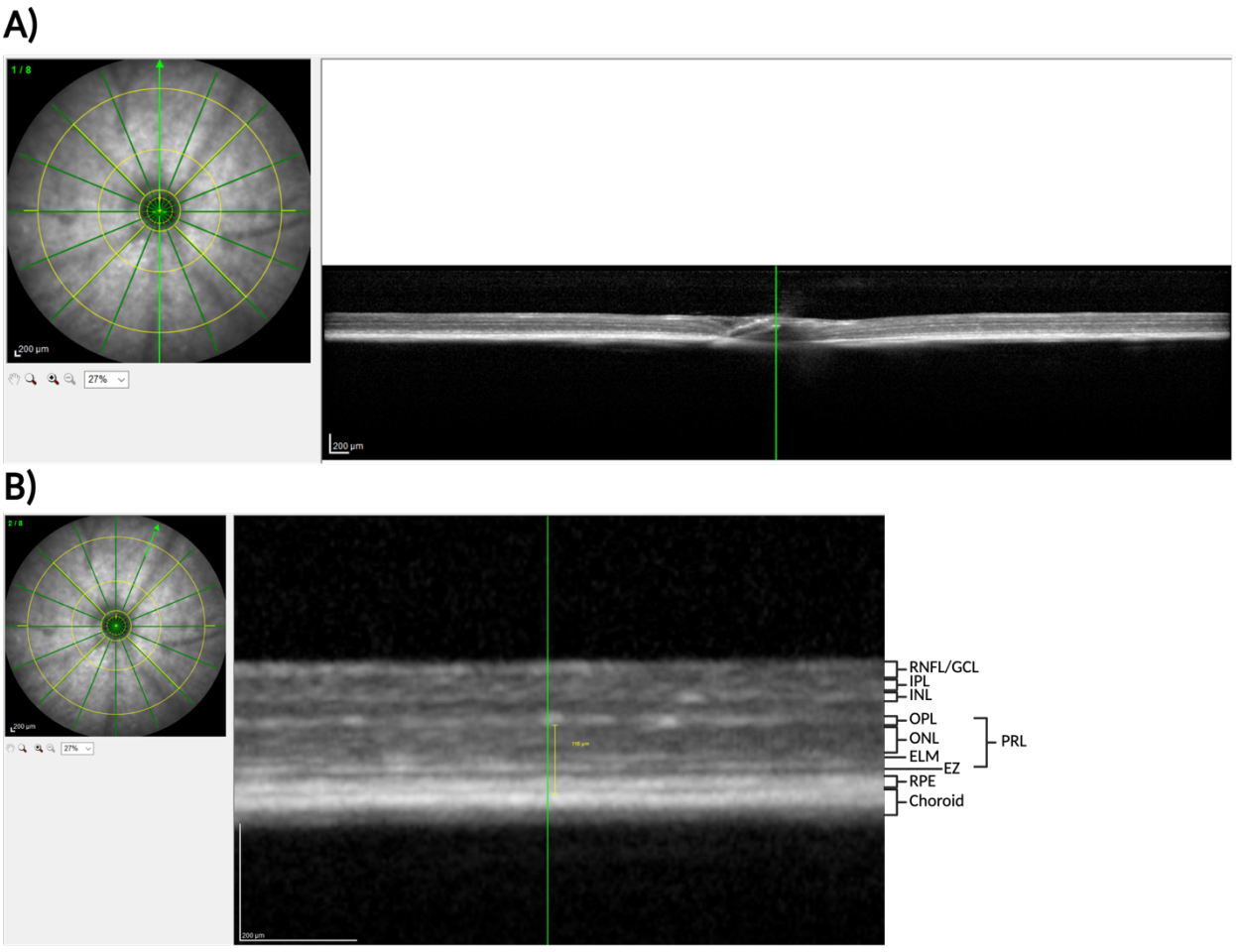


Figure 1.2 Example of SD-OCT scan of CGFP mouse

A) SD-OCT scan of transgenic CGFP mouse centered at optic nerve. B) Zoom in of SD-OCT scan to highlight individual layers labeled as: RNFL, retinal nerve fiber layer; GCL, ganglion cell layer; IPL, inner plexiform layer; INL, inner nuclear layer; OPL, outer plexiform layer; ONL, outer nuclear layer; ELM, external limiting membrane; EZ, ellipsoid zone; PRL, photoreceptor layer; RPE, retinal pigment epithelium; choroid.

The ability to quickly visualize retinal layers has cemented OCT in its diagnostic role. OCT is commonly used to diagnose and monitor a wide breadth of retinal diseases including macular holes, macular degeneration, diabetic retinopathy, and IRDs (Just to name a few!). It is important to note that the applications of OCT are not limited to the retina. Within ophthalmology OCT also plays a critical role in diagnosis and monitoring of glaucoma and other diseases affecting the optic nerve as well as corneal pathologies.

1.2.2 – Confocal Scanning Laser Ophthalmoscopy

Confocal scanning laser ophthalmoscopy (cSLO) is another *in-vivo* imaging modality that has become crucial to retinal physicians and researchers. cSLO relies on focusing laser beams on a target and subsequent scattered light rays of ocular structures, typically within the retina or optic nerve head, are detected and provide tomographic information[58]. Imaging the fundus has evolved from simple color photos in fundus photography to advanced techniques captured by cSLO such as fluoresceine angiography (FA), indocyanine green angiography (ICGA) and different forms of auto-fluorescent (AF) imaging. More recently, technologies have been created which combine imaging modalities such as OCT and cSLO to allow multi-modal imaging with correlation of imaging findings within a specific location[59].

FA and ICGA utilize water soluble dyes to visualize the retinal and choroidal vasculature[60]. While not used in this thesis, clinically, this imaging technique is of great diagnostic value in assessing perfusion and neovascularization of the retina and choroid in processes such as retinal vein occlusions, diabetic retinopathy, uveitis, and oncologic processes[61].

AF imaging has gained tremendous significance in clinical and translational applications. The basic concept of fundus AF (FAF) is based on the presence of fluorophores within photoreceptors and the retinal pigment epithelium[62]. Through fluorophore detection, changes in the retina can be observed. This is of particular value in understanding IRDs where photoreceptor and RPE degeneration occur[63]. For example, in some forms of RP, a hyperfluorescent ring can be seen surrounding the macula. The ring is thought to demarcate healthy vs. unhealthy retina, as lipofuscin levels increase due to photoreceptor degeneration[64,65]. Indeed, AF has been used to quantify lipofuscin fluorescence in RP and cone disease[66,67]. Various disease specific FAF findings have been observed and aid in diagnosis but are well beyond the scope of this thesis. Notably though, using FAF images alone, a deep-learning neural network was shown to be able to distinguish between three IRDs and healthy retina, highlighting the utility of FAF[68]. Since IRDs have phenotypic and genetic heterogeneity imaging alone is unlikely to diagnose, but it will remain a vital tool for screening and monitoring disease progression or treatment response.

In bench research, AF additionally provides a method to image fluorescent proteins *in-vivo*. For example, green fluorescence can be imaged using blue AF (BAF) and green AF (GAF), which is used throughout this thesis. An example of cSLO images of the CGFP mouse can be seen in Figure 1.3. Clinically, BAF imaging has been used to study inflammatory diseases of photoreceptors in correlation with other cSLO modalities[69]. Additionally, both BAF and GAF have been used to size atrophic RPE lesions in *ABCA4* related retinopathies and have demonstrated their usefulness in IRD monitoring[70].

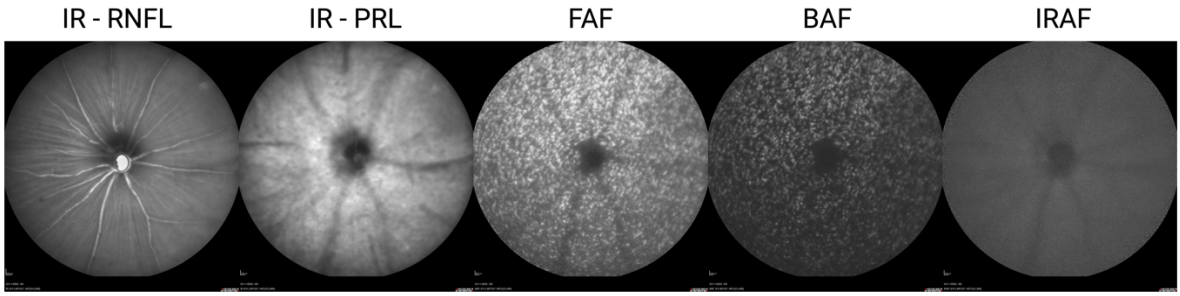


Figure 1.3 cSLO Imaging of CGFP mouse retina

cSLO images of CGFP mouse retina, all images centered on optic nerve. From left to right: Infrared (IR) in focal plane of retinal nerve fiber layer (RNFL), IR in focal plane of photoreceptor layer (PRL), fundus auto-fluorescence (FAF), blue auto-fluorescence (BAF), infrared auto-fluorescence (IRAF).

1.3 CRISPR Biology

1.3.1 – Basic Principles of CRISPR-Cas9

The discovery of clustered regularly interspaced short palindromic repeats (CRISPR) loci in conjunction with CRISPR-associated (Cas) genes, as a gene modulating technique has revolutionized the field of genetics. First discovered in *E. coli* [71], CRISPR alongside Cas genes were later found in several prokaryotes and it was demonstrated that the CRISPR-Cas system acts as an acquired immune response to foreign nucleic acids[72–74].

The CRISPR-Cas9 system was adapted by scientists to silence DNA in a targeted manner[75]. In this elegant system, a single guide RNA (sgRNA) composed of a CRISPR RNA (crRNA) and trans-activating RNA (tracrRNA) directs the Cas endonuclease to a specific protospacer adjacent motif (PAM) next to the target DNA sequence. After PAM site recognition, the Cas9 protein unwinds the DNA, allowing the sgRNA to hybridize with the exposed DNA strand. If the sgRNA and DNA sequences match, the Cas9 endonuclease cuts the DNA, creating a double-stranded break (DSB)[75] (Figure 1.5).

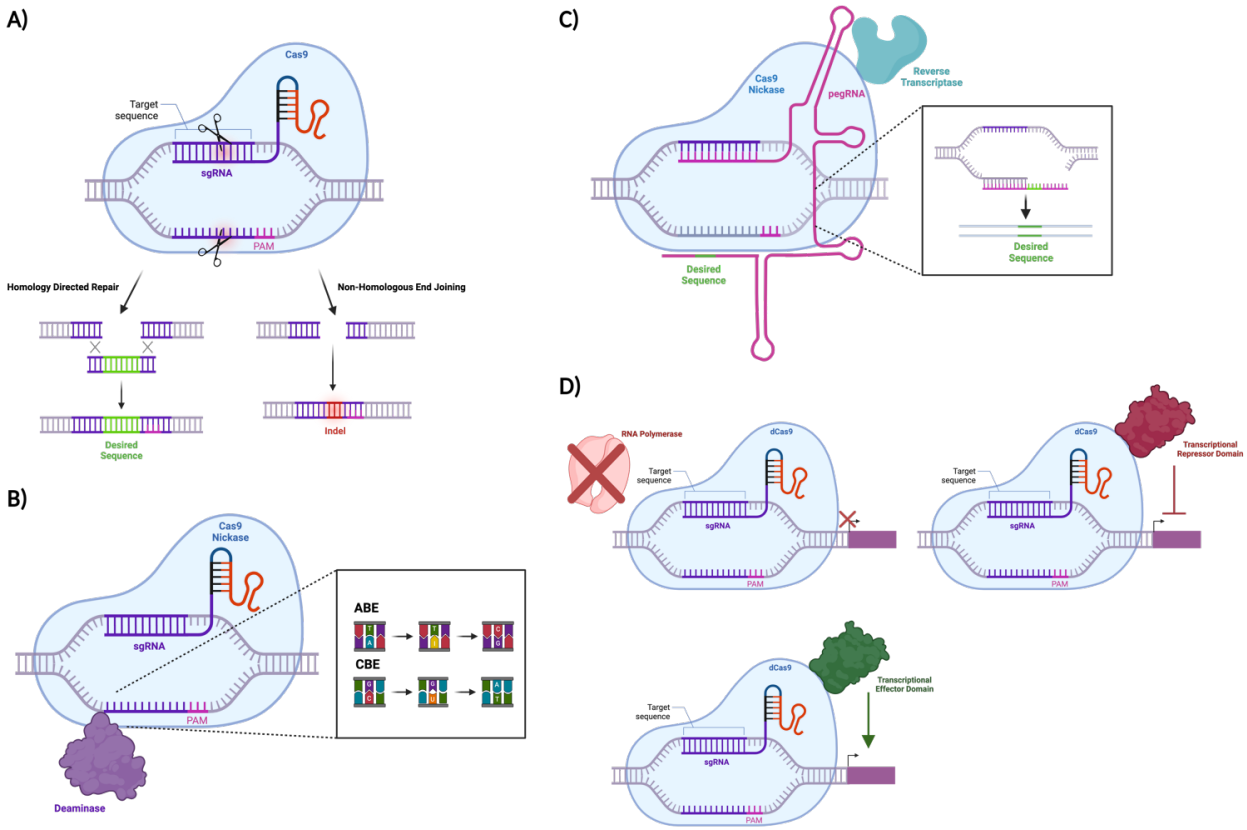


Figure 1.5 Summary of gene editing strategies

A) CRISPR-Cas9 system highlighting sgRNA binding to target DNA sequence upstream of the Cas-specific PAM site. Following DSBs, DNA is repaired either via the NHEJ or HDR pathway. B) Base-editor systems of ABE and CBE highlighting the mismatch repair pathway to cause single nucleotide substitutions at a specified site. C) Prime-editor system with pegRNA including the desired DNA sequence for insertion. D) Epigenetic systems of CRISPRi (decrease transcription) via inhibition of RNA Polymerase or a transcriptional repressor domain and CRISPRa (increase transcription) via a transcriptional effector domain.

The damaged DNA is subsequently repaired using either non-homologous end joining (NHEJ), or homology directed repair (HDR)[76,77]. NHEJ is an error prone repair mechanism that results in random insertions and deletions (indels), leading to gene disruption. The indels created by NHEJ are particularly useful as a potential therapeutic strategy for autosomal dominant IRDs. By

disrupting the region of a mutated gene, this allows for allele specific gene disruption with preservation of the other wildtype allele. Alternatively, a nonmutated region can be targeted, causing disruption of both alleles. DSBs can also be repaired by HDR, which relies on the presence of a homologous donor sequence to cause insertion of a specific DNA sequence, following the DSB, potentially restoring wildtype sequence[78]. To date, most *in-vivo* gene editing treatment strategies for IRDs rely on the NHEJ pathway and are briefly discussed in section 1.1 of this chapter.

1.3.2 – Base Editing and Prime Editing

While NHEJ mediated repair allows targeted gene disruption and is feasible to knockout a disease-causing allele, there are instances where insertion of a precise sequence would be beneficial. Due to the imbalance of NHEJ vs. HDR following DSBs, HDR is unlikely to be a feasible method to precisely correct mutations. Recently, two CRISPR-Cas mediated systems, base editing and prime editing, have been developed which enable precise mutation correction without reliance on either NHEJ or HDR.

1.3.2.1 - Base Editing

The original DNA base editor systems include cytosine base editors (CBE) and adenine base editors (ABE)[79,80]. CBE systems cause C->T transitions while ABE systems cause A->G[81]. Performing such transitions could enable correction of T->C mutations (or A->G if targeting the reverse strand) and G->A mutations (or T->C if targeting the reverse strand). The basic components of these systems include a Cas enzyme to direct repair and a single-stranded DNA

modifying enzyme, a DNA deaminase, which induces the desired nucleotide change[81]. Since the discovery of CBE in 2016, various modifications have been added to the cytosine deaminase or Cas enzyme to increase the efficiency of editing and reduce bystander effects[82]. One of the most important modifications to the system was the creation of the adenosine deaminase enzyme, which is not naturally occurring. By engineering the adenosine deaminase in combination with the Cas9 enzyme, the ABE system was born[80]. Compared to CBE systems, ABE has significantly lower indel formation and off target effects. More recently, base editing systems have been developed which support C->G transversions, greatly expanding the therapeutic potential of base-editing[83].

Several *in-vivo* studies have demonstrated the success of the technology in tissues of the liver, skeletal muscle, heart, CNS, and eye[84]. In the retina, ABEs were used to correct an Rpe65 mutation causing LCA2 in the *rd12* mouse model. By targeting this mutation, the authors of these studies showed 14-15% base editing with restoration of visual function[85,86]. Additionally, Jo et. al isolated RPE65 expressing cells and within that cell population reported 89% editing[85]. Building on the first base editing paper, the Liu and Palczewski labs demonstrated increased editing efficiencies and rescue/preservation of cone cells in the rd12 mouse treated with an ABE, furthering its potential therapeutic use for LCA2[87.]

The first clinical trial involving base editing is underway, led by Verve Therapeutics. The trial targets a mutation in *PCSK9* which leads to dangerously high LDL-C levels as seen in familial hypercholesterolemia. The high LDL-C levels cause increased risk of significant cardiovascular

disease and plaque formation. The company uses an ABE and sgRNA targeting *PCSK9* packaged in lipid nanoparticles to deliver an injection to the liver[88]. Results from phase 1 of VERVE-101 demonstrated dose-dependent reductions in LDL-C levels, with an average reduction of 46%[89]. The company has also launched VERVE-102, which targets the *PCSK9* mutation with the same ABE and sgRNA but differs in the lipid nanoparticle and receptors that allow entry to the hepatocyte cells[89]. The results of these clinical trials, editing a single base pair of the human genome, are eagerly awaited.

1.3.2.2 - Prime Editing

Beyond the transition mutations amenable to base editors, prime editing has greatly expanded targeted mutation correction. The main components of the prime editing system consist of a Cas9 nickase (nCas9), an engineered reverse transcriptase (RT), and a prime editing guide RNA (pegRNA)[90]. Similar to a sgRNA, the pegRNA directs nCas9 to the targeted DNA region. However, the pegRNA additionally contains the sequence of the desired DNA alteration that will be transcribed by the RT. In the original paper, Anzalone et. al demonstrated the ability of a prime editing system to correct all 24 single-nucleotide substitutions *in-vitro* with an average editing efficiency of 33%[90]. Since discovery of the system, numerous modifications have been tested to refine the editing potential and decrease off-target and bystander effects[81,91]. The ability of prime editing systems to cause insertions, deletions, or single-base substitutions could in theory correct up to 89% of known disease-causing mutations in humans[90].

Additional modifications to the prime editing system have been introduced to further the *in-vivo* potential of prime editing, demonstrating editing efficiencies up to 42% in the brain, 46% in the liver, and 11% in the heart when delivered via AAV[92]. More recently, the Liu group engineered virus-like particles (eVLPs) which allow transient delivery of the prime editing system in ribonucleic protein (RNP) form[93]. In their paper, two ocular genes were targeted *in-vivo*: a 4bp mutation in *MFRP* which causes retinal degeneration in humans, and a nonsense mutation in *RPE65* implicated in LCA2. With a single subretinal injection, 15% editing at the targeted *MRFP* mutation was observed in the retina with restored protein expression of MFRP in the RPE. Targeting the *RPE65* mutation caused editing rates of 7.2% on bulk RPE cells, the highest prime editing rate in this *in-vivo* model to date, and 14% when analyzing cDNA with associated full-length RPE65 expression via western blot[93]. Beyond the applications of prime editing to correct a mutation, the ability to deliver this system as RNPs leads to transient expression which greatly decreases the off-target effects that remain a concern within all CRISPR-based gene therapies.

1.3.3 – Epigenetic editing: CRISPRi and CRISPRa

Finally, mutation-independent methods of gene regulation have been engineered, targeting gene expression at an epigenetic level. CRISPR interference (CRISPRi) and CRISPR activation (CRISPRa) act at the RNA level to down or up-regulate gene transcription. Within eukaryotes, transcription relies on the interaction of RNA polymerase II and transcription factors to bind to a promoter within a DNA sequence. Specialized protein domains within transcription factors allow them to interact with cellular proteins to cause increased or decreased gene expression. Epigenetic editing systems take advantage of the transcriptional domains, cleverly fusing them to an

inactivated Cas9 protein (dCas9) which is unable to cleave DNA. A sgRNA guides the dCas9 fusion complex to a targeted DNA region, typically the promoter sequence, allowing the transcriptional domains to cause targeted changes in gene expression[75]. The inducible and reversible nature of the epigenetic editing systems make them attractive candidates for eukaryotic gene regulation.

1.3.3.1 - CRISPR interference

RNA interference (RNAi) and active Cas9 systems are both able to cause decreased gene expression. However, off-target effects and inefficient knockdown limit their use. CRISPRi provides an additional method of gene silencing while expanding the range of targets amenable to gene silencing.

Upon dCas9-sgRNA binding, the complex sterically blocks transcriptional elongation[94,95]. While this interaction alone causes decreased gene expression, the addition of transcriptional repressor domains improves the level of gene silencing. Among the repressor domains, the Kruppel-associated box (KRAB) is one of the most used. The KRAB domain causes DNA to adopt a heterochromatin state, in which DNA is tightly bound to histone proteins, preventing the interaction with RNA Polymerase II, and therefore blocking transcription[96]. The use of multiple transcriptional repressor domains within a dCas9 system has demonstrated even higher levels of gene silencing[97] while the use of multiple sgRNAs has demonstrated the ability to silence multiple genes in parallel[98]. Titrating the level of dSaCas9 or sgRNA expression via inducible promoters has also demonstrated the feasibility of controlled gene repression [99]. Within ophthalmology, the dCas9-KRAB system was utilized *in-vivo* to silence activity of the *Rho* gene, which is mutated in

dominantly inherited RP[100]. The ability to induce gene silencing without causing permanent changes to the genome and the ability to control gene repression levels could both prove to be of great value in treating dominantly inherited IRDs and other AD diseases[101].

1.3.3.2 - CRISPR activation

Previously, increasing the level of gene expression was reliant on gene augmentation, where a healthy gene is delivered to the cellular population of interest. While this strategy has great therapeutic benefit, demonstrated by the success of Luxturna, a gene replacement for *RPE65*, high gene levels have caused toxic damage to the retina. CRISPRa provides a potential solution, as levels of gene activation can be modified by the number of effector domains in a system[102]. As well as controlling the level of gene activation, in CRISPRa multiple genes can be targeted at once[103]. Excitingly, Bohm et. al delivered a CRISPRa system to the mouse retina, causing targeted transcriptional activation of M-opsin (*OPN1MW*) in cone photoreceptors[104]. The applications of CRISPRa and CRISPRi have already proven their utility in genetic screens and showcased their potential therapeutic benefit[105].

1.4 Clinical Trials in Ophthalmology

Within ophthalmology, great progress is being made in gene therapy applications for IRDs. The eye is an attractive target organ, with easy accessibility, immune-privileged status [106], and presence of a tight junction mediated blood-retinal barrier [107].

1.4.1 – Gene Therapy for IRDs

In 2017, Luxturna was approved by the Food and Drug Administration (FDA) as the first AAV based approved gene therapy treatment[108]. Luxturna is approved for treatment of IRD in individuals with a biallelic mutations in the *RPE65* gene, which encodes the retinoid isomerase protein responsible for conversion of 11-trans-retinyl to 11-cis-retinal throughout phototransduction[109]. The biallelic mutation is seen in Leber Congenital Amaurosis 2 (LCA2) and autosomal-recessive RP[110,111]. Treatment is delivered as a single subretinal injection of a functional *RPE65* transgene packaged in AAV2. Gene replacement remains a promising avenue to treat conditions which lead to loss of function, such as autosomal recessive disorders, where supplementation with a healthy gene copy can restore function.

A similar gene supplementation strategy has been used for X-linked disorders such as XLRP. Mutations in the *RPGR* gene accounts for 10-20% of RP and is the most common form of XLRP, leading to severe phenotype[112,113]. In the first clinical trial, Nightstar Therapeutics (now Biogen Inc.) and The University of Oxford developed a codon optimized *RPGR* sequence that was driven by the human rhodopsin kinase 1 (hGRK1) promoter, packaged in AAV8, and delivered via subretinal injection[114]. Safety and efficacy were demonstrated in the subsequent phase 1/2

clinical trial and gain of visual function as a secondary endpoint demonstrated promising results[115]. Applied Genetic Technologies Corporation (now Beacon Therapeutics), utilized a very similar gene supplementation strategy, packaging codon optimized RPGR driven by the hGRK1 promoter in a variant of AAV2 prior to subretinal injection. Results of the phase I/II and extension show a favorable safety profile and evidence of visual improvement in the high dose branch[116]. Results of subsequent phases from each company are eagerly awaited. Additional strategies to treat XLRP are discussed in detail elsewhere[117] and ongoing clinical trials are summarized in Table 1.2.

Several additional clinical trials are utilizing gene supplementation to treat IRDs including LCA, Stargardt disease, Retinoschisis, Achromatopsia, Choroideremia, and various causes of RP. Ongoing clinical trials for the mentioned IRDs are summarized in Table 1.2.

While Luxturna represents a significant advancement in gene therapy, gene replacement strategies are only feasible in loss of function conditions. In the case of conditions which lead to dominant negative or gain of function effects, a different strategy must be employed.

The first ophthalmologic CRISPR-based clinical trial, led by Editas Medicine, targeted the IVS26 point mutation in the *CEP290* gene as a potential treatment for LCA10. *CEP290* encodes a protein involved in outer segment photoreceptor regeneration and phototransduction[118]. The IVS26 mutation causes a premature stop codon and loss of function[119]. While the loss of function mutations can be treated with gene replacement, this trial demonstrates the feasibility of using

active CRISPR gene editing within the eye. Building on preclinical data, EDIT-101 uses AAV5 based delivery of hGRK1-SaCas9 with two U6 driven sgRNAs targeting both ends of the mutated *CEP290* DNA region in hopes to correct splicing [120]. The phase 1/2 clinical trial, BRILLIANCE, enrolled 14 subjects with the IVS26 mutation to receive subretinal injections of the EDIT-101 vector. In an update in November 2022, after 12 months of follow-up, the company announced three of the 14 subjects experienced clinically meaningful improvements in best corrected visual acuity (BCVA) with an acceptable safety profile [121]. Interestingly, two of the three treatment responders were homozygous for the IVS26 mutation. Unfortunately, Editas Medicine paused enrollment for the trial and are currently looking for commercial partners to continue development. Only one other clinical trial is currently using Cas9 gene disruption in ophthalmology to target the *Rho* gene, which is implicated in RP[122]. Once again, this trial targets a loss of function, highlighting the feasibility of gene editing within ophthalmology. Use of an active CRISPR system to correct a gain of function or dominant negative remains to be tested.

The results of these clinical trials are likely the first of many in a new era of gene therapy research for IRDs. While it is exciting to think about the potential utility of CRISPR-based therapies, it is important to consider off-target effects and immune responses and continue utilizing preclinical models to test these therapies prior to use in human subjects.

Table 1.2 Ongoing Gene Therapy Clinical Trials in IRDs

Condition	Gene Replacement Target	Gene Therapy Product	Injection	Phase	Completion Date	Sponsor	Trial ID
X-linked Retinitis Pigmentosa	RPGR	AAV8-hGRK1-RPGR (BIIB112)	Subretinal	4	2026	NightstaRx Ltd. (Biogen Inc.)	NCT03584165
		AAV2tYF-GRK1-hRPGRco (AGTC-501)	Subretinal	1/2	2025	Applied Genetics Technologies Corporation (Beacon Therapeutics)	NCT03316560
				2/3	2029		NCT04850118
		AAV.R100-hcoRGPR (4D-125)	Intravitreal	1/2	2029	4D Molecular Therapeutics	NCT04517149
		FT-002	Intraocular	1	2027	Frontera Therapeutics	NCT05874310
		AAV5-hRKp.RPGR	Subretinal	3	2024	MeiraGTx (Janssen Research & Development, LLC)	NCT04671433
				3	2029		NCT04794101
		AAV5-hRKp.RPGR	Subretinal	3	2029	Janssen Pharmaceutical K.K.	NCT05926583
LCA10	IVS26 of CEP290*	AAV5-hGRK1-SaCas9 (EDIT-101)	Subretinal	1/2	2025	Editas Medicine	NCT03872479
	CEP290	AAV5-*Nr2e3* (OCU400)	Subretinal	1/2	2024	Ocugen	NCT05203939
LCA2	RPE65		Subretinal	1/2	2030		NCT01208389

		AAV2-hRPE65v2 (voretigene neparvovec)		3	2029	Spark Therapeutics	NCT00999609
				Obs.	2030		NCT03602820
		AAV9-CAG-RPE65 (HG004)	Subretinal	1/2	2025	HuidaGene Therapeutics Co, Ltd	NCT05906953 and NCT06088992
		rAAV2-CBSB-hRPE65	Subretinal	1	2026	University of Pennsylvania	NCT00481546
		FT-001	Subretinal	1/2	2029	Frontera Therapeutics	NCT05858983
LCA1	GUCY2D	AAV5-hGRK1-GUCY2D (ATSN-101)	Subretinal	1/2	2027	Atsena Therapeutics Inc	NCT03920007
LCA5	LCA5	AAV8-hLCA5 (OPGx-001)	Subretinal	1/2	2027	Opus Genetics Inc.	NCT05616793
RP	Rho, PDE6B	AAV5-*Nr2e3 (OCU-400)*	Subretinal	1/2	2024	Ocugen	NCT05203939
				3	2026		NCT06388200
	Rho	rAAV- Cas9 (ZVS203e)*	Subretinal	1	2026	Peking University Third Hospital	NCT05805007
	Rho, PDE6A, PDE6B	AAV-RdCVF-RdCVFL (SPVN06)	Subretinal	1	2029	SparingVision	NCT05748873
	PDE6B	AAV2/5-hGRK1-hPDE6B (HORA-PDE6B)	Subretinal	1/2	2029	eyeDNA	NCT03328130
	PDE6A	rAAV.hPDE6A	Subretinal	1/2	2027	STZ eyetrial	NCT04611503
	RLBP1	AAV8-hRLBP1 (CPK850)	Subretinal	1/2	2026	Novartis Pharmaceuticals	NCT03374657
	CNGA1	AAV2.NN-CNGA1 (VG901)	Intravitreal	1	2025	ViGeneron GmbH	NCT06291935

	Optogenetics	rAAV2-CAG-ChronosFP (BS01)	Intravitreal	1/2	2029	Bionic Sight LLC	NCT04278131
		rAAV-PsCatCh2.0 (ZM-02)	Intravitreal	1	2028	Zhongmou Therapeutics	NCT06292650
		rAAV2.7m8-CAG-CHrimsonR-tdTomato(GS030)	Intravitreal	1/2	2025	GenSight Biologics	NCT03326336
		AAV2-ChR2 (RST-001)	Intravitreal	1/2	2024	AbbVie	NCT02556736
Choroideremia	CHM	AAV2-REP1 (BIIB111)	Subretinal	3	2026	NightstaRx Ltd. (Biogen Inc.)	NCT03584165
		4D-R100AAV-CHM (4D-110)	Intravitreal	1	2027	4D Molecular Therapeutics	NCT04483440
Achromatopsia	CNGA3	rAAV.hCNGA3	Subretinal	1/2	2027	STZ eyetrial	NCT02610582
		rAAV2tYF-PR1.7-hCNGA3 (AGTC-402)	Subretinal	1/2	2026	Applied Genetic Technologies Corp (Beacon Therapeutics)	NCT02935517
	CNGB3	rAAV2tYF-PR1.7-hCNGB3 (AGTC-401)	Subretinal	1/2	2026		NCT02599922
Leber's Hereditary Optic Neuropathy	ND4	scAAV2-P1ND4v2	Intravitreal	1	2024	Byron Lam	NCT02161380
		rAAV2/2-ND4 (GS010)	Intravitreal	3	2024	GenSight Biologics	NCT03293524
		rAAV2-ND4 (NFS-01)	Intravitreal	2/3	2025	Huazhong University of Science and Technology	NCT03153293

		rAAV2-*ND4* *(*NR082)	Intravitreal	1/2	2029	Neurophth Therapeutics Inc	NCT05293626
				2/3	2028		NCT04912843
	ND1	rAAV2-ND1 (NFS-02)		1/2	2029		NCT05820152
X-linked juvenile retinoschisis	RS1	AAV8-scRS/IRBPhRS	IVT	1/2	2025	VegaVect, Inc.	NCT02317887
		AAV-RS1 (JWK002)	Subretinal	1	2029	Genevector Biotechnology Co., Ltd	NCT06345898
		LX103	Intravitreal	Obs.	2028	Innostellar Biotherapeutics	NCT05814952
		AAV.SPR-hGRK1-hRS1syn (ATSN-201)	Subretinal	1/2	2029	Atsena Therapeutics Inc.	NCT05878860
		rAAV-hRS1 (ZM-01)	Intravitreal	1	2027	Zhongmou Therapeutics	NCT06066008
		AAV-RS1 (IVB102)	Intravitreal	1	2029	InnoVec Biotherapeutics Inc.	NCT06289452
Stargardt Disease	RORA	AAV5-hRORA (OCU410ST)	Subretinal	1/2	2025	Ocugen	NCT05956626
	ABCA4	Dual AAV-ABCA4 (JWK006)	Subretinal	1/2	2029	West China Hospital	NCT06300476

* Use an active Cas9 system, not gene supplementation.

1.4.2 – Gene Therapy Beyond the Eye

Outside of ophthalmology, new gene therapy treatments continue to advance research and possible therapeutic interventions. Since the approval of Luxturna, several other treatments which deliver a functional copy of a disease-causing mutation have been approved[123]. Vyjuvek delivers a functional copy of the *COL7A1* gene, which is mutated in dystrophic epidermis bullosa[124]. Zolgensma has been approved to deliver a functional copy of *SMN* via AAV9 to patients with spinal muscular atrophy[125]. Roctavian delivers a functional copy of the *F8* gene restoring production of Factor VIII in patients with severe Hemophilia A[126]. For patients with Hemophilia B, Hemgenix uses AAV5 to deliver a functional *F9* gene, increasing the activity of Factor IX[127] while Beqvez uses AAVrh74 to deliver *F9*[128,129]. Elevidys is approved for treatment of Duchenne muscular dystrophy, delivering a micro-dystrophin gene via AAVrh74[130,131].

Mechanisms beyond gene replacement have also begun to reach clinical trials outside of the eye, with the development of a gene-therapy based treatment for non-muscle invasive bladder cancer. Intravesicular administration of Astiladrin delivers interferon-a2b via a replication-deficient recombinant adenovirus[132]. Transfected uroepithelial cells then produce IFN-a2b, activating apoptosis and death of cancerous cells[133].

The FDA recently approved the first cell-based gene therapy, Zynteglo, to treat transfusion dependent beta-thalassemia (TDT). The treatment consists of an infusion of CD34+ hematopoietic stem cells and progenitor cells (HSPCs) previously transduced with the B-globin gene via lentiviral delivery. Results of the trial demonstrated transfusion independence in both

adult and pediatric patients[134]. The same company, Bluebird Bio, used a similar strategy to develop Lyfgenia to treat sickle cell disease (SCD) via delivery of a functional B-globin gene[135] and Skysona for treatment of cerebral adrenoleukodystrophy patients with an *ABCD1* mutation[136]. Other approved cell-based gene therapies include Lenmeldy for treatment of metachromatic leukodystrophy with *ARSA* genetic mutations[137].

Excitingly, beyond replacing genes through HSPCs, the DNA of HSPCs have been edited via the CRISPR-Cas9 system. Vertex Pharmaceuticals and CRISPR Therapeutics developed a gene editing therapy, Casgevy, to treat SCD and TDT. By electroporating HSPCs with a Cas9 system targeted to *BCL11A* prior to patient infusion, levels of fetal hemoglobin rose enough in participants to maintain transfusion independence and eliminate vaso-occlusive events[138,139]. While follow-up is necessary to elucidate all effects of these approved cell-based gene therapies, the development and approval marks an exciting time for gene editing applications.

As of April 2024, no other gene editing therapies have been approved, but many investigative therapies remain in clinical trials. Great strides have been made in gene therapy with the approval and success of gene replacement and cellular-based strategies like those discussed above. Use of gene editing therapies such as targeted gene knockout, base editing, prime editing, or epigenetic regulation will no doubt be of tremendous therapeutic value in correcting disease-causing mutations.

1.5 Thesis Aims

As genetic diagnosis and gene therapy technologies advance, it is critical to identify disease causing mutations that may be amenable to gene supplementation therapy and/or gene editing strategies. Several cone specific genes have been identified in IRDs that may be amenable to gene editing via a CRISPR-Cas9 system. This thesis broadly focuses on targeting photoreceptors of a transgenic mouse line using AAV and investigating the use of CRISPR-SaCas9 to target a cone specific gene *in-vivo*.

1.) Assess vector and delivery optimization of AAV5 in combination with a ubiquitous vs. photoreceptor-specific promoter in a mouse model which expresses EGFP under a cone-specific promoter (CGFP model).

2.) Investigate *in-vivo* knockdown of EGFP in EGFP-expressing photoreceptors using an active Cas9 system.

3.) *In-vitro* screening of sgRNA candidates which target the red-opsin gene (OPN1LW) for epigenetic repression applications.

Chapter 2: Methods & Materials

2.1 Molecular

2.1.1 – PCR

PCR was carried out using KOD HotStart DNA Polymerase Master Mix, unless stated otherwise, using manufacturer's instructions. Briefly, 12.5uL KOD Master Mix, 10-50ng of template DNA, 0.5uM primers, and brought to a total volume of 20uL with molecular grade water and run on a SimpliAmp or BioRad thermocycler. General PCR conditions for KOD HotStart Polymerase are outlined in Table 2.1. PCR products were visualized using gel electrophoresis to determine size and check for unspecific products or contaminants.

Custom primers (Sigma-Aldrich or Integrated DNA Technologies) were designed to amplify a region of interest and sequences can be found in the appendix. Primers were designed to be 17-21bp in length, GC content 40-60%, melting temperature (Tm) between 55-65 °C and within 2°C of each other for pairs, with no more than 3 subsequent base pair repeats.

2.1.2 – PCR Purification

PCR products were purified using the QIAquick PCR Purification Kit (Qiagen) using manufacturer's instructions. Briefly, PCR products were mixed with binder buffer. DNA was captured via a silica-gel membrane column, washed, and eluted using provided elution buffer. DNA yield was measured via nanodrop technology.

Table 2.1 General PCR conditions for KOD HotStart DNA Polymerase

Step	Temperature (°C)	Time	Number of Cycles
Polymerase Activation	95°C	2 minutes	1
Denaturing	95°C	20 seconds	35-40
Annealing	Lowest Primer Tm	10 seconds	
Extension	70°C	10 seconds/kb (<500bp amplicon) 15 seconds/kb (500-1000bp amplicon) 20 seconds/kb (1-3kb amplicon) 25 seconds/kb (>3kb amplicon)	
Final Extension	70°C	5 minutes	1

2.1.3 – Gel Electrophoresis

1-2% agarose gels were made using agarose (Sigma-Aldrich) diluted in Tris/Acetate/EDTA (TAE) buffer (ThermoFischer) and GelRed Nucleic Acid Stain (Biotium). Gels were run with a Quick-Load 1kb (New England Biolabs) or Quick-Load 100bp (New England Biolabs) ladder in a tank containing TAE for 1-2 hours at a voltage between 100-120V. Bands were visualized, and gels imaged on a UV transilluminator (NuGenius by SYNGENE).

2.1.4 – Gel Extraction

DNA bands were extracted using the QIAquick Gel Extraction Kit (Qiagen) using manufacturer's instructions. Briefly, Individual DNA bands were visualized and carefully isolated under UVblue light. Bands were dissolved in buffer at 97°C. DNA was captured via a silica-gel membrane column, washed, and eluted using provided elution buffer. DNA yield was measured via nanodrop technology.

2.1.5 – Genomic DNA Extraction

Genomic DNA (gDNA) was extracted using the QIamp Mini Kit (Qiagen) following manufacturer's instructions for a given tissue type. Cell pellets were thawed and resuspended in PBS, followed by lysis using proteinase K for 10 minutes. Retinal tissue was mechanically disrupted using a tissue homogenizer and resuspended in PBS, followed by 1 hour lysis using proteinase K, vortexing every 20 minutes. In all instances, gDNA was captured via a silica-gel membrane column, washed, and eluted using provided elution buffer. gDNA yield was measured via nanodrop technology.

2.1.6 – Restriction Enzyme Digest

All plasmids were digested using commercially available restriction enzymes (New England Biolabs), using manufacturer's instructions. Where appropriate, plasmids were dephosphorylated using shrimp alkaline phosphatase (rSAP) (New England Biolabs). Digested products were visualized using gel electrophoresis (section 2.1.3), extracted (section 2.1.4), and purified (section 2.1.2. Single and no-enzyme controls were run in parallel to confirm enzyme activity.

Table 2.2 Restriction enzyme digests performed on each plasmid

Plasmid	Enzymes for plasmid cloning	Enzyme for oligonucleotide insertion	ITR Confirmation
pCAG-DsRed	HindIII, BglII		XmaI
phGRK1-DsRed	HindIII, BglII		
phGRK1-SaCas9		BsaI	
pEFS-SaCas9		BsaI	
pEFS-dSaCas9		BsaI	
pPsiCHECK2		NheI	

2.1.7 – sgRNA Annealing and Phosphorylation

Custom oligonucleotides were phosphorylated in a 1:1 ratio of forward:reverse using T4 PNK (New England Biolabs) following manufacturer's instructions. The reaction was denatured at 37°C for 20 minutes and annealed by incubating at 95°C for 4 minutes before stepwise cooling to 25°C over 45 minutes using thermocycler (SimpliAmp; ThermoFisher).

2.1.8 – Plasmid Ligation

A linearized backbone and insert were ligated at a ratio of 1:8 (Backbone:Insert) for 12 hours at room temperature using T4 DNA Ligase (New England Biolabs) in 10x T4 DNA Ligase buffer (New England Biolabs). Ligase-deficient and backbone only control reactions were run in parallel to assess self-ligation.

2.1.9 – Plasmid Amplification and Isolation

Ligation products were transformed into XL10-Gold Ultracompetent Cells (Agilent Technologies) following the manufacturers protocol. Cultures were then spread onto Luria Broth (LB)-Agar culture plates prepared with 100Pg/mL ampicillin (Sigma-Aldrich) and incubated at 37°C overnight.

For screening of successfully ligated plasmids, individual bacterial colonies were picked and cultured in LB. The culture broth was centrifuged to obtain bacterial cell pellets, and plasmids isolated using the Zyppy Plasmid Miniprep Kit (Zymo Research). For AAV production and

transfection experiments, endotoxin-free plasmid preparations were created using the NucleoBond Xtra Maxi Endotoxin-Free (Takara Bio).

2.1.10 – PCR Cloning

To create the hGRK1-DsRed plasmid, a CAG-DsRed plasmid (Gift from Michelle McClements) was digested using HindIII and BglII and dephosphorylated using rSAP. The resulting product was visualized with gel electrophoresis. The backbone fragment containing DsRed was extracted and purified. The hGRK1 sequence of a hGRK1-SaCas9 plasmid (Gift from Ariel Kantor) was PCR amplified with primers designed to add HindIII and BglII overhangs to the 5' and 3' end, respectively. The PCR product was visualized by gel electrophoresis to confirm expected band size and digested with HindII and BglII before PCR purification. The resulting DsRed backbone and hGRK1 insert were ligated using T4 DNA Ligase in a 1:7 (backbone:insert) ratio. The process is outlined in Figure 2.1. The ligation product was transformed into XL10-Gold Ultracompetent Cells, spread onto LB-Agar plates with ampicillin, and allowed to grow at 37°C overnight. Individual colonies were selected and cultured in LB before miniprep and Sanger sequencing.

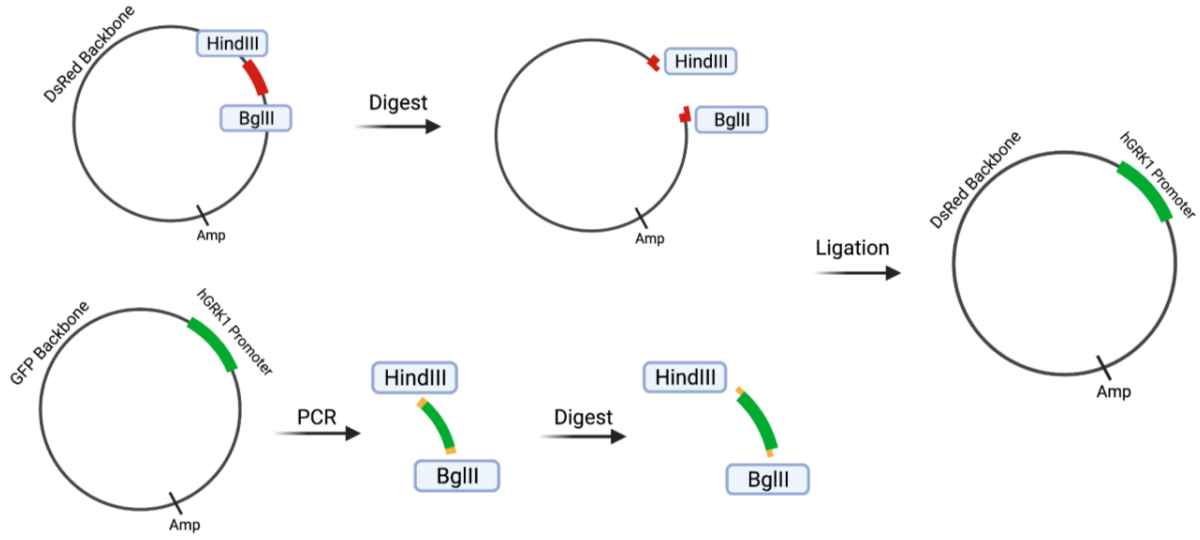


Figure 2.1 Overview of PCR Cloning

Overview of PCR based cloning to change CAG promoter to hGRK1 promoter in DsRed backbone. pCAG-DsRed digested with HindIII and BglII. hGRK1 promoter PCR amplified using primers adding HindIII and BglII restriction enzyme sites. PCR product digested with HindIII and BglII. Digested DsRed backbone and digested hGRK1 PCR product ligated to produce phGRK1-DsRed.

2.1.11 – Cloning sgRNAs into plasmids

sgRNAs were cloned into parent plasmids which contained the sgRNA scaffold. The sgRNA was ordered as two separate oligonucleotides with BsaI restriction enzyme overhangs on the 5' and 3' ends. The oligonucleotides were phosphorylated and annealed (section 2.1.7). The parent plasmid was digested with BsaI (section 2.1.6), a small amount was visualized with gel electrophoresis to confirm digestion, while the rest was PCR purified (section 2.1.2). The purified digested plasmid and annealed sgRNA were ligated with T4 ligase (section 2.1.8) at an insert:ligation ratio of 8:1. The ligation product was transformed into XL10 Gold Ultracompetent Cells (Agilent Technologies) and expanded using miniprep (section 2.1.9). Miniprep products

were sent for sanger sequencing to confirm sgRNA insertion (section 2.1.12) and ITR presence was confirmed with XmaI restriction enzyme digest (section 2.1.6). If proceeding with AAV production or a high concentration was needed, the plasmid was Maxiprepped (section 2.1.9).

2.1.12 – Sanger Sequencing

All sequencing was performed through GENEWIZ by Azenta. Samples were purified before being diluted to 10-50ng/uL with molecular grade water. Samples were sent either premixed of predefined following manufacturer's instructions.

2.2 Cell and Tissue Culture

2.2.1 – Subculturing HEK293T Cell Line

Cryopreserved human embryonic kidney 293 cells (HEK293T cells, GenTarget Inc, USA), were resuscitated and cultured in complete medium created from High-Glucose Dubecco Modified Eagle Medium (DMEM) (Gibco) with L-glutamine, supplemented with 10% foetal bovine serum (FBS) (Gibco) and 1% penicillin-streptomycin (P/S) (Sigma-Aldrich). Cells were cultured at 37°C in a 5% CO2 humidified incubator (ThermoElectron). Cells were passaged every 3-5 days prior to reaching confluency.

2.2.2 – Plasmid Transfection of Cultured Cells

See section 2.2.8 for details of transfection for Dual Luciferase Assay and section 2.2.9 for details of transfection for TIDE analysis.

2.2.3 – HEK293T Cell Pelleting

Cells were pelleted for downstream applications such as gDNA extraction. In this instance, media was removed from wells and cells were washed with sterile PBS. Cells were dissociated using TrypLE Express Enzyme (Gibco) and neutralized with complete medium. The cell suspension was transferred to an Eppendorf tube on ice before being spun at 3000xg for 10 minutes at 4°C. The supernatant was removed, and the cell pellet was resuspended with 500uL of sterile PBS before being centrifuged at 3000xg for 10 minutes at 4°C. The supernatant was removed, and cell pellets were stored at –80°C.

2.2.4 – Subculturing CGFP Fibroblasts

Cryopreserved CGFP derived fibroblasts from skin biopsies (Gift from Dr. Maria Kaukonen, Univeristy of Oxford) were resuscitated and cultured in complete medium made of High-Glucose DMEM supplemented with 1% L-glutamine, 20% FBS (Gibco) filtered through a 0.22-micron filter, 1% GlutaMAX (Gibco), and 1% P/S (Sigma-Aldrich). This medium will be referred to as skin medium for the remainder of this thesis. Cells were cultured on 100mm plates at 37°C in a 5% CO2 humidified incubator. Cells were passaged every 3-5 days prior to reaching confluency.

2.2.5 – Electroporation of Mouse Fibroblast Cells

Confluent 100mm plates were dissociated with TrypLE Express Enzyme (Gibco) and neutralized with skin medium before mechanical disruption of cell adhesions with a 1000uL sterile pipette tip. An aliquot of the cell suspension was mixed with equal part trypan blue and counted (TC20 Automated Cell Counter, BioRad). The remainder of the suspension was placed into a 15mL falcon tube and centrifuged at 500xg for 5 minutes at 20°C. Supernatant was removed and the cell pellet was resuspended in R-Buffer (Invitrogen™ Neon™ Transfection System) to reach a density of $1x10^5$ cells/10uL. Per each reaction, $1x10^5$ cells were combined with 300-900ng of plasmid DNA and electroporated using settings in Table 2.3. After electroporation, cells were seeded into a 24-well or 6-well plate with 500uL of skin media in each well. Cells were left between 3-14 days and media was changed at day 3 post-transfection to remove cell debris following electroporation. Plates were imaged using EVOS microscope (section 2.2.7).

Table 2.3 Electroporation parameters for CGFP Fibroblasts

Voltage	Time	Pulses
1650V	10ms	3

2.2.6 – Fibroblast Cell Pelleting

Media was removed from wells and cells were washed with 500 uL sterile PBS. Cells were dissociated using TrypLE Express Enzyme (Gibco) and neutralized with skin medium before mechanical disruption with a sterile pipette tip. The cell suspension was transferred to an Eppendorf tube on ice before being spun at 3000xg for 10 minutes at 4°C. The supernatant was removed, and the cell pellet was resuspended with 500uL of sterile PBS before being centrifuged at 3000xg for 10 minutes at 4°C. The supernatant was removed, and cell pellets were stored at –80°C.

2.2.7 – EVOS Imaging

HEK293T cells and CGFP fibroblasts were imaged using the EVOS FL Auto 2 Cell Imaging System (ThermoFischer) to elucidate the presence of EGFP, auto-fluorescence, cell health, and cell structure. Gain of individual channels (green, brightfield) were adjusted so that no saturation is visible with maximum signal gained with off-set function sometimes used to minimize background noise. Images were acquired with 10x and 4x objectives and exported as .tiff files for analysis using ImageJ.

2.2.8 – Dual Luciferase Assay

The dual luciferase assay (DLA) was used to screen the efficiency of sgRNA candidates for CRISPRi applications. This method relies on emission of two different luciferase genes under the control of 2 different promoters to quantitatively measure gene expression, Figure 2.2. For sgRNA screening, the region of interest is cloned into the PsiCHECK2 plasmid (Promega) using NheI restriction sites, upstream of the Renilla gene. In this case, regions of the OPN1LW gene were cloned into the vector (section 2.1.11) and correct insertion and direction confirmed by sanger sequencing. sgRNA candidates targeting the OPN1LW gene were cloned into pEFS-dSaCas9.KRAB-MeCP2 (section 2.1.11) and insertion was verified by sanger sequencing. If the sgRNA candidate binds the region of interest, transcription of Renilla luciferase should be disrupted relative to Firefly luciferase expression.

Confluent HEK293T cells were diluted in phenol red-free complete medium supplemented with 10% FBS and 1% P/S. and seeded in a 96 well plate Corning White Polystyrene Microplate (Sigma-Aldrich) at a density of 4.5E+5 cells/mL. 100uL of the cell suspension was added to each well and left for 24 hours until approximately 80% confluent. Of note, wells along the plate edge were not used to avoid interference with luciferase measurement readings. 24-hours post-seeding, wells were transfected using TransIT-LT1 transfection reagent (MirusBio), OptiMEM reduced serum media (ThermoFischer), 300ng pEFS-dSaCas9.KRAB-MeCP2 DNA, and 500ng of PsiCHECK2 plasmid DNA. Cells were transfected with one of the 3 test parameters in Table 2.4. 48-hours post-transfection, Renilla and Firefly luciferase expression were measured using the Dual-Glo Luciferase Assay (Promega) following manufacturer instructions. Quantitative luciferase

expression was measured on a FLUOstar Omega plate reader and results were exported to Excel for analysis. Normalized Renilla luciferase expression in test samples was compared to normalized Renilla expression of corresponding positive control.

Table 2.4 Dual luciferase assay test conditions

Positive Control (Max Renilla)	Negative Control (No Renilla)	SgRNA Screen
PsiCHECK2 w/ OPN1LW region + pEFS-dSaCas9 w/ nontargeting gRNA	pEFS-dSaCas9 w/ OPN1LW sgRNA candidate	PsiCHECK2 w/ OPN1LW region + pEFS-dSaCas9 w/ OPN1LW sgRNA candidate

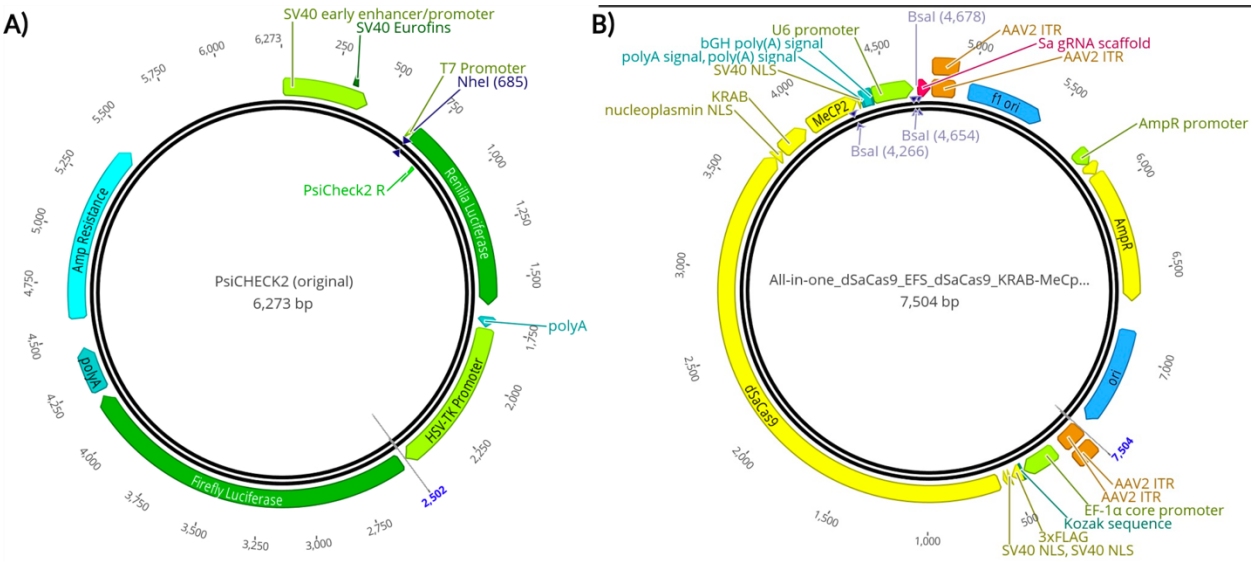


Figure 2.2 Map of parent plasmids used in dual luciferase assay

A) Map of PsiCHECK2 plasmid (Promega) with NheI restriction enzyme site used to clone in OPN1LW gene regions. B) Map of pEFS-dSaCas9.KRAB-MeCP2 with BsaI restriction enzyme sites used to clone in sgRNA candidates.

2.2.9 – Tracking of Indels via Decomposition (TIDE) Analysis

TIDE analysis was developed as a method to determine the editing efficiency of genome-editing methods, such as CRISPR, within the DNA of a pool of cells[140]. The traces of edited DNA are compared to untransfected controls and estimates the number of insertions or deletions (indels) in a sample. Briefly, cells were harvested, transfected, or electroporated and left for an appropriate amount of time before being pelleted. gDNA was extracted and the region of interest PCR amplified using primers 200bp upstream and 500bp downstream of the expected cut site. Purified PCR products were sent for sanger sequencing using the forward primer. Chromatogram files of samples were uploaded into TIDE software alongside sequence data of unmodified DNA. Decomposition was assessed and the window adjusted as necessary to produce clean reads.

2.2.9.1 - Neural Retina Harvesting

Details of neural retina cell harvesting for TIDE analysis can be found in section 2.5.3.

2.2.9.2 - HEK293T Transfection

Confluent HEK293T cells were diluted in complete medium and seeded in a 12 well plate at a density of 1E+5 cells/well. Approximately 24 hours post-seeding when cells were ~80% confluent, wells were transfected using TransIT-LT1 transfection reagent (MirusBio), OptiMEM reduced serum media (ThermoFischer), and 500ng of pEFS-SaCas9 with OPN1LW sgRNA. 48-hours post-transfection, media was changed to complete medium with 2% FBS and 1% P/S.

2.2.9.3 - CGFP Fibroblast Electroporation

Details can be found in section 2.2.5. Briefly, $1x10^5$ CGFP fibroblast cells were electroporated using 600-900ng of pEFS-SaCas9 with OPN1LW sgRNA with settings in Table 2.3. Following electroporation, cells were seeded into a 24-well or 6-well plate with 500uL of skin media in each well. Cells were left between 7-14 days and media was changed at day 3 post-transfection to remove cell debris following electroporation. Plates were imaged using EVOS microscope (section 2.2.7) to confirm successful electroporation.

2.2.10 – Interference of CRISPR Edits (ICE) Analysis

ICE Analysis is a software developed by Synthego, which quantifies overall editing efficiency and identifies the types of edits present in a sample exposed to CRISPR. Similar to TIDE, analysis is done on sanger sequencing results of samples exposed to the relevant CRISPR system. Resulting chromatogram files of sequencing data as prepared in section 2.2.9 were uploaded into ICE software alongside sequencing data of unmodified DNA and a specified sgRNA to assess the editing efficiencies and types of edits induced.

2.3 AAV5 Production

2.3.1 – Transfection

HEK293T cells were resuscitated from cryopreservation and allowed to equilibrate before proceeding with AAV5 production (section 2.2.1). Cells were expanded from T75 to T175 to Hyperflasks (Corning) so that for each virus to be produced, two Hyperflasks (Corning) were seeded. Cells were expanded into Hyperflasks in complete medium (DMEM High Glucose, 10% FBS, 2mM L-Glutamine, 50,000 units penicillin, 100ug/mL streptomycin) and allowed to grow for 72 hours.

Cells were transfected using the TransIT-VirusGEN transfection reagent (MirusBio) with a total of 500ug of DNA split between pDP5 (Plasmid Factory, Germany) and plasmid of interest and incubated for 72 hours at 37°C. Plasmid DNA amounts were calculated to deliver an equal molar ratio of each plasmid (Table 2.5). pDP5 contains the helper, *rep2*, and *cap5* genes needed for AAV generation. Transgene plasmids were purified with NucleoBond Xtra Maxi Endotoxin-Free (Takara Bio) (section 2.1.9) and digested with XmaI (section 2.1.6) to confirm presence of ITRs prior to transfection. At time of transfection, medium was changed to DMEM high glucose, 2% FBS, 2mM L-Glutamine, 50,000 units penicillin, 100ug/mL streptomycin.

Table 2.5 Plasmid concentrations for AAV transfection to deliver equal molar ratio

	Plasmid	Size (kb)	Amount/Transfection (ug)
1	pPD5 (AAV5 Backbone)	21.8	405
	phGRK1-DsRed	5.1	95
2	pPD5 (AAV5 Backbone)	21.8	376
	pCAG-DsRed	7.2	124
3	pPD5 (AAV5 Backbone)	21.8	378
	phGRK1-SaCas9-F10	7.1	122
	phGRK1-SaCas9 NT	7.1	122

2.3.2 – Harvesting and Lysing

Transfected cells were left in the Hyperflasks for 72 hours then detached by physical disruption and centrifuged for 10 minutes at 1200g at 20°C in 500mL plastic centrifuge bottles. The supernatant was removed, and the cell pellet was resuspended with lysis buffer (1M Trizma base, 150mM NaCl, pH 8.5) and a Mini EDTA-free protease inhibitor pellet (Roche). Cells were frozen at –80°C for 1 hour then thawed at 37°C for 15 minutes. The freeze/thaw cycle was repeated for 3 complete cycles. On the final thaw, 5uL Benzonase (50U/mL) (Merck) was added to the lysate and incubated at 37°C for 45 minutes, shaking every 15 minutes. Following incubation, the lysate was centrifuged at 3,700g for 20 minutes at 20°C while iodixanol gradients were prepared (Table 2.6).

2.3.3 – Isolation of AAV Particles

Isolation of AAV5 was achieved using iodixanol gradient ultracentrifugation. The iodixanol preparations were layered in OptiSeal tubes (VWR) and the AAV lysate was carefully layered on top of the fractions (Figure 2.3). Of note, one 15mL AAV lysate requires 2 iodixanol gradients. Any remaining space in the OptiSeal tube was filled to the top using lysis buffer. The OptiSeal tubes

were sealed and placed in a 70 Ti rotor in an Optima XW-90 ultracentrifuge (Beckman Coulter) and spun at 59,000rpm for 90 minutes at 20°C. Following centrifugation, the AAV particles diffuse between the interface of the 60% and 40% iodixanol fractions (Figure 2.3). AAV was aspirated by piercing the OptiSeal tubes with an 18g needle attached to a 5 mL syringe, with attention not to disturb the 25% fraction with proteinaceous material – this was transferred to a sterile falcon tube and stored at 4°C for a maximum of 12 hours.

Table 2.6 Preparations for *two* iodixanol gradients

Fraction	**Iodixanol (Sigma)**	**5M NaCl**	**5X PBS-MK**	**H_2O**	**Phenol Red (Sigma)**	**Volume Added to Each Tube**
15%	4ml	3.2ml	3.2ml	5.6ml	-	7.2 mL
25%	5ml	-	2.4ml	4.6ml	20µl	4.8mL
40%	6.7ml	-	2ml	1.3ml	-	4mL
60%	10ml	-	-	-	20µl	4mL

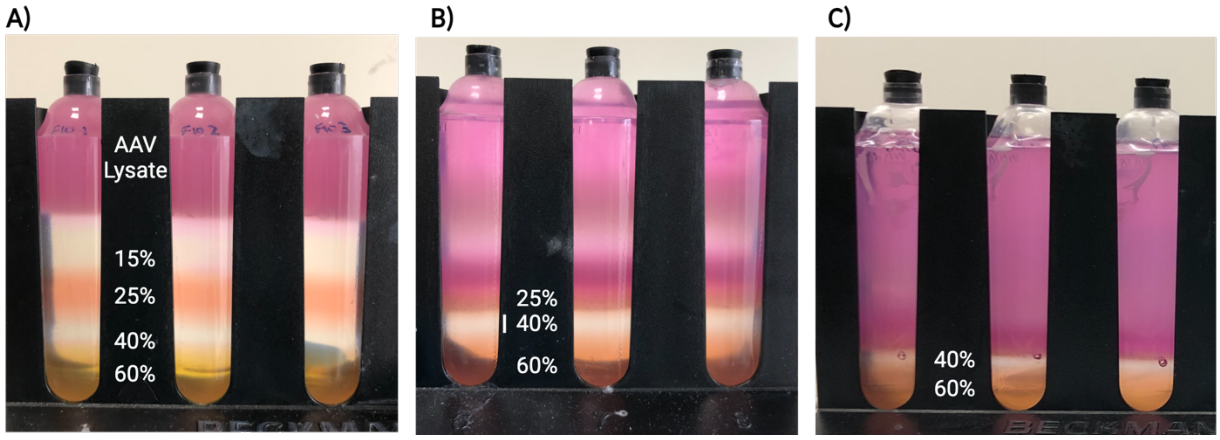


Figure 2.3 Iodixanol gradients

A) Iodixanol gradient before ultracentrifugation showing distinct layers with AAV lysate above fractions. B) Iodixanol gradient after ultracentrifugation. AAV is isolated in the 40% fraction and is annotated with a vertical white line. C) Iodixanol gradient after AAV aspiration with preservation of the interface between 40% and 25% fractions.

2.3.4 – AAV Purification and Concentration

An Amicon Ultra Filter 100K (Merck) was equilibrated by adding 5mL of PBS to the filter and centrifuging at 3,000g for 15 minutes at 20°C. PBS was added to the collected iodixanol fraction from section 2.3.3 to make the total volume 15mL – this volume was mixed by pipetting up and down and added to the equilibrated filter. The sample was centrifuged at 3,000g at 20°C until the volume was reduced to 500uL. After discarding flow through, 15mL of PBS was added to the filter and centrifuged at 3,000g at 20°C until the volume was reduced to 500uL. This step was repeated 3 times. On the final wash, the volume was reduced to 250uL, leaving purified AAV. 10uL aliquots of purified AAV were prepared and stored at –80°C. The filter was washed with 500uL PBS leaving AAV wash - 100uL aliquots of AAV wash were prepared and stored in -80°C. Table 2.9 lists all AAV vectors and titers produced throughout the MSc (Res) project.

2.3.5 – Viral Titer

Purified AAV vectors were digested with DNAse at 37°C for 30 minutes before heating to 95°C for 10 minutes. Vital titer was measured with SYBR Green based quantitative PCR (qPCR) (BioRad) using primers against hGRK1 or DsRed (Table 2.7). Purified and digested AAV vectors were diluted 1:10 and 1:100 before mixing with primers and SYBR Green. A standard curve against the linearized parent backbone was used as a control. The standard curve was made from 1:10 serial dilutions of the linearized parent backbone, ranging from 0.0001ng/uL to 1ng/uL. Samples were loaded onto a RT-PCR machine (CFX Connect Optics Module, BioRad) and run under conditions in table 2.8, followed by melt curve analysis. All reactions were performed in triplicate. Viral genome copy number was determined for each AAV sample based on copy number within the standard curve.

Table 2.7 qPCR primers used for viral titer

Name	Sequence	Region Amplified
GRK1 F1	CTGAATTCGGTACCGGGCC	hGRK1 Promoter
GRK1 R1	CGAAGGCAGCGCGCAGC	
RFP qPCR F1	CGACTACAAGAAGCTGTCC	DsRed
RFP qPCR R1	AAGTTCACGCCGATGAAC	
RFP qPCR F2	CCGTAATGCAGAAGAAG	
RFP qPCR R2	GTAGATGGACTTGAACTC	
RFP qPCR F3	CGTAATGCAGAAGAAGAC	
RFP qPCR R3	TAGATGGACTTGAACTCC	

Table 2.8 qPCR conditions

Step	**Temperature (°C)**	**Time**	**Number of Cycles**
Polymerase Activation	95°C	3 minutes	1
Denaturing	95°C	10 seconds	40
Annealing/Extension	55-62°C	30 seconds	
Melt Curve	60-95°C with 0.5°C increments	5 seconds /temp	1

2.3.6 Sodium Dodecyl Sulfate-Polyacrylamide Gel Electrophoresis (SDS-PAGE)

SDS-PAGE was performed to assess AAV purity and confirm correct protein synthesis via presence of the three viral capsid proteins, VP1 (87 kDa), VP2 (72 kDa), and VP3 (62 kDa). 10uL purified AAV was mixed with 5uL protein loading buffer and 10uL PBS. This was denatured at 95°C for 10 minutes before loading onto a 10% TGX gel (BioRad) alongside a protein ladder. The gel was run in Tris/Glycine/SDS running buffer (National Diagnostics) at 100V for 105 minutes. The gel was briefly washed in distilled water then stained using Biosafe G-250 Coomasie Blue (BioRad) for 2-5 hours and washed once more in distilled water before imaging on LICOR Odyssey FC Imager.

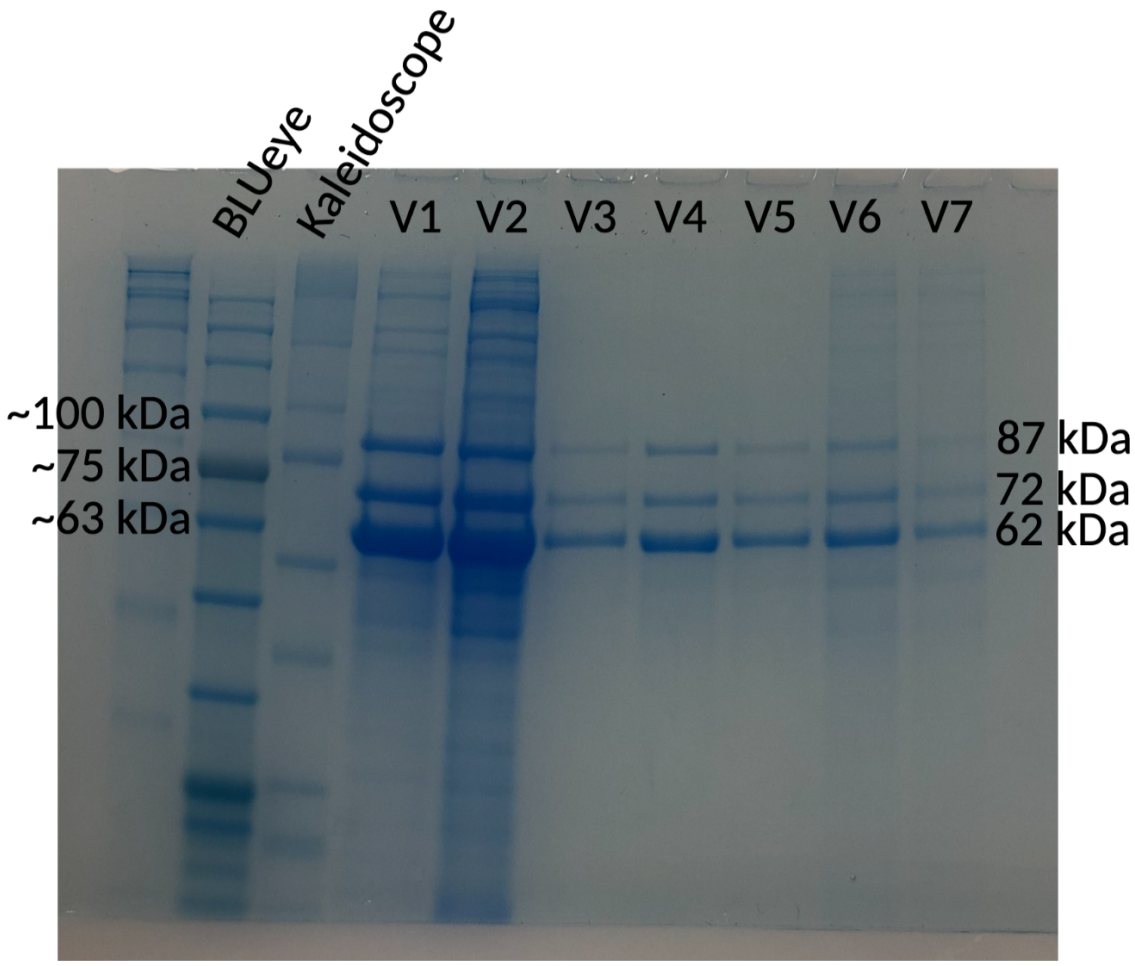


Figure 2.4 SDS-PAGE of all AAV vectors

Biosafe G-250 Coomasie Blue (BioRad) stained SDS-PAGE gel of all viruses produced. VP1 (87 kDa), VP2 (72 kDa), VP3 (62 kDa) present in all viral preps. Lane 1 loaded with unlabeled protein ladder (was loaded to test use), lane 2 loaded with BLUeye prestain protein ladder (Sigma), lane 3 loaded with Precision Plus Protein Kaleidoscope Prestained Protein Standards (BioRad).

Table 2.9 All AAV produced throughout MSc (Res) with viral titer

Name	**Virus**	**Viral Titer** (gc/mL)
V1	AAV5-CAG-DsRed	$1.1x10^{12}$
V2	AAV5-hGRK1-DsRed	$4.1x10^{12}$
V3	AAV5-hGRK1-SaCas9-F10	$5.2x10^{12}$
V4	AAV5-hGRK1-SaCas9 NT	$2.5x10^{11}$
V5	AAV5-hGRK1-SaCas9 NT	$3.4x10^{12}$
V6	AAV5-hGRK1-SaCas9-F10	$1.6x10^{13}$
V7	AAV5-hGRK1-DsRed	$1.5x10^{13}$

2.4 In Vivo

UK Home Office Project License PP3038118 and Personal License I41398566 (Ellen Rhodes) were used throughout this thesis. All animal procedures were conducted in accordance with the Associated for Research and Vision & Ophthalmology (ARVO) statements on the care and use of animals in ophthalmic research.

2.4.1 – Genotyping

CGFP mice were ear clipped and crude DNA was isolated from tissue using alkaline (NaOH) based extraction method. Briefly, 75uL NaOH (10mM) was added to tissue and heated at 98°C for 2 hours using a thermocycler. Samples were vortexed and spun down. 75uL HCl (10mM) was added, and solution was mixed and spun down. Supernatant was removed and stored at –20°C unless being used immediately for PCR. Isolated crude DNA was PCR amplified using primers in the EGFP region (see appendix) and products were run on an 1.5% agarose gel to identify EGFP positive mice.

2.4.2 – Anesthesia

For subretinal injections and in vivo imaging of mice eyes, general anesthesia was induced by a single intraperitoneal injection of ketamine (Narketan, Vetoquinol, UK, final concentration 8mg/ml) and xylazine (Rompun, Byer, final concentration 1mg/ml) at a dose of 0.1ml/10g BW. Reversal was achieved by a subcutaneous injection of atipamezole (Antisedan, Zoetis, final concentration 0.2mg/ml) at a dose of 0.1ml/10g BW.

2.4.3 – Pupil Dilation

Pupils of mice eyes were dilated to facilitate retinal visualization for injections and in vivo imaging. Dilation was achieved using 1% tropicamide followed by 2.5% phenylephrine hydrochloride (Bausch & Lomb), allowing each drop to absorb for 5 minutes.

2.4.4 – Subretinal Injections

All subretinal injections throughout this thesis were performed with the generous help of Dr. Ahmed Salman. Details of injections as follows. Mice were anesthetized and pupils dilated as stated in section 2.4.3. Proxymetacaine hydrochloride 0.5% (Bausch & Lomb) drops were used as a topical anesthetic. The head of the mouse was positioned in a custom foam stabilizer to facilitate fundus visualization. The superior rectus muscle was held using toothed titanium forceps (WPI) to stabilize the globe. Anterior chamber paracentesis was delivered in the inferonasal region using a 33g needle (TSK Laboratory) to prevent reflux on subsequent subretinal injection. The cornea was immersed in Viscotears (Alcon Laboratories Ltd) and a 6mm glass coverslip was placed over the cornea. The coverslip was adjusted to maximize fundus visualization under the operating microscope (Leica Biosystems). A 10uL Nanofil glass syringe (Precision Instruments) with a 35g needle (WPI) was flushed with sterile PBS then loaded with 1.5uL of AAV vector or PBS. The globe was stabilized again by grasping the superior rectus. The needle was advanced to the superior retina and inserted into the subretinal space. To avoid bypassing the subretinal space, vectors were injected as soon as the needle bevel was visualized under the microscope. Critical steps can be seen in Figure 2.5. The needle was retracted, the coverslip removed, and a Chlorampenicol 0.5% (Bausch & Lomb) antibiotic drop placed on the

cornea. The globe was covered in Viscotears and the mouse allowed to recover after administration of anesthetic reversal agent. Extent of retinal detachment was visualized and rated 1 to 5 based on subretinal bleb size, as well as presence of hemorrhage, or any additional abnormalities.

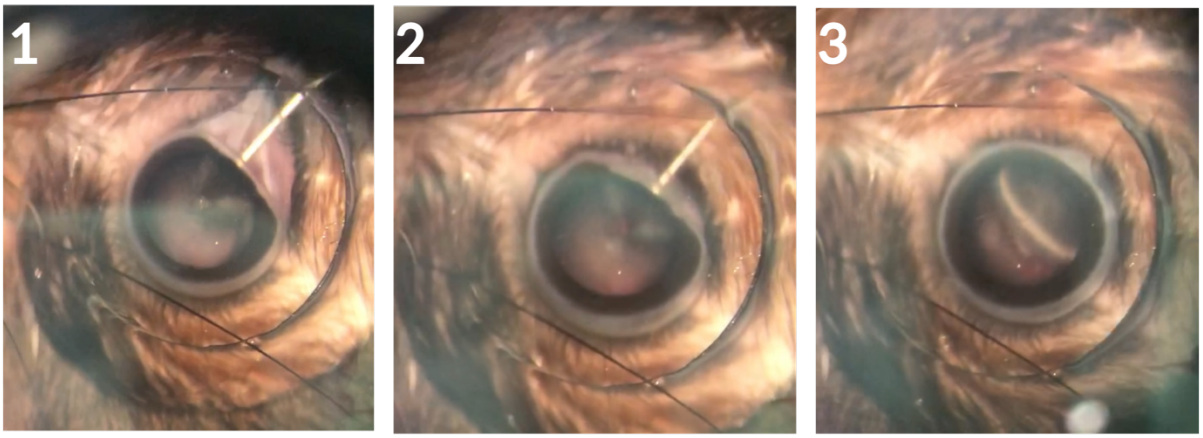


Figure 2.5 Delivery of superior subretinal injection

Panel 1 showing superior rectus being held with bevel of injection needle in subretinal space. Panel 2 showing injection needle positioned in subretinal space after release of the superior rectus to facilitate plunger depression. Panel 3 showing superior subretinal bleb achieved from injection.

2.4.5 – Confocal-Scanning-Laser Ophthalmoscopy and Optical Coherence Tomography

Mice were anesthetized and pupils dilated. Retinal images were taken using a SpectralisTM microscope (Heidelberg Engineering, Germany) with a 55° lens. Contact lenses (3.2mm diameter, Cantor and Nissel) were centered over dilated pupils of mice using 0.3% Hypermellose coupling fluid (Blumont Healthcare Ltd). Mice were placed on a platform and the pupil aligned with the camera lens.

Confocal Scanning Laser Ophthalmoscopy (cSLO)

cSLO images were captured using SpectralisTM microscope (Heidelberg Engineering, Germany). Images were taken with either infrared or fluorescent channels with automatic normalization function turned off to avoid light compensation/saturation. Automatic real-time (ART) functionality was used which allows tracking of the eye and creates an average composite image from 20 images. First, the photoreceptor layer was identified by greatest near infrared reflectance mode (NIR) with the optic nerve located in the center of images. Subsequent cSLO images were all taken in this focal plane: fundus autofluorescence (FAF), blue autofluorescence (BAF), green autofluorescence (GAF), and infrared autofluorescence (IRAF). FAF images were taken at maximum exposure. BAF allows visualization of EGFP using a 486nm blue diode excitation laser and 500-700nm bandpass filter. Similarly, GAF allows visualization of DsRed using a 788nm green diode excitation laser and LP568 or 530nm barrier filter. BAF and GAF images were taken at decreasing sensitivity settings from 100% to 50%. IRAF uses a 820nm diode laser and was imaged at maximum exposure.

Optical Coherence Tomography (OCT)

OCT images were taken directly after cSLO imaging and captured 16 radially oriented cross-sectional B scans of the retina. ART was used to average 25 individual B scans for each of the 16 captured images. Photoreceptor layer (measured from the bottom of the outer nuclear layer (ONL) to the top of the retinal pigment epithelium (RPE)) measurements were taken 3000um from the center of the optic nerve using a built-in function in the Heidelberg software to overlay the EDTRS grid for standardization. Three measurements were taken for both the superior and

inferior regions of the retina and averaged (Figure 2.6). In injected eyes, superior measurements represent areas within the subretinal bleb while the inferior measurements are un-transduced.

2.4.6 – Mean Grey Fluorescence Measurements of cSLO Images

Mean grey fluorescence of BAF cSLO images was assessed using ImageJ to quantify EGFP protein expression. Images were first exposed to a Gaussian blur to smooth the pixels. Next, a semicircle area of either the superior or inferior retina was defined. Both the superior and inferior retinal areas were analyzed for each sample allowing for avoidance of the optic nerve head. Finally, the mean grey fluorescence was measured and data exported to GraphPad Prism for statistical analysis. .Tif files were batch processed with ImageJ and run with the macros found in appendix 8.4.

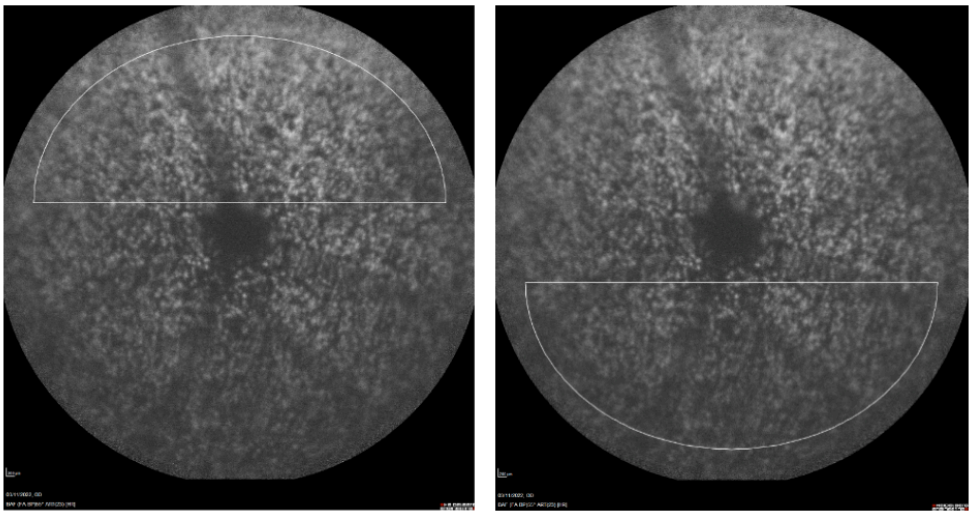


Figure 2.7 Defined areas for mean grey fluorescence measurements

Example of BAF cSLO image with superior (left) and inferior (right) semicircular regions used for MGF.

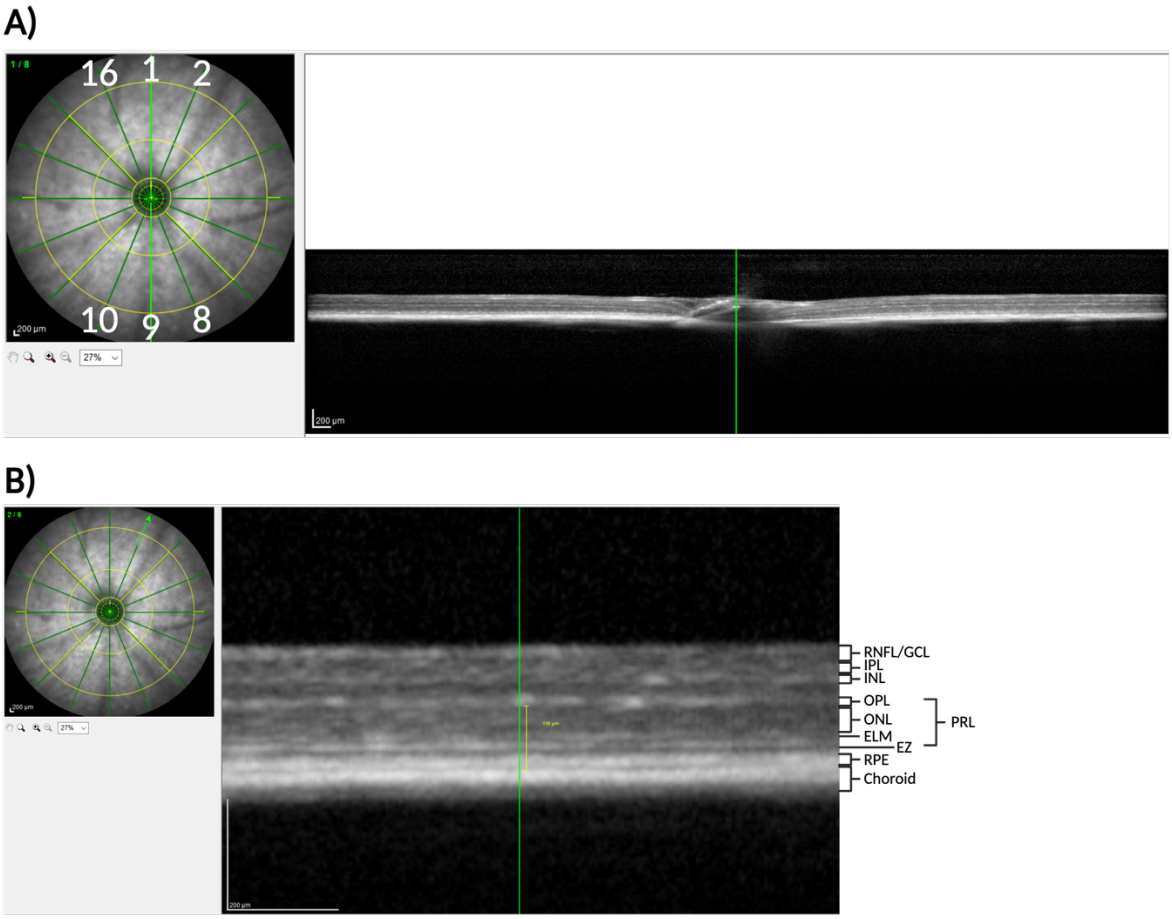


Figure 2.6 Example of OCT Measurements

A) Example of cSLO image demonstrating location of the 16 radial B scans. The ETDRS overlay is seen in yellow and is centered on the optic disc. The intersection of the B scan and outer yellow line is used to standardize measurement location at 3000uM from center of the optic disc. Measurements from scans 1, 2, and 16 are averaged to represent superior photoreceptor layer thickness. Measurements from scans 8-10 are averaged to represent the inferior photoreceptor layer thickness. B) Zoomed in area of B scan 2. Vertical green line 3000uM from center of optic disc. Vertical yellow line is an example photoreceptor layer measurement. Retinal layer identification: RNFL, retinal nerve fiber layer; GCL, ganglion cell layer; IPL, inner plexiform layer; INL, inner nuclear layer; OPL, outer plexiform layer; ONL, outer nuclear layer; ELM, external limiting membrane; EZ, ellipsoid zone; PRL, photoreceptor layer; RPE, retinal pigment epithelium.

2.5 Tissue Analysis

2.5.1 – Enucleation and Tissue Collection

Eyes were extracted after dual confirmation of death. The superior rectus muscle was isolated to preserve dorsal-ventral directionality. The muscle was grasped using forceps and the surrounding tissue was dissected using scissors. After extraction, the eye was fixed in 4% Paraformaldehyde (PFA) (ThermoFischer) for 10 minutes. The eye was then placed in 0.01M sterile PBS and a 30g needle was used to create an opening between the iris and sclera. Dissection scissors were gently guided into the opening and the cornea and associated structures were circumferentially cut away from the posterior eye cup. The lens was gently removed to prevent retinal detachment.

If proceeding to IHC, the posterior eye cup was post-fixed in 4% PFA for 30 minutes at 4°C, rinsed in 0.01M sterile PBS at 4°C, and progressively placed in an increasing sucrose series (5%, 10%, 20%, 30%) at 4°C for approximately 2 hours at each concentration. Following the sucrose series, the eye cup was placed in optimal cutting temperature (OCT) compound (VWR), flash frozen with isopentane on dry ice, and stored at -80° C prior to cryosectioning.

If isolating the neural retina, an edge of the sclera was grasped using 2 pairs of forceps and a lateral motion was used to disrupt the RPE without disturbing the retina. The retina was isolated, flash frozen in an Eppendorf tube on dry ice, and stored at -80°C.

2.5.2 – DNA Extraction

See section 2.1.4 for details of DNA extraction from retinae.

2.5.3 – Tracking of Indels via Decomposition (TIDE) Analysis

See section 2.2.9 for additional details. To assess editing efficiency of active Cas9 systems, TIDE software was used. Primers were designed to amplify an area 200bp before and 500bp after the expected cut site. After gDNA extraction from retinae, PCR amplification, and purification, samples were sent for sanger sequencing. Chromatograms were uploaded into TIDE software alongside a control sample with no predicted editing. Quantified editing efficiency and the major types of small insertions and deletions was provided by the software.

2.5.4 – Immunohistochemistry

Frozen eye cups were cut with a Leica cryostat at –20°C into 12um sections and placed on SuperFrost slides (VWR International). Slides were allowed to dry at room temperature then placed in -20°C overnight before staining. Frozen slides were allowed to dry at room temperature and marked with a hydrophobic pen. Slides were washed with 1xPBS, permeabilized with 0.1% Triton, and blocked with 5% bovine serum albumin (BSA) and 5% appropriate serum (Donkey or Goat serum) in 0.1% Triton. The slides were incubated with the appropriate primary antibody in blocking solution for 16 hours, washed three times in 0.1% Triton and incubated with an appropriate secondary antibody for 1 hour in dark conditions. 1:1000 Hoescht was used as a nuclear stain and left to sit for 5 minutes before washing with 1xPBS. Slides were mounted

(Invitrogen™ SlowFade™ Gold Antifade Mountant) and stored at 4°C before confocal imaging. Details of primary and secondary antibodies can be found in Table 2.9.

Table 2.9 List of Primary and Secondary Antibodies

Type	Antibody	Host	Dilution
Primary	Anti-Cone Arrestin AB15282, Millipore	Rabbit	1:500
	HA-Tag Antibody NB600-362, Novus Biologicals	Goat	1:400
	Living Colors® DsRed Polyclonal Antibody 632496, Takara	Rabbit	1:500
Secondary	Donkey anti-Rabbit IgG (H+L) Highly Cross-Adsorbed Secondary Antibody, Alexa Fluor™ 647 A-31573, ThermoFischer	Donkey	1:500
	Donkey anti-Goat IgG (H+L) Cross-Adsorbed Secondary Antibody, Alexa Fluor™ 568 A-11057, ThermoFischer	Donkey	1:500

2.5.5 – Confocal Microscopy

Confocal microscopy was performed using the LSM-710 confocal microscope using Zen software (Zeiss) and the FLUOVIEW FV3000 confocal laser scanning microscope using associated FV3000 software (Olympus). Exposure of individual channels was optimized using power, gain, and offset before image acquisition. All images were taken at a size of 1024x1024 pixels. 10x, 40x, and 63x objectives were used. Z-stack images were taken at an optimal thickness as determined by each software program. Images from the LSM-710 were exported as .lsm files and images from the FV3000 exported as .oir files. Both file types were processed using FIJI ImageJ software (NIH). Z-stack images were merged at maximum intensity.

2.6 Statistics

GraphPad Prism (v9) was used for all statistical analysis and graph production. All data are shown as the mean ± SEM, unless otherwise stated. For comparisons involving two groups with one independent variable a one-way ANOVA was applied, with Tukey's post-test used for multiple comparison testing of significant differences between groups. For analysis of more than two groups with more than two independent variables, a two-way ANOVA was applied, with Sidak's post-test for multiple comparison test used to test significance between groups. Throughout this thesis, p values <0.05 were considered statistically significant.

Chapter 3: Pilot *in-vivo* study of AAV5 packaged delivery to the CGFP mouse retina

3.1 Introduction

Transgenic models are a valuable tool to test preclinical gene therapy and gene editing approaches. In typical experimental flow, new strategies are tested in relevant *in-vitro* models, followed by *in-vivo* studies, culminating with clinical trials. There are few suitable animal models to study cone photoreceptors[141]. Within the mouse retina, only ~2.8% of photoreceptors are estimated to be cones[142]. Nonetheless, murine disease models and transgenic lines continue to be vital for preclinical studies due to their relative ease in breeding and ability to induce desired mutations. The transgenic CGFP mouse model, which will be used throughout this thesis, was engineered to express EGFP in medium-wave sensitive (MWS) cone photoreceptors under the control of the human OPN1 cone-specific promoter[143]. In this model, the small subpopulation of EGFP expressing cones allows visualization of individual cone cells using cSLO imaging, with a higher density of fluorescent cones present in the dorsal retina[144]. The ability to visualize individual cone cells is particularly important in evaluating cone-specific targeting with a given CRIPSR-Cas system.

In many retinal degenerative diseases, rod photoreceptors degenerate followed by cone degradation[145]. Effective gene editing and gene therapy approaches focused on retinal degeneration require precise targeting of specific cell types. Due to the fluorescent nature of the cones in the CGFP mouse line, it represents a suitable model to test cone photoreceptor targeting using AAV-based delivery, in mice. To begin testing this, dosing limitations of AAV5 and broad

transduction patterns of vectors in the CGFP mouse were first explored. A construct was engineered to express the DsRed reporter gene under the control of the ubiquitous cytomegalovirus enhancer fused to chicken beta-actin (CAG) promoter or the human rhodopsin kinase (hGRK1) promoter, which is known to be active in photoreceptors[146], and packaged into adeno-associated virus serotype 5 (AAV5). AAV5 was chosen to package the transgene due to the serotype's well-studied photoreceptor tropism[147–149]. Similarly, the hGRK1 promoter demonstrates species conservation[150] and has shown successful photoreceptor transduction in mice[49,151] as well as NHP[152] and canine[153] animal models. The selection of AAV serotype and promoter is vital to limit expression to target cells and minimize off-target effects.

The combination of AAV5 and the hGRK1 promoter has been shown to successfully transduce photoreceptors in NHP[152] and humans. Editas Medicine has an ongoing clinical trial with a CRISPR based treatment for Leber Congenital Amaurosis (LCA) which utilizes the same combination of AAV5 and the hGRK1 promoter, showing successful transduction of photoreceptors[120]. Additional studies in retinal organoids further support the use of this combination with AAV5 demonstrating rod and cone transduction[154,155].

To evaluate photoreceptor transduction patterns and dosing limitations in the CGFP mouse, the hGRK1-DsRed and CAG-DsRed vectors were packaged into AAV5 particles and subretinally injected into eyes of CGFP mice. Expression of EGFP and DsRed proteins were assessed *in-vivo* with cSLO imaging and *ex-vivo* tissue analysis. This initial study provides the foundation for the remainder of this thesis focused on murine cone targeting for future CRISPR-based therapies.

3.2 Materials and Methods

3.2.1 – Plasmid Cloning

Protocols for plasmid cloning are outlined in Chapter 2. Both plasmids used throughout this chapter contain the red fluorescent protein, DsRed. Expression of DsRed is controlled via the CAG promoter in one (CAG-DsRed) or the hGRK1 promoter in the other (hGRK1-DsRed). The hGRK1-DsRed plasmid was made using PCR-based cloning, detailed in section 2.1.10. Both CAG-DsRed and hGRK1-DsRed were sequenced using Sanger Sequencing prior to AAV production and produced with endotoxin free kits.

3.2.2 – Cell Culture and AAV Production

Details of AAV production can be found in section 2.3. Briefly, CAG-DsRed and hGRK1-DsRed plasmids were individually transfected alongside pDP5 and TransIT-VirusGEN into hyperflasks seeded with HEK293T cells. ITRs were verified with XmaI restriction enzyme digest prior to transfection. Transfected cells were harvested and lysed to obtain maximum viral particle yield prior to isolation of AAV particles using iodixanol gradient. AAV5-CAG-DsRed and AAV5-hGRK1-DsRed were purified using ultrafiltration and stored at -80°C. Both viruses were titrated to obtain maximum yield using qPCR and AAV purity assessed by SDS-PAGE prior to *in-vivo* use.

3.2.3 – *In-Vivo* Analysis

Details of *in-vivo* work can be found in section 2.4. In all cases, CGFP mice were genotyped to identify EGFP positive subjects for *in-vivo* work. Following anesthesia and pupil dilation, 6-week-

old mice underwent subretinal injections of either AAV vector or PBS. Details of injections completed throughout this chapter can be found in Table 3.1.

Following subretinal injections, mice were left for 3-6 weeks and imaged periodically using cSLO/OCT. cSLO/OCT images were taken to assess for and retinal toxicity and photoreceptor layer (PRL) thickness, respectively. PRL measurements were taken as described in section 2.4.5.

Table 3.1 Details of DsRed Experiments

Dose (genome copies/mL)	Injection Group	Number of Eyes
$5x10^{11}$	Non-Injected	3
	PBS	4
	AAV5-CAG-DsRed	8
	AAV5-hGRK1-DsRed	7
$1x10^{12}$	PBS	9
	AAV5-hGRK1-DsRed	9

3.2.4 – Tissue Analysis

Details of IHC can be found in section 2.5.4. Briefly, posterior eye cups were isolated following the final imaging session for each study. The eye cups were taken through an increasing concentration sucrose series prior to fixation in OCT. The eye cups were cut into 12uM slices on a Leica Cryostat and left to dry on superfrost slides. Slides were stained using Hoescht to identify nuclei and Anti-cone arrestin to identify cone cells. Finally, slides were imaged using the LSM-710 confocal microscope to look for endogenous EGFP expression, DsRed expression, cone arrestin staining, and Hoescht staining. Generated images were exported as .lsm files and analyzed on ImageJ.

3.2.5 – Statistical Analysis

PRL measurements were taken described in section 2.4.5. Briefly, the PRL thickness of 3 OCT scans in the superior central retina were averaged to a single measurement. The same was done for the inferior retina. Individual values on graphs in this chapter represent the average of 3 measurements of a single retinal area. The effect of injection on PRL thickness was analyzed using a two-way ANOVA with multiple comparison correction.

3.3 Results

3.3.1 – Cloning and AAV Production

To test the ability of the CAG and hGRK1 promoters to drive the expression of a fluorescent protein *in-vivo*, the hGRK1 sequence was inserted upstream of the full-length DsRed sequence, so DsRed is expressed under the control of the hGRK1 promoter. An overview of the PCR based cloning is detailed in Figure 2.1. PCR based cloning was used to isolate the hGRK1 promoter from a plasmid (Figure 3.1 – A) which was then inserted into the DsRed parent plasmid (Figure 3.1 – B). The CAG-DsRed plasmid was digested with HindIII and BglII and confirmed with gel electrophoresis (Figure 3.2 - A). The fragment containing DsRed was isolated and purified prior to ligation with the hGRK1 fragment. The hGRK1 promoter was PCR amplified using primers that added the restriction enzyme sites HindIII and BglII to the 3' and 5' end of the promoter, respectively (Figure 3.2 - B). The resulting PCR fragment was then isolated via gel electrophoresis and purification before restriction enzyme digest with HindIII and BglII to generate sticky ends. The resulting hGRK1 PCR product and the DsRed backbone were ligated. The sequence of CAG-DsRed and the generated hGRK1-DsRed plasmids were verified with sanger sequencing following endotoxin-free purification. The full sequence of the plasmids can be found in the appendix.

Three AAV vectors were produced: AAV5-CAG-DsRed (V1) and AAV5-hGRK1-DsRed (V2, V7). All vectors underwent restriction enzyme digest with XmaI to confirm presence of ITRs and plasmids were fully sequenced prior to virus production (Figure 3.2 - C). Following AAV production, viruses were analyzed with SDS-PAGE, verifying correct viral capsid protein generation (Figure 2.4).

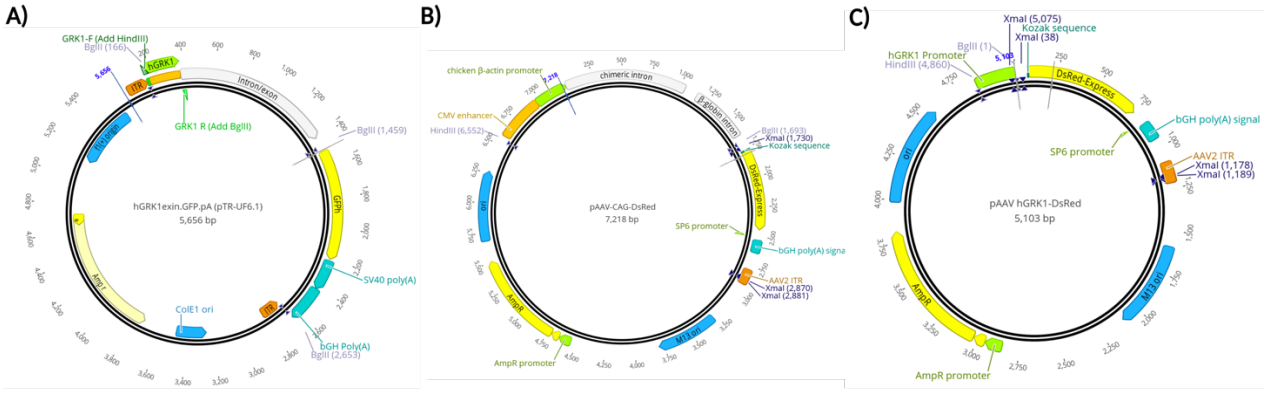


Figure 3.1 Maps of plasmids used to generate hGRK1-DsRed

A) Plasmid map of hGRK1-GFP. hGRK1 promoter shown with primers used to amplify hGRK1 region adding the restriction enzyme sites HindIII to the 3' end and BglII to the 5' end. **B)** Circular plasmid map of CAG-DsRed with BglII and HindIII sites used to isolate DsRed backbone. XmaI sites also shown. **C)** Circular map of generated hGRK1-DsRed plasmid with BglII, HindIII, and XmaI restriction enzyme sites shown.

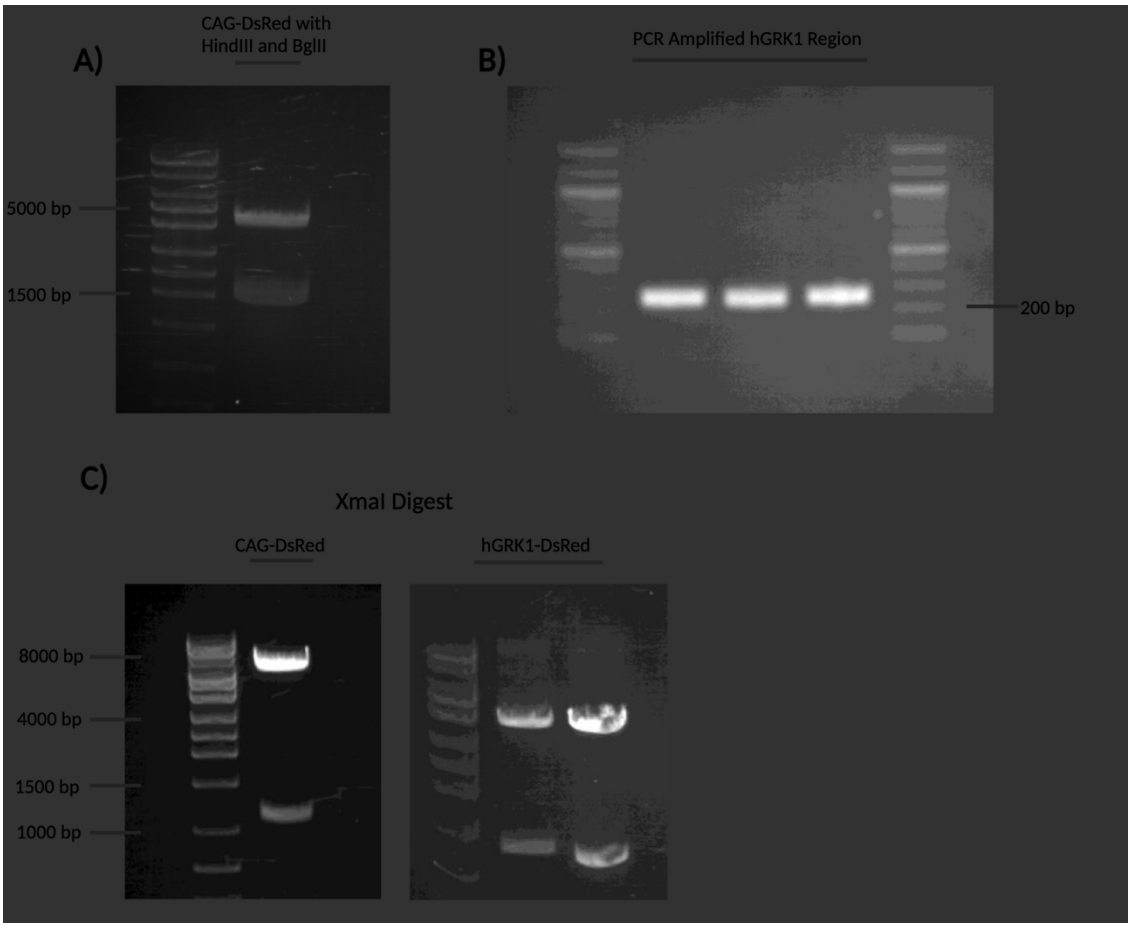


Figure 3.2 Cloning and AAV Production of GRK1-DsRed and CAG-DsRed

A) UV exposure image of agarose gel with CAG-DsRed plasmid digested with HindIII and BglII restriction enzymes with expected bands at 4.86 kb and 2.36 kb, respectively. **B)** UV exposure image of agarose gel loaded with PCR product of hGRK1 region with expected band at 238 bp. **C)** UV exposure image of agarose gels loaded with CAG-DsRed and hGRK1-DsRed plasmids after restriction enzyme digest with XmaI. CAG-DsRed bands expected at 6.07 kb and 1.14 kb, hGRK1-DsRed bands expected at 3.89 kb and 1.14 kb.

3.3.2 – Subretinal injections of AAV5-CAG-DsRed and AAV5-hGRK1-DsRed at $5x10^{11}$ gc/mL in CGFP mice

Initially, transduction patterns of photoreceptors in the CGFP mouse were explored via expression of DsRed under the control of the universal promoter (CAG) or photoreceptor-specific promoter (hGRK1). Confocal scanning laser ophthalmoscopy (cSLO) with different fluorescent

channels allowed individual visualization of green and red fluorescence in the mouse retina *in-vivo* following subretinal injections. A viral dose of $5x10^{11}$ gc/mL was chosen as the initial dose for subretinal injections based on prior AAV-based experiments within the MacLaren lab.

3-weeks post-injection, cSLO imaging of AAV5-CAG-DsRed injected mice demonstrated robust retinal transduction based on imaging with the green autofluorescence (GAF) channel, which detected red fluorescence extending past the superior subretinal bleb into the inferior aspect of the retina (Figure 3.3). This vector also showed evidence of widespread toxicity on infrared autofluorescence (IRAF) images, with hyperfluorescent areas representing areas of cell death and inflammation (Figure 3.3). Areas of cell death were limited to areas of the retina transduced with the viral vector. Imaging 6-weeks post-injection showed continued red fluorescence on GAF imaging and retinal toxicity evidenced by IRAF imaging (Figure 3.3). The area transduced by AAV5-CAG-DsRed appears unchanged between 3 and 6-weeks post-injection.

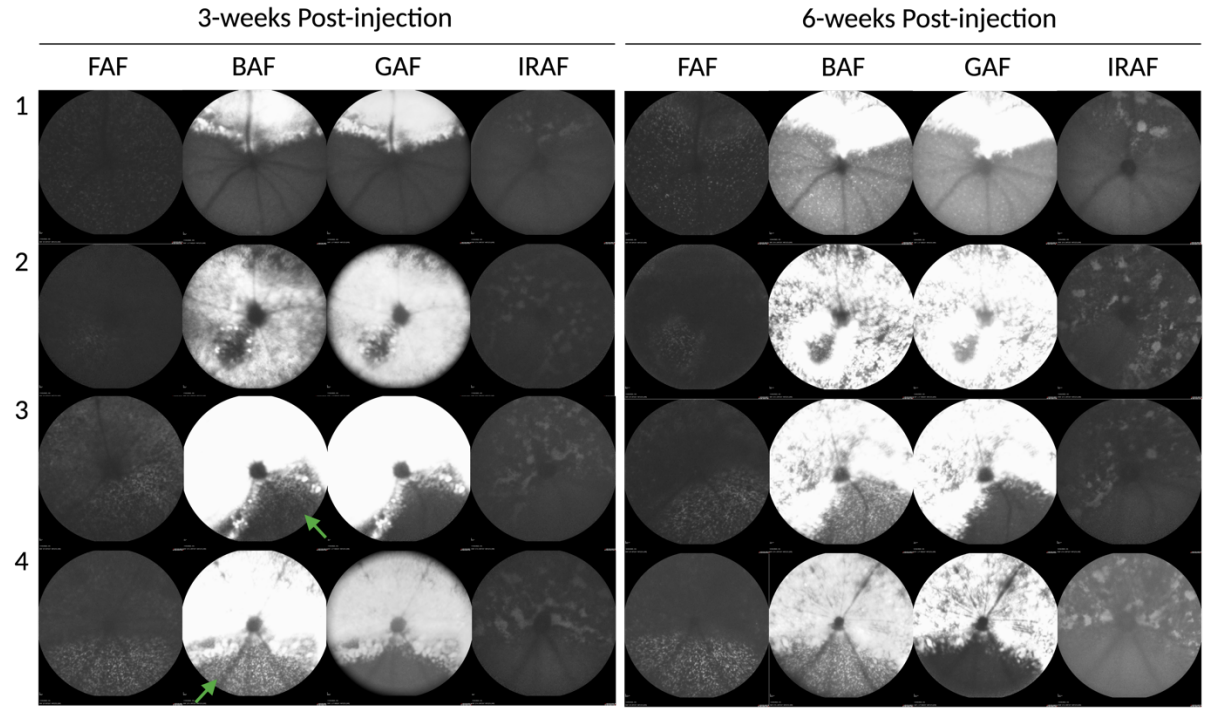


Figure 3.3 cSLO imaging of CGFP retinas following subretinal injection of AAV5-CAG-DsRed at $5x10^{11}$ gc/mL

Representative fundus auto-fluorescence (FAF), blue auto-fluorescence (BAF), green auto-fluorescence (GAF), and infrared auto-fluorescence (IRAF), images of CGFP mice (n=4) at 3 and 6-weeks post-injection of AAV5-CAG-DsRed at a viral dose of $5x10^{11}$ gc/mL. All images centered around optic nerve with area of subretinal bleb in superior aspect. Green arrows highlight EGFP expressing cone cells in inferior retina of rows 3 and 4.

Optical coherence tomography (OCT) scans were taken to assess retinal health and structure and to quantify PRL thickness. At 3-weeks post-injection, there was significant PRL thinning in the superior and inferior aspect of AAV5-CAG-DsRed injected eyes although there was more thinning superiorly (Figure 3.4, A-B). Thinning in the superior retinae of AAV5-CAG-DsRed injected eyes was widely variable, with some retinae demonstrating almost complete loss of the photoreceptor layer at 3 and 6-weeks post-injection. Thinning spreading into the inferior retina was observed in

one subject (Figure 3.4, red arrow). PRL measurements 6-weeks post-injection did not show a significant difference based on injection or location (Figure 3.4, C). At this timepoint, only two measurements were taken for the PBS injected branch, which could decrease the injection effect seen. OCT scans demonstrate subretinal deposits in the superior (rows 1-4) and inferior (row 2) retinae at 3 and 6-weeks post-injection (blue arrows).

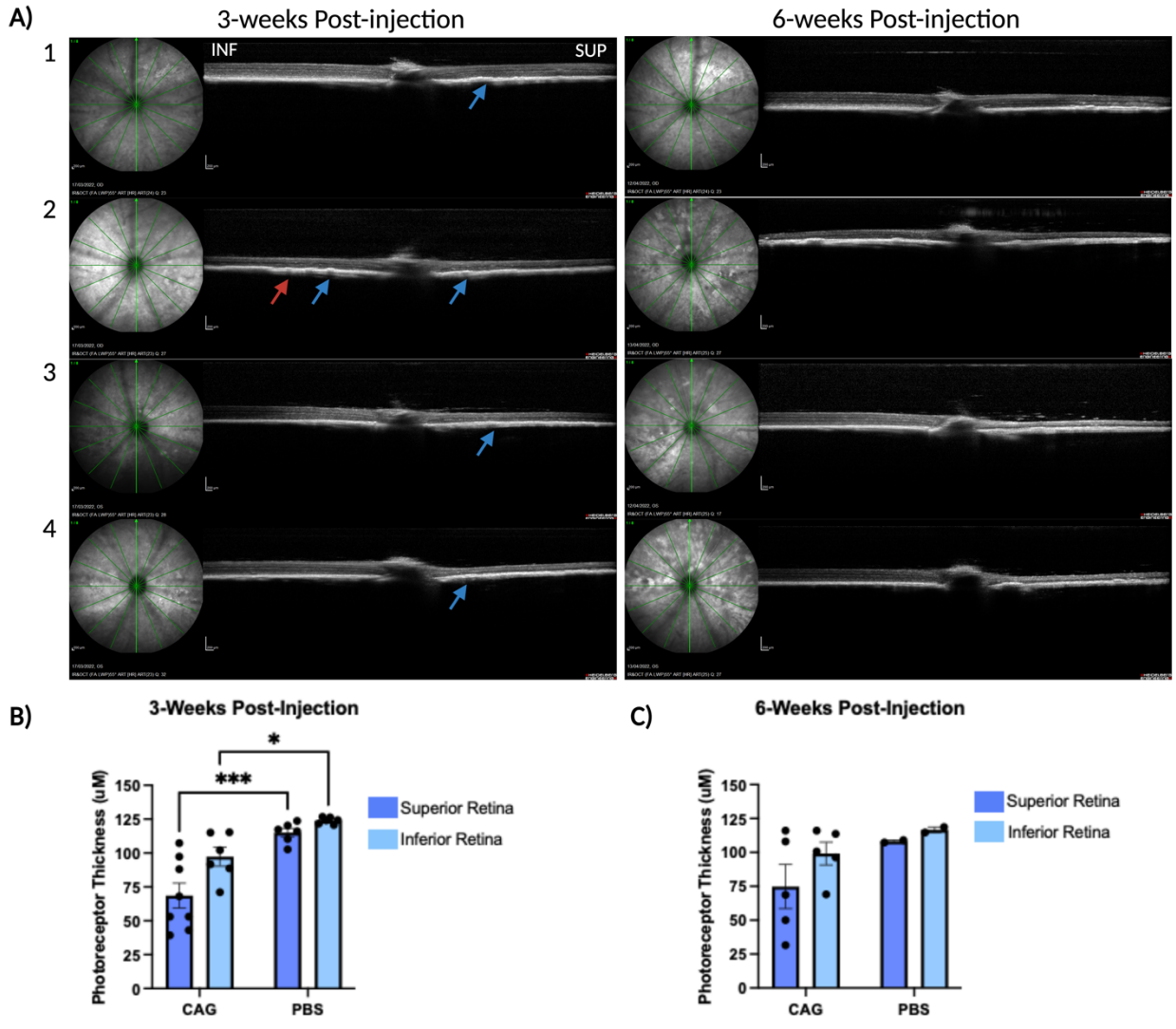


Figure 3.4 OCT scans and photoreceptor layer measurements of CGFP retinas following subretinal injection of AAV5-CAG-DsRed at 5x10^{11} gc/mL

A) Representative OCT scans centered around optic nerve of CGFP mice (n=4) at 3 and 6-weeks post-injection of AAV5-CAG-DsRed at a viral dose of 5x10^{11} gc/mL. The vertical green arrow represents area of

scan shown on right column with the inferior retina (INF) on the left and superior retina (SUP) on the right. Row 2 demonstrates additional thinning of photoreceptor layer in inferior retina (red arrow). Examples of subretinal deposits shown with blue arrows. **B)** PRL thickness measurements from OCT scans for AAV5-CAG-DsRed (*n*=7) and PBS (*n*=6) injected cohorts 3-weeks post-injection in the superior retina (subretinal injection site) and inferior retina (noninjected site). Individual values represent mean of 3 PRL thickness measurements ±SEM. Two-way ANOVA compared PRL thickness vs. injection and location: Injection effect *F(1,22)=29.08 p<0.0001*, location effect *F(1,22)=7.677 p=0.0111*, interaction effect *F(1,22)=2.130 p=0.1586*. Sidak's multiple comparisons showed a significant difference in PRL thickness for AAV5-CAG-DsRed vs. PBS injected eyes in superior *p*=0.0001 and inferior *p=0.0264* retina. **C)** Photoreceptor thickness measurements from OCT scans of AAV5-CAG-DsRed (*n*=5) and PBS (*n*=2) injected cohorts 6-weeks post-injection in the superior and inferior retina. Individual values represent mean of 3 PRL thickness measurements ±SEM. Two-way ANOVA did not show any significant effect of injection or location. Sidak's multiple comparisons did not show a significant difference in PRL thickness between injection type in each location.

AAV5-hGRK1-DsRed injected eyes were also imaged 3 and 6-weeks post-injection. Robust DsRed expression was observed once again, with some extension into the inferior retina. At 6-weeks post-injection DsRed expression persisted, with some subjects demonstrating extension of the transduced area at 6-weeks post-injection compared to 3-weeks post-injection (Figure 3.5, blue arrows). Notably, IRAF imaging did not demonstrate retinal toxicity at 3-weeks post-injection. However, in one subject IRAF imaging 6-weeks post-injection did show hyperfluorescent areas in the superior retina (Figure 3.5, red arrow).

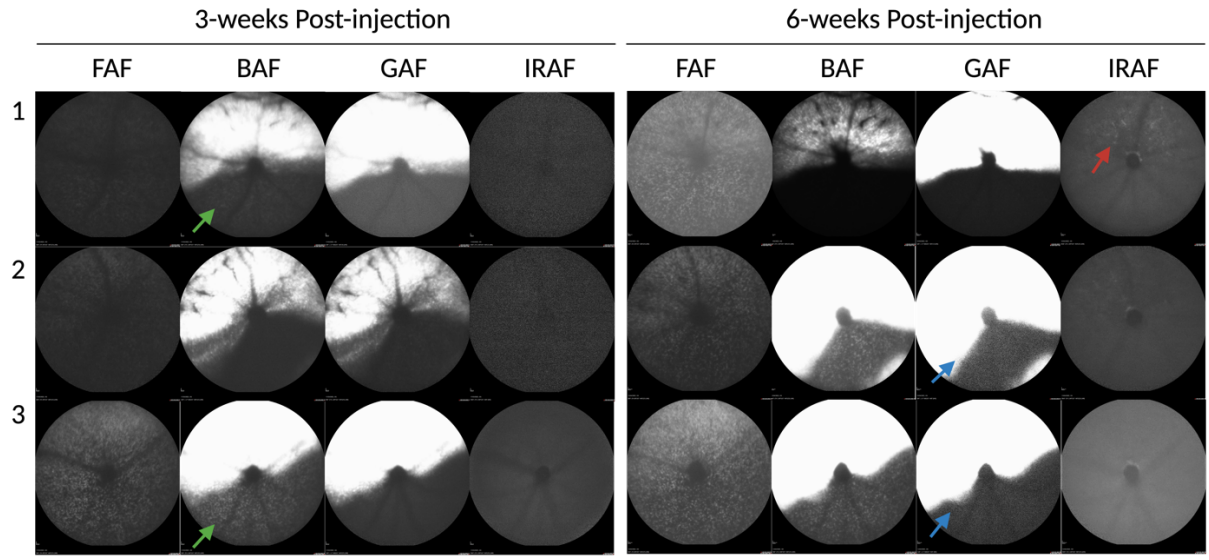


Figure 3.5 cSLO imaging of CGFP retinas following subretinal injection of AAV5-hGRK1-DsRed at 5x10^{11} gc/mL

Representative SLO scans of FAF, BAF, GAF, and IRAF images of CGFP mice (n=3) at 3 and 6-weeks post-injection of AAV5-hGRK1-DsRed at a viral dose of 5x10^{11} gc/mL. All images centered around optic nerve with area of subretinal bleb in superior aspect. Green arrows highlight EGFP expressing cone cells in inferior retina. Blue arrows highlight extension of red fluorescence in inferior retina. Red arrow highlights hyperfluorescent areas concentrated in superior retina.

OCT scans were also performed at 3 and 6-weeks post-injection for the AAV5-hGRK1-DsRed injected eyes. 3-weeks post-injection, there was significant PRL thinning in the superior retina (Figure 3.6, A-B). While PRL thinning was observed, the absolute degree in AAV5-hGRK1-DsRed injected retinae at 3-weeks post-injection was less than the thinning seen in AAV5-CAG-DsRed injected eyes (Figure 3.7). Some thinning in the superior retina is expected from surgical trauma. 6-weeks post-injection, PRL thinning persisted. Once again, PRL measurements 6-weeks post-injection were skewed by low subject number for PBS injected eyes (Figure 3.6, C). Notably, unlike

AAV5-CAG-DsRed injected retinae (Figure 3.4, blue arrows), no subretinal deposits are seen in OCT scans of AAV5-hGRK1-DsRed injected retinae at 3 or 6-weeks post-injection (Figure 3.6, A).

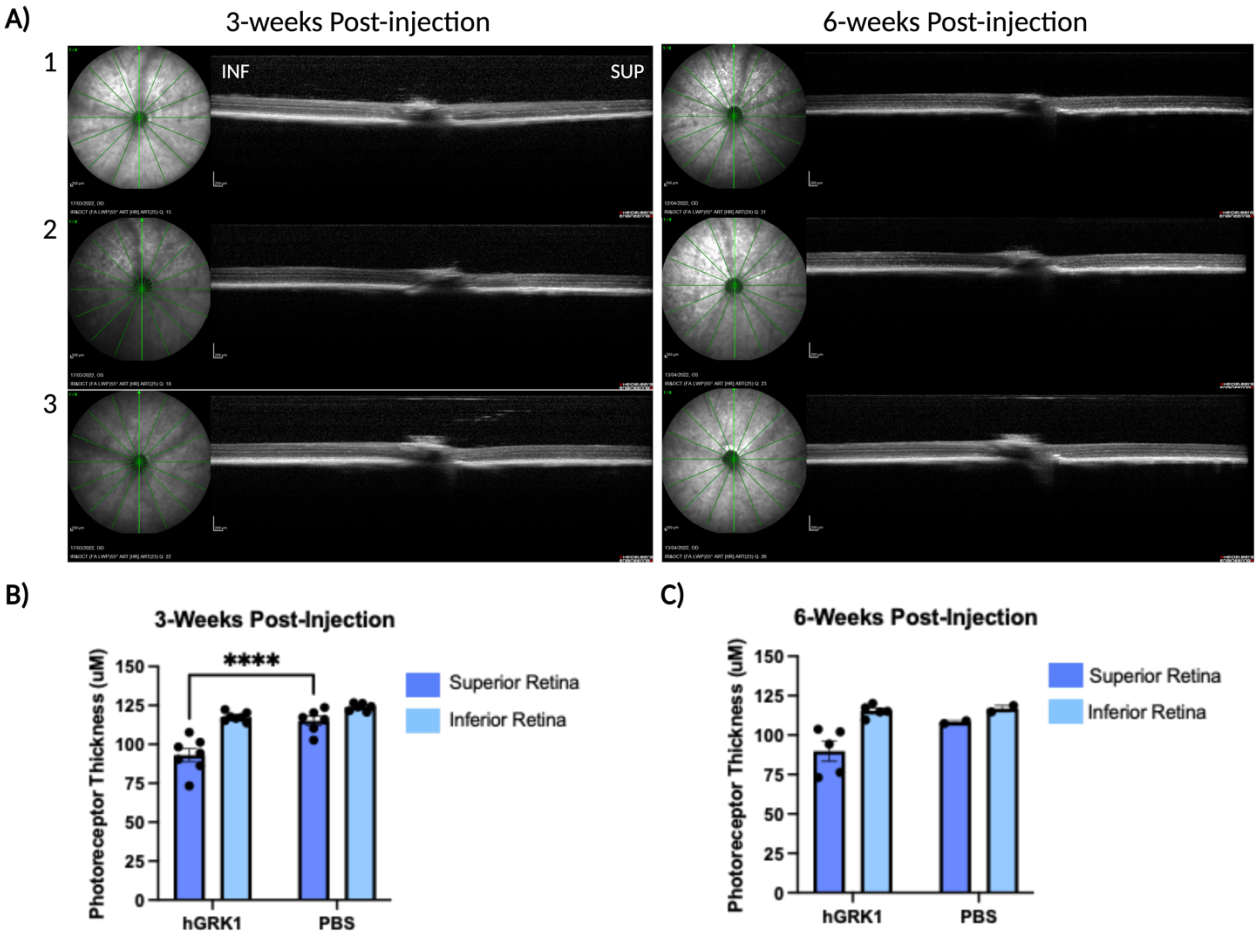


Figure 3.6 OCT scans and photoreceptor layer measurements of CGFP retinas following subretinal injection of AAV5-hGRK1-DsRed at 5x10^{11} gc/mL

A) Representative OCT scans centered around optic nerve of CGFP mice (n=3) 3 and 6-weeks post-injection of AAV5-hGRK1-DsRed at a viral dose of 5x10^{11} gc/mL. The vertical green arrow represents area of scan shown on right column with the inferior retina (INF) on the left and superior retina (SUP) on the right. **B)** PRL thickness measurements from OCT scans for AAV5-hGRK1-DsRed (*n*=7) and PBS (*n*=6) injected cohorts 3-weeks post-injection in the superior and inferior retina. Individual values represent mean of 3 PRL thickness measurements ±SEM. Two-way ANOVA compared PRL thickness vs. injection and location: Injection effect *F(1,22)=25.46 p<0.0001*, location effect *F(1,22)=35.50 p<0.0001*, interaction effect *F(1,22)=7.783 p=0.0107*. Sidak's multiple comparisons showed a significant difference in PRL thickness for

AAV5-hGRK1-DsRed vs. PBS injected eyes in superior retina $p<0.0001$ and no difference in inferior retina $p=0.2341$. **C)** Photoreceptor thickness measurements from OCT scans for AAV5-hGRK1-DsRed ($n=5$) and PBS ($n=2$) injected cohorts 6-weeks post-injection in the superior and inferior retina. Individual values represent mean of 3 PRL thickness measurements ±SEM. Two-way ANOVA did not show any significant effect of injection or location. Sidak's multiple comparisons did not show a significant difference in PRL thickness between injection type in each location.

To better elucidate the effect each injection type had on PRL thickness, the three different injection types were compared 3-weeks post-injection (Figure 3.7). Two-way ANOVA showed there was a significant effect on PRL thickness based on injection and location. Additionally, multiple comparisons allowed direct comparison between injection groups within a location. AAV5-CAG-DsRed caused the most thinning overall in both the superior and inferior retina and was significantly thinned compared to AAV5-hGRK1-DsRed and PBS in both retinal locations. AAV5-hGRK1-DsRed caused significant thinning in the superior retina when compared to PBS, but was not observed in the inferior region, suggesting significant PRL thinning in the region of the subretinal bleb with sparing outside of the injection site (Figure 3.7).

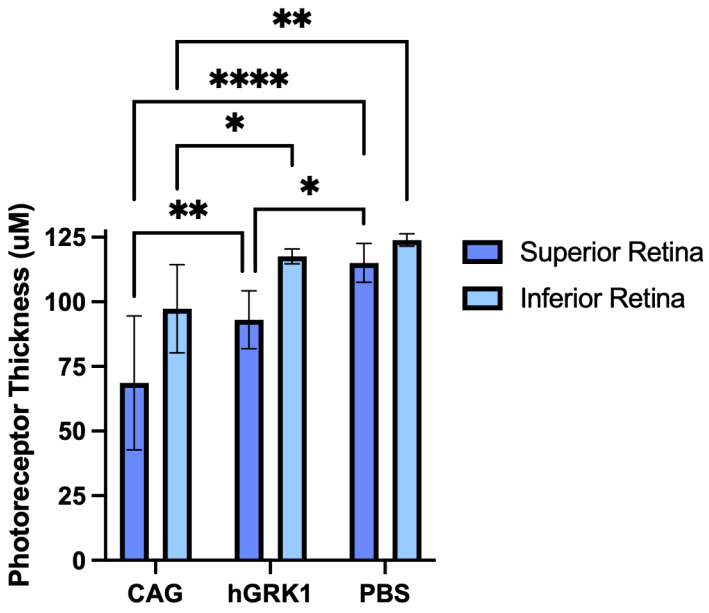


Figure 3.7 Mean PRL thickness 3-Weeks post-injection of AAV5-CAG-DsRed, AAV5-hGRK1-DsRed, or PBS

Mean PRL thickness of superior and inferior retina regions in each injection group 3-weeks post-injection. Mean CAG superior: 68.61 uM. Mean CAG inferior: 97.28 uM. Mean hGRK1 superior: 93.07 uM. Mean hGRK1 inferior: 117.61 uM. Mean PBS superior: 115.06 uM. Mean PBS inferior: 123.94 uM. Bars represent mean ±SEM. Two-way ANOVA compared PRL thickness vs. injection and location: Injection effect *F(2, 34)=20.59 p<0.0001*, location effect *F(1,34)=19.79 p<0.0001*, interaction effect *F(2, 34)=1.601 p=0.2165*. Tukey's multiple comparisons showed several significant differences in PRL thickness in superior retina: CAG vs. hGRK1 *p=0.0075*, CAG vs. PBS *<0.0001*, hGRK1 vs. PBS *p=0.0281* and inferior retina: CAG vs. hGRK1 *p=0.0449*, CAG vs. PBS *p=0.009*. No difference was seen in the inferior retina between hGRK1 vs. PBS *p=0.7190*.

Immunohistochemistry (IHC) analysis was performed on AAV5-hGRK1-DsRed injected eyes to broadly identify transduction patterns of cells which expressed the DsRed protein. Cone cells were stained with anti-cone arrestin while endogenous expression of DsRed and EGFP were imaged without antibody staining as the AAV vector and cone cells of CGFP mice express DsRed

and EGFP, respectively. IHC analysis showed robust transduction of photoreceptors (Figure 3.8, 3.9).

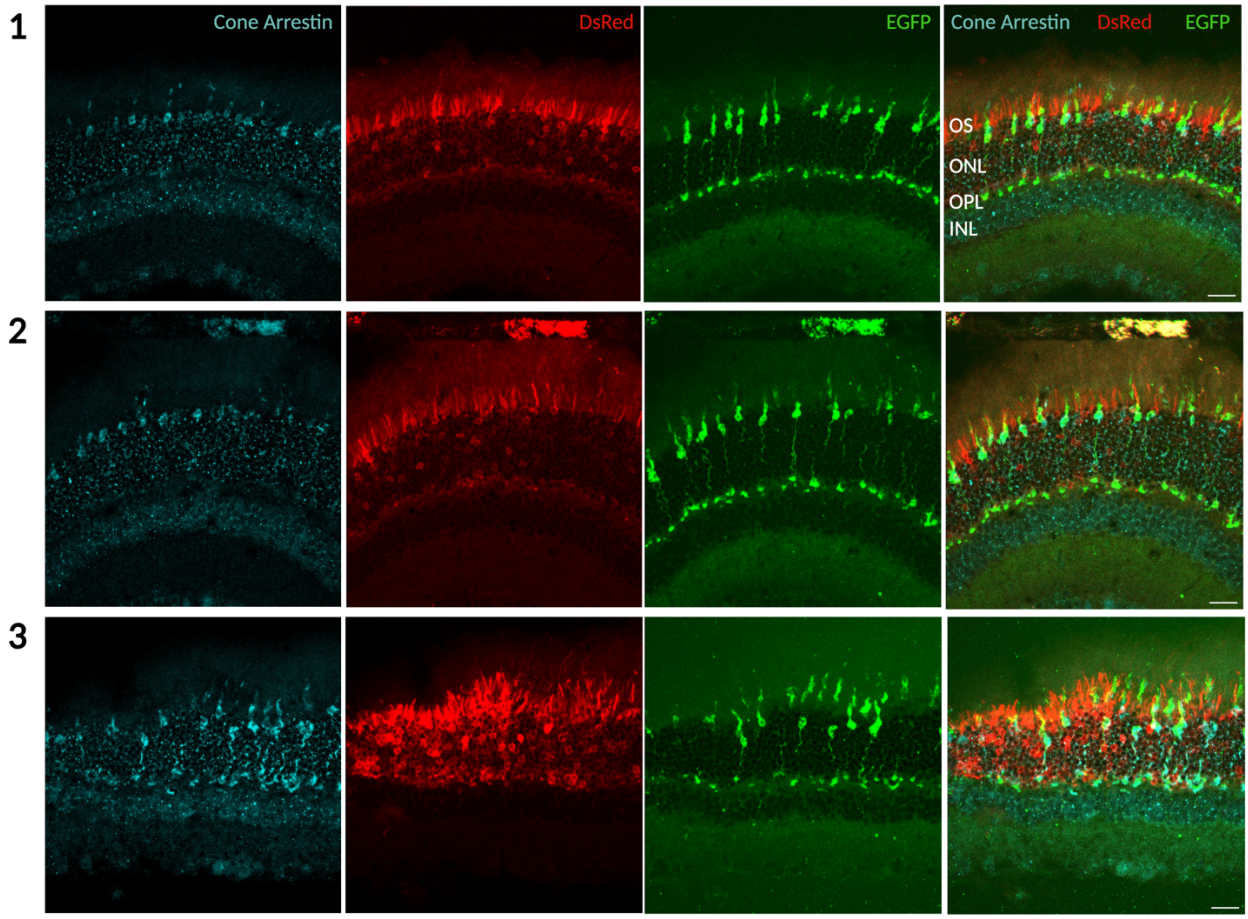


Figure 3.8: Immunohistochemistry of 3 retinal sections following subretinal injection of AAV5-hGRK1-DsRed at $5x10^{11}$ gc/mL

Confocal images of IHC slides. Retinal layers labeled as outer segment (OS), outer nuclear layer (ONL), outer plexiform layer (OPL) and inner plexiform layer (IPL). Rows represent 3 individual eyes injected with AAV5-hGRK1-DsRed 6-weeks following subretinal injection. Cone cells stained with cone arrestin (CA) in cyan. Cells expressing DsRed are represented in red channel. Endogenous EGFP expressing cone cells in green channel. The final column represents merged images. DsRed shows variable but robust transduction of rod photoreceptors. Little evidence of colocalization of cone markers (CA or EGFP) with DsRed in merged images was seen. Scale bar = 20uM.

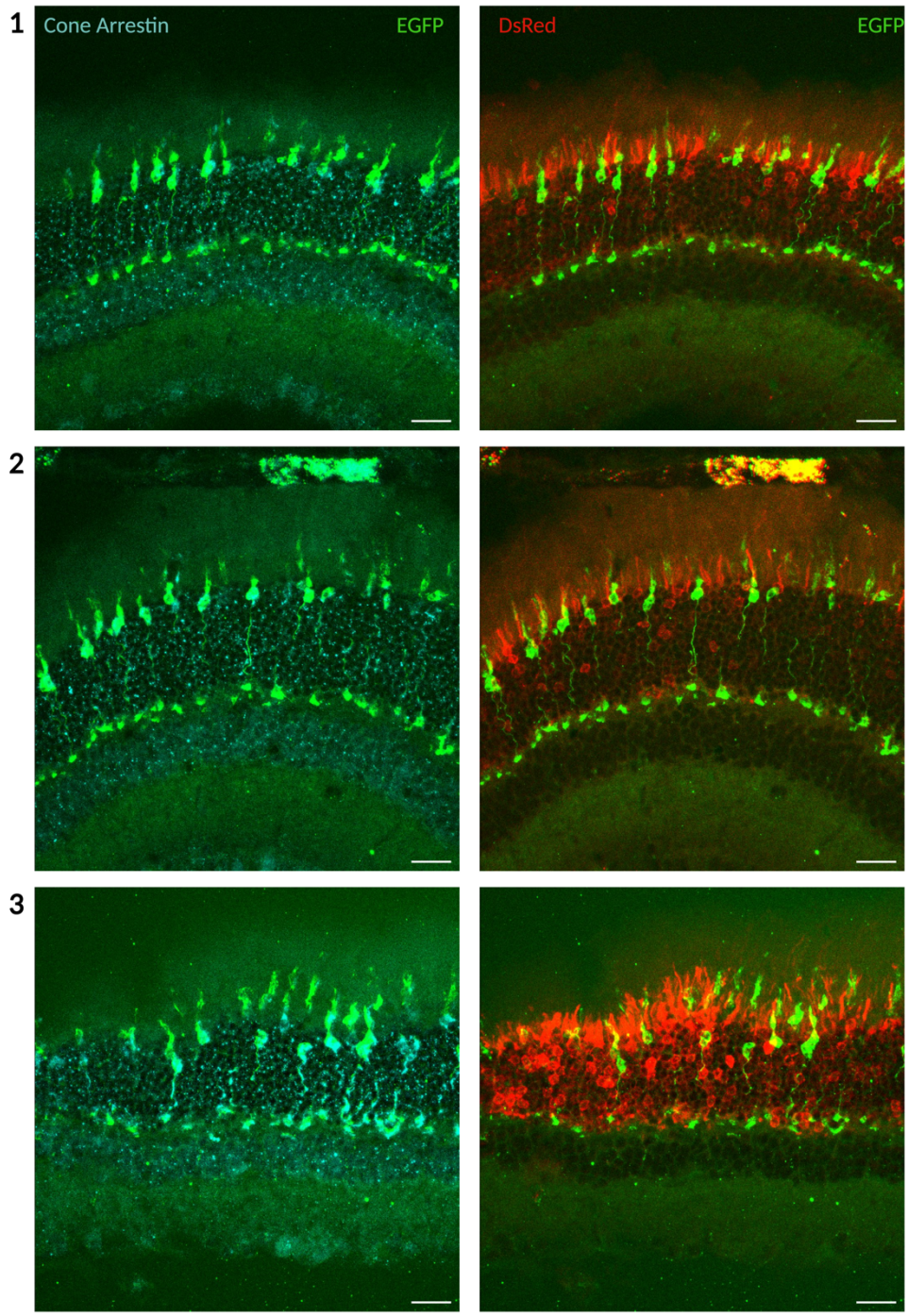


Figure 3.9: Zoomed merge images of IHC of retinal sections from Figure 3.8

Confocal images of IHC slides. Rows represent 3 individual eyes injected with AAV5-hGRK1-DsRed 6-weeks following subretinal injection. Cone cells stained with cone arrestin (CA) in cyan. Cells expressing DsRed are represented in red channel. Endogenous EGFP expressing cone cells in green channel. Scale bar = 20uM.

3.3.3 – Dose escalation response of subretinal injections of AAV5-hGRK1-DsRed at $1x10^{12}$ gc/mL

Since subretinal injection of AAV5-hGRK1-DsRed at a viral dose of $5x10^{11}$ gc/mL demonstrated less retinal thinning, the viral dose was titrated up to further assess dosing limitations in the CGFP mouse retina. Due to the toxicity of the AAV5-CAG-DsRed vector at the initial (low) dose, it was not feasible to test a higher dose of this vector. For the next arm of this study, AAV5-hGRK1-DsRed was subretinally injected at a higher viral dose of $1x10^{12}$ gc/mL.

cSLO images and OCT scans were taken 5-weeks post-injection. The 5-week timepoint was chosen as the prior experiment established DsRed expression peaks around 5-weeks post-injection before plateauing. GAF images show varied transduction of superior portions of the mouse retina (Figure 3.10, blue arrows). In the majority of subjects, the area transduced was less pronounced than in retinae injected at the initial lower dose. BAF imaging shows preservation of EGFP positive cone cells. IRAF imaging does not show evidence of hyperfluorescent areas throughout the retina, suggesting no photoreceptor death or toxicity (Figure 3.10).

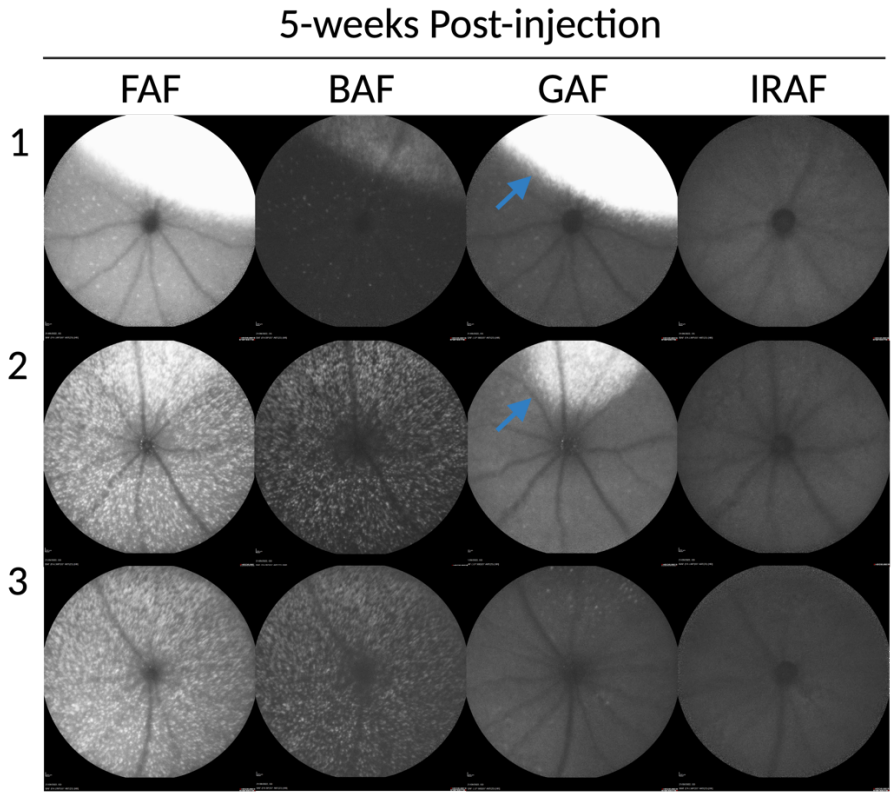


Figure 3.10 cSLO imaging of CGFP retinas following subretinal injection of AAV5-hGRK1-DsRed at 1x10^{12} gc/mL

Representative cSLO images of fundus auto-fluorescence (FAF), blue auto-fluorescence (BAF), green auto-fluorescence (GAF), and infrared auto-fluorescence (IRAF), images of CGFP mice (n=3) 5-weeks post-injection of AAV5-hGRK1-DsRed at a viral dose of 1x10^{12} gc/mL. All images centered around optic nerve with area of subretinal bleb in superior aspect. FAF images show preservation of green fluorescence (white), representing cone cells with EGFP. BAF images show bleed through of red fluorescence into blue channel in row 1, with evidence of EGFP expressing cone cells in all subjects. GAF images show red fluorescence in superior retina of rows 1 and 2 (blue arrows). IRAF images without hyperfluorescent areas throughout retina.

PRL thickness measured on OCT scans 5-weeks post-injection demonstrates lack of AAV5-hGRK1-DsRed vector toxicity at a dose of 1x10^{12} gc/mL with no significant difference in superior or

inferior PRL measurements compared to PBS injected retinae (Figure 3.11). Additionally, there is a lack of surgical related trauma as evidenced by preservation of PRL thickness between hGRK1 injected eyes and PBS injected eyes. There were no observed areas of hyperfluorescent subretinal deposits on OCT imaging (Figure 3.11).

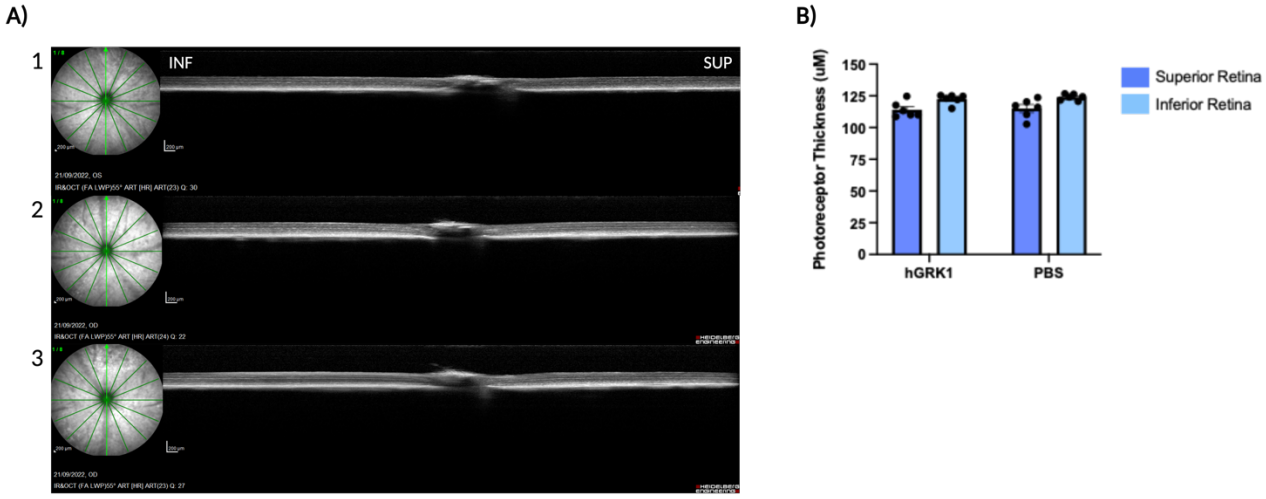


Figure 3.11 OCT scans and photoreceptor layer measurements of CGFP retinas following subretinal injection of AAV5-hGRK1-DsRed at 1x10^{12} gc/mL

A) Representative OCT scans centered around optic nerve of CGFP mice (n=3) 5-weeks post-injection of AAV5-hGRK1-DsRed at a viral dose of 1x10^{12} gc/mL. The vertical green arrow represents area of scan shown on right column with the inferior retina (INF) on the left and superior retina (SUP) on the right. All rows show preservation of superior and inferior photoreceptor layer 5-weeks post-injection. **B)** PRL thickness measurements from OCT scans for AAV5-hGRK1-DsRed (*n*=6) and PBS (*n*=6) injected cohorts 5-weeks post-injection in the superior and inferior retina. Individual values represent mean of 3 PRL thickness measurements ±SEM. Two-way ANOVA compared PRL thickness vs. injection and location: Injection effect *F(1,20)=0.3107 p=0.5834*, location effect *F(1,20)=15.62 p=0.0008*, interaction effect *F(1,20)=0.01027 p=0.9203*. Sidak's multiple comparisons showed no significant difference in PRL thickness for AAV5-hGRK1-DsRed vs. PBS injected eyes in superior or inferior retina.

3.4 Discussion

3.4.1 – CAG and hGRK1 promoters drive DsRed expression in photoreceptors

One of the aims of this thesis was to explore the possibility of targeting photoreceptors in the CGFP mouse retina using AAV. The expression of EGFP within a subpopulation of cone cells makes the CGFP mouse an attractive candidate for CRISPR-based experiments, which will be investigated further throughout the remainder of this thesis.

The ubiquitous CAG promoter and the photoreceptor specific hGRK1 promoter were first assessed in their ability to drive DsRed expression in the CGFP mouse retina following subretinal injection. Both CAG and hGRK1 drove expression of DsRed in photoreceptors in the CGFP mouse model at a dose of $5x10^{11}$ gc/mL. At this dose, CAG injected eyes consistently showed DsRed fluorescence in the mouse retina on cSLO imaging. If successful transduction occurred, red fluorescence should be expected in the superior aspect of the retina at the site of AAV vector injection (subretinal bleb). Indeed, CAG injected retinae showed red fluorescence in the superior retina extending into inferior regions, suggesting the ability of the CAG vector to extend transgene expression beyond the subretinal bleb. Several studies have demonstrated AAV packaged expression beyond the subretinal bleb *in-vivo*[153]. cSLO imaging of hGRK1 injected mice retinae similarly showed DsRed fluorescence within the superior retina with some extension into inferior retinal regions. In the higher dose branch of AAV5-hGRK1-DsRed injected at $1x10^{12}$ gc/mL, DsRed fluoresence was again observed in the superior retina on cSLO imaging. IHC analysis showed robust expression of DsRed in photoreceptors of both vectors at a viral dose of $5x10^{11}$ gc/mL, supporting the results of cSLO imaging.

3.4.2 – Retinal Damage and Toxicity

The AAV5-CAG-DsRed vector caused significant retinal damage and toxicity across subjects when subretinally injected at a dose of $5x10^{11}$ gc/mL. In contrast, eyes injected with AAV5-hGRK1-DsRed at the same dose and the higher dose of $1x10^{12}$ gc/mL did not show pronounced areas of retinal damage or toxicity. Similarly, across experiments, eyes injected with the same volume of sterile PBS did not have evidence of retinal toxicity or damage. Taken together, this suggests the AAV5-CAG-DsRed vector alone caused toxicity and damage to retinae of the CGFP mice.

PRL measurements from OCT scans post-injection showed thinning of the superior retina among both vector groups at a dose of $5x10^{11}$ gc/mL. PRL thinning was most pronounced in AAV5-CAG-DsRed injected retinae, with some subjects showing complete PRL disruption. While there was PRL thinning 3-weeks post-injection in AAV5-hGRK1-DsRed injected retinae, the level of thinning in the superior retina was decreased, with a mean thickness of 93.07uM among hGRK1 injected eyes, vs. a mean thickness of 68.61uM among CAG injected eyes. Significant thinning was observed 3-weeks post-injection between CAG vs. hGRK1 injected eyes in both the superior retina (injection site) and inferior retina (noninjected), suggesting AAV5-CAG-DsRed caused significant PRL thinning throughout the retina. PBS injections across groups caused minimal thinning in the superior retina, with a mean thickness of 92.8% of matched inferior measurements. Some thinning in the superior retina, generally below 10%, is expected as a post-injection change due to surgical trauma. At a viral dose of $1x10^{12}$ gc/mL the AAV5-hGRK1-DsRed injected retinae showed no significant PRL thinning in the superior retina. Due to the thinning seen in the lower dose, this was somewhat unexpected. However, the AAV vector injected

throughout the higher dose experiment was from a different AAV batch production so differences in vector production could have led to decreased toxicity when injected at a higher dose.

Within AAV production various factors can influence the toxicity of a vector. Endotoxin, a lipopolysaccharide (LPS) found on the external membranes of gram-negative bacteria, is a common contaminant of AAV. While we reduce the likelihood of endotoxin introduction by using an endotoxin-free kit to prepare plasmid DNA, the use of aseptic technique with proper sterilization, and AAV purification via ultracentrifugation, it is possible the AAV5-CAG-DsRed vector was contaminated, leading to retinal toxicity. Methods to purify AAV samples from endotoxin often led to a decreased viral titer. However, Kondratova et. al have tested a method of endotoxin removal that leads to high levels of viral titer recovery[156]. For AAV5 they report up to 96% recovery of viral titer after LPS decontamination. The purification and concentration method used for AAV vectors produced throughout this thesis is similar. However, in the above paper a detergent is added to the PBS washes to help dissociate LPS micelles. While the addition of a detergent could add additional protection from endotoxin, it is unlikely there was a high level in samples as AAV5-CAG-DsRed and AAV5-hGRK1-DsRed were initially produced side by side under identical conditions. A limulus amebocyte lysate assay (LAL assay) could be performed to test levels of endotoxin in the AAV vectors.

We also consider variability in viral titer measurements leading to imprecise doses being injected. There are a variety of ways an AAV vector titer is achieved. These include physical titer, infectious

titer, and the ratio of full to empty viral capsids. qPCR is widely used and accepted as a method for physical titer and quantifies the concentration of viral genomes in a sample. This method of viral titration was used throughout this thesis and is the method used for preclinical dosing. Titering by qPCR relies on a standard curve, most often generated from plasmid DNA[157]. When titering the DsRed vectors, a variety of primer pairs were designed and tested to establish a reliable standard curve. Primers targeting DsRed and a portion of the hGRK1 promoter were chosen as they could be used to titer multiple AAV vectors. The polyA tail of AAV is commonly used as a target[157] , however, a unique target was available and used in this case. When generating a standard curve, a primer pair against hGRK1 produced the highest efficiency and was subsequently used for all AAV titers which contained the hGRK1 promoter. Primers against DsRed did not produce equal amplification efficiencies compared to those against hGRK1. Due to time limitations with *in-vivo* work, the AAV5-CAG-DsRed was titered with the primer pairs against DsRed. The lower efficiency of the standard curve may have underestimated the titer of the AAV5-CAG-DsRed, and the dose injected was higher than calculated.

Droplet digital PCR (ddPCR) has been shown to have decreased variability[158] and does not rely on a standard curve. Dobnik et. al demonstrated the ability to titer AAV samples with ddPCR using established qPCR methods, suggesting relative ease in transitioning to this method[158]. While ddPCR is emerging as a more reliable and accurate method to titer AAV vectors, ddPCR is less accessible and has a higher cost. Wang et. al suggested a qPCR method which uses an AAV reference in place of transgene DNA as the standard. In their paper, they propose the use of relative potency, comparing an AAV sample to a known AAV reference standard[159]. They also

suggest use of a "non-digested" AAV sample which produced titers comparable to those generated from ddPCR[159,160]. Due to the importance of a correct viral titer for dosing, the use of alternative methods to titer the AAV vectors should be investigated.

Finally, physical titer does not discern the ratio of empty to full viral capsid particles. Scanning electron microscopy (SEM) is used to determine the ratio of empty to full particles but is not routinely used. It is possible that the ratio was significantly different between AAV vectors leading to differences in infectivity. While AAV5-CAG-DsRed and AAV5-hGRK1-DsRed were made side by side, variation in production and cell health is possible. SEM would also show presence of fragmented genomes or damaged viral capsids, both of which would decrease the infectious titer.

Reasons for such widespread damage in the CGFP mouse may also be due to an excess of fluorescent proteins with both EGFP and DsRed expressed in photoreceptors. A phenotype study done on the CGFP mouse demonstrated EGFP expression alone did not cause the dominant cone degeneration seen in the model[144]. Another study similarly demonstrated GFP was not toxic to the rat retina[161]. It is therefore possible that expression of the DsRed protein under a universal promoter is toxic.

3.4.3 – Dose Response

Both AAV5-CAG-DsRed and AAV5-hGRK1-DsRed were initially subretinally injected into CGFP mice eyes at a viral dose of $5x10^{11}$ gc/mL. At this dose both vectors produced robust DsRed expression on cSLO imaging and on IHC in photoreceptors. The AAV5-CAG-DsRed caused

significant damage and toxicity, as discussed above, while the AAV5-hGRK1-DsRed caused less PRL thinning without evidence of retinal damage on cSLO imaging. A lower viral dose of AAV5-CAG-DsRed should be tested to further characterize dosing limitations of this vector in murine photoreceptors. However, due to time constraints of the MSc, results from the hGRK1 vector suggested the initial dose was safe and therefore this vector was prioritized going forward. AAV5-hGRK1-DsRed vector was reproduced and injected at a higher dose of $1x10^{12}$ gc/mL. Interestingly, at the higher viral dose less DsRed expression was seen on cSLO imaging. This could be due to a variety of factors including incorrect titering leading to a lower dose injected or a difference in subretinal injection technique. Since all subretinal injections were performed by Dr. Ahmed Salman, it is unlikely there was a significant difference in injection technique between cohorts. Once again, due to the variability in viral titer measurement, it is most likely the vector was injected at an incorrect dose. Methods to obtain a reliable titer between samples will be vital moving forward for any future experiments with these vectors or the CGFP mouse line.

At both doses, the AAV5-hGRK1-DsRed vector did not show evidence of subretinal inflammation on OCT scans. However, there was significant PRL thinning in the superior aspect of retinae injected at the lower dose while there was no difference in high dose injected retinae. It is possible the second batch of AAV made of this vector was “cleaner”, leading to decreased inflammatory response, or the titer was incorrect, leading to a lower dose injected.

3.5 Conclusions

This chapter represents an *in-vivo* pilot study to evaluate the efficacy of encapsulating a photoreceptor specific promoter (hGRK1) in AAV5 to transduce the retina in the CGFP mouse line. The results of this chapter demonstrate successful promoter switching by plasmid cloning, AAV production, and *in-vivo* techniques, which establish important first steps for the remainder of this thesis. *In-vivo* results show the ability of both the CAG and hGRK1 promoters to drive expression of DsRed in photoreceptors in the CGFP mouse line. Retinal toxicity and damage within the CAG branch of this chapter highlight the importance of promoter choice and careful AAV production and titering.

Chapter 4: *In-vivo* disruption of cone-specific EGFP with a CRISPR-SaCas9 system

4.1 Introduction

While cone photoreceptor cells account for a small percentage of the retina, their function is vital to human vision. Cone cells are responsible for photic, color, high-acuity, and central vision[141]. The canonical visual cycle has been well established and relies of retinal pigment epithelium (RPE) cells to recycle chromophore to both photoreceptor cell types, rods and cones[162]. The function of cone cells which allow species to see in bright light conditions suggests there is rapid recycling of chromophore[163]. To maintain the high activity of cone cells, research suggests a cone-specific visual cycle in addition to the canonical pathway[163]. Humans possess trichromatic vision due to three distinct cone opsin proteins: long-wavelength (L), medium-wavelength (M), and short-wavelength (S). The different cone opsins are sensitive to different frequency photons[141] allowing for color discrimination.

Mice are dichromatic, possessing the M and S cone opsins in a dorsal-ventral gradient within the retina with a higher concentration of M-opsin dorsally and S-opsin ventrally[164–166]. In the CGFP mouse model, it has been demonstrated that there is a higher concentration of EGFP expression cone cells dorsally[144]. While mice have a small population of cone photoreceptors, they remain an important animal model for development of potential treatments for inherited retinal disorders (IRDs) involving cones. Studies looking at gene replacement therapies for achromatopsia, an ocular disorder mediated by cone opsin dysfunction, have shown the feasibility of AAV based delivery to cone cells in mice despite the low cell population[9,17,167–170].

The cone dystrophies (COD) and cone-rod dystrophies (CORD) are hallmarked by degeneration of cone photoreceptors, often followed by rods[4]. Within COD/CORDs, the disorders inherited in an autosomal dominant fashion may be amenable to gene-editing using the CRISPR-Cas9 system. Allele-specific and complete knockout targets of CRISPR-based therapies to treat COD/CORDs are discussed in detail in Chapter 1 of this thesis.

Chapter 3 demonstrated evidence of transduction of rod and cone photoreceptors using a combination of the hGRK1 promoter and AAV5-packaged delivery. To explore the potential of a future CRISPR-based genome editing system being applied in cone photoreceptors, I continued to investigate cone cell targeting with a Cas9 endonuclease vector.

Binding of the Cas9 endonuclease results in a double-stranded break (DSB) in the DNA at a site complementary to the designed single-guide RNA (sgRNA)[171]. In this manner, if appropriately designed, delivered, and expressed, the CRISPR-Cas9 system can achieve targeted DNA editing. To evaluate use of a CRISPR-Cas9 system in cone cells, a hGRK1-SaCas9 plasmid with an EGFP targeting sgRNA was packaged into AAV5 particles and subretinally injected into the eyes of CGFP mice. EGFP expression was assessed both *in-vivo* using cSLO imaging and *ex-vivo* using tissue analysis. To monitor retinal health and response to injection, cSLO imaging and OCT scans were performed. Finally, DNA editing within the neural retinal cell population was assessed via tracking of indels by decomposition (TIDE) analysis. This chapter represents one of the first attempts of DNA editing within cone photoreceptors of mice using a CRISPR-Cas9 system delivered via AAV.

4.2 Materials and Methods

4.2.1 – Plasmid Cloning

Protocols for plasmid cloning are outlined in Chapter 2. The hGRK1-SaCas9 plasmid was a gift from Ariel Kantor. To insert the EGFP targeting sgRNA (F10), the hGRK1-SaCas9 plasmid was linearized using BsaI restriction enzyme digest and confirmed on gel electrophoresis. The oligonucleotides containing the EGFP sequence for targeting were annealed and phosphorylated prior to ligation with the linearized hGRK1-SaCas9 plasmid using T4 ligase. The unmodified plasmid was used as a non-targeting control. Both the unmodified hGRK1-SaCas9 and hGRK1-SaCas9-F10 plasmids were sequenced using Sanger Sequencing prior to AAV production and produced with endotoxin free kits.

4.2.2 – Cell Culture and AAV Production

AAV production is described in section 2.3. Briefly, hGRK1-SaCas9 and hGRK1-SaCas9-F10 were individually transfected alongside pDP5 and TransIT-VirusGEN into hyperflasks seeded with HEK293T cells. ITRs were verified with XmaI restriction enzyme digest prior to transfection. Transfected cells were harvested and lysed to obtain maximum viral particle yield prior to isolation of AAV particles using iodixanol gradient. AAV5-hGRK1-SaCas9 and AAV5-hGRK1-SaCas9-F10 were purified using ultrafiltration and stored at -80°C. All viruses were titrated using qPCR and AAV purity assessed by SDS-PAGE prior to *in-vivo* use.

4.2.3 – TIDE Analysis

TIDE analysis is discussed in section 2.2.9. Briefly, genomic DNA (gDNA) of retinal cells of CGFP mice injected with AAV was isolated. Target sequences were PCR amplified and sanger sequenced prior to analysis with TIDE software.

4.2.4 – Sequencing the opsin locus control region and EGFP

The opsin locus control region (OPSIN-LCR) and EGFP sequence of the CGFP mouse genome was fully sequenced prior to sgRNA design for this chapter and for epigenetic applications discussed in Chapter 5. The neural retinae of CGFP mice were isolated as described in section 2.5.1 and gDNA was isolated as described in section 2.1.5. KOD HotStart Polymerase was used to PCR amplify ~2kb regions of the OPSIN LCR-EGFP sequence. Primers were designed every ~700bp to cover overlaps between regions, allowing sequencing of the full 7.2kb segment containing the OPSIN-LCR and EGFP regions. Following PCR amplification, products were confirmed using gel electrophoresis (2.1.3) and PCR purified (2.1.2) before being sent for Sanger sequencing (2.1.12). Following sequencing, .ab1 files were imported into the software, Geneious Prime, and aligned to a reference sequence of the predicted OPSIN-LCR (Gene ID: 107604627) and EGFP genomes.

4.2.5 – *In-Vivo* Analysis

Details of *in-vivo* work can be found in section 2.4. For all experiments, CGFP mice were genotyped to identify EGFP positive subjects for *in-vivo* work. Additionally for this chapter, all EGFP positive mice identified by genotyping were anesthetized and pupils were dilated for cSLO imaging prior to subretinal injections. 6-week-old CGFP mice underwent subretinal injections of

either AAV vector or PBS. Details of injections completed throughout this chapter can be found in Table 4.1.

Following subretinal injections, mice were left for 5-9 weeks and imaged periodically using cSLO/OCT. cSLO images were taken to assess EGFP expression and retinal toxicity. OCT scans allowed visualization of the individual retinal layers and measurement of the photoreceptor layer (PRL) thickness. PRL measurements were taken as described in section 2.4.5. Mean grey fluorescence of cSLO images was performed as described in section 2.4.6.

Table 4.1 - Details of SaCas9 *in-vivo* Experiments

Dose (genome copies/mL)	Injection Group	Number of Eyes
$5x10^{11}$	Non-Injected	3
	PBS	15
	AAV5-hGRK1-SaCas9	10
	AAV5-hGRK1-SaCas9-F10	9
$5x10^{12}$	PBS	11
	AAV5-hGRK1-SaCas9-F10	11
$1x10^{13}$	PBS	9
	AAV5-hGRK1-SaCas9-F10	9

4.2.6 – Tissue Analysis with Immunohistochemistry

Details of IHC can be found in section 2.5.4. Briefly, posterior eye cups were harvested following the final imaging session for each study. The fixed eye cups were taken through a series of increasing sucrose concentration prior to embedding in OCT. The eye cups were cryosectioned into 12uM slices on a Leica Cryostat and left to dry on superfrost slides. Slides were stained with Anti-cone arrestin to identify cone cells, and Anti-Hemagglutinin (HA) tag to localize the AAV5-

hGRK1-SaCas9 vector. Hoescht was used for nuclear counter-staining. Finally, slides were imaged using the LSM-710 confocal microscope (section 2.5.5). Generated images were exported as .lsm files and analyzed on ImageJ.

4.2.7 – Statistical Analysis

All statistical analyses and graphs were produced using Graphpad Prism (v9).

Mean Grey Fluorescence

Following analysis via ImageJ as described in section 2.4.6, mean grey fluorescence (MGF) values of cSLO images were entered into GraphPad prism for analysis. Mixed-effects analysis or Two-way ANOVA with Sidak's multiple comparisons compared MGF vs. injection and time.

Immunohistochemistry Analysis

The number of cones and EGFP positive cones were counted in ImageJ for three retinae injected with AAV5-hGRK1-SaCas9-F10. For each retina, three regions of the superior (injection site) and three regions of the inferior (noninjected site) retina were counted. A ratio of EGFP positive cones relative to total cones was calculated. Two-way ANOVA analyzed the effect of viral dose and location on the ratio of EGFP positive cones relative to total cones.

4.3 Results

4.3.1 – Sequencing the CGFP mouse

Before sgRNA design and selection, the opsin locus control region (OPSIN-LCR) and EGFP regions of the CGFP mouse genome needed to be sequence verified. Due to difficulty amplifying the 7.2kb region, the region was split into six ~2kb segments. Primers were designed to amplify each of six segments of the OPSIN-LCR-EGFP region. The segments were PCR amplified before confirmation with gel electrophoresis (Figure 4.1, A). Sequencing primers were designed every ~700bp to allow overlap between sequencing reads (Figure 4.1, B). The full sequence of the OPSIN-LCR and EGFP region can be found in the appendix.



Figure 4.1 Sequencing the OPSIN-LCR and EGFP region

A) UV exposure image of agarose gel with gradient PCR at 55°C, 60°C, and 65°C for segment 1 followed by segments 2-6 and a negative control. All segment bands expected at ~2kb. B) Sequencing trace highlighting overlap between segment 3 and segment 4 within the OPSIN-LCR with alignment to predicted genome sequence (Gene ID: 107604627).

4.3.2 – Cloning and AAV production

To test an active Cas9 system in the CGFP mouse, a previously screened sgRNA candidate which targets EGFP was chosen. For the remainder of this thesis, this sgRNA will be referred to as F10. In her thesis, Dr. Caroline Peddle screened multiple EGFP targeting sgRNA candidates and demonstrated efficient *in-vivo* EGFP disruption in the NRL-EGFP[172] (RGFP) mouse model using sgRNA F10[173]. The EGFP sequence of the RGFP and CGFP mice lines were confirmed to be identical via Sanger Sequencing, supporting *in-vivo* use of F10 in the CGFP line.

F10 was cloned into the hGRK1-SaCas9 plasmid and verified by sanger sequencing prior to AAV production (Figure 4.2). Four batches of AAV were produced: AAV5-hGRK1-SaCas9 (V4 and V5) and AAV5-hGRK1-SaCas9-F10 (V3 and V6). The unmodified hGRK1-SaCas9 plasmid was used as a non-targeting active Cas9 counterpart. All viral preps were titered (Table 2.9) and SDS-PAGE analysis was performed (Figure 2.4, A-B) – Described in section 2.3. All vectors underwent restriction enzyme digest with XmaI to confirm presence of ITRs and plasmids were fully sequenced prior to virus production (Figure 4.2, C).

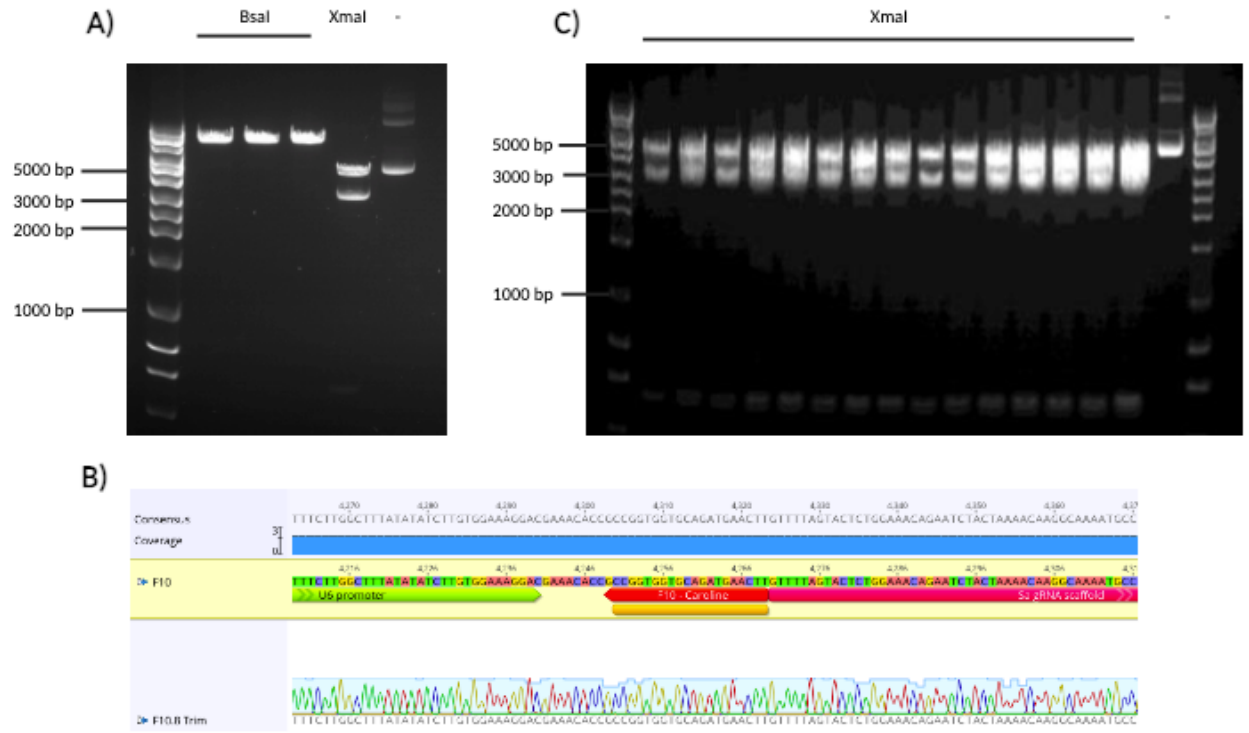


Figure 4.2 Generating active SaCas9 plasmids for AAV production

A) UV exposure image of agarose gel of hGRK1-SaCas9 after BsaI restriction enzyme digest (lanes 2-5), XmaI restriction enzyme digest (lane 6), and undigested plasmid. BsaI band expected at 7kb. XmaI bands expected at 4kb and 2.7kb. B) Sanger sequencing trace shows insertion of F10 sgRNA into hGRK1-SaCas9 with alignment to predicted genome sequence. C) UV exposure image of agarose gel of hGRK1-SaCas9-F10 after XmaI restriction enzyme digest (lanes 2-16) and undigested plasmid (lane 17). XmaI bands expected at 4kb and 2.7kb.

4.3.3 – Retinal toxicity with increasing AAV dose

We were interested in AAV5 dosing limitations in the CGFP mouse model; therefore, three viral doses were tested for subretinal injections: $5x10^{11}$ gc/mL (low), $5x10^{12}$ gc/mL (mid), and $1x10^{13}$ gc/mL (high). Subretinal injections of the vectors were initially dosed at $5x10^{11}$ gc/mL based on data from the previous chapter and prior work in the MacLaren lab. Due to viral titers achieved and limitations in EGFP positive subject numbers, all doses were tested using the EGFP targeting

vector, AAV5-hGRK1-SaCas9-F10. To assess retinal health and vector toxicity, OCT scans, PRL measurements, and IRAF cSLO images were performed.

Low Dose

When injected at the low dose, OCT scans showed significant PRL thinning in the superior retina of eyes injected with AAV5-hGRK1-SaCas9-F10 5-weeks post-injection when compared to PBS injected eyes (Figure 4.3, A-B). Some thinning was observed In PBS injected eyes; however, this was within the expected range (1-10%) of PRL thinning due to the traumatic nature of subretinal injections. No retinal toxicity (hyperfluoresence) was seen on IRAF images of cSLO imaging 5-weeks post-injection of the EGFP targeting vector (Figure 4.6, A).

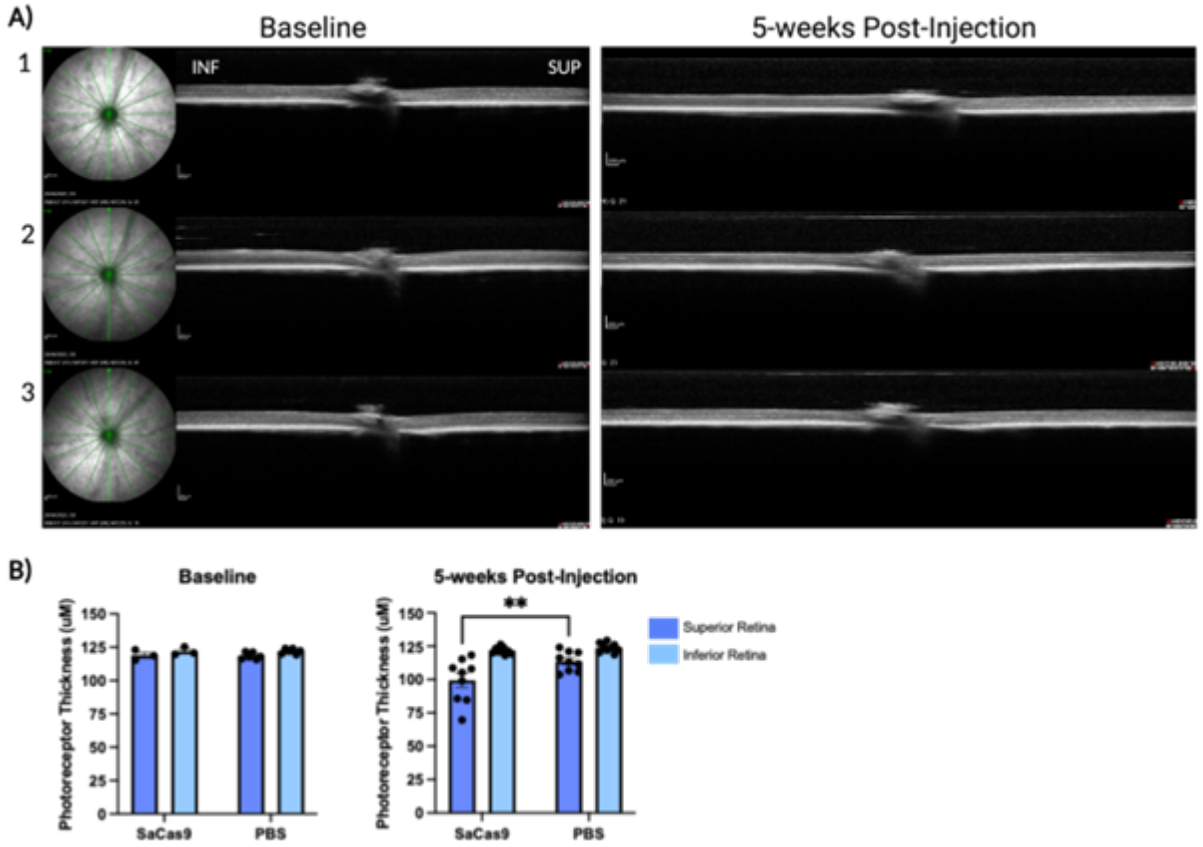


Figure 4.3 OCT and PRL analysis following subretinal injection of AAV5-hGRK1-SaCas9-F10 at 5x10^{11} gc/mL

A) Representative OCT scans centered around optic nerve of CGFP mice (n=3) at baseline and 5-weeks post-injection of AAV5-hGRK1-SaCas9-F10 at a viral dose of 5x10^{11} gc/mL. The vertical green arrow represents area of scan shown on right column. The inferior (INF) aspect of the retina is marked on the left with the superior (SUP) aspect of the retina on the right. B) Photoreceptor layer thickness measurements from OCT scans for PBS and AAV5-hGRK1-SaCas9-F10 (SaCa9) injected cohorts at baseline (n=3) and 5-weeks post-injection (n=9) in the superior retina (subretinal injection site) and inferior retina (noninjected site). Individual values represent mean of 3 PRL thickness measurements ±SEM. Two-way ANOVA at baseline showed no significant difference in photoreceptor layer thickness due to retinal location or injection group. 5-weeks post-injection, two-way ANOVA showed a significant difference in PRL thickness for SaCas9: Injection effect *F(1, 32)=7.242 p=0.0112*, location effect *F(1, 32)=28.64 p<0.0001*, interaction effect *F(1, 32)=3.850 p=0.0585*. Sidak's multiple comparisons test showed a significant difference in the superior retina between SaCas9 and PBS injections, *p=0.0049*.

Mid Dose

OCT scans and associated PRL measurements of retinae injected with a mid-dose showed significant thinning in the superior retina of SaCas9 injected eyes when compared to PBS injected eyes (Figure 4.4, A-B). However, IRAF imaging did not show evidence of retinal toxicity on cSLO images 5-weeks post-injection (Figure 4.8, A).

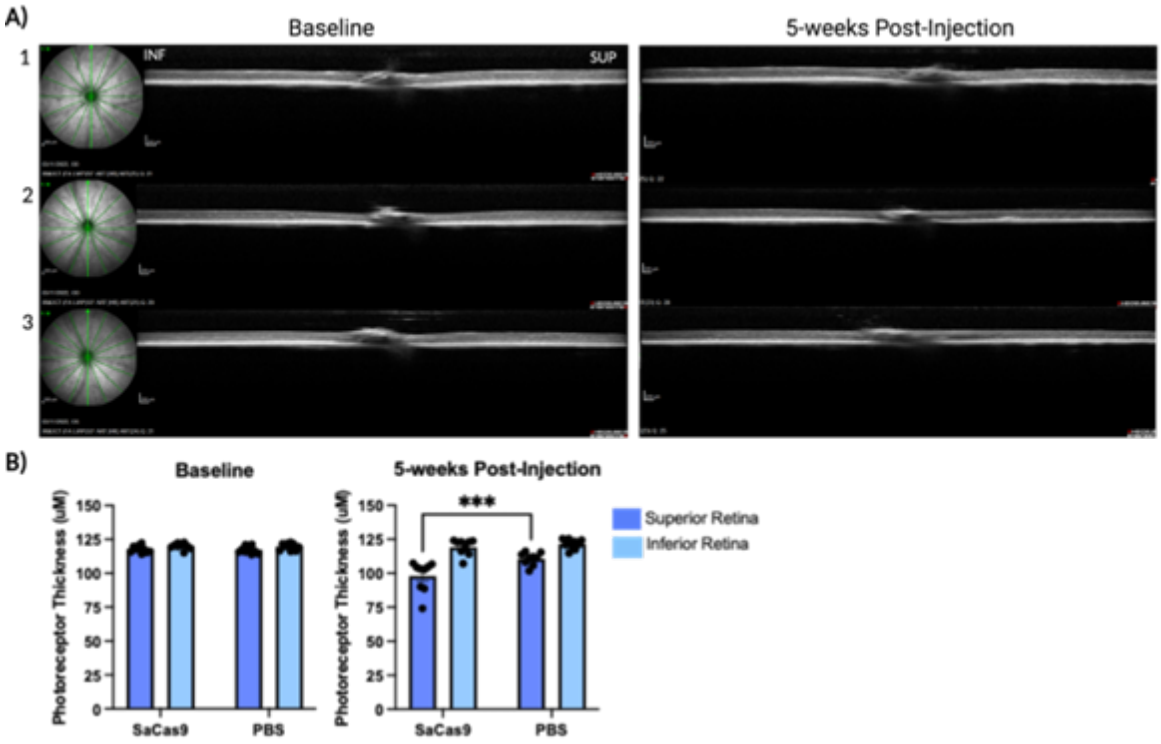


Figure 4.4 OCT and PRL analysis following subretinal injection of AAV5-hGRK1-SaCas9-F10 at $5x10^{12}$ gc/mL

A) Representative OCT scans centered around optic nerve of CGFP mice (n=3) at baseline and 5-weeks post-injection of AAV5-hGRK1-SaCas9-F10 at a viral dose of $5x10^{12}$ gc/mL. The vertical green arrow represents area of scan shown on right column. The inferior (INF) aspect of the retina is marked on the left with the superior (SUP) aspect of the retina on the right. B) Photoreceptor thickness measurements from OCT scans for AAV5-hGRK1-SaCas9-F10 (n=10) and PBS (n=10) injected cohorts at baseline (n=10) and 5-weeks post-injection (n=9) in the superior retina (subretinal injection site) and inferior retina (noninjected site). Individual values represent mean of 3 PRL thickness measurements ±SEM. Two-way ANOVA at baseline showed no significant difference in photoreceptor layer thickness due to retinal location or injection group. 5-weeks post-injection, two-way ANOVA showed a significant difference in PRL thickness: Injection effect *F(1, 33)=10.84 p=0.0024*, location effect *F(1, 33)=49.74 p<0.0001*, interaction effect *F(1, 33)=5.097 p=0.0307*. Sidak's multiple comparisons test showed a significant difference in the superior retina between SaCas9 and PBS injections, *p=0.0010*.

High Dose

When injected at the high dose OCT scans showed post-injection thinning in the superior retina (Figure 4.5, A-B) with evidence of subretinal blebs (green arrows) representing macrophages [18,19] . An example of pronounced PRL thinning in the superior retina is shown in Figure 4.10, B, with red bars highlighting the PRL. PRL measurements at all time points post-injection show significant thinning in the superior retina compared to PBS injected eyes with progression of thinning as time post-injection increased (Figure 4.10, C). There was no significant difference in inferior PRL thickness between PBS vs. SaCas9 injected eyes at any timepoint, however, similar to the superior retina, there was progression of PRL thinning as time post-injection increased (Appendix 8.2). There was marked retinal toxicity on IRAF imaging 5-weeks post-injection as evidenced by the widespread hyperfluorescent areas (Figure 4.10, red arrows). This cell death and inflammation persisted on cSLO imaging at 7 and 9-weeks post-injection.

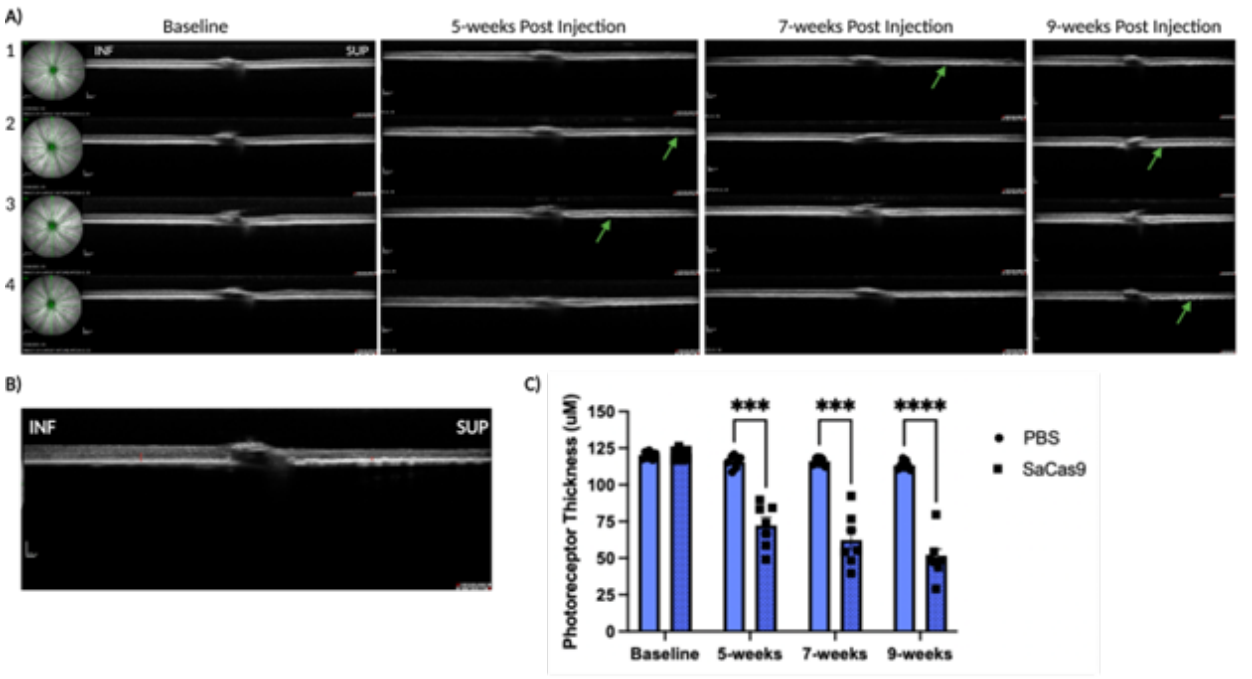


Figure 4.5 OCT and PRL analysis following subretinal injection of AAV5-hGRK1-SaCas9-F10 at $1x10^{13}$ gc/mL

A) Representative OCT scans centered around optic nerve of CGFP mice (n=4) at baseline, 5-weeks, 7-weeks, and 9-weeks post-injection of AAV5-hGRK1-SaCas9-F10 at a viral dose of $1x10^{13}$ gc/mL. The vertical green arrow represents area of scan shown on right column. The inferior (INF) aspect of the retina is marked on the left with the superior (SUP) aspect of the retina on the right. All scans show thinning of the photoreceptor layer in the superior aspect of the retina at post-injection timepoints. B) Zoomed in OCT scan demonstrating photoreceptor layer thinning in superior aspect (right) vs. inferior aspect (left). C) Photoreceptor thickness measurements of the superior retina from OCT scans for AAV5-hGRK1-SaCas9-F10 and PBS injected cohorts at baseline, 5-weeks, 7-weeks, and 9-weeks post-injection (n=7). Individual values represent mean of 3 PRL thickness measurements ±SEM. Two-way ANOVA showed a significant difference in PRL thickness: Injection effect *F(1, 12)=78.22 p<0.0001*, time effect *F(1.535, 18.42)=89.18 p<0.0001*, subject effect *F(12, 36)=6.318 p<0.0001*, interaction effect *F(3, 36)=62.42 p<0.0001*. Sidak's multiple comparisons test showed a significant change in PRL between PBS vs. SaCas9 injection at 5-weeks (p=0.0006), 7-weeks (p=0.0008), and 9-weeks (p<0.001) post-injection.

4.3.4 – Active SaCas9 system disrupts EGFP *in-vivo*

Due to the importance of EGFP visualization to assess EGFP disruption over time, all mice used for *in-vivo* work in this chapter were imaged with cSLO imaging at baseline and at various timepoints, beginning 5-weeks following subretinal injection. IHC analysis was also performed to assess retinal morphology and presence of EGFP positive cone photoreceptors.

Low Dose

The first cohort of mice received subretinal injections at a viral dose of $5x10^{11}$ gc/mL. At baseline, fundus autofluorescence (FAF) and blue autofluorescence (BAF) images demonstrate EGFP expressing cone cells (individual white dots) and IRAF images show no hyperfluorescent areas, which can represent areas of cell death or inflammation (Figure 4.6, A). 5-weeks after subretinal injections IRAF images continue to show no hyperfluorescent areas indicating no cell death or inflammation was present 5-weeks following injection (Figure 4.6, A). 5-weeks post-injection, FAF and BAF continue to show EGFP expressing cone cells. However, in the superior retina (injection site) of some subjects there is decreased green fluorescence on BAF imaging (green arrows) which may indicate EGFP disruption in cone cells (Figure 4.6, A, rows 1-2). To quantify EGFP expression within the injection site, cSLO images were used to calculate mean grey fluorescence (MGF) of the superior retina. Contrary to visual inspection of EGFP on cSLO images, at 5-weeks post-injection there was no difference in MGF of the superior retina compared to baseline for retinae injected with either PBS or low dose AAV5-hGRK1-SaCas9-F10 (Figure 4.6, B).

A nontargeting AAV5-hGRK1-SaCas9 vector was also tested in the low dose branch. Baseline images once again show EGFP expressing cone cells on FAF and BAF without hyperfluorescent areas on IRAF. At 5-weeks post-injection, FAF and BAF images show continued EGFP expression in cones, as expected (Figure 4.6, C). One subject (row 3) demonstrated hyperfluorescent areas on IRAF imaging (Figure 4.6, red arrow) suggesting cell death or inflammation as a result of surgical trauma from subretinal injection. Unfortunately, due to limitations in subject number, only 3 mice injected with the nontargeting vector were imaged at baseline and 5-weeks post-injection. MGF analysis of the 3 retinae show no difference between PBS vs. SaCas9 injected eyes between time points, corroborating the continued EGFP expression seen on cSLO (Figure 4.6, D).

IHC of low dose retinae show robust anti-HA staining, a marker for AAV5-hGRK1-SaCas9-F10 within the subretinal bleb with normal cone cell morphology visualized via anti-cone arrestin staining (Figure 4.7). No colocalization of anti-HA and anti-cone arrestin staining was observed (Figure 4.7).

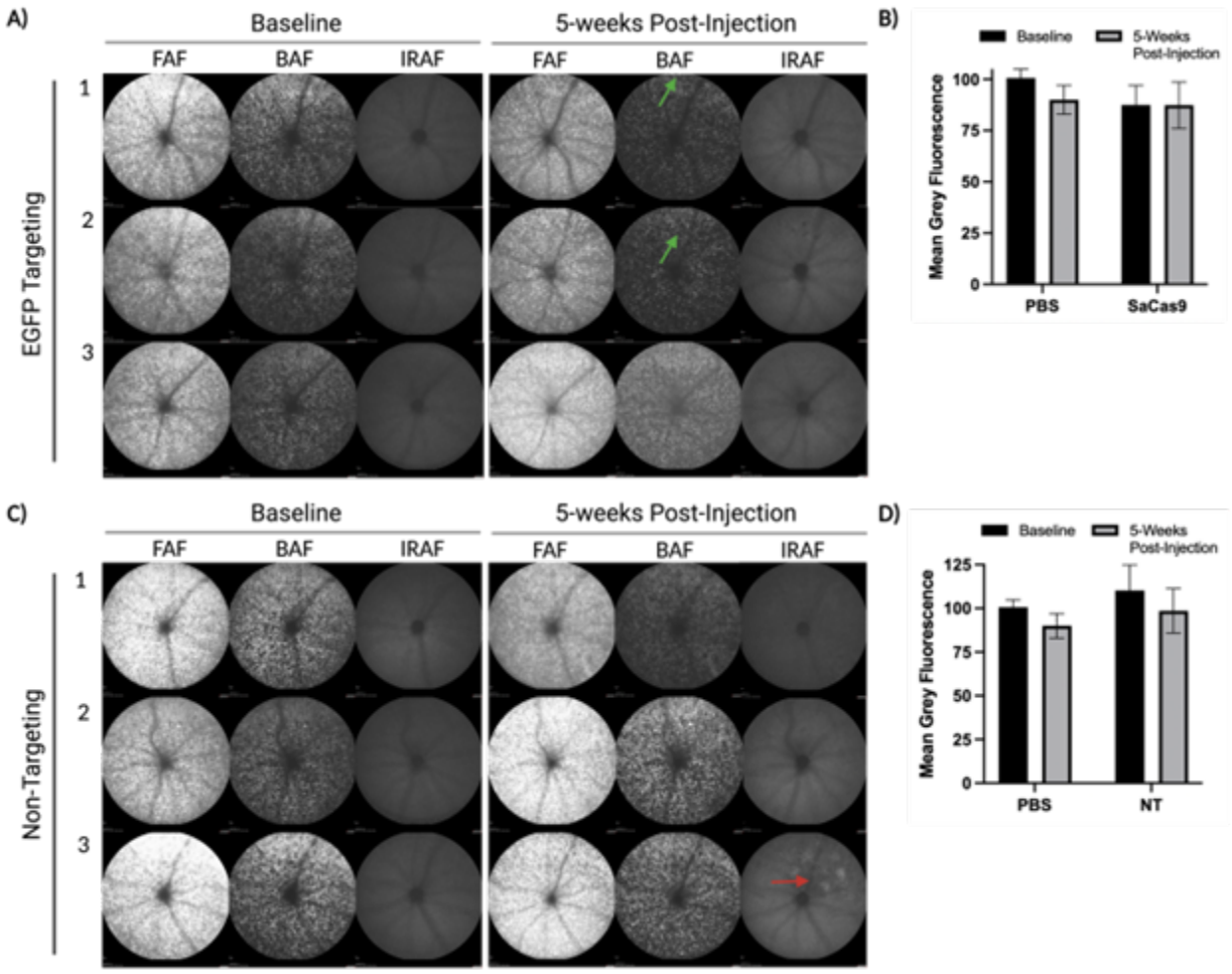


Figure 4.6 cSLO imaging and MGF of CGFP retinas following subretinal injection of AAV5-hGRK1-SaCas9-F10 or AAV5-hGRK1-SaCas9 at 5x10^{11} gc/mL

A) Representative fundus auto-fluorescence (FAF), blue auto-fluorescence (BAF), and infrared auto-fluorescence (IRAF), images of CGFP mice (n=3) at baseline and 5-weeks post-injection of AAV5-hGRK1-SaCas9-F10 at a viral dose of 5x10^{11} gc/mL. All images centered around optic nerve with area of subretinal bleb in superior aspect. Green arrows highlight area of interest. B) Mean grey fluorescence of superior retina at baseline and 5-weeks post-injection of PBS vs. AAV5-hGRK1-SaCas9-F10 (n=9). Bars represent mean ±SEM. Mixed-effects analysis compared MGF vs. injection and time: Injection effect *F(1,29)=0.5167 p=0.4780*, time effect *F(1,29)=0.2414 p=0.6269*, interaction effect *F(1,29)=0.2262 p=0.6379*. Sidak's multiple comparisons showed no difference in MGF at 5-weeks compared to baseline for either PBS or SaCas9 injection groups. C) Representative FAF, BAF, and IRAF images of CGFP mice (n=3) at baseline and 5-weeks post-injection of AAV5-hGRK1-SaCas9 at a viral dose of 5x10^{11} gc/mL. All images centered around optic nerve with area of subretinal bleb in superior aspect. Red arrow highlights area of

hyperfluorescence. D) Mean grey fluorescence of superior retina at baseline and 5-weeks post-injection of PBS vs. AAV5-hGRK1-SaCas9 (n=3). Bars represent mean ±SEM. Mixed-effects analysis compared MGF vs. injection and type: Injection effect *F(1,23)=0.6450 p=0.4301*, time effect *F(1,23)=0.9688 p=0.3352*, interaction effect *F(1,23)=0.002122 p=0.9637*. Sidak's multiple comparisons showed no difference in MGF at 5-weeks compared to baseline for either PBS or NT injection groups.

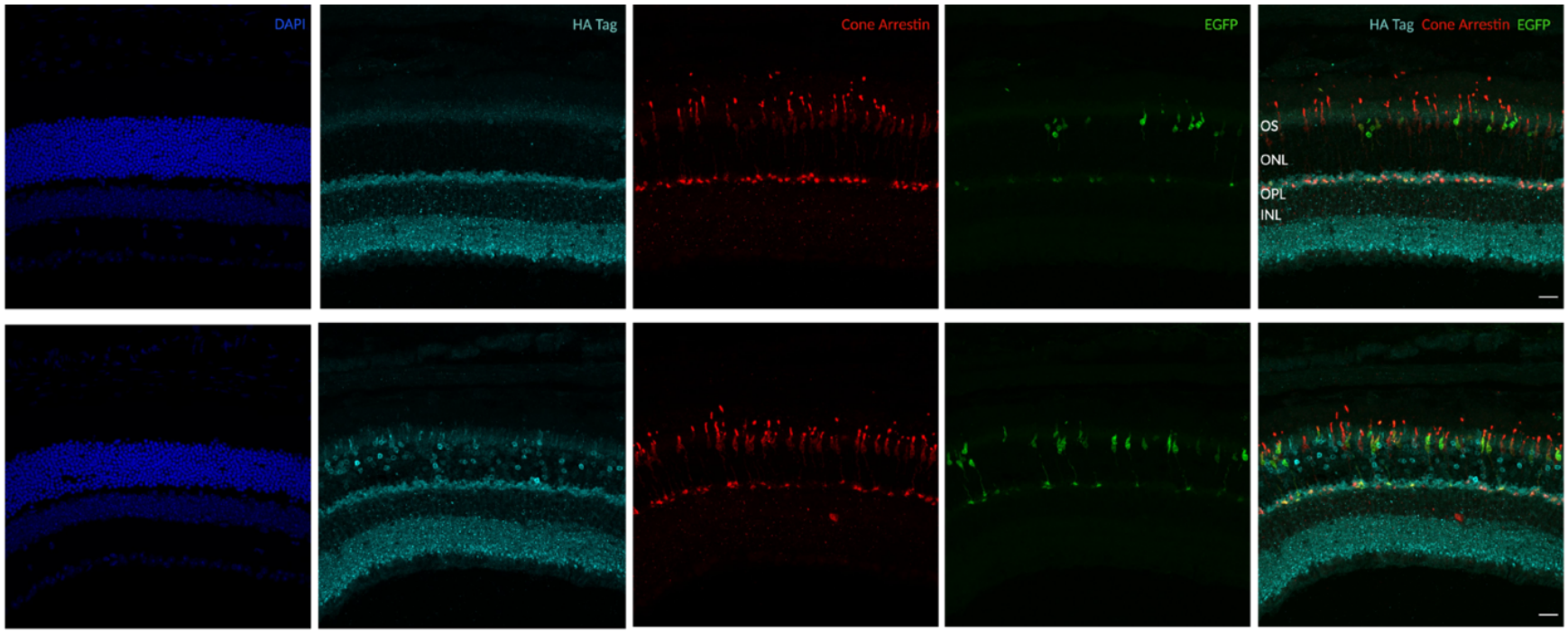


Figure 4.7 IHC analysis following subretinal injection of AAV5-hGRK1-SaCas9-F10 at 5x10^{11} gc/mL

Confocal image of representative IHC section of low dose injected retina within the subretinal bleb (lower row) and outside of bleb (noninjected, upper row) stained with DAPI, anti-HA, and anti-cone arrestin. Retinal layers labeled as outer segment (OS), outer nuclear layer (ONL), outer plexiform layer (OPL) and inner nuclear layer (INL). Scale bar=20uM.

Mid Dose

Next, a viral dose of $5x10^{12}$ gc/mL was subretinally injected as the mid-level dose of the study arm. In keeping with prior findings, baseline images showed EGFP expressing cone cells throughout the retina in FAF and BAF modes while IRAF did not show areas of hyperfluoresence (Figure 4.8, A). 5-weeks post-injection BAF images showed decreased green fluorescence throughout the retina in some subjects (Figure 4.8, A row 1 and 2) and only in the superior aspect of others (green arrow). While interpretation of cSLO images is subjective, results of MGF analysis show decreased MGF 5-weeks post-injection of mid dose of AAV5-hGRK1-SaCas9-F10, suggesting EGFP disruption (Figure 4.8, B). Importantly, IRAF images post-injection do not have areas of hyperfluoresence suggesting no significant cell death or inflammation is present 5-weeks following subretinal injections (Figure 4.8, A).

IHC of the subretinal bleb showed preservation of retinal layers with normal cone cell morphology (Figure 4.9). In noninjected areas distinct retinal layers were present with increased thickness of the ONL compared to areas within the subretinal bleb. Within the subretinal bleb, photoreceptor transduction was observed via anti-HA staining with some colocalization of anti-HA and anti-cone arrestin (Figure 4.9).

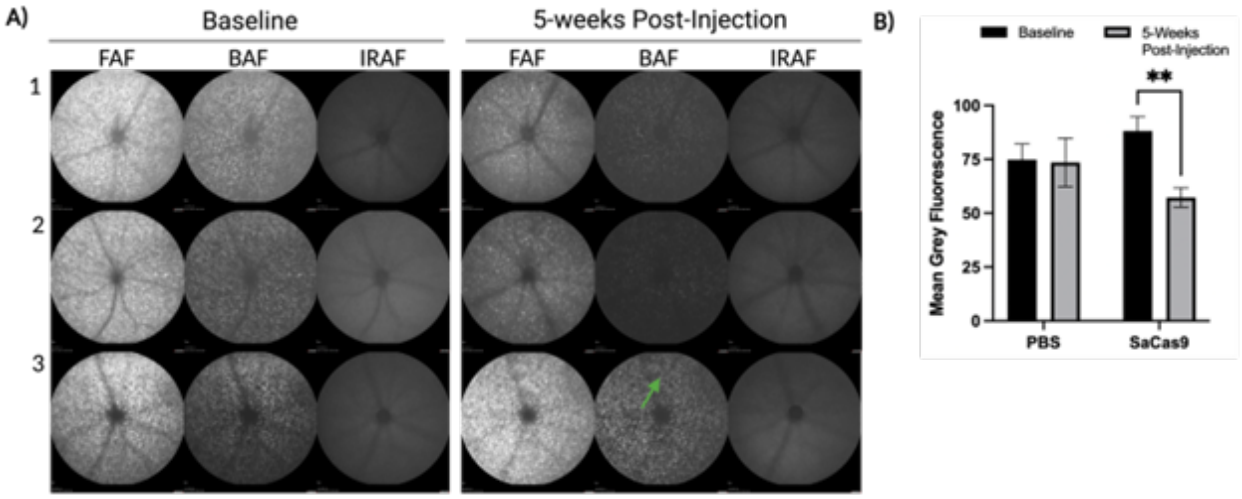


Figure 4.8 cSLO imaging and MGF of CGFP retinas following subretinal injection of AAV5-hGRK1-SaCas9-F10 at 5x10^{12} gc/mL

A) Representative FAF, BAF, and IRAF images of CGFP mice (n=3) at baseline and 5-weeks post-injection of AAV5-hGRK1-SaCas9-F10 at a viral dose of 5x10^{12} gc/mL. All images centered around optic nerve with area of subretinal bleb in superior aspect. Green arrow highlights decreased fluorescence in superior retina. B) Mean grey fluorescence of superior retina at baseline and 5-weeks post-injection of PBS vs. AAV5-hGRK1-SaCas9-F10 (n=11). Bars represent mean ±SEM. Two-way ANOVA compared MGF to injection and time: Injection effect *F(1,20)=0.02950 p=0.8654*, time effect *F(1,20)=5.764 p=0.0262*, interaction effect *F(1,20)=4.861 p=0.0393*. Sidak's multiple comparisons showed a significant difference in MGF at 5-weeks compared to baseline for SaCas9 group, *p=0.0079*, and no difference in PBS group, *p=0.9881*.

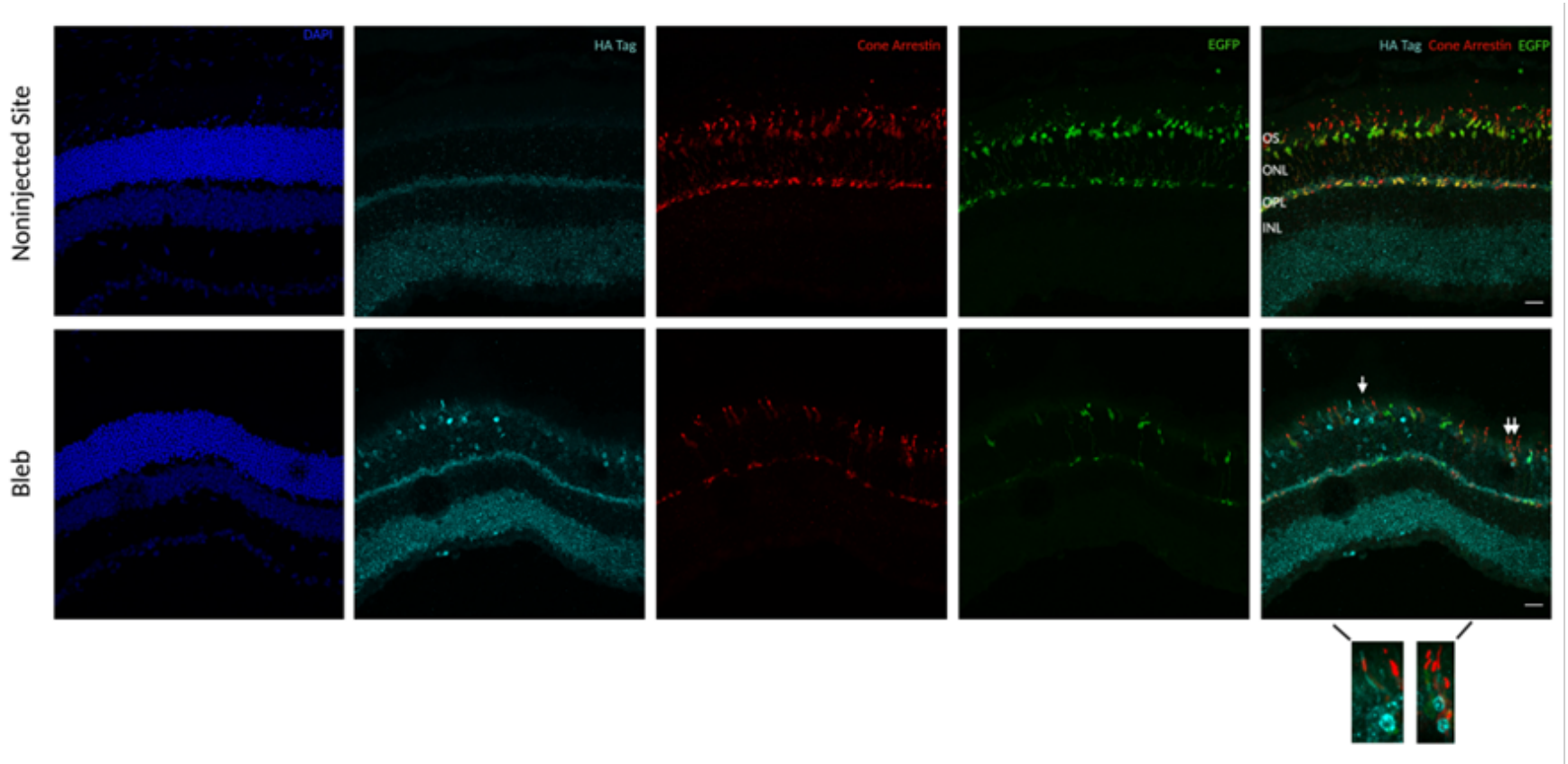


Figure 4.9 IHC following subretinal injection of AAV5-hGRK1-SaCas9-F10 at $5x10^{12}$ gc/mL

Confocal image of representative IHC section of mid dose injected retina within the subretinal bleb (lower row) and outside of bleb (noninjected, upper row) stained with DAPI, anti-HA, and anti-cone arrestin. Zoom in of cone photoreceptors highlighted by arrows. Retinal layers labeled as outer segment (OS), outer nuclear layer (ONL), outer plexiform layer (OPL) and inner nuclear layer (INL). Scale bar=20uM.

High Dose

For the final, high-dose, arm of the study subretinal injections of AAV5-hGRK1-SaCas9-F10 were dosed at $1x10^{13}$ gc/mL. Mice were followed for up to 9-weeks post-injection to assess for changes in EGFP expression. Baseline images were similar to prior study arms (Figure 4.10, A). 5-weeks post-injection, BAF images showed decreased green fluorescence in the superior aspect of the retina of all subjects (Figure 4.10, rows 1-4) with some extension into the inferior retina (green arrow). Decreased green fluorescence observed in BAF imaging persisted to 7 and 9-weeks post-injection, with progression into the inferior retina in one subject (Figure 4.10, blue arrow). At high dose, there was evidence of cell death or inflammation on IRAF imaging in some subjects (red arrows) which persisted to 7 and 9-weeks post-injection. (Figure 4.10, A). MGF showed decreased EGFP expression at all timepoints following subretinal injection without progression (Figure 4.10, B).

IHC demonstrated robust photoreceptor transduction with evidence of colocalization of anti-HA and anti-cone arrestin, supporting cone transduction, but confirms significant retinal disruption, with some retinae showing complete obliteration of the ONL (Figure 4.11 A-B).

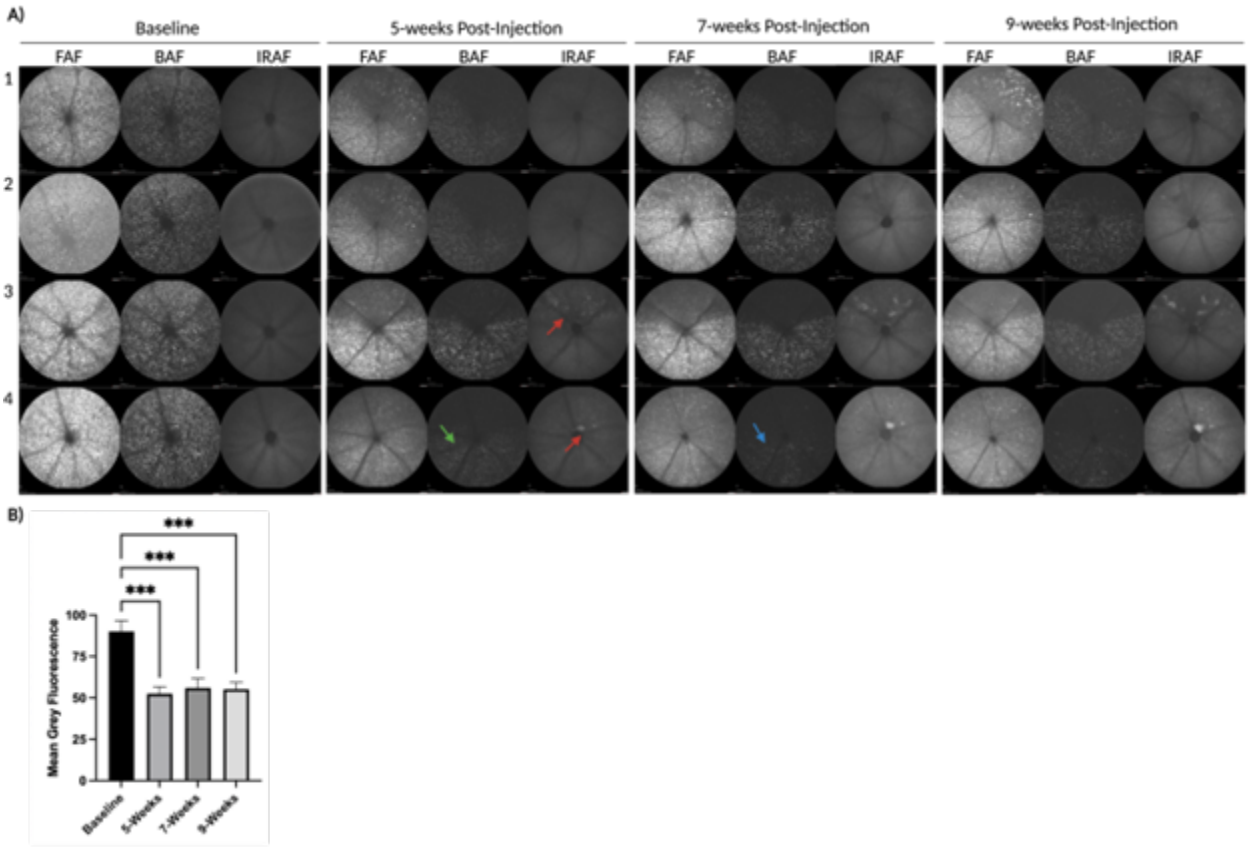


Figure 4.10 cSLO imaging and MGF of CGFP retinas following subretinal injection of AAV5-hGRK1-SaCas9-F10 at 1x10^{13} gc/mL

A) Representative fundus auto-fluorescence (FAF), blue auto-fluorescence (BAF), and infrared auto-fluorescence (IRAF), images of CGFP mice (n=4) at baseline, 5-weeks post-injection, 7-weeks post-injection, and 9-weeks post-injection of AAV5-hGRK1-SaCas9-F10 at a viral dose of 1x10^{13} gc/mL. All images centered around optic nerve with area of subretinal bleb in superior aspect. Green arrow shows decreased fluorescence in inferior retina of one subject. Red arrows highlight hyperfluorescent areas on IRAF imaging. Blue arrow highlights progression of decreased fluorescence on BAF image at 7-weeks post-injection. B) Mean grey fluorescence of superior retina at baseline and 5, 7, and 9-weeks post-injection of AAV5-SaCas9-F10 at high dose (n=9). One-way ANOVA compared mean grey fluorescence across timepoints *F (3, 29)=11.33, p<0.0001*. Tukey's multiple comparison test showed a significant difference between baseline and all timepoints following injection: baseline vs. 5-weeks *p=0.0002*, baseline vs. 7-weeks *p=0.0004*, baseline vs. 9-weeks *p=0.0007*. There was no difference between post-injection time.

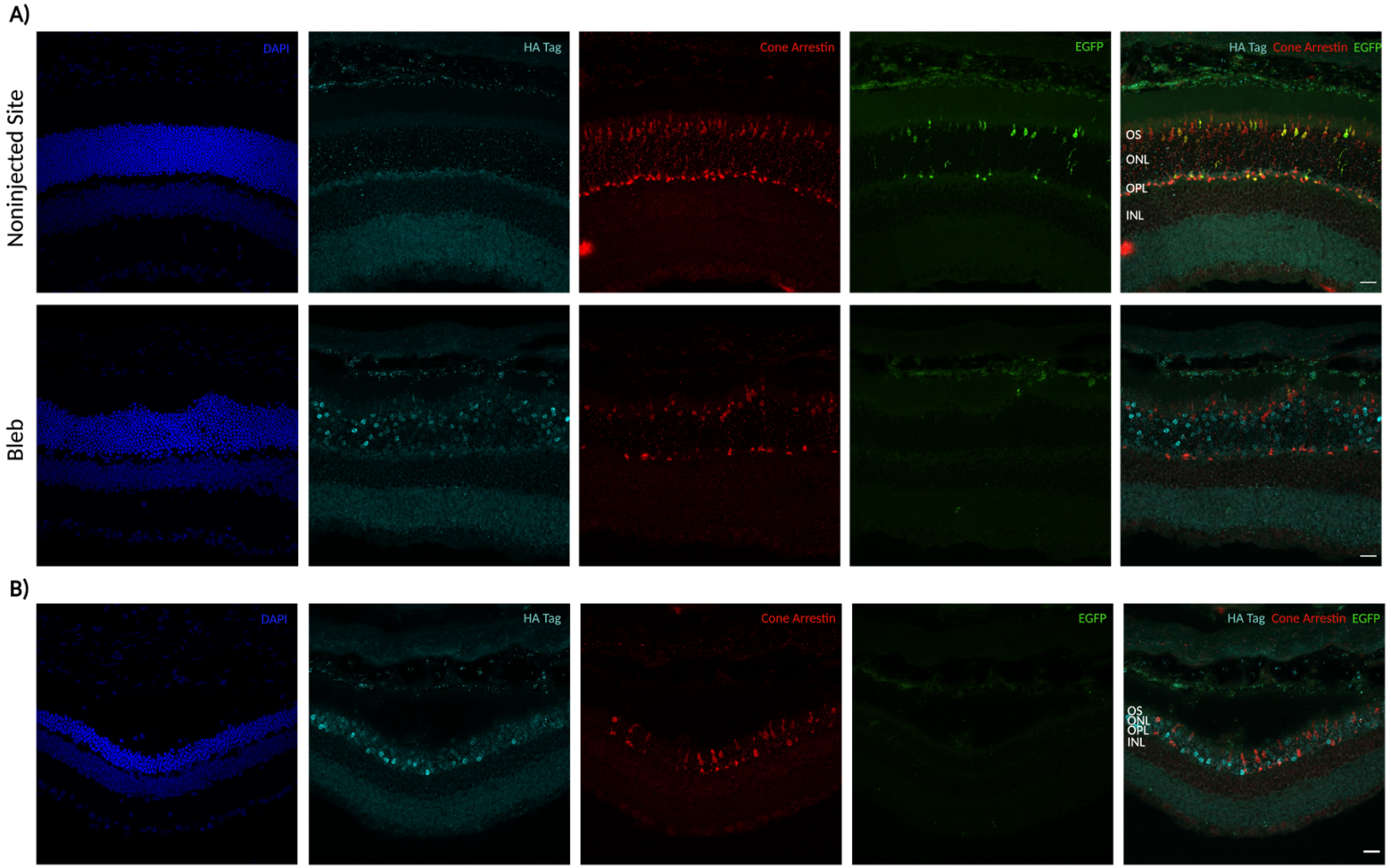


Figure 4.11 OCT and PRL analysis following subretinal injection of AAV5-hGRK1-SaCas9-F10 at 1x10^{13} gc/mL

A) Confocal image of representative IHC section of high dose injected retina within the subretinal bleb (lower row) and outside of bleb (noninjected, upper row) stained with DAPI, anti-HA, and anti-cone arrestin. Retinal layers labeled as outer segment (OS), outer nuclear layer (ONL), outer plexiform layer (OPL) and inner nuclear layer (INL). Scale bar=20uM. B) Confocal image of representative IHC section of high dose highlighting ONL thinning. Scale bar=20uM.

4.3.5 – Dose Response

While PRL thinning was observed across doses, there was a significant difference between PRL measurements in the superior aspect of the retina when injected at a high dose vs. all other injection conditions (Figure 4.12, A). The mean superior retinal PRL thickness at 5-weeks post-injection was 110.6uM for PBS, 99.41uM for low dose, 97.93uM for mid dose, and 75uM for high dose (Figure 4.12, A). There was no significant difference on pairwise comparison between any other injection groups, suggesting the PRL thinning observed in low and mid dose groups, retains an acceptable PRL thickness following subretinal injection of AAV5-hGRK1-SaCas9-F10.

Mean grey fluorescence was measured to assess for *in-vivo* changes in EGFP expression. At 5-weeks post-injection, there was a significant difference in measurements across doses (Figure 4.12, B). Additionally, there was a significant decrease in mean grey fluorescence between low dose vs. mid and high, but no difference between mid and high. This result suggests EGFP disruption is comparable between mid and high doses.

Retinal sections from each dose were processed and stained for IHC analysis (Figure 4.12). As the AAV5 vector had a hemagglutinin tag, this was stained against as a marker for expression of the transgenes within the AAV5 (cyan). Cone cells were identified with anti-cone arrestin (red). Endogenous EGFP was imaged without an antibody (green). For mid and high doses, individual sections within the subretinal bleb and outside of the injection site (noninjected) were analyzed to determine the number of EGFP positive cones and the number of cones stained with cone arrestin. All cones should stain with cone arrestin, so a decrease in ratio of EGFP expressing

cones/total cones, is a way to assess EGFP disruption via the SaCas9 vector (arrow). Indeed, analysis showed a significant decrease in the ratio based on dose and location (Figure 4.12, C). Within the mid dose, a number of cone cells expressing EGFP remained, although the ratio decreased. This contrasts with the high dose, sections, where no slides analyzed contained any EGFP positive cones, despite the presence of morphologically healthy cone cells (Figure 4.12, D).

When analyzing the retinal sections, the edge of the subretinal bleb (injection site) was noted to show a stark drop of EGFP expressing cones with all high dose sections, some mid dose, and no low dose. Representative retinal sections from each dose are shown in Figure 4.13. The presence of EGFP positive cones outside of the subretinal bleb followed by absence of EGFP expressing cones within the subretinal bleb of mid and high dose retinae suggest EGFP disruption due to the SaCas9 system, changes in expression profiles in cone photoreceptors due to toxicity, or potentially a combination of the two.

Taken together, the results of the dose response analyses demonstrate evidence of EGFP disruption *in-vivo* and *ex-vivo* without evidence of pronounced retinal thinning, though changes to the retinal structure were observed, via injection of AAV5-hGRK1-SaCas9-F10 at a dose of $5x10^{12}$ gc/mL.

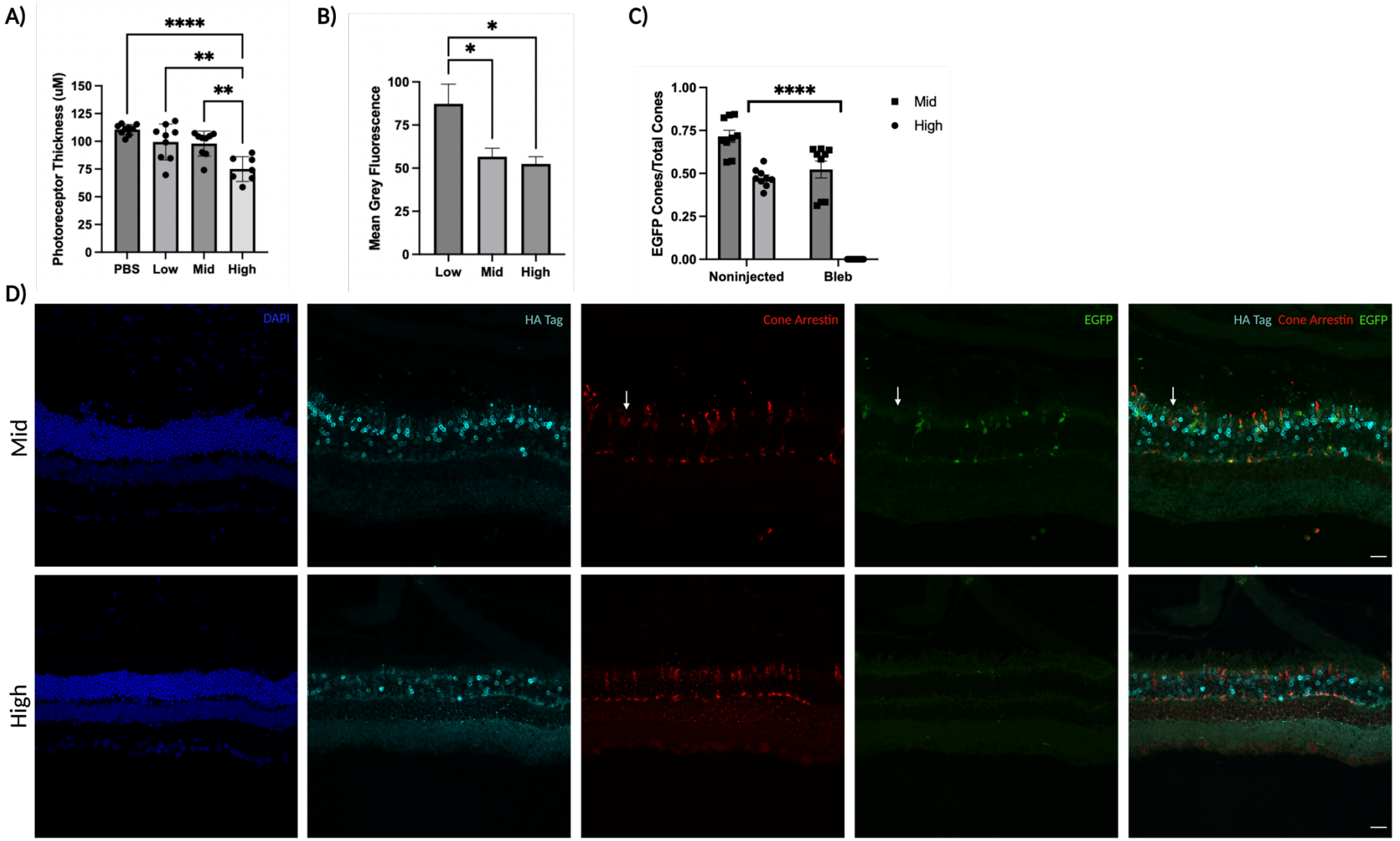

A)
Photoreceptor Thickness (uM)
PBS
Low
Mid
High
****
**
**
B)
Mean Grey Fluorescence
Low
Mid
High
*
*
C)
EGFP Cones/Total Cones
Noninjected
Bleb
****
Mid
High
D)
Mid
High
DAPI
HA Tag
Cone Arrestin
EGFP
HA Tag Cone Arrestin EGFP

Figure 4.12 Dose Response Analyses

A) Superior photoreceptor layer measurements across doses 5-weeks post-injection, n=9 (PBS, low, mid) n=7 (high). One-way ANOVA showed a significant difference in PRL thickness according to dose (*F=12.61, p<0.0001*). Tukey's multiple comparisons test showed significant differences in PRL thickness between the following groups: PBS and high (*p<0.0001*), low and high (*p=0.0013*), and mid and high (*p=0.0026*). There was no significant difference of superior PRL thickness between eyes injected with PBS vs. low or mid dose. B) Mean grey fluorescence across doses 5-weeks post-injection. One-way ANOVA compared mean grey fluorescence across low, mid, and high doses (treatment) *F (2, 24)=6.226 p=0.0066*. Tukey's multiple comparison test showed significant difference between low vs. mid *p=0.0190* and low vs. high *p=0.0114*. There was no difference between mid vs. high *p=0.9205*. C) Ratio of EGFP positive cones relative to total cones on IHC analysis. Two-way ANOVA analyzed the effect of viral dose and location on the ratio of EGFP positive cones relative to total cones: Dose effect *F(1, 32)=146.4 p<0.0001*, Location effect *F(1, 32)=111.2 p<0.0001*, Interaction effect *F(1, 32)=19.67 p=0.0001*. D) Confocal image of representative IHC sections within subretinal bleb of mid and high dose stained with anti-HA and anti-cone arrestin. Arrow highlights cone stained with anti-cone arrestin without EGFP. Retinal layers labeled as outer segment (OS), outer nuclear layer (ONL), outer plexiform layer (OPL) and inner nuclear layer (INL). Scale bar=20uM.

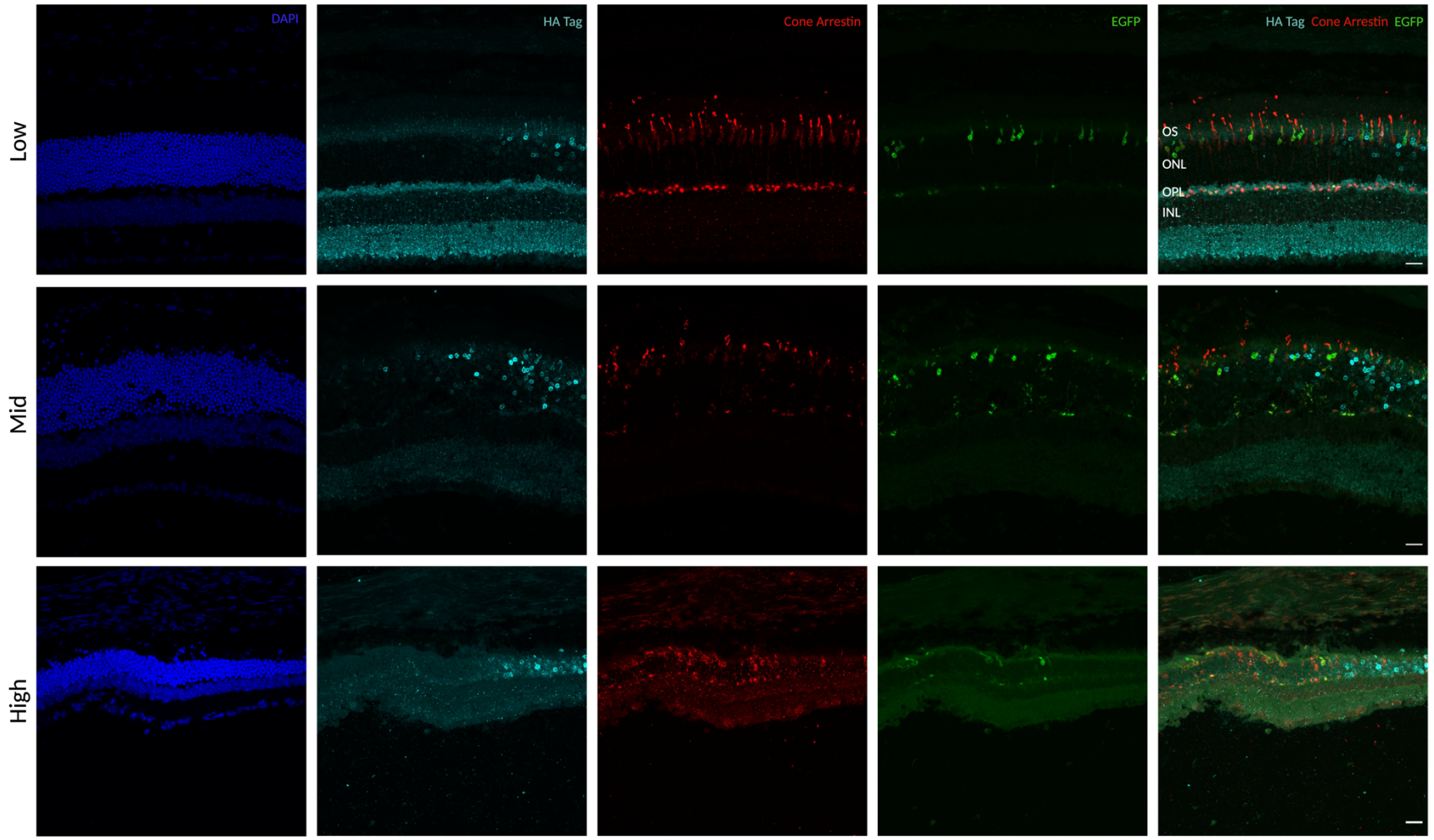


Figure 4.13 Subretinal Bleb Edge

Confocal images of representative IHC sections of subretinal bleb edge of retinae injected with low, mid, or high doses of AAV5-hGRK1-SaCas9-F10 stained with anti-HA and anti-cone arrestin. Retinal layers labeled as outer segment (OS), outer nuclear layer (ONL), outer plexiform layer (OPL) and inner nuclear layer (INL). Scale bar=20uM.

4.3.6 – Assessing DNA Editing

Tracking of indels by decomposition (TIDE) analysis allows an estimation of the editing efficiency of genome-editing tools, such as an active CRISPR-Cas9 system, within the DNA of a pool of cells[140]. The entire neural retinae of mice injected with the low dose of AAV5-hGRK1-SaCas9-F10, AAV5-hGRK1-SaCas9, or PBS were isolated and gDNA was extracted before PCR amplification using primers designed to amplify the region containing the predicted SaCas9 cut site. The purified PCR products were sent for Sanger sequencing and sequencing chromatograms were uploaded into TIDE software for analysis. TIDE analysis showed low editing efficiencies from retinae injected with low dose SaCas9-EGFP targeting, nontargeting, or PBS vectors. Editing efficiencies were between 1.2-2.6% for PBS injected eyes, 1.8-2.5%, for eyes injected with the nontargeting gRNA vector, and 1.7-2.1% for eyes injected with the EGFP targeting vector. Due to time constraints, samples from the mid and high dose branches were not assessed for DNA editing via TIDE.

4.4 Discussion

4.4.1 – EGFP Disruption

This chapter investigated *in-vivo* use of an active SaCas9 system under the control of the hGRK1 promoter and packaged via AAV5 to assess EGFP disruption within cone cells of the CGFP mouse. *In-vivo* cSLO imaging allowed real-time visualization of EGFP expression via blue autofluorescence (BAF) in the retinae of CGFP mice. To quantify the fluorescence of EGFP expressing cone cells, mean grey fluorescence (MGF) of BAF images was calculated. The mid and high doses of AAV5-hGRK1-SaCas9-F10 caused a 64% and 58% decrease, respectively, in mean grey fluorescence in the superior region of the retina, where the subretinal injection was performed. The decrease in MGF suggests there are fewer EGFP expressing cones at 5-weeks post-injection compared to baseline, representing EGFP disruption within cone cells. The EGFP targeting sgRNA, F10, was chosen for *in-vivo* application from previous studies in the MacLaren lab which demonstrated decreased EGFP expression as measured by 36% decrease in MGF in a mouse model which expresses EGFP in rod photoreceptors[173]. Indeed, the results of MGF analysis in this chapter support the broad use of F10 for EGFP targeted *in-vivo* applications and use of AAV5-hGRK1-SaCas9-F10 to disrupt EGFP expression *in-vivo* in the CGFP mouse line.

While it is likely that EGFP disruption occurred due to SaCas9 activity, the decrease in EGFP expression could also represent cell death or a change in cone expression profiles following transduction. If enough cone cells initially expressing EGFP were damaged, it is possible the decrease in MGF is attributable to cell death. This could be especially true in the high dose branch, where marked photoreceptor layer thinning was observed on OCT scans, PRL measurements, and

IHC analysis. However, the decrease in MGF observed in high dose injected retinas was similar to mid dose, where the general retinal structure was preserved despite some indications of morphological changes apparent in some retinal sections, suggesting cell death alone is not responsible for decreased EGFP expressing cone cells.

Additionally, variation in cSLO images could affect visualization of EGFP expressing cone cells. While all efforts were made to minimize variation in imaging sessions by using a standardized protocol and a sole person responsible for imaging, *in-vivo* imaging is a difficult skill to master. Use of near infrared reflectance mode to locate the outer retinal allowed precise identification of the focal plane in which all images were taken[176,177]. There is a natural cone-gradient in the CGFP mouse, with higher numbers of EGFP expressing cone cells in the dorsal retina[144], aligning with the superior aspect of all images in this thesis. When performing the MGF analysis, it was noted that the inferior portion of the retina had consistently lower fluorescence, keeping with the previously published EGFP gradient[144]. Due to the observed gradient in the CGFP model, it was not possible to normalize MGF values to the inferior retinal portion to control for eye-specific factors. While there is inevitably some variation in cSLO imaging, all measures were taken to reach the same focal plane in each imaging session. With minimal variation, the observed decrease in MGF suggests SaCas9 mediated disruption of EGFP.

IHC analysis was also performed to assess EGFP knockout. Retinal sections from mid and high dose branches were analyzed to quantify the number of EGFP expressing cone cells and the number of cells stained with anti-cone arrestin, a cone cell marker, as a measure of the total cone

cell population. Within areas of the subretinal bleb, where the AAV5 was injected, there was a decrease in the ratio of EGFP positive cone cells/total cone cells compared to noninjected areas of the retina, further supporting knockout of EGFP due to the SaCas9 system. Within the subretinal bleb of high dose retinal sections, the number of EGFP positive cone cells dropped drastically, frequently displaying no cone cells with EGFP expression. While this may suggest death of cone cells within the bleb, if cell death alone was the cause of this, one would not expect to see the presence of any cone cells in the region. However, in areas without EGFP expression, morphologically healthy cone cells are present. For this reason, results of IHC analysis suggest disruption of EGFP within cone cells via subretinal injection of AAV5-hGRK1-SaCas9-F10 at mid and high doses with maintenance of the cone cell population.

4.4.2 – DNA Editing

Within a simple CRISPR-Cas9 system, the main outcome aims to cause double stranded breaks (DSBs) in a specified region of DNA. The DSBs are subsequently repaired following two major pathways, nonhomologous end joining (NHEJ) and homology directed repair (HDR)[178,179]. The majority of DSBs are repaired via NHEJ, which is particularly error prone, causing the formation of insertions or deletions (indels)[180,181]. The presence of indels generated by an active CRISPR-Cas9 system can be assessed by PCR amplification of the targeted DNA region. Various software programs are available to predict the formation of indels within a DNA sample via sanger sequencing traces. The most used programs to detect editing include Tracking of Indels via Decomposition (TIDE)[140] and Synthego Interference of CRISPR Edits (ICE)[182]. Both TIDE and ICE have demonstrated their ability to assess indels *in-vitro* producing results comparable to next

generation sequencing (NGS), the gold standard for CRISPR studies. A paper sought to compare the different software programs, including TIDE and ICE, to detect indel formation in *in-vivo* somatic cells, a similar cell population to that of this chapter. In doing so, Brockman et. al., found high variability of indel frequency, size, and number between programs when analyzing the same *in-vivo* sample[183].

In this chapter, TIDE analysis was performed on sequencing results of retinal cells following subretinal injection of low dose ($5x10^{11}$ gc/mL) AAV5-hGRK1-SaCas9-F10 or AAV5-hGRK1-SaCas9. TIDE analysis revealed low editing efficiencies for both the EGFP targeting and nontargeting SaCa9, as well as PBS injected retinae. The low editing efficiencies and variability within sample repeats led to low confidence in TIDE software to detect *in-vivo* EGFP disruption. This was especially true following results of MGF and IHC analysis demonstrating decreased EGFP expression in the mid and high dose branches. Due to time constraints of the MSc, only the low dose branch of this chapter was analyzed via TIDE. With evidence of EGFP disruption in results of MGF/IHC analyses, it is possible DNA editing would have been detected via TIDE for retinae injected at these doses.

Within the CGFP mouse EGFP expression is driven by the OPN1LW promoter, limiting its expression to cone photoreceptors. However, the sequence of EGFP under the OPN1LW promoter is present in all retinal cells. As the entire neural retina was isolated for TIDE analysis in this chapter and the hGRK1 promoter targets both rod and cone cells, it could be argued that DNA editing should be detected if enough cells were edited. As only retinae from the low dose

were analyzed via TIDE, it is possible that there was lower photoreceptor transduction, and the level of editing was below the threshold for indel detection. It is also possible that the SaCas9 system disrupted the DNA of a subset of photoreceptors, however, the number of edited cells was so dilute it was again below the threshold of detection.

It is also possible Cas9 was not successfully expressed in photoreceptors. However, IHC analysis of all doses demonstrate staining via an anti-HA tag antibody. The HA tag is a commonly used epitope tag and was placed within the SaCas9 plasmid. The presence of the HA tag does not guarantee Cas9 expression, however, it does show successful transduction of the plasmid via AAV5 to the photoreceptors of CGFP mice. There is no reason to suggest retinal cells in the CGFP mice are abnormal prior to subretinal injections of AAV5, so if all cellular machinery is functional, the Cas9 packaged in AAV5 should be expressed following successful delivery to the photoreceptors.

Other methods to detect the presence of indels following exposure to the CRISPR-Cas9 system were considered. The gold standard in genome editing experiments is next generation sequencing (NGS), which provides quantitative and qualitative analysis of indel formation. While NGS is one of the most sensitive methods of indel detection, it comes at a high financial and labor cost. For the timeline and experimental design of the MSc, NGS was not considered as a feasible method for indel detection. Subcloning is a lower cost option and another method to assess indel formation which was explored in Chapter 5 of this thesis.

Without concrete evidence of DNA editing, one must consider the possibility there was a problem at any point in experimental flow, including vector production. The inverted terminal repeats (ITRs) of AAV are known to be required for AAV replication, packaging, and vector persistence[184]. Without the ITRs, AAV would be nonfunctional. Due to the high GC content and highly stable secondary structure of ITRs, they are prone to spontaneous deletions and errors during replication[185]. As this is a known problem, methods including use of XL10 Gold Cells for propagation were implored for vector production. Following plasmid cloning, ITRs were confirmed prior to AAV5 production via restriction enzyme digest using XmaI and gel electrophoresis. Since the XmaI restriction enzyme digest produced the expected bands, it is unlikely the ITR regions were missing. However, it is possible that small deletions or point mutations within the ITR regions were undetected. AAV5-hGRK1-SaCas9 and AAV5-hGRK1-SaCas9-F10 plasmids were also sent for standard sanger sequencing prior to AAV5 production. Once again, the high GC content and secondary structure of the ITR regions make it difficult to read through during sequencing. Specialized sequencing methods to read through these regions have been developed by the sequencing service, Azenta UK, the company used for all sequencing in this thesis and could be used in the future to confirm full ITR presence and lack of mutations within the region.

Perhaps the most feasible method to elucidate if editing occurred in photoreceptors of the CGFP mouse would be to include a fluorescent reporter in vector design, allowing only transduced cells to be isolated via fluorescence-activated cell sorting (FACS) and analyzed for indel formation. FACS is a specialized form of flow cytometry, where a mixture of cells can be separated based on

cell specific surface markers. For the application of this thesis chapter, whole mice retinae could be sorted into subpopulations of cells including rod and cone photoreceptors. FACS is an attractive candidate to evaluate cone targeting. However, it also has drawbacks within this experimental setting. Within the mouse retina only 2.8% of photoreceptors are cone cells[142]. To have a cell suspension with enough cone photoreceptors to be detected via flow cytometry, many retinae would be required. This would significantly increase the number of mice needed, vector produced and could increase variability within subretinal injections. Additionally, mechanisms regulating cell death are activated as soon as perfusion ceases, so minimization of dissection time would need to be greatly optimized to capture viable cells. While FACs alone would not be able to differentiate between editing in rods vs. cones, as the hGRK1 targets all photoreceptors, the fact that the AAV5 vector colocalizes with cone cells in any extent, suggests that if editing is seen, this would be occurring in both rod and cone photoreceptors. Other *in-vivo* ophthalmologic CRISPR studies have utilized a fluorescent protein in vector design to allow selection of only transduced cells via FACS. By only selecting transduced cells for analysis, the dilatory effect of unedited cells is decreased. Using FACS, Yu et. al showed indel formation of 11.95% within the EGFP locus following subretinal injection of a SpCas9 system targeting EGFP[186]. In a different study targeting GUCY2D, which causes a gain of function mutation in cone-rod dystrophy 6 (CORD6), the authors showed 28.7% indel formation following subretinal injection of wildtype mice using a dual vector system and FACS analysis[31]. Another study targeting a GUCY2D mutation in rod photoreceptors isolated the entire neural retina to assess DNA editing, similar to what was done throughout this thesis. In their paper, the authors showed indel formation up to 8.45% and 20.1% in the low and high dose branches using UDiTaS analysis[32].

While the authors also used the hGRK1 promoter to drive SaCas9 expression, prior studies and the data in this thesis support robust transduction of rods, making the targeting of GUCY2D within rods, a potentially more accessible target than the EGFP in cone cells of the CGFP mouse. While it is possible to detect editing using the entire neural retina, FACS greatly increases the ability to assess indel formation and would be of great value to assess editing in cone photoreceptors, which constitute such a small fraction of all cells in the retina.

Despite no evidence of DNA editing via TIDE within the low-dose branch, *in-vivo* and *ex-vivo* tissue analyses suggest DNA disruption of EGFP at mid and high doses of AAV5-hGRK1-SaCas9-F10. Results of TIDE analysis for the mid and high dose branches would provide more clarity on the level of DNA editing and indel formation following exposure to the active SaCas9 system.

4.4.3 – Dose Response

Three viral doses of AAV5-hGRK1-SaCas9-F10 were subretinally injected into eyes of 6-week-old CGFP mice: low ($5x10^{11}$ gc/mL), mid ($5x10^{12}$ gc/mL), and high ($1x10^{13}$ gc/mL). The response to the subretinal injection was monitored via cSLO imaging and MGF measurements, OCT scans and PRL measurements, and IHC analysis. For dose response analyses, doses were compared between branches 5-weeks post-injection. Results of the dose study suggest use of a viral dose of AAV5 between $5x10^{12}$ and $1x10^{13}$ gc/mL.

At high dose, several experimental measures suggest the viral load was too high with evidence of retinal toxicity. This is particularly true when looking at OCT scans and PRL measurements. In

the high dose branch, there was severe thinning noted on OCT with significant thinning in the PRL when compared to all doses. Additionally, widespread areas of cell death and inflammation were seen on cSLO IRAF images within the area of the subretinal bleb. A study looking at subretinal injections in mice reported that at 5-weeks post-injection, the area of retinal detachment was reattached and stable, but photoreceptor damage was still present[187]. Unfortunately, the study did not comment on when photoreceptor damage was fully repaired. However, within the high dose branch of this chapter, the hyperfluorescent areas persisted through 9-weeks, suggesting no rescue of retinal photoreceptors up to that time point. While the high dose appeared to cause the most EGFP disruption, especially in IHC demonstrating no EGFP expression, the impact of photoreceptor damage or death cannot be ignored.

On the other hand, the mid dose caused EGFP knockout in cone cells without significant retinal toxicity. PRL thinning was observed in all doses, however, the level of thinning in the mid dose was comparable to the low dose and PBS injected eyes. Some thinning is expected following subretinal injection due to the traumatic nature of the injection and is consistent with previous data and data from PBS injected eyes[187,188]. The fact that thinning was not significantly lowered compared to PBS or low dose measurements, support the use of a viral dose of $5x10^{12}$ gc/mL of AAV5 as safe within the CGFP mouse. Additionally, a study using subretinal injection to deliver a copy of CNGB1, a rod specific gene implicated in retinitis pigmentosa, packaged in AAV5 to a knockout mouse model found the ideal dose to be 10^{12} gc/mL. At this dose, the authors were able to show successful expression of CNGB1 with rescue/reactivation of the CNGA1 protein, alongside return of function of the rod CNG channels and rod functionality[189]. Taken together,

these results suggest that within the mouse retina, it is possible that an ideal dose to target photoreceptors using AAV5 lies around 10^{12} gc/mL.

4.4.4 – Improving Cone Targeting

One of the main areas of interest of this thesis was CRISPR-Cas9 editing of a cone specific gene via the photoreceptor specific promoter, hGRK1, and AAV5 packaged delivery. All aspects of the gene editing system were chosen based on photoreceptor specificity and targeting. While the combination has been largely successful in rod transduction, the results of this chapter highlight some of the unique challenges of targeting cones *in-vivo*.

Use of a cone specific promoter vs. the photoreceptor specific hGRK1 promoter to drive expression of SaCas9 was considered. Studies on gene therapy for achromatopsia have identified a variety of cone specific promoters that could be investigated for use in the CGFP mouse. The promoters include the L-opsin promoters[169] (PR2.1) and S-opsin promoter[190,191]. In a subsequent study, modifications to the PR2.1 promoter identified a shortened 1.7kb version which drove expression of transgenes in cone cells of primates and mice[192]. It is possible that switching the promoter to a cone specific subtype could yield more efficient transduction in the CGFP mouse retina and should be investigated.

Another method to assess CRISPR-based gene editing therapies within cone photoreceptors is the use of a different *in-vivo* model. Like the CGFP mouse, a mouse line has been established which expresses GFP under the control of Chrnb4 promoter[193]. The Chrnb4-GFP mouse has a

unique advantage in that GFP is expressed in all cone subtypes. However, the levels of GFP are below the threshold to be imaged *in-vivo* and visualization has only been shown with an anti-GFP antibody, greatly limiting the *in-vivo* application of the Chrbb4-GFP mouse line[194]. Building on the CGFP mouse, which expresses EGFP under the L-opsin promoter (OPN1LW), Liu et. al developed a mouse model additionally missing both copies of the Nrl gene[195]. Knockout of the Nrl gene has previously been shown to cause a cone-enriched retina, as the Nrl gene is crucial for rod cell development[196]. The novel mouse line generated by Liu et. al demonstrated increased EGFP positive cones and S-opsin in the dorsal region of the retina when compared to CGFP mice. Together, this suggests the OPN1LW-EGFp-Nrl-/- has increased S-opsin cones and a higher proportion of cone cells expressing EGFP. The increase in cone cell population in this model could be of particular interest to the aims of this thesis to test cone photoreceptor targeting and use of a CRISPR-SaCas9 system to knockout a cone specific gene.

A worthwhile method to assess EGFP disruption more accurately within cone cells would be RT-qPCR. Within CRISPR-based studies, it is common to utilize RT-qPCR to quantify mRNA levels of targets of interest. For the current study, levels of EGFP mRNA would be particularly useful in measuring the success of EGFP disruption via SaCas9. Levels of other targets of interest including the sgRNA and SaCas9 itself, would further elucidate dose response and help quantify levels needed for cone cell transduction. By incorporating RT-qPCR into the experimental workflow, this would allow for an experimental design optimized to verify EGFP disruption at multiple levels: DNA via indel detection, mRNA via RT-qPCR, and protein via *in-vivo* imaging and *ex-vivo* tissue analysis.

4.5 Conclusions

This chapter explored the use of an active SaCas9 system within photoreceptors of mice using AAV5 packaged delivery and the photoreceptor specific, hGRK1 promoter. *In-vivo* cSLO imaging and MGF measurements showed evidence of EGFP disruption within cone cells which was corroborated with evidence of EGFP disruption in IHC analysis. The use of an active CRISPR-Cas9 system within cone cells of CGFP mice validates the CGFP mouse line as a valuable animal model to test the use of gene editing strategies for IRDs involving cone photoreceptors. The combination of the hGRK1 promoter and AAV5 packaged delivery is also validated as a combination to deliver gene editing therapies such as CRISPR-Cas9 to photoreceptors of mice. Finally, the dose response branch of this chapter suggests irreversible retinal thinning and toxicity when AAV5 is subretinally injected at a viral dose of $1x10^{13}$ gc/mL, with a safe dose between $5x10^{11}$ gc/mL and $5x10^{12}$ gc/mL. At a dose of $5x10^{12}$ gc/mL, there is evidence of EGFP disruption via the SaCas9 system with some observed changes to retinal structure.

Chapter 5: In-vitro sgRNA screening for epigenetic dSaCas9 repression

5.1 Introduction

Since the discovery of CRISPR-Cas9 as a genome editing system, the toolbox of CRISPR-Cas9 based editing methods has rapidly expanded. Aside from direct DNA editing using the Cas endonuclease family, techniques which target epigenetic mechanisms have evolved, including CRISPR activation (CRISPRa) and CRISPR interference (CRISPRi). These methods act at the transcriptional level to activate or silence transcription of genes, respectively[197]. Like an active CRISPR-Cas gene editing system, the specificity of CRISPRa and CRISPRi are based on the sgRNA design, allowing precise allele-specific targeting. As such, researchers have shown the ability to selectively activate or repress gene transcription within bacteria or human cells[95,98].

Within the ocular system, many IRDs are inherited in an autosomal dominant pattern and cause gain-of-function mutations. While these mutations may be amenable to gene editing via an active CRISPR-Cas9 system to knockout the gene, this results in a permanent change to the genome. The use of CRISPRi to cause gene silencing is an attractive alternative to traditional CRISPR-Cas9 DNA editing due to reversibility, the potential to titrate gene silencing effects, decreased off target effects, and the absence of double-stranded DNA breaks[99,101].

The basic components of a CRISPRi system are a catalytically inactive “dead” Cas9 protein (dCas9) which is unable to cleave DNA, a sgRNA, and a PAM site[98]. While dCas9 alone is able to sterically

interfere with transcription, the addition of transcriptional regulators has been shown to increase effects of gene silencing[94,95,98]. Yeo et al. engineered an enhanced CRISPRi system by fusing dCas9 to two transcriptional regulators, Kruppel-associated box (KRAB) and methyl CpG binding protein 2 (MeCP2)[97]. A previous member of the MacLaren lab, Dr. Ariel Kantor, developed a similar CRISPRi system including the repressor domains KRAB and MeCP2, which will be used throughout this chapter.

Continuing to build on the use of the CGFP mouse line as a preclinical *in-vivo* model to test gene editing techniques, use of CRISPRi was evaluated *in-vitro* against a cone-specific target. As previously described, within the CGFP mouse genome, EGFP is fused downstream of the opsin locus control region (OPSIN-LCR), which contains the red pigment gene (OPN1LW). In this chapter, several sgRNA candidates which target the red-opsin promoter locus were screened *in-vitro* using a dual luciferase assay (DLA) and a fibroblast cell line derived from the CGFP mouse. A protocol for electroporation and maintenance of the fibroblast cell line was also established prior to sgRNA candidate screening.

5.2 Materials and Methods

5.2.1 – Plasmid Cloning

Protocols for plasmid cloning are outlined in Chapter 2. Briefly, ~50bp regions of the OPSIN-LCR were cloned into PsiCHECK2 vector for use in the dual luciferase assay (DLA). sgRNA candidates targeting OPN1LW were cloned into the EFS-dSaCas9.KRAB-MeCP2 vector. A nontargeting EFS-dSaCas9.KRAB-MeCP2 was also amplified and isolated for the DLA.

For sgRNA screening in the CGFP fibroblast cell line, OPN1LW targeting sgRNA candidates were cloned into EFS-SaCas9. A nontargeting EFS-SaCas9 plasmid was also amplified and isolated.

Finally, the EGFP targeting sgRNA, F10, used throughout Chapter 4, was cloned into EFS-SaCas9 for use in the CGFP fibroblast cell line.

5.2.2 – Cell Culture

General methods of subculturing and harvesting of the HEK293T and CGFP Fibroblast cell lines can be found in section 2.2.

5.2.3 – CGFP Fibroblast Electroporation

Additional details can be found in section 2.2.5. CGFP fibroblast cells were electroporated with using the Invitrogen™ Neon™ Transfection System. Electroporation details of key experiments of this chapter are summarized in Table 2.1.

Table 2.1 Details of Electroporation Studies

Plasmid	DNA (ng)	Time Left (days)
pCAG-EGFP	300-900	1-7
pCMV-EGFP	300-900	1-7
pEFS-EGFP	300-900	1-7
pEFS-SaCas9-OPN1LW	600	14
pEFS-SaCas9-F10	600	14

5.2.4 – HEK293T Transfections for TIDE Analysis

Details can be found in section 2.2.9. Briefly, confluent HEK293T cells were transfected using the TransIT-LT1 transfection reagent (MirusBio) with 500ng of pEFS-SaCas9 with OPN1LW sgRNA. The cells were left for 48-hours before cell pelleting and gDNA extraction.

5.2.5 – TIDE Analysis

Details can be found in section 2.2.9. For the OPN1LW sgRNA candidate screening discussed in this chapter, HEK293T cells were transfected with EFS-SaCas9 plasmids each containing a unique sgRNA candidate. The same plasmids were electroporated into CGFP fibroblast cells for additional screening. The cells were pelleted, gDNA was extracted, and the region of interest was PCR amplified. The purified PCR product was sent for sanger sequencing and the resulting chromatogram files were uploaded alongside unmodified DNA into TIDE software to assess for decomposition.

5.2.6 – ICE Analysis

Details can be found in section 2.2.10. Samples assessed via TIDE were additionally run through ICE software to assess for discrepancies in editing rates or presence of indels.

5.2.7 – Subcloning Analysis

Subcloning is an alternative method to detect insertions and deletions following exposure to a gene editing system. A region including the predicted cut site was PCR amplified using GoTaq DNA polymerase (Promega), which creates a 3'-A overhang. The resulting PCR product was ligated into the pGEM-T Easy Vector (Promega), which contains 3'-T overhangs on both sides of the insertion site. The ligation product was transformed into XL10-Gold cells and plated using Isopropyl β-D-1-thiogalactopyranoside (IPTG) and X-gal for blue-white colony selection. Blue-white screening allows identification of clones with the correct DNA insert. For each sample, 24 clones with recombinant DNA were isolated, and 3 replicates were analyzed per condition. Following miniprep and sanger sequencing, the resulting sequence was uploaded into Geneious Prime and compared to the unedited plasmid.

5.2.8 – Dual Luciferase Assay

Details can be found in section 2.2.8. In this chapter, sgRNA candidates targeting OPN1LW were screened for CRISPRi. Each sgRNA candidate was individually cloned into the EFS-dSaCas9.KRAB-MeCP2 plasmid. Targeted regions of OPN1LW were cloned into the PsiCHECK2 plasmid. The resulting plasmids were sent for sanger sequencing prior to use. Each sgRNA candidate was screened using the test conditions listed in Table 2.4 and luciferase expression of each was measured, normalized, and compared to a positive control.

5.2.9 – EVOS Imaging

Details can be found in section 2.2.7. Both HEK293T and CGFP fibroblast cells were imaged using the EVOS FL Auto 2 Cell Imaging System to assess auto-fluorescence, cell health, and cell structure. For electroporation studies, the presence of EGFP expression was additionally elucidated.

5.2.10 – Statistical Analysis

Three independent replicates were performed per condition in the dual luciferase assay and samples used for TIDE analysis. GraphPad Prism (v9) was used for all statistical analysis and graph production.

5.3 Results

5.3.1 – OPN1LW sgRNA screening with dual luciferase assay

A dual luciferase assay (DLA) was used for primary screening of OPN1LW targeting sgRNA candidates. The DLA is an effective and efficient way to screen large numbers of sgRNA candidates for CRISPRi. This assay relies on the plasmid design of the PsiCHECK2 vector, where two luciferase enzymes, renilla and firefly, are under the control of two separate promoters, SV40 and HSK-TV, respectively (Figure 5.1). In this assay, firefly luminescence should be unaffected by CRISPRi mechanisms and acts as an internal control to normalize luminescence readings. If transcriptional repression occurs via exposure to a CRISPRi system, expression of renilla luciferase should be affected due to the insertion location of the DNA region of interest upstream of the renilla transcriptional start stie, disrupting the open reading frame and preventing renilla transcription. To assess the transcriptional repression ability of OPN1LW targeting sgRNAs, 50bp regions of the OPN1LW promoter sequence complementary to the designed sgRNA candidates were cloned into the PsiCHECK2 plasmid. Fourteen 20bp OPN1LW sgRNA candidates were designed and each individually cloned into the EFS-dSaCas9.KRAB-MeCP2 plasmid (data not shown).

Following transfection, eight sgRNA candidates produced consistent and significant repression of renilla luciferase (Figure 5.1). The best performing sgRNA candidates (g4, g5, g6, g8, g10, and g12) caused expression of renilla to decrease to approximately half of normal levels. Interestingly, these sgRNA candidates were located at various distances from the transcriptional start site (TSS). g6 and g8 are the sgRNA candidates located closest to the TSS at -191bp and -182bp,

respectively, while other sgRNA candidates such as g4 (-861bp) and g5 (-778bp) were located much further away. sgRNA candidates g5, g6, and g8 were chosen for subsequent screening based on the NNGRRT PAM site and different locations from the TSS.

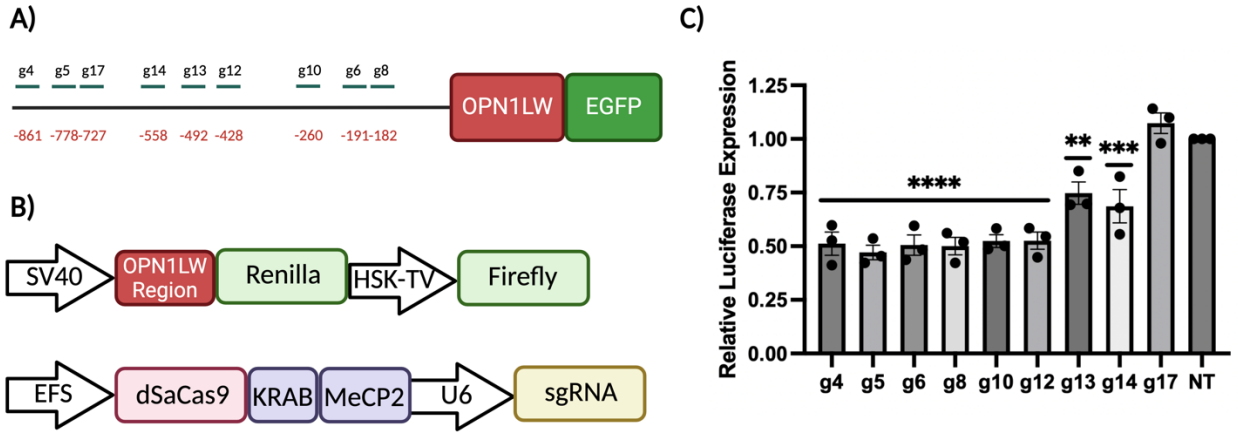


Figure 5.1 Details and results of sgRNA screening using dual luciferase assay

A) Schematic diagram showing the location of OPN1LW targeting sgRNA candidates relative to OPN1LW transcriptional start site and fusion with EGFP. **B)** Design of PsiCHECK2 vector (top) and repressor construct (bottom) for dual transfection in HEK293T cells. **C)** Relative luciferase expression of DLA for each sgRNA candidate. Each data point represents the average of a technical triplicate for each biological replicate, error bars as mean value +/- SEM. All values normalized to samples transfected with a nontargeting sgRNA. One-way ANOVA with Dunnett's multiple comparisons test identified 8 sgRNA candidates which significantly decreased relative luciferase expression, ****$p<0.0001$, ***$p=0.0009$, **$p=0.007$.

5.3.2 – Universal promoters drive expression of EGFP in CGFP fibroblast cell line

Following an initial sgRNA screen using the DLA, which identified 8 sgRNA candidates which caused significant repression of renilla, the next step was to test the sgRNAs within the genome of the CGFP mouse. Once again, the CGFP mouse is an elegant *in-vivo* model to test the use of CRISPR-based gene therapies. Within the OPSIN-LCR of the CGPF mouse, OPN1LW is fused to

EGFP. By targeting the OPN1LW region with sgRNA design, the EFS-dSaCas9.KRAB-MeCP2 repressor construct could cause a decrease in EGFP expression if successfully designed, delivered, and expressed.

Before proceeding with *in-vivo* CRISPRi studies, a fibroblast cell line derived from a skin punch of a CGFP mouse was used for further sgRNA screening. Dr. Maria Kaukonen, a post-doctoral member of the lab, established the CGFP fibroblast cell line that will be used for the remainder of this chapter.

As the CGFP fibroblast line had not been previously used, promotor activity was first tested. Three ubiquitous promoters, cytomegalovirus enhancer fused to the chicken beta-actin promoter (CAG), cytomegalovirus (CMV), and elongation factor 1-alpha short intron-less (EFS), were chosen to drive expression of EGFP. Fibroblasts were electroporated using the Invitrogen™ Neon™ Transfection System with either pCAG-EGFP, pCMV-EGFP, or pEFS-EGFP as detailed in section 2.2.5. Increasing plasmid DNA concentrations were also tested to assess for optimal plasmid DNA concentration for sgRNA screening experiments and to assess for evidence of cell toxicity. Fibroblasts were imaged between 48 hours to 1-week post-electroporation.

1-week post-electroporation pCMV-EGFP demonstrated the greatest number of fibroblasts expressing EGFP followed by pEFS-EGFP, and finally pCAG-EGFP (Figure 5.2). All plasmid DNA concentrations tested showed successful electroporation of fibroblasts and EGFP expression though 600ng provided the best balance between cell death and EGFP expression.

Following electroporation significant cell debris was observed in the samples (Figure 5.3, A). The protocol was modified to change cell media 3 days following electroporation to remove cell debris while allowing sufficient time for cell adhesion. Fibroblasts not exposed to electroporation did not show evidence of cell debris, suggesting the cell debris was due to damage caused by electroporation. Additionally, with the amount of cell debris initially noted, it was important to assess autofluorescence of the damaged cells to confirm EGFP was indeed expressed. Autofluorescence was assessed using the RFP channel of the EVOS imaging system and confirmed autofluorescence present only in cell debris, with no evidence of autofluorescence observed in EGFP positive fibroblasts (Figure 5.3, B).

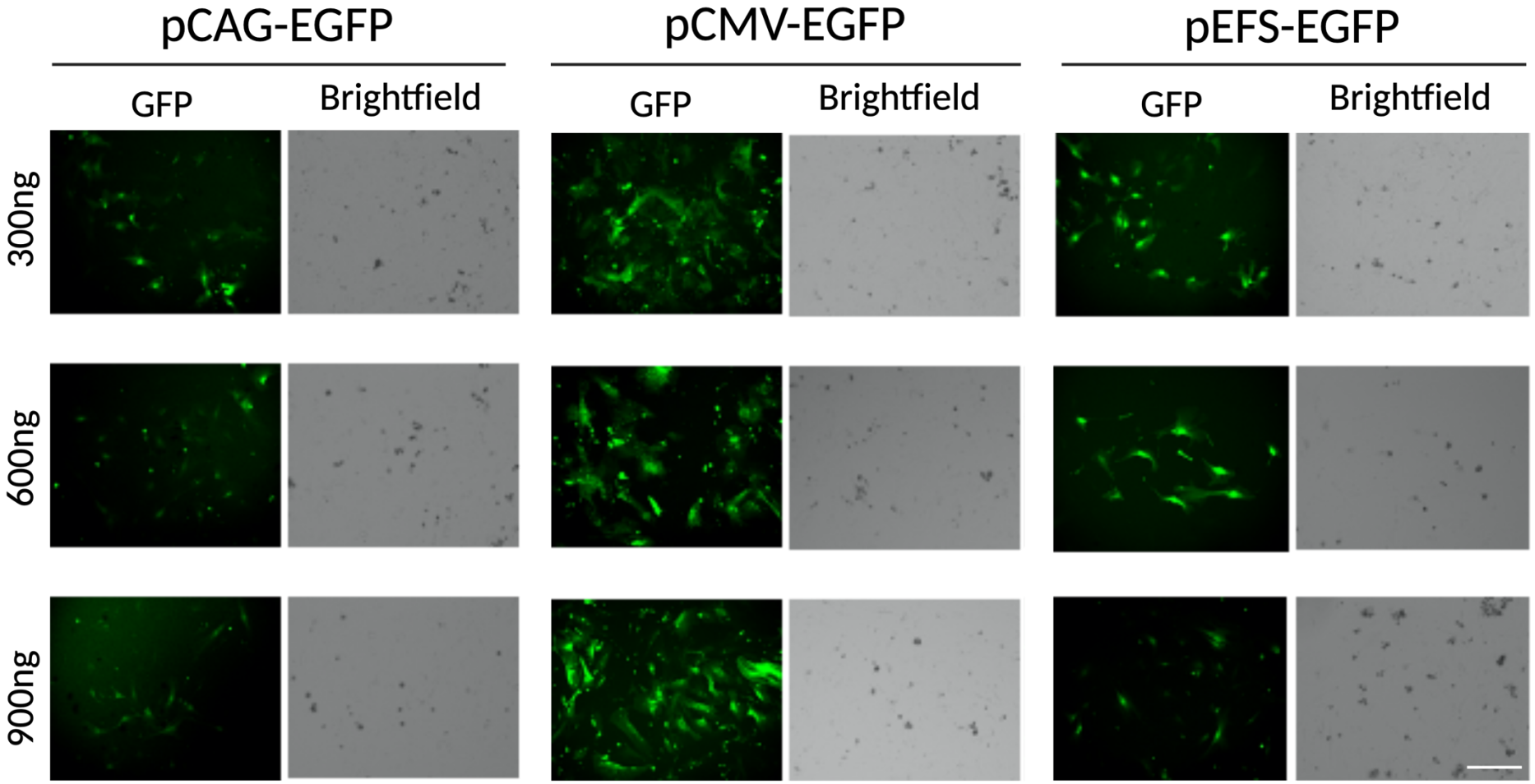


Figure 5.2 EGFP expression in CGFP fibroblasts 1-week post-electroporation

Representative BAF and brightfield images from CGFP fibroblasts 1-week post-electroporation with ubiquitous promoter plasmids (pCAG=EGFP, pCMV-EGFP, pEFS-EGFP) and increasing DNA concentrations (300ng, 600ng, 900ng). Scale bar =275uM.

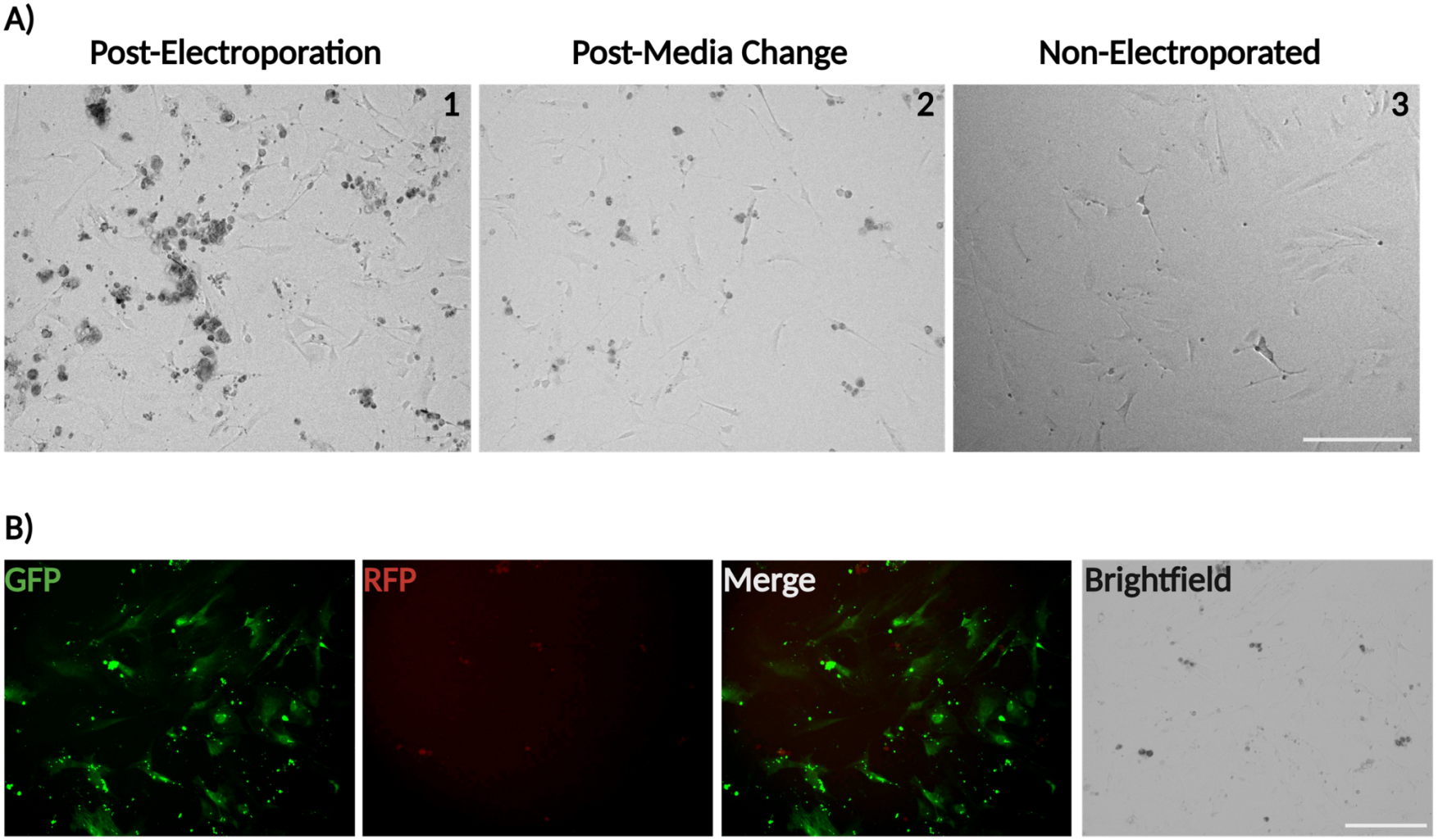


Figure 5.3 Optimization of electroporation of CGFP fibroblasts

A) Representative examples of brightfield images of CGFP fibroblasts showcasing varying cell debris: Left image with significant cell debris post-electroporation, center image with cell debris following media change 3-days post-electroporation, right image is a negative control not exposed to electroporation. B) Representative images using GFP channel, RFP channel, brightfield, along with merged RFP/GFP. Scale bar =275uM.

5.3.3 – Evaluating on-target sgRNA efficiency *in-vitro*

After demonstrating ubiquitous promoter activity in the CGFP fibroblast cell line, three of the top performing sgRNA candidates from the DLA were further screened using the CGFP fibroblast line. With confirmation of EFS activity, g5, g6, and g8 were individually cloned into pEFS-SaCas9. g17 was also cloned into pEFS-SaCas9 and was used as a negative control, as this sgRNA did not cause any gene silencing in the DLA. While an active SaCas9 system differs significantly in the gene silencing mechanism to a dSaCas9 system, this method of sgRNA screening was pursued to assess sgRNA binding specifically within the CGFP genome, as this was the intended *in-vivo* use of the vector. To elucidate this, CGFP fibroblasts were electroporated with 600ng of EFS-SaCas9-OPN1LW plasmid DNA. gDNA was extracted from the electroporated cells and the region of interest, including the predicted cut site, was PCR amplified before sanger sequencing. Resulting sequence traces were uploaded for TIDE analysis to predict editing efficiency of the active SaCas9 system with OPN1LW targeting sgRNAs. TIDE analysis did not reliably demonstrate the presence of indels across experimental replicates.

Due to the novelty of the CGFP fibroblast line and electroporation protocol, subcloning, an alternative method of measuring indels, was pursued for a subset of sgRNAs in an active SaCas9 system. In her thesis, Dr. Caroline Peddle found that for a given sgRNA, TIDE estimated the editing rate 37.4% lower than subcloning analysis[173]. A nontargeting sgRNA and one OPN1LW targeting sgRNA (g6) were chosen to assess the presence of indels via subcloning. For each sample, 24 clones were generated in triplicate for each condition. The resulting sequences were aligned to the unmodified CGFP sequence and assessed for the presence any insertions or deletions.

Subcloning analysis did not identify the presence of indels in the CGFP fibroblasts exposed to EFS-SaCas9 or EFS-SaCas9-g6.

F10, the EGFP targeting sgRNA was also probed via subcloning in to assess DNA editing in CGFP fibroblasts. EFS-SaCas9-F10 was electroporated and subcloning analysis did not identify the presence of indels. However, within the sequencing traces, two subclones of CGFP fibroblasts exposed to EFS-SaCas9-F10 showed increased baseline noise (red stars) within the expected editing window for F10, suggesting the possibility of DNA editing within the CGFP fibroblast cell line (Figure 5.4).

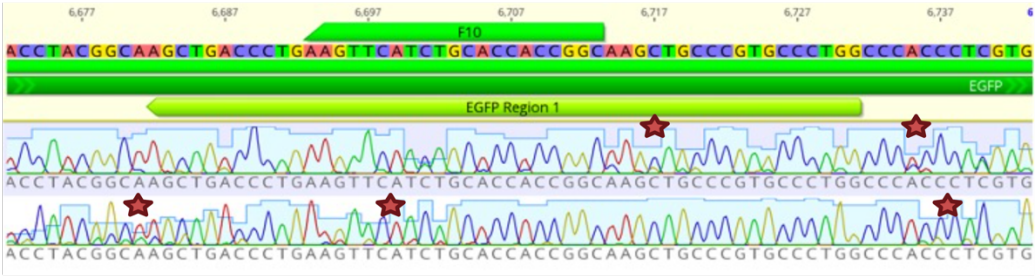


Figure 5.4 Results of subcloning analysis for sgRNA F10

Sequencing traces of two colonies from subcloning following transfection of CGFP fibroblasts with EFS-SaCas9-F10 showing increased baseline noise (red stars) within the predicted editing window of F10.

HEK293T cells were also used for OPN1LW sgRNA candidate screening following the DLA. First, the OPSIN-LCR region of the HEK293T cell line was sequenced. Unmodified HEK293T cells were pelleted and gDNA was extracted before PCR amplification and sequencing. The entire OPSIN-LCR was sequenced as discussed in section 4.3.1. Most importantly, the sequence of the OPSIN-

LCR was confirmed to be the identical between HEK293T cells and the CGFP mouse genome (Figure 5.5).



Figure 5.5 Sequencing the OPSIN-LCR in HEK293T cells

Sequencing traces of gDNA from HEK293T cells aligned to the OPSIN-LCR-EGFP fusion sequence of the CGFP mouse. **A)** Example showing region of the OPSIN-LCR in HEK293T cells with 8 sgRNA candidates aligned to CGFP mouse genome. **B)** Zoomed in sequencing traces of top image including sgRNA candidates g6, g8, g9, and g10 (red) with corresponding PAM sites (pink).

Following sequence verification of the OPSIN-LCR, HEK293T cells were transfected with EFS-SaCas9 with OPN1LW targeting sgRNAs. gDNA was extracted and the area of interest was PCR amplified before sanger sequencing. Sequencing chromatograms were uploaded to TIDE software proceeded by ICE software alongside the unedited sequence. Neither TIDE or ICE analysis demonstrated reliable evidence of DNA editing in the HEK293T cells exposed to EFS-SaCas9-OPN1LW.

5.4 Discussion

5.4.1 – Screening OPN1LW sgRNA candidates using the DLA

This chapter sought to screen several sgRNA candidates targeting the red-opsin gene (OPN1LW) for CRISPR interference (CRISPRi) applications. The sgRNA candidates were screened using a variety of *in-vitro* methods including a dual luciferase assay (DLA), transfections in HEK293T cells, and via electroporation in CGFP fibroblast cells.

The basic CRISPRi mechanism relies on the catalytically inactive "dead" SaCas9 protein (dSaCas9) to sterically block transcription factors from accessing the DNA. When the sgRNA is designed near the TSS, this prevents transcriptional initiation, while a sgRNA downstream of the TSS prevents transcriptional elongation[94,98]. The sgRNA candidates in this chapter were designed to block transcriptional initiation. When blocking initiation, the optimal sgRNA binding site is suggested between -50 to +250bp from the TSS[198,199]. However, a study targeting the green opsin (OPN1MW) with a CRISPR activation (CRISPRa) system, tested sgRNA candidates located -60 to -260bp from the TSS and showed increased gene expression both *in-vitro* and *in-vivo*[104]. Based on the similarity in gene target, the sgRNA candidates targeting the red opsin gene in this chapter were all designed upstream to the TSS.

Fourteen sgRNA candidates were initially designed in Geneious Prime software for use within a dSaCas9 system using the PAM sites NNGRRT and NNGRR(N). The NNGRRT PAM site is associated with higher levels of editing than the more promiscuous NNGRR(N) PAM site[200]. The 1kb region upstream of the OPN1LW TSS was probed for SaCas9 associated PAM sites. Once identified, 20bp

sgRNAs were designed immediately upstream to the PAM sites. Of the sgRNA candidates, four were associated with the more efficient NNGRRT PAM site (g3, g4, g5, g6). Indeed, the DLA identified significant gene repression using three of the sgRNA candidates, g4, g5, and g6. g3 did not show consistent gene repression across experimental replicates. Four additional sgRNA candidates using the NNGRR(N) PAM site also caused significant gene disruption in the DLA.

Of the three sgRNA candidates which use the NNGRRT PAM site, g6 and g8 are additionally the candidates located nearest to the TSS at -191bp and -182bp, respectively. The location of g6 and g8 are similar to sgRNA locations used for OPN1MW activation in the Bohm. et. al. study, further supporting the importance of the location of sgRNA around -200bp from the TSS[104]. This is also somewhat in alignment with other sgRNA screening studies which identified -50 to +250bp from the TSS as the optimal sgRNA position[198,199]. Interestingly, g4 and g5, located -861bp and -778bp from the TSS, also caused similar levels of repression in the DLA to g6 and g8. While the location to the TSS is further, it is possible chromatin accessibility in that region of the OPSIN-LCR is more open than in intermediate sgRNA positions tested.

Following screening, six additional NNGRRT PAM sites have been identified between -190 to +14bp of the TSS. Further sgRNA screening using a combination of the NNGRRT PAM site and sgRNA location closer to the TSS, could potentially produce more efficient gene repression using the EFS-dSaCas9.KRAB-MeCP2 repressor system. Additional considerations to optimize gene repression include the use of multiple sgRNAs targeting the same gene within a CRISPRi system,

which might increase efficiency of repression. One study by Chavez et al. reported the use of multiple sgRNAs led to increased gene activation in a CRISPRa system[201].

Overall, initial sgRNA screening with the DLA identified several OPN1LW targeting sgRNA candidates which caused robust gene repression. The results of this chapter support sgRNA design using the NNGRRT PAM site for use with dSaCas9, as well as sgRNA location -200bp from the TSS as the optimal distance for sgRNA design. The influence of chromatin structure at sgRNA binding sites may additionally play a role in repression efficiencies. Additional testing using multiple sgRNA candidates in combination would be worthwhile to potentially improve the degree of transcriptional repression achieved.

5.4.2 – Use of the CGFP fibroblast cell line

The pilot study using the CGFP fibroblast cell line evaluated ubiquitous promoter activity before proceeding with CRISPR-based *in-vitro* work. Three universal promoters, EFS, CAG, and CMV demonstrated the ability to drive expression of EGFP in the CGFP fibroblast line following electroporation. Plasmid DNA concentrations ranged from 300ng-900ng and all produced robust EGFP expression on live cell imaging. This initial study provides the basis for future use of EFS, CAG, or CMV to drive plasmid DNA expression in CGFP fibroblast cells via electroporation.

While EGFP expression was relatively easy to assess with cell imaging, the effect of DNA editing with an active SaCas9 system in the CGFP fibroblast cells was not as clear. Within the CGFP fibroblast cell line, OPN1LW is not transcribed. Therefore, use of the EFS-dSaCas9.KRAB-MeCP2

repressor system with OPN1LW targeting sgRNAs was not possible. As an alternative, the OPN1LW sgRNA candidates were cloned into the EFS-SaCas9 plasmid. These active SaCas9 plasmids were electroporated into CGFP fibroblasts using settings established in the pilot study to further elucidate sgRNA binding within the CGFP genome.

Despite identification of multiple sgRNA candidates capable of gene repression in the DLA, TIDE analysis of CGFP fibroblasts following exposure to the active SaCas9 system did not show expected editing efficiencies. The low editing efficiencies seen with TIDE could be due to a myriad of reasons, some of which will be discussed below.

TIDE software was developed as a method to predict the presence of insertions or deletions within a DNA sequencing trace after exposure to a gene editing system compared to an unedited sequencing trace of the same DNA region. To predict editing efficiencies, the software relies on the quality of both the PCR product containing the predicted cut site and the sequencing results[140]. A simple method to assess the quality of DNA following PCR amplification is to run the products using gel electrophoresis. Prior to all sequencing done throughout this thesis, PCR products were exposed to gel electrophoresis to crudely assess DNA quality. Images of the samples used for TIDE analysis for this chapter demonstrate clean bands, supporting a pure PCR product (Appendix, 8.3). Additionally, the DNA concentration of all samples intended to be PCR amplified were quantified immediately following gDNA isolation, and presence of contaminants was assessed using NanoDrop spectrophotometry. Following PCR amplification, samples were again assessed via NanoDrop. Based on imaging and absorption data of the isolated gDNA and

PCR products, it is unlikely that the quality of DNA following PCR amplification meaningfully contributed to the low editing efficiencies seen with TIDE analysis.

The methodology and practice of sequencing is beyond the scope of this thesis, however, some difficulties with sequencing are commonly encountered in CRISPR-based labs. Several of the samples sent for TIDE in this chapter were discussed with GENEWIZ and repeated. Ideally, all sequencing would have been repeated, however, due to time limitations of the MSc and the novelty of the CGFP fibroblast line, this was not feasible. Additional optimization of transfection via electroporation within the CGFP cell line followed by replication of experimental conditions would provide clarification regarding OPN1LW sgRNA binding and activity of the tested SaCas9 system.

Beyond the limitations of TIDE, in transient transfection experiments, expression of plasmid DNA is dependent on the length of time the cells are left and the rate of cell division. It is therefore possible for the plasmid of interest to be diluted out, as it is only present in the initial cells that were transfected and subsequently able to express the desired proteins. Electroporation is a method of transient transfection; therefore, plasmid DNA does not integrate into the host genome and as such is limited by time and the rate of cell division. In the preliminary experiments comparing promoter activity within CGFP fibroblasts, results indicated maintained transgene expression at 1-week but were not tested up to 2-weeks as was done in the SaCas9 branch. After electroporation with the EFS-SaCas9 constructs, the fibroblast cells were allowed to grow for

varying amounts of time up to 14 days to attempt to maximize yield. To minimize sample variation, all samples assessed for DNA editing were left for 14 days following electroporation.

While DNA editing can generally be expected to begin between 48-72 hours after transfection, the exact time to isolate gDNA following electroporation to assess DNA editing in fibroblasts is not well defined. In a study by Bajwa et al., buffalo fibroblasts were electroporated with an active SpCas9 system and left for 8-10 days following puromycin selection and allowed to reach 70-80% confluency before gDNA isolation to assess for genome editing. In this manner the authors showed editing efficiencies up to 26.7% via TIDE, 24% via ICE, and evidence of indels via subcloning[202]. It is possible the EFS-SaCas9 constructs were successfully electroporated into CGFP fibroblasts and those cells expressed the necessary CRISPR-associated proteins to generate DSBs. However, if the population of cells in which this occurred was quite small, in part due to the long time-period following electroporation, the effect of DNA editing, as predicted in TIDE analysis, may be underestimated. The addition of puromycin selection along with use of a fluorescent reporter gene within the EFS-SaCas9 plasmid would improve identification of cells successfully electroporated and expressing the plasmid DNA. Within this cell pool, a more accurate measurement of DNA editing would be possible, and the dilatory effects of non-transfected cells would be minimized.

To attempt to elucidate the potential dilatory effect within the fibroblast cell pool, subcloning was performed on a subset of CGFP fibroblasts exposed to SaCas9 constructs. Subcloning analysis did not reveal the presence of insertions or deletions in fibroblasts transfected with EFS-SaCas9-

F10, EFS-SaCas9-g6, or nontargeting EFS-SaCas9. While subcloning did not demonstrate the presence of indels, 2 sequencing traces of cells exposed to EFS-SaCas9-F10 did show increased baseline noise compared to unedited DNA within the expected editing window. In subcloning analysis, individual sequence traces are manually compared to unedited DNA. The increased baseline noise noted during the analysis may represent DNA editing and further supports the use of F10 for gene knockout in the CGFP mouse, as was discussed in Chapter 4.

It is also possible that the EGFP gene which was targeted for is not accessible in the CGFP fibroblast line, leading to low detected editing rates. While the DNA of the CGFP fibroblasts carry the genetic sequence for EGFP, different cell types possess different epigenetic modifications and the EGFP genomic region may be inaccessible in fibroblasts vs. photoreceptor cells as was investigated in Chapter 4.

As discussed in detail in Chapter 1, the mechanism of gene disruption between an active Cas9 system and a catalytically inactive dCas9 system acts at different points of protein expression. A more accurate way to investigate the use of the dSaCas9 repressor system after sgRNA screening but prior to *in-vivo* studies would be within retinal organoids or human retinal explants. In his thesis, Dr. Ariel Kantor, who designed the EFS-dSaCas9.KRAB-MeCP2 plasmid used throughout this chapter, demonstrated high levels of gene repression in iPSc derived retinal organoids after exposure to the same dSaCas9 system[203]. Other groups have similarly utilized retinal organoids to investigate epigenetic modifications and shown successful gene repression[204]. Within ophthalmology, a recent study by Burnight et al., demonstrated the use of CRISPRi to repress the

production of the rhodopsin protein in human retinal explants and *in-vivo*[100]. Since this thesis has focused specifically on cone photoreceptor targeting, the use of cone-enriched retinal organoids could additionally be of interest. Cone-enriched retinal organoids have been developed and shown to possess light responses similar to the fovea of primates[205–208].

5.4.3 – Optimizing electroporation of CGFP fibroblasts

Within the electroporation system there are multiple parameters that could influence the transfection efficiency of cells. These include voltage, the number of pulses, pulse duration, cell confluency, cell passage number, cell type, plasmid DNA concentration, and time left following electroporation. For all experiments discussed in this chapter, the following parameters were kept constant: voltage of 1650V, pulse number of 3, pulse duration of 10ms, cell density of $1x10^5$ cells/10uL, and cell type. Cell passage number, plasmid DNA concentration, and time left following electroporation varied by experimental condition. The initial electroporation settings used in this chapter were chosen based on the work of Dr. Maria Kaukonen, a previous member of the MacLaren lab.

A study by Hyder et al. sought to optimize electroporation settings using a fluorescent reporter plasmid. To do this, multiple parameters were tested for use in bovine fibroblasts and demonstrated the highest transfection efficiencies at 400V using 10ug of supercoiled plasmid DNA in $3x10^5$ cells/100uL[209]. While this study uses fetal bovine fibroblasts, which differ from dermally derived mouse fibroblasts, and does not attempt to deliver gene editing systems, it provides a nice framework for systemically testing different electroporation settings which could

be applied for CGFP fibroblasts. Perhaps more relevant to the desired delivery of CRISPR-based systems, the study by Bajwa et al. demonstrated electroporation of adult buffalo fibroblasts with an active CRISPR-Cas9 system following electroporation optimization. In their study they found optimal settings to be 300V with one 20ms pulse using 10ug of plasmid DNA in $1x10^6$ cells/100uL[202].

In both of the above studies, the voltage used for electroporation is significantly lower than the 1650V used in this chapter. It is possible that lowering the voltage could cause less cell death, however, it is also possible the high voltage is needed to transfect the dermal fibroblasts. While some cell death is expected due to the traumatic and physical nature of electroporation, it is possible the amount of cell debris seen in this chapter was high and caused apoptotic cascades in healthy CGFP fibroblasts. Additionally, both studies used a higher plasmid DNA concentration and cell density. The initial electroporation kit tested with the CGFP fibroblasts was limited to a maximum cell density of $1x10^5$. This in turn limited the plasmid DNA concentration, as some evidence of cell toxicity was seen with concentrations of 900ng. After multiple tests with the initial electroporation kit, a kit allowing cell densities up to $1x10^6$ along with higher plasmid DNA concentrations was tested. Unfortunately, the new kit was only able to be used once prior to termination of the experimental timeframe of the MSc. It is possible that investigation of electroporation parameters including voltage, pulse number, pulse duration, cell density, cell passage number, and plasmid DNA concentration specific to the dermally derived mouse fibroblasts could yield higher transfection efficiencies.

5.5 Conclusions

This chapter represents the *in-vitro* branch of a CRISPRi focused experiment. sgRNAs were designed, cloned, and screened to identify top candidates targeting the red-opsin gene (OPN1LW). Several sgRNA candidates demonstrated gene repression in a dual luciferase assay supporting the use of the NNGGRT PAM site and sgRNA location -200bp from the TSS. A pilot study using the CGFP fibroblast line demonstrated promoter activity of EFS, CAG, and CMV within the cell line following electroporation. An active SaCas9 system was tested in the CGFP fibroblast cell line highlighting the need for further optimization of the electroporation protocol to assess the effect of gene editing mechanisms.

Chapter 6: General Discussion

6.1 Summary of Thesis Aims and Outcomes

This thesis broadly focuses on targeting murine cone photoreceptors to investigate CRIPSR-based gene editing applications. Here, I will summarize the work completed on each of the aims of this thesis.

1.) Assessment of vector and delivery optimization of AAV5 in combination with a ubiquitous vs. photoreceptor-specific promoter in a mouse model which expresses EGFP under a cone-specific promoter (CGFP model).

Transduction of photoreceptors (rods and cones) via AAV5 packaged delivery of a fluorescent protein, DsRed, was assessed to elucidate vector limitations and broad transduction patterns of a photoreceptor specific (hGRK1) and ubiquitous (CAG) promoter. Following successful plasmid cloning and AAV5 production, subretinal injections of AAV5-hGRK1-DsRed or AAV5-CAG-DsRed were performed on the CGFP mouse model. Both vectors produced robust DsRed expression within photoreceptors. The CAG vector demonstrated retinal toxicity and significant photoreceptor layer (PRL) thinning while the hGRK1 vector transduced photoreceptors with no significant toxicity with PRL thinning observed only in the superior retina. With evidence of broad photoreceptor transduction, the combination of hGRK1 and AAV5 was validated as a logical choice for the next thesis aim. In addition, this aim of the thesis was critical to master *in-vivo* and *in-vitro* techniques that would be used throughout the remainder of the thesis.

2.) Investigating *in-vivo* knockdown of EGFP in EGFP-expressing photoreceptors using an active Cas9 system.

Following photoreceptor transduction driven by the hGRK1 promoter in the CGFP mouse model, I next sought to disrupt a cone specific reporter gene (EGFP) using an active CRISPR-SaCas9 system. Within the CGFP mouse, EGFP is expressed in a subset of cone cells under the control of the cone-specific OPSIN-LCR promoter. Disruption of EGFP at the DNA level was attempted using AAV5-hGRK1-SaCas9 with an EGFP targeting sgRNA, F10. Three escalating doses were subretinally injected into the eyes of CGFP mice to elucidate a complete dosing study of AAV5 within the mouse retina. EGFP disruption was evident with both mid and high dose, suggesting successful knockdown of the cone specific EGFP gene. Dose analyses demonstrated an acceptable safety profile of AAV5 when injected at or below $5x10^{12}$ gc/mL.

3.) *In-Vitro* screening of sgRNA candidates which target the red-opsin gene (OPN1LW) for epigenetic repression applications.

Finally, I undertook the main *in-vitro* branch of a CRISPRi focused project. For this branch of the thesis, the OPSIN-LCR region of the CGFP mouse was targeted for epigenetic repression using an inactive Cas9 gene editing approach. Various sgRNA candidates targeting the OPSIN-LCR were designed prior to screening using a dual-luciferase assay, transfections in HEK293T cells, and electroporation with CGFP derived fibroblasts. The dual luciferase assay demonstrated several

sgRNA candidates with significant levels of gene repression. Those sgRNA candidates were then screened in HEK293T cells and CGFP fibroblasts. Prior to screening, I validated the use of multiple ubiquitous promoters in the CGFP fibroblast line and optimized electroporation parameters. TIDE analysis for both HEK293T cells and CGFP fibroblast cells did not yield DNA editing in an active SaCas9 counterpart. Despite this, the sgRNA candidates which caused reliable gene repression based on the dual-luciferase assay represent possible candidates for future *in-vivo* epigenetic experiments in the CGFP mouse line.

6.2 Improving Cone Photoreceptor Targeting

One of the main goals of this thesis was to assess a combination of AAV5 and the hGRK1 promoter to target cone photoreceptor cells of mice for gene editing applications. With this combination, successful transduction of cone and rod photoreceptors caused expression of a fluorescent protein (DsRed) within these cells. More excitingly, an active SaCas9 system caused disruption of a cone specific reporter gene (EGFP). These results validate the established use of hGRK1 and AAV5 within the field of ophthalmologic gene therapy. Importantly, this thesis validates their use in a murine model, the CGFP mouse, as a preclinical model poised to test different gene editing methodologies in cone photoreceptors. While cone transduction did occur, the level was much lower than rods, suggesting cone transduction is not as robust as that of rods. There are several potential mechanisms to explain this, some of which will be discussed below.

6.2.1 – Promoter and Delivery

Within any gene editing experiment, choice of promoter and delivery method are critical to limit transgene expression to the cell population of interest. Prior literature review helped inform promoter and AAV serotype choice for this thesis, with both hGRK1 and AAV5 demonstrating photoreceptor specificity across species, including non-human primates and humans[152,210]. Mice have very few cone photoreceptor cells relative to rods and subretinal AAV delivery preferentially transduces rods and RPE cells. Consequently, low cone transduction was seen in the CGFP mouse following subretinal administration of vectors of interest.

One of the simplest ways to attempt to improve the efficiency of cone targeting is to switch the promoter driving expression of the transgene or Cas9 system. As discussed in Chapter 4, cone specific promoters exist which could drive expression more efficiently and solely to cone cells. Studies focused on achromatopsia have identified the L-opsin promoter (PR2.1), a shortened PR2.1 promoter, and the S-opsin promoter as options for cone specific targeting[169,190–192]. A subsequent study compared various cone targeting promoters and found almost exclusive targeting of cone cells using an engineered chimeric IRBPe/GNAT2 promoter in mice[211]. While it is certainly worthwhile to find the most efficient manner to target cone cells for gene editing applications, the hGRK1 promoter remains a strong candidate for cone targeting. hGRK1 is widely used in ophthalmology to target both populations of photoreceptors including its use in various clinical trials such as EDIT-101[120,212]. Like changing the promoter in a gene editing system, the serotype of AAV used to deliver the system can be modified. Multiple serotypes have been shown to transduce photoreceptors, including AAV2, AAV5, and AAV8[213]. I began packaging the plasmids used throughout this thesis in AAV8 to explore delivery via an alternative AAV serotype, however, time limitations did not allow *in-vivo* administration to assess for differences in transduction patterns. Once again, keeping clinical applications in mind for vector design and testing, AAV5 is commonly used in clinical trials and demonstrates a favorable photoreceptor expression pattern. Nevertheless, changing the serotype could lead to better photoreceptor transduction in the CGFP mouse.

Alternative delivery methods to transduce photoreceptors exist, including non-viral delivery vehicles such as nanoparticles. Nanoparticles are attractive candidates for gene therapy delivery

with a well-known safety profile, increased cargo capacity compared to AAV, small size, and the ability to cross cell barriers[214]. Various *in-vitro* studies have demonstrated the feasibility of delivering the CRISPR-Cas9 system, highlighting the potential of nanoparticles[214,215]. Most recently, the Liu and Palczewski labs engineered virus like particles (eVLPs) to efficiently deliver Cas9, base, or prime editing systems *in-vivo* to photoreceptors[93,216]. Further *in-vivo* studies using nanoparticles will highlight the current limitations of the technology and potential use for gene editing delivery.

6.2.2 – Dose and Toxicity

In the first two aims of my thesis, I elucidated the transduction pattern of retinal cells based on the combination of the hGRK1 promoter and AAV5-based delivery. Subretinal injection of AAV5-hGRK1-DsRed caused robust DsRed expression within the mouse retina. The specific cell types transduced with the vector were determined using IHC, with rod photoreceptors robustly expressing DsRed and some evidence of cone transduction. The results for the AAV5-hGRK1-SaCas9 branches were largely similar, with robust rod transduction and limited cone cell transduction. Results of the dose escalation done in Chapter 4 suggest a viral dose of $5x10^{12}$ gc/mL is nontoxic to the mouse retina while achieving photoreceptor transduction.

The primary viral dose used for the DsRed portion of the thesis, $5x10^{11}$ gc/mL, was equivalent to the low dose cohort of the active SaCas9 branch. At $5x10^{11}$ gc/mL, robust rod transduction was observed when injected with AAV5-hGRK1-DsRed. However, when AAV5-hGRK1-SaCas9-F10 was injected at the same dose, no EGFP disruption within cone cells was observed. At higher doses,

EGFP expression within cone cells was decreased, suggesting the Cas9 machinery was successfully delivered and expressed within cone cells. It is possible that in the initial DsRed experiment and low-dose SaCas9 branch $5x10^{11}$ gc/mL was simply too low to cause efficient transgene expression within cone cells.

Additionally, cone cells have a high rate of metabolism, putting them at increased sensitivity to states of oxidative stress[217]. Introduction of AAV is known to be immunogenic, leading to inflammatory states and increased cellular stress[218]. Since cone cells are more influenced by these states, it is possible cellular machinery to produce a functional protein is impacted via introduction of AAV and the transgene, leading to decreased expression in cone cells vs. rods.

While robust transduction was observed, significant retinal toxicity was seen when AAV was injected at high dose and when transgene expression was driven by a ubiquitous promoter. These findings suggest that in addition to a high viral dose of AAV, high transgene expression may also be toxic to the retina. Within the CGFP mouse line, expression of EGFP alone was not found to cause the dominant cone degeneration[144]. However, expression of two fluorescent proteins within cone cells may be toxic to the retina. A recent study examined the effect of TdTomato, a fluorescent protein derived from DsRed, on the retina in a transgenic mouse line[219]. The authors showed expression of TdTomato caused retinal dysfunction with associated molecular, ultrastructural, and functional changes. There was significant downregulation of mitochondrial and retinal genes in retinae of TdTomato expressing mice[219]. Based on their similar origin, the retinal toxicity observed from DsRed expression in this thesis could be similar to TdTomato

associated toxicity. This is especially true when one considers the high metabolic state of cones and sensitivity to oxidative stress with the mitochondrial dysfunction observed with TdTomato.

6.2.3 – Measuring Editing Rates

Within CRISPR-based studies, measurement of editing efficiencies are assessed via a wide array of computational and molecular tools. In this thesis, formation of indels following exposure to active SaCas9 systems were assessed using TIDE analysis, which is used to determine the spectrum and frequency of mutation across the genome of PCR amplified fragments. Analyses of genomic DNA from exposed cell populations produced variable editing efficiencies across biologic and technical replicates. Some of the constraints of this method are discussed in Chapters 4 and 5, however, analyses of editing remain necessary for any tested gene editing system.

In Chapter 4, an active SaCas9 system was assessed to disrupt EGFP expression in cone photoreceptors. TIDE analysis did not show reliable editing efficiencies when analyzing genomic DNA from the entire neural retina, potentially due to the dilatory effect of untargeted cells. However, methods investigating EGFP expression at the protein level suggest successful DNA disruption was achieved. The disparity in observed EGFP disruption at the protein vs. DNA level highlights the need for streamlined methods of assessing DNA editing *in-vitro* and *in-vivo*. The addition of analysis at the mRNA level via RT-qPCR or western blot could additionally be used to probe the extent of EGFP disruption. Alternatively, isolation of the cone photoreceptor population via FACS may lead to better sensitivity in detecting editing rates as only the specific cell population of interest, which was targeted, is analyzed, minimizing the dilatory effect.

In Chapter 5, several sgRNAs were screened *in-vitro* for epigenetic repression applications. Initial screening with an established dual-luciferase assay (DLA) identified several sgRNA candidates which produced consistent and high levels of gene repression. However, when tested in a counterpart active SaCas9 system, the same sgRNA candidates did not demonstrate indel formation via TIDE analysis. Aside from differences between a dSaCas9 system and SaCas9 system, DNA disruption was expected following the identification of candidates via the DLA. When testing these sgRNA candidates with an active SaCas9 system, a CGFP fibroblast line isolated from CGFP mice was used in addition to HEK293T cells. The CGFP fibroblast line was novel to the lab and methods to optimize electroporation efficiencies were made prior to use with SaCas9. Despite this, high levels of cell death occurred following electroporation, significantly limiting the interpretation of the effect of SaCas9. While screening the sgRNA candidates in an active SaCas9 system did not show efficient editing, it is possible that the sgRNA candidates identified by the well-established DLA could be used for *in-vivo* applications within the MacLaren lab.

6.3 Clinical Applications and Considerations

Significant progress has been made in gene supplementation strategies for IRDs including autosomal recessive and X-linked disorders. Gene supplementation works nicely for monogenic diseases inherited in this manner, as delivering a functional gene copy can often lead to restored protein levels necessary for function. The approval of Luxturna for biallelic RPE65 associated IRDs represents a huge step for gene augmentation strategies. With a variety of gene replacement strategies in clinical trial for IRDs, the approval of additional gene therapeutics is fast approaching.

On the other hand, for IRDs which cause a gain of function or dominant negative effect, gene supplementation may not be enough. To circumvent this, silencing of the mutated gene may be explored. One method of gene silencing is use of the CRISPR-Cas9 system, which acts at the DNA level to cause double-stranded breaks, leading to indel formation with effective gene silencing. Gene knockout using CRISPR-Cas9 has been achieved *in-vivo* for a wide range of genes associated with IRDs[220]. The clinical trial by Editas Medicine which uses an active CRISPR-SaCas9 system to disrupt a point mutation in *CEP290* is one of the first clinical trials to use CRISPR in humans[210]. Demonstrating a favorable safety profile and improvement in photoreceptor function, EDIT-101 will no doubt pave the way for future CRISPR-based therapies, not limited to the eye.

With the ongoing expansion of the CRISPR toolbox with base and prime editing, the number of disease-causing mutations amenable to gene editing has dramatically increased. In theory, up to 89% of disease-causing mutations identified within the human genome could be corrected with

prime editing. As the scope of gene therapy and gene editing broadens, it remains critical to monitor the response to treatment and continue to optimize targeted treatments for patient safety and benefit.

6.3.1 – Off Target Effects

Within a CRISPR-Cas9 or CRISPRi system, if the sgRNA binds at a partially homogenous sequence to the target region, off target effects can occur[221]. Downstream consequences of off target effects are not yet fully understood, however, changes to DNA outside of the target region raise concern for cell dysfunction/apoptotic mechanisms or the accumulation of mutations leading to malignancy. Despite an incomplete understanding of off-target effects for each gene editing application, several tools have been developed and implemented to minimize the potential of undesired editing within the genome[222,223].

In-silico methods provide an initial prediction of off-targets based on alignment with the intended subject genome or by scoring and ranking sgRNA candidates based on alignment data[224]. The goal of *in-silico* methods is to help identify sgRNA and PAM options which lead to the highest specificity of binding to the target DNA region. Because these methods do not rely on the complex cellular mechanisms and machinery needed to mediate gene editing, they do not provide a full picture of potential off-target effects. *In-vitro* assays including CIRCLE-seq or SITE-seq (among many others) are classified as "cell-free" and aim to identify off-targets by identifying break sites based on aspects of the Cas9 system and provide a more unbiased measure of off-target effects. Other cell-culture based *in-vitro* assays such as GUIDE-seq and whole genome

sequencing (WGS) provide analysis of potential off-target effects closest to an *in-vivo* study, as these methods analyze DNA on cells exposed to the gene editing system and thus rely on cellular machinery to elucidate gene-editing. *In-vivo* analyses of off-target effects now also exist, providing the most robust assessment of off-target effects as this is the best representation of gene editing for human applications. Finally, alongside the rapid advancement of artificial intelligence and computational power, machine learning and deep learning programs are being developed to inform on and off-target effects of gene editing systems[225].

Compared to the classic CRISPR-Cas9 system, other gene editing systems may pose a lower risk of off-target effects. While DNA editing causes permanent changes to the genome, systems like CRISPRi/CRISPRa which interact with the genome lead to transient changes. Modifications to gene editing systems may allow transient expression via small-molecule interactions, drug-inducible promoters, or systems which self-target[226–228]. Additionally, early studies using base and prime editing show lower off-target effects compared to CRISPR-Cas9, with prime editing exhibiting the lowest levels of off-targets[92,229].

As scientific knowledge expands, designing gene editing systems with high on-target efficiency and low off-targets becomes more attainable. Screening various combinations of components of a gene editing system may be greatly aided by computational tools. While *in-vitro* and *in-vivo* testing with subsequent off-target analyses will continue to be of great importance in preclinical design to minimize unnecessary alterations to the genome.

6.3.2 – Immune Response

It is well known that administration of AAV leads to an immune response, involving both the innate and adaptive branches of the immune system [218,230,231]. Within the eye, immune response to subretinal administration of AAV was shown to be primarily mediated via a Type 1 immunity, which aims to protect the host against intracellular microbes[175]. This finding is not surprising, since AAV particles must enter the cell to deliver the packaged transgene or CRISPR-based system[232].

In addition to the immune response to AAV itself, due to the bacterial origin on the CRISPR-Cas system, individuals naturally possess neutralizing anti-Cas9 antibodies prior to receiving gene therapy. Prevalence estimates of antibodies against SaCas9 and SpCas9, two of the most widely used Cas9 endonucleases, is not well defined but thought to be present in the majority of the population[233,234]. Preexisting immunity to Cas9 variants may cause immune mediated destruction of cells targeted for gene editing. This is a significant hurdle to overcome, as killing the edited cells is counterproductive to the goals of gene editing.

Important to applications of gene editing for IRDs, a study looking into the ocular immune response suggests that preexisting antibodies may present a lower risk within the eye following exposure to Cas9[235]. The eye is considered immune privileged, poised to reduce inflammation and protect the vital sense of vision[236]. Despite this immune privilege, intraocular inflammation occurs and can be vision threatening. Indeed, following gene therapy administration, intraocular inflammation has been observed and in the worst cases, has led to permanent vision loss[237,238].

Within clinical trial data, intravitreal delivery as opposed to subretinal injection, has been associated with increased rates of inflammation following gene therapy[239].

Experimental design of gene therapy studies, including clinical trials for IRDs, attempt to mitigate the immune response with immunosuppression, typically achieved by administration of corticosteroids[240]. Corticosteroids are a well-studied and cost-effective method to achieve immunosuppression, however, other immunosuppressants remain to be fully studied for concurrent use with gene therapy. It is possible these other agents may hold a more favorable immunosuppression profile, however, the side effects of some of the more powerful immunosuppressants will need to be considered.

Insufficient immunosuppression may contribute to intraocular inflammation following gene therapy administration. With multiple years since approval of Luxturna, long-term follow up in treated patients will inform possible long-term effects of AAV-delivered gene therapy. Recently, chorioretinal atrophy has been associated with treatment with Luxturna[241]. While the full mechanism of CRA remains to be elucidated, the contribution of the immune response to sustained gene therapy cannot be ignored.

Alternative gene therapy delivery methods exist such as lentivirus, lipid nanoparticles, gold nanoparticles, or more recently, engineered-virus-like particles. Further studies are necessary to elucidate the immune response to these methods. However, it is possible that these delivery methods may pose a decreased risk of an immune response due to their nonviral nature

(excluding lentivirus). For some tissues and gene editing tools, these delivery mechanisms may lead to equivalent or improved transduction compared to AAV. It is no question the expanding repertoire of delivery methods will be of great importance as gene editing tools continue to develop.

Once again, strategies to minimize the spatial and temporal expression of gene editing systems will be critical to minimize undesired editing and immune responses. Despite these aspects of gene editing, the rapidity of scientific discovery will no doubt lead to increased understanding and new methods of regulating gene editing systems.

6.3.3 – Future Directions

In-vivo testing of gene editing systems is a necessary step in the development of novel therapeutics. Non-human primates (NHPs) are the only animal model which possess the cone-rich macula and large cortical visual processing area similar to humans[242]. For this reason, NHPs remain widely used for final studies of gene editing treatments prior to clinical trial. While the retinae of NHP are closely related to humans, care, maintenance, and testing of NHP subjects comes at a significant cost[243]. Additionally, ethical considerations prohibit use of transgenic NHP models, limiting pre-clinical disease models.

The most used laboratory animals, mice and rats, both lack a macula. This is particularly relevant to this thesis, as cone photoreceptors were the target cell population of interest and only represent ~2.8% of the mouse retina[142]. Other large animals such as dogs, pigs, sheep, and cats

contain a central area of the retina with high photoreceptor density, including cones, but this area is not equivalent to the macula and fovea found in humans and NHP[244]. Due to the relative ease of conducting research with rodents, including the ability to alter the genome, it is inevitable that they will continue to be valuable *in-vivo* models in gene editing development pipelines. However, it is important to remember differences in retinal organization greatly limit their translational use.

The lack of suitable animal models presents a challenge in the development of gene therapies for IRDs. However, the development of 3D retinal organoids (ROs) derived from human induced pluripotent stem cells (iPSCs) shows great promise as an adjuvant or alternative to animal models. Differentiation of ROs has demonstrated the presence of mature photoreceptors suitable to study potential therapies for IRDs[245]. A cone-rich retinal organoid was also induced, providing a novel method to test therapies targeted at cone cells[205]. Importantly, tropism to AAV, the most used gene therapy delivery method, has been established, furthering support of ROs to study gene therapies[246]. In this manner, ROs represent a physiologic *in-vitro* alternative to animal models. Additionally, the ability to isolate these cells and create organoids from patient samples greatly expands the modelling of IRDs and ability to test gene editing treatments.

6.3.4 – Final Considerations

The current era of gene editing is quite exciting. Preclinical studies have demonstrated the ability to the use various systems like CRISPR-Cas9, base-editing, prime-editing, and epigenetic modulators to treat various models of IRDs. This preclinical work has informed the first CRISPR-

based clinical trial, EDIT-101, which demonstrated a favorable safety profile and evidence of meaningful improvement in vision in phase 1/2[210]. It is no doubt that as gene editing continues to evolve, additional clinical trials will follow. As these therapeutics continue to develop, we must also consider the implications patients face.

As discussed above, the safety profile of CRISPR-based therapies must continue to be studied and improved on. This will likely occur at various stages of development. Design of the chosen editor systems will be important to limit off-target effects and undesired genomic editing. Limiting expression of the editor system may also contribute to a more favorable safety profile and decreased immune response. While different delivery methods may cause less immune response and subsequent intraocular inflammation. With a multitude of ways to improve the safety of these therapies, I have no doubt the field of gene editing will continue to expand.

In addition to the importance of safety, the decision of when to treat remains of great discussion. Many of the IRDs discussed throughout this thesis are progressive, including the cone and cone-rod dystrophies. As the disease progresses, more retinal cells are subject to dysfunction and disorganization[4]. Many of the current investigative treatments rely on the presence of functional retinal cells to produce a functional protein, in the case of gene augmentation, or to gain benefit from silencing of a mutated gene with editing systems. As such, it is possible that treating patients at an earlier age may provide even more benefit[247,248]. With the advances in next generation sequencing and specific IRD gene panels now readily available, screening patients for IRD related genes has never been easier. Further studies are needed to elucidate differences in timing of

treatment, but the progressive nature of many of the IRDs argue earlier treatment may preserve or improve vision and lead to decreased retinal degeneration.

Finally, there is a significant cost associated with developing a gene therapy treatment from the ground up. With the advancement of computational tools, it may become possible to screen large combinations of gene editing components and delivery methods to create a specific and safe gene editor, bypassing much experimental lab work with a considerable price tag. Once developed, society must also consider the exorbitant cost of the gene therapy, as evidenced by the $425,000 price of Luxturna. The high cost is prohibitive and necessitates discussion within the scientific, pharmaceutical, and medical communities to ensure future gene therapies will be accessible to all.

6.4 Concluding Thoughts

From my college courses at University of Colorado Boulder, where I first heard CRISPR technology described, I have been intrigued by the ability to alter the human genome. Since then, the field has exploded, now harboring the ability to precisely change a single nucleotide. The therapeutic potential of gene editing feels unlimited, and I have great hope in the development of safe and effective treatments for debilitating disease. As I enter the next stage of my career as a physician, I will carry with me fondly the scientific reasoning and skills I have gained during my time in the MacLaren lab.

Chapter 7: References

1. Economics, D. Access. The socioeconomic impact of inherited retinal dystrophies (IRDs) in the United Kingdom. *Retinal International* (2019).
2. Pontikos, N. *et al.* Genetic Basis of Inherited Retinal Disease in a Molecularly Characterized Cohort of More Than 3000 Families from the United Kingdom. *Ophthalmology* **127**, 1384–1394 (2020).
3. Sullivan, L. S. P. D. S. P. P. T. U. of T. H. S. C. H. T. RetNet Retinal Information Network.
4. Gill, J. S., Georgiou, M., Kalitzeos, A., Moore, A. T. & Michaelides, M. Progressive cone and cone-rod dystrophies: clinical features, molecular genetics and prospects for therapy. *British Journal of Ophthalmology* **103**, 711 (2019).
5. Sahel, J.-A., Marazova, K. & Audo, I. Clinical characteristics and current therapies for inherited retinal degenerations. *Cold Spring Harb Perspect Med* **5**, a017111 (2014).
6. Susanne Kohl, Ms. P. H. J. M. D. F. B. W. Ms. P. and D. Z. M. P. D. FEBO. *Achromatopsia*.
7. Kohl, S. *et al.* CNGB3 mutations account for 50% of all cases with autosomal recessive achromatopsia. *European Journal of Human Genetics* **13**, 302–308 (2005).
8. Komáromy, A. M. *et al.* Gene therapy rescues cone function in congenital achromatopsia. *Hum Mol Genet* **19**, 2581–2593 (2010).
9. Pang, J. *et al.* AAV-Mediated Cone Rescue in a Naturally Occurring Mouse Model of CNGA3-Achromatopsia. *PLoS One* **7**, e35250 (2012).
10. Gootwine, E. *et al.* Gene Augmentation Therapy for a Missense Substitution in the cGMP-Binding Domain of Ovine *CNGA3* Gene Restores Vision in Day-Blind Sheep. *Investigative Opthalmology & Visual Science* **58**, 1577 (2017).
11. Michaelides, M. *et al.* First-in-Human Gene Therapy Trial of AAV8-hCARp.hCNGB3 in Adults and Children With CNGB3-associated Achromatopsia. *Am J Ophthalmol* **253**, 243–251 (2023).
12. Reichel, F. F. *et al.* Three-year results of phase I retinal gene therapy trial for CNGA3-mutated achromatopsia: results of a non randomised controlled trial. *British Journal of Ophthalmology* **106**, 1567–1572 (2022).
13. Schwartz, M., Haim, M. & Skarsholm, D. X-linked myopia: Bornholm Eye Disease. *Clin Genet* **38**, 281–286 (1990).
14. McClements, M. *et al.* Variations in Opsin Coding Sequences Cause X-Linked Cone Dysfunction Syndrome with Myopia and Dichromacy. *Investigative Opthalmology & Visual Science* **54**, 1361 (2013).
15. Nathans, J., Piantanida, T. P., Eddy, R. L., Shows, T. B. & Hogness, D. S. Molecular Genetics of Inherited Variation in Human Color Vision. *Science (1979)* **232**, 203–210 (1986).
16. Zhang, Y. *et al.* Gene-based Therapy in a Mouse Model of Blue Cone Monochromacy. *Sci Rep* **7**, 6690 (2017).
17. Deng, W.-T. *et al.* Human L- and M-opsins restore M-cone function in a mouse model for human blue cone monochromacy. *Mol Vis* **24**, 17–28 (2018).
18. Haim, M., Fledelius, H. C. & Skarsholm. X-linked myopia in danish family. *Acta Ophthalmol* **66**, 450–456 (1988).
19. Allikmets, R. *et al.* A photoreceptor cell-specific ATP-binding transporter gene (ABCR) is mutated in recessive Starqardt macular dystrophy. *Nat Genet* **15**, 236–246 (1997).
20. Zernant, J. *et al.* Analysis of the *ABCA4* Gene by Next-Generation Sequencing. *Investigative Opthalmology & Visual Science* **52**, 8479 (2011).

21. Schulz, H. L. *et al.* Mutation Spectrum of the *ABCA4* Gene in 335 Stargardt Disease Patients From a Multicenter German Cohort—Impact of Selected Deep Intronic Variants and Common SNPs. *Investigative Opthalmology & Visual Science* **58**, 394 (2017).
22. Molday, R. S. & Zhang, K. Defective lipid transport and biosynthesis in recessive and dominant Stargardt macular degeneration. *Prog Lipid Res* **49**, 476–492 (2010).
23. Grieger, J. C. & Samulski, R. J. Packaging Capacity of Adeno-Associated Virus Serotypes: Impact of Larger Genomes on Infectivity and Postentry Steps. *J Virol* **79**, 9933–9944 (2005).
24. Han, Z., Conley, S. M., Makkia, R. S., Cooper, M. J. & Naash, M. I. DNA nanoparticle-mediated ABCA4 delivery rescues Stargardt dystrophy in mice. *Journal of Clinical Investigation* **122**, 3221–3226 (2012).
25. Piotter, E., McClements, M. E. & MacLaren, R. E. Therapy Approaches for Stargardt Disease. *Biomolecules* **11**, 1179 (2021).
26. Birtel, J. *et al.* Clinical and genetic characteristics of 251 consecutive patients with macular and cone/cone-rod dystrophy. *Sci Rep* **8**, 4824 (2018).
27. Yusuf, I. H. *et al.* Rescue of cone and rod photoreceptor function in a CDHR1-model of age-related retinal degeneration. *Molecular Therapy* **32**, 1445–1460 (2024).
28. Udar, N. *et al.* Identification of GUCY2D gene mutations in CORD5 families and evidence of incomplete penetrance. *Hum Mutat* **21**, 170–171 (2003).
29. Molday, R. S. & Moritz, O. L. Photoreceptors at a glance. *J Cell Sci* **128**, 4039–4045 (2015).
30. Biasi, A. *et al.* A Novel GUCA1A Variant Associated with Cone Dystrophy Alters cGMP Signaling in Photoreceptors by Strongly Interacting with and Hyperactivating Retinal Guanylate Cyclase. *Int J Mol Sci* **22**, 10809 (2021).
31. McCullough, K. T. *et al.* Somatic Gene Editing of *GUCY2D* by AAV-CRISPR/Cas9 Alters Retinal Structure and Function in Mouse and Macaque. *Hum Gene Ther* **30**, 571–589 (2019).
32. Mellen, R. W. *et al.* Development of an AAV-CRISPR-Cas9-based treatment for dominant cone-rod dystrophy 6. *Mol Ther Methods Clin Dev* **30**, 48–64 (2023).
33. Boon, C. J. F. *et al.* The spectrum of retinal dystrophies caused by mutations in the peripherin/RDS gene. *Prog Retin Eye Res* **27**, 213–235 (2008).
34. Conley, S. M. & Naash, M. I. Gene Therapy for PRPH2-Associated Ocular Disease: Challenges and Prospects. *Cold Spring Harb Perspect Med* **4**, a017376–a017376 (2014).
35. Rahman, N., Georgiou, M., Khan, K. N. & Michaelides, M. Macular dystrophies: clinical and imaging features, molecular genetics and therapeutic options. *British Journal of Ophthalmology* **104**, 451–460 (2020).
36. Qi, J. H. *et al.* Sorsby Fundus Dystrophy Mutation in Tissue Inhibitor of Metalloproteinase 3 (TIMP3) promotes Choroidal Neovascularization via a Fibroblast Growth Factor-dependent Mechanism. *Sci Rep* **9**, 17429 (2019).
37. Elsayed, M. E. A. A., Kaukonen, M., Kiraly, P., Kapetanovic, J. C. & MacLaren, R. E. Potential CRISPR Base Editing Therapeutic Options in a Sorsby Fundus Dystrophy Patient. *Genes (Basel)* **13**, 2103 (2022).
38. Cehajic-Kapetanovic, J. *et al.* Clinical and Molecular Characterization of *PROM1* -Related Retinal Degeneration. *JAMA Netw Open* **2**, e195752 (2019).
39. Yang, Z. *et al.* Mutant prominin 1 found in patients with macular degeneration disrupts photoreceptor disk morphogenesis in mice. *Journal of Clinical Investigation* (2008) doi:10.1172/JCI35891.
40. Bhattacharya, S. *et al.* Prominin-1 Is a Novel Regulator of Autophagy in the Human Retinal Pigment Epithelium. *Investigative Opthalmology & Visual Science* **58**, 2366 (2017).
41. Hartong, D. T., Berson, E. L. & Dryja, T. P. Retinitis pigmentosa. *The Lancet* **368**, 1795–1809 (2006).
42. Cehajic-Kapetanovic, J. *et al.* Impaired glutamylation of RPGR ^{ORF15} underlies the cone-dominated phenotype associated with truncating distal ORF15 variants. *Proceedings of the National Academy of Sciences* **119**, (2022).

43. Benson, M. D. *et al. RPGR* : Deep Phenotyping and Genetic Characterization With Findings Specific to the 3'-end of ORF15. *Investigative Opthalmology & Visual Science* **64**, 19 (2023).
44. Menghini, M., Cehajic-Kapetanovic, J. & MacLaren, R. E. Monitoring progression of retinitis pigmentosa: current recommendations and recent advances. *Expert Opin Orphan Drugs* **8**, 67–78 (2020).
45. Bakondi, B. *et al.* In Vivo CRISPR/Cas9 Gene Editing Corrects Retinal Dystrophy in the S334ter-3 Rat Model of Autosomal Dominant Retinitis Pigmentosa. *Molecular Therapy* **24**, 556–563 (2016).
46. Giannelli, S. G. *et al.* Cas9/sgRNA selective targeting of the P23H Rhodopsin mutant allele for treating retinitis pigmentosa by intravitreal AAV9.PHP.B-based delivery. *Hum Mol Genet* **27**, 761–779 (2018).
47. Gumerson, J. D. *et al.* Restoration of RPGR expression in vivo using CRISPR/Cas9 gene editing. *Gene Ther* **29**, 81–93 (2022).
48. Qin, H. *et al.* Vision rescue via unconstrained in vivo prime editing in degenerating neural retinas. *Journal of Experimental Medicine* **220**, (2023).
49. Yu, W. *et al.* Nrl knockdown by AAV-delivered CRISPR/Cas9 prevents retinal degeneration in mice. *Nat Commun* **8**, 14716 (2017).
50. Georgiou, M., Fujinami, K. & Michaelides, M. Retinal imaging in inherited retinal diseases. *Ann Eye Sci* **5**, 25–25 (2020).
51. Fujimoto, J. G., Pitris, C., Boppart, S. A. & Brezinski, M. E. Optical Coherence Tomography: An Emerging Technology for Biomedical Imaging and Optical Biopsy. *Neoplasia* **2**, 9–25 (2000).
52. Lee, B. *et al.* High-Speed, Ultrahigh-Resolution Spectral-Domain OCT with Extended Imaging Range Using Reference Arm Length Matching. *Transl Vis Sci Technol* **9**, 12 (2020).
53. Chan, A. Normal Macular Thickness Measurements in Healthy Eyes Using Stratus Optical Coherence Tomography. *Archives of Ophthalmology* **124**, 193 (2006).
54. Adhi, M., Aziz, S., Muhammad, K. & Adhi, M. I. Macular Thickness by Age and Gender in Healthy Eyes Using Spectral Domain Optical Coherence Tomography. *PLoS One* **7**, e37638 (2012).
55. Ferguson, L. R., Dominguez II, J. M., Balaiya, S., Grover, S. & Chalam, K. V. Retinal Thickness Normative Data in Wild-Type Mice Using Customized Miniature SD-OCT. *PLoS One* **8**, e67265 (2013).
56. Li, Q. *et al.* Noninvasive imaging by optical coherence tomography to monitor retinal degeneration in the mouse. *Invest Ophthalmol Vis Sci* **42**, 2981–9 (2001).
57. Staurenghi, G., Sadda, S., Chakravarthy, U. & Spaide, R. F. Proposed Lexicon for Anatomic Landmarks in Normal Posterior Segment Spectral-Domain Optical Coherence Tomography. *Ophthalmology* **121**, 1572–1578 (2014).
58. Mohankumar, A. G. B. *Scanning Laser Ophthalmoscope*. (StatPearls, 2023).
59. Helb, H. *et al.* Clinical evaluation of simultaneous confocal scanning laser ophthalmoscopy imaging combined with high-resolution, spectral-domain optical coherence tomography. *Acta Ophthalmol* **88**, 842–849 (2010).
60. Flower, R. W. & Hochheimer, B. F. A clinical technique and apparatus for simultaneous angiography of the separate retinal and choroidal circulations. *Invest Ophthalmol* **12**, 248–61 (1973).
61. Fischer, J., Otto, T., Delori, F., Pace, L. & Staurenghi, G. Scanning Laser Ophthalmoscopy (SLO). in *High Resolution Imaging in Microscopy and Ophthalmology* 35–57 (Springer International Publishing, Cham, 2019). doi:10.1007/978-3-030-16638-0_2.
62. Delori, F. C. *et al.* In vivo fluorescence of the ocular fundus exhibits retinal pigment epithelium lipofuscin characteristics. *Invest Ophthalmol Vis Sci* **36**, 718–29 (1995).
63. Pole, C. & Ameri, H. Fundus Autofluorescence and Clinical Applications. *J Ophthalmic Vis Res* (2021) doi:10.18502/jovr.v16i3.9439.
64. Sparrow, J. R., Wu, Y., Kim, C. Y. & Zhou, J. Phospholipid meets all-trans-retinal: the making of RPE bisretinoids. *J Lipid Res* **51**, 247–261 (2010).
65. Jauregui, R. *et al.* Disease asymmetry and hyperautofluorescent ring shape in retinitis pigmentosa patients. *Sci Rep* **10**, 3364 (2020).

66. Schuerch, K. *et al.* Quantifying Fundus Autofluorescence in Patients With Retinitis Pigmentosa. *Investigative Opthalmology & Visual Science* **58**, 1843 (2017).
67. Gliem, M. *et al.* Quantitative Fundus Autofluorescence and Genetic Associations in Macular, Cone, and Cone–Rod Dystrophies. *Ophthalmol Retina* **4**, 737–749 (2020).
68. Miere, A. *et al.* Deep Learning-Based Classification of Inherited Retinal Diseases Using Fundus Autofluorescence. *J Clin Med* **9**, 3303 (2020).
69. Mantovani, A., Herbort, C. P., Hedayatfar, A. & Papasavvas, I. Blue-Light Fundus Autofluorescence (BAF), an Essential Modality for the Evaluation of Inflammatory Diseases of the Photoreceptors: An Imaging Narrative. *Diagnostics* **13**, 2466 (2023).
70. Müller, P. L. *et al.* Comparison of Green Versus Blue Fundus Autofluorescence in *ABCA4* -Related Retinopathy. *Transl Vis Sci Technol* **7**, 13 (2018).
71. Ishino, Y., Shinagawa, H., Makino, K., Amemura, M. & Nakata, A. Nucleotide sequence of the iap gene, responsible for alkaline phosphatase isozyme conversion in Escherichia coli, and identification of the gene product. *J Bacteriol* **169**, 5429–5433 (1987).
72. Mojica, F. J. M., D□ez-Villase□or, C., Garc□a-Mart□nez, J. & Soria, E. Intervening Sequences of Regularly Spaced Prokaryotic Repeats Derive from Foreign Genetic Elements. *J Mol Evol* **60**, 174–182 (2005).
73. Pourcel, C., Salvignol, G. & Vergnaud, G. CRISPR elements in Yersinia pestis acquire new repeats by preferential uptake of bacteriophage DNA, and provide additional tools for evolutionary studies. *Microbiology (N Y)* **151**, 653–663 (2005).
74. Barrangou, R. *et al.* CRISPR Provides Acquired Resistance Against Viruses in Prokaryotes. *Science (1979)* **315**, 1709–1712 (2007).
75. Jinek, M. *et al.* A Programmable Dual-RNA–Guided DNA Endonuclease in Adaptive Bacterial Immunity. *Science (1979)* **337**, 816–821 (2012).
76. Gallagher, D. N. & Haber, J. E. Repair of a Site-Specific DNA Cleavage: Old-School Lessons for Cas9-Mediated Gene Editing. *ACS Chem Biol* **13**, 397–405 (2018).
77. MAO, Z., BOZZELLA, M., SELUANOV, A. & GORBUNOVA, V. Comparison of nonhomologous end joining and homologous recombination in human cells. *DNA Repair (Amst)* **7**, 1765–1771 (2008).
78. Sansbury, B. M., Hewes, A. M. & Kmiec, E. B. Understanding the diversity of genetic outcomes from CRISPR-Cas generated homology-directed repair. *Commun Biol* **2**, 458 (2019).
79. Komor, A. C., Kim, Y. B., Packer, M. S., Zuris, J. A. & Liu, D. R. Programmable editing of a target base in genomic DNA without double-stranded DNA cleavage. *Nature* **533**, 420–424 (2016).
80. Gaudelli, N. M. *et al.* Programmable base editing of A•T to G•C in genomic DNA without DNA cleavage. *Nature* **551**, 464–471 (2017).
81. Kantor, A., McClements, M. & MacLaren, R. CRISPR-Cas9 DNA Base-Editing and Prime-Editing. *Int J Mol Sci* **21**, 6240 (2020).
82. Song, J., Zhuang, Y. & Yi, C. Programmable RNA base editing via targeted modifications. *Nat Chem Biol* **20**, 277–290 (2024).
83. Kurt, I. C. *et al.* CRISPR C-to-G base editors for inducing targeted DNA transversions in human cells. *Nat Biotechnol* **39**, 41–46 (2021).
84. Newby, G. A. & Liu, D. R. In vivo somatic cell base editing and prime editing. *Molecular Therapy* **29**, 3107–3124 (2021).
85. Jo D.H. Jang H.-K. Cho C.S. Han J.H. Ryu G. Jung Y. Bae S. Kim J.H. Therapeutic adenine base editing corrects nonsense mutation and improves visual function in a mouse model of Leber congenital amaurosis. *bioRxiv* (2021).
86. Suh, S. *et al.* Restoration of visual function in adult mice with an inherited retinal disease via adenine base editing. *Nat Biomed Eng* **5**, 169–178 (2020).
87. Choi, E. H. *et al.* In vivo base editing rescues cone photoreceptors in a mouse model of early-onset inherited retinal degeneration. *Nat Commun* **13**, 1830 (2022).

88. Lee, R. G. *et al.* Efficacy and Safety of an Investigational Single-Course CRISPR Base-Editing Therapy Targeting *PCSK9* in Nonhuman Primate and Mouse Models. *Circulation* **147**, 242–253 (2023).
89. Verve Therapeutics. Our PCSK9 Programs. https://www.vervetx.com/our-programs/verve-101-102 (2024).
90. Anzalone, A. V. *et al.* Search-and-replace genome editing without double-strand breaks or donor DNA. *Nature* **576**, 149–157 (2019).
91. Chen, P. J. & Liu, D. R. Prime editing for precise and highly versatile genome manipulation. *Nat Rev Genet* **24**, 161–177 (2023).
92. Davis, J. R. *et al.* Efficient prime editing in mouse brain, liver and heart with dual AAVs. *Nat Biotechnol* **42**, 253–264 (2024).
93. An, M. *et al.* Engineered virus-like particles for transient delivery of prime editor ribonucleoprotein complexes in vivo. *Nat Biotechnol* (2024) doi:10.1038/s41587-023-02078-y.
94. Larson, M. H. *et al.* CRISPR interference (CRISPRi) for sequence-specific control of gene expression. *Nat Protoc* **8**, 2180–2196 (2013).
95. Gilbert, L. A. *et al.* CRISPR-Mediated Modular RNA-Guided Regulation of Transcription in Eukaryotes. *Cell* **154**, 442–451 (2013).
96. Groner, A. C. *et al.* KRAB–Zinc Finger Proteins and KAP1 Can Mediate Long-Range Transcriptional Repression through Heterochromatin Spreading. *PLoS Genet* **6**, e1000869 (2010).
97. Yeo, N. C. *et al.* An enhanced CRISPR repressor for targeted mammalian gene regulation. *Nat Methods* **15**, 611–616 (2018).
98. Qi, L. S. *et al.* Repurposing CRISPR as an RNA-Guided Platform for Sequence-Specific Control of Gene Expression. *Cell* **152**, 1173–1183 (2013).
99. Li, X. *et al.* tCRISPRi: tunable and reversible, one-step control of gene expression. *Sci Rep* **6**, 39076 (2016).
100. Burnight, E. R. *et al.* CRISPRi-Mediated Treatment of Dominant Rhodopsin-Associated Retinitis Pigmentosa. *CRISPR J* **6**, 502–513 (2023).
101. Peddle, C. F., Fry, L. E., McClements, M. E. & MacLaren, R. E. CRISPR Interference–Potential Application in Retinal Disease. *Int J Mol Sci* **21**, 2329 (2020).
102. Cheng, A. W. *et al.* Multiplexed activation of endogenous genes by CRISPR-on, an RNA-guided transcriptional activator system. *Cell Res* **23**, 1163–1171 (2013).
103. Zhou, H. *et al.* In vivo simultaneous transcriptional activation of multiple genes in the brain using CRISPR–dCas9-activator transgenic mice. *Nat Neurosci* **21**, 440–446 (2018).
104. Böhm, S. *et al.* A gene therapy for inherited blindness using dCas9-VPR-mediated transcriptional activation. *Sci Adv* **6**, eaba5614 (2020).
105. Bendixen, L., Jensen, T. I. & Bak, R. O. CRISPR-Cas-mediated transcriptional modulation: The therapeutic promises of CRISPRa and CRISPRi. *Molecular Therapy* **31**, 1920–1937 (2023).
106. Taylor, A. W. Ocular immune privilege. *Eye* **23**, 1885–1889 (2009).
107. Naylor, A., Hopkins, A., Hudson, N. & Campbell, M. Tight Junctions of the Outer Blood Retina Barrier. *Int J Mol Sci* **21**, 211 (2019).
108. Russell, S. *et al.* Efficacy and safety of voretigene neparvovec (AAV2-hRPE65v2) in patients with RPE65 -mediated inherited retinal dystrophy: a randomised, controlled, open-label, phase 3 trial. *The Lancet* **390**, 849–860 (2017).
109. Redmond., T. M. *et al.* Rpe65 is necessary for production of 11-cis-vitamin A in the retinal visual cycle. *Nat Genet* **20**, 344–351 (1998).
110. Morimura, H. *et al.* Mutations in the RPE65 gene in patients with autosomal recessive retinitis pigmentosa or Leber congenital amaurosis. *Proceedings of the National Academy of Sciences* **95**, 3088–3093 (1998).
111. Thompson, D. A. *et al.* Genetics and phenotypes of RPE65 mutations in inherited retinal degeneration. *Invest Ophthalmol Vis Sci* **41**, 4293–9 (2000).

112. Raghupathy, R. K., Gautier, P., Soares, D. C., Wright, A. F. & Shu, X. Evolutionary Characterization of the Retinitis Pigmentosa GTPase Regulator Gene. *Investigative Opthalmology & Visual Science* **56**, 6255 (2015).
113. Talib, M. *et al.* CLINICAL AND GENETIC CHARACTERISTICS OF MALE PATIENTS WITH RPGR-ASSOCIATED RETINAL DYSTROPHIES. *Retina* **39**, 1186–1199 (2019).
114. Fischer, M. D. *et al.* Codon-Optimized RPGR Improves Stability and Efficacy of AAV8 Gene Therapy in Two Mouse Models of X-Linked Retinitis Pigmentosa. *Molecular Therapy* **25**, 1854–1865 (2017).
115. Cehajic-Kapetanovic, J. *et al.* Initial results from a first-in-human gene therapy trial on X-linked retinitis pigmentosa caused by mutations in RPGR. *Nat Med* **26**, 354–359 (2020).
116. Beacon Therapeutics. Beacon Therapeutics Announces Positive 12-Month Data from Phase 2 SKYLINE Trial of AGTC-501 in Patients with X-Linked Retinitis Pigmentosa. https://www.beacontx.com/news-and-events/beacon-therapeutics-announces-positive-12-month-data-from-phase-2-skyline-trial-of-agtc-501-in-patients-with-x-linked-retinitis-pigmentosa/ (2024).
117. Martinez-Fernandez de la Camara, C., Cehajic-Kapetanovic, J. & MacLaren, R. E. Emerging gene therapy products for RPGR-associated X-linked retinitis pigmentosa. *Expert Opin Emerg Drugs* **27**, 431–443 (2022).
118. Drivas, T. G. & Bennett, J. CEP290 and the Primary Cilium. in 519–525 (2014). doi:10.1007/978-1-4614-3209-8_66.
119. den Hollander, A. I. *et al.* Mutations in the CEP290 (NPHP6) Gene Are a Frequent Cause of Leber Congenital Amaurosis. *The American Journal of Human Genetics* **79**, 556–561 (2006).
120. Maeder, M. L. *et al.* Development of a gene-editing approach to restore vision loss in Leber congenital amaurosis type 10. *Nat Med* **25**, 229–233 (2019).
121. Editas Medicine. Editas Medicine Announces Clinical Data Demonstrating Proof Of Concept Of EDIT-101 From Phase 1/2 BRILLIANCE Trial. https://ir.editasmedicine.com/news-releases/news-release-details/editas-medicine-announces-clinical-data-demonstrating-proof (2022).
122. Safety and Tolerability Study of Gene Editing Drug ZVS203e in Participants With Retinitis Pigmentosa. *ClinicalTrials.Gov* https://clinicaltrials.gov/study/NCT05805007 (2023).
123. Approved Cellular and Gene Therapy Products. *U.S. Food and Drug Administration* https://www.fda.gov/vaccines-blood-biologics/cellular-gene-therapy-products/approved-cellular-and-gene-therapy-products (2024).
124. Guide, S. V. *et al.* Trial of Beremagene Geperpavec (B-VEC) for Dystrophic Epidermolysis Bullosa. *New England Journal of Medicine* **387**, 2211–2219 (2022).
125. Strauss, K. A. *et al.* Onasemnogene abeparvovec for presymptomatic infants with two copies of SMN2 at risk for spinal muscular atrophy type 1: the Phase III SPR1NT trial. *Nat Med* **28**, 1381–1389 (2022).
126. Ozelo, M. C. *et al.* Valoctocogene Roxaparvovec Gene Therapy for Hemophilia A. *New England Journal of Medicine* **386**, 1013–1025 (2022).
127. Pipe, S. W. *et al.* Gene Therapy with Etranacogene Dezaparvovec for Hemophilia B. *New England Journal of Medicine* **388**, 706–718 (2023).
128. George, L. A. *et al.* Efficacy and Safety in 15 Hemophilia B Patients Treated with the AAV Gene Therapy Vector Fidanacogene Elaparvovec and Followed for at Least 1 Year. *Blood* **134**, 3347 (2019).
129. Samelson-Jones, B. J. *et al.* Follow-up of More Than 5 Years in a Cohort of Patients with Hemophilia B Treated with Fidanacogene Elaparvovec Adeno-Associated Virus Gene Therapy. *Blood* **138**, 3975 (2021).
130. Mendell, J. R. *et al.* Assessment of Systemic Delivery of rAAVrh74.MHCK7.micro-dystrophin in Children With Duchenne Muscular Dystrophy. *JAMA Neurol* **77**, 1122 (2020).
131. Mendell, J. R. *et al.* Long-term safety and functional outcomes of delandistrogene moxeparvovec gene therapy in patients with Duchenne muscular dystrophy: A phase 1/2a nonrandomized trial. *Muscle Nerve* **69**, 93–98 (2024).

132. Boorjian, S. A. *et al.* Intravesical nadofaragene firadenovec gene therapy for BCG-unresponsive non-muscle-invasive bladder cancer: a single-arm, open-label, repeat-dose clinical trial. *Lancet Oncol* **22**, 107–117 (2021).
133. Narayan, V. M. & Dinney, C. P. N. Intravesical Gene Therapy. *Urologic Clinics of North America* **47**, 93–101 (2020).
134. Locatelli, F. *et al.* Betibeglogene Autotemcel Gene Therapy for Non–β^0/β^0 Genotype β-Thalassemia. *New England Journal of Medicine* **386**, 415–427 (2022).
135. Kanter, J. *et al.* Lovo-cel gene therapy for sickle cell disease: Treatment process evolution and outcomes in the initial groups of the <scp>HGB</scp> -206 study. *Am J Hematol* **98**, 11–22 (2023).
136. Duncan, C. *et al.* Updated Safety and Efficacy Outcomes from an Ongoing Phase 2/3 Trial of Lenti-D Autologous Hematopoietic Stem Cell Gene Therapy for the Treatment of Cerebral Adrenoleukodystrophy. *Biology of Blood and Marrow Transplantation* **25**, S89–S90 (2019).
137. Fumagalli, F. *et al.* Lentiviral haematopoietic stem-cell gene therapy for early-onset metachromatic leukodystrophy: long-term results from a non-randomised, open-label, phase 1/2 trial and expanded access. *The Lancet* **399**, 372–383 (2022).
138. Frangoul, H. *et al.* CRISPR-Cas9 Gene Editing for Sickle Cell Disease and β-Thalassemia. *New England Journal of Medicine* **384**, 252–260 (2021).
139. Locatelli, F. *et al.* Exagamglogene Autotemcel for Transfusion-Dependent β-Thalassemia. *New England Journal of Medicine* (2024) doi:10.1056/NEJMoa2309673.
140. Brinkman, E. K., Chen, T., Amendola, M. & van Steensel, B. Easy quantitative assessment of genome editing by sequence trace decomposition. *Nucleic Acids Res* **42**, e168–e168 (2014).
141. Mustafi, D., Engel, A. H. & Palczewski, K. Structure of cone photoreceptors. *Prog Retin Eye Res* **28**, 289–302 (2009).
142. Jeon, C.-J., Strettoi, E. & Masland, R. H. The Major Cell Populations of the Mouse Retina. *The Journal of Neuroscience* **18**, 8936–8946 (1998).
143. FEI, Y. & HUGHES, T. E. Transgenic expression of the jellyfish green fluorescent protein in the cone photoreceptors of the mouse. *Vis Neurosci* **18**, 615–623 (2001).
144. Lipinski, D. M. *et al.* Characterization of a Dominant Cone Degeneration in a Green Fluorescent Protein–Reporter Mouse with Disruption of Loci Associated with Human Dominant Retinal Dystrophy. *Invest Ophthalmol Vis Sci* **52**, 6617–6623 (2011).
145. McClements, M. E., Staurenghi, F., MacLaren, R. E. & Cehajic-Kapetanovic, J. Optogenetic Gene Therapy for the Degenerate Retina: Recent Advances. *Front Neurosci* **14**, (2020).
146. Young, J. E., Vogt, T., Gross, K. W. & Khani, S. C. A Short, Highly Active Photoreceptor-Specific Enhancer/Promoter Region Upstream of the Human Rhodopsin Kinase Gene. *Investigative Opthalmology & Visual Science* **44**, 4076 (2003).
147. Lotery, A. J. *et al.* Adeno-Associated Virus Type 5: Transduction Efficiency and Cell-Type Specificity in the Primate Retina. *Hum Gene Ther* **14**, 1663–1671 (2003).
148. Surace, E. M. & Auricchio, A. Versatility of AAV vectors for retinal gene transfer. *Vision Res* **48**, 353–359 (2008).
149. Wiley, L. A. *et al.* Assessment of Adeno-Associated Virus Serotype Tropism in Human Retinal Explants. *Hum Gene Ther* **29**, 424–436 (2018).
150. Young, J. E., Gross, K. W. & Khani, S. C. Conserved structure and spatiotemporal function of the compact rhodopsin kinase (GRK1) enhancer/promoter. *Mol Vis* **11**, 1041–51 (2005).
151. Khani, S. C. *et al.* AAV-Mediated Expression Targeting of Rod and Cone Photoreceptors with a Human Rhodopsin Kinase Promoter. *Investigative Opthalmology & Visual Science* **48**, 3954 (2007).
152. Boye, S. E. *et al.* The human rhodopsin kinase promoter in an AAV5 vector confers rod- and cone-specific expression in the primate retina. *Hum Gene Ther* **23**, 1101–15 (2012).

153. Bruewer, A. R. *et al.* Evaluation of Lateral Spread of Transgene Expression following Subretinal AAV–Mediated Gene Delivery in Dogs. *PLoS One* **8**, e60218 (2013).
154. Lane, A. *et al.* Modeling and Rescue of RP2 Retinitis Pigmentosa Using iPSC-Derived Retinal Organoids. *Stem Cell Reports* **15**, 67–79 (2020).
155. Quinn, P. M. *et al.* Human iPSC-Derived Retinas Recapitulate the Fetal CRB1 CRB2 Complex Formation and Demonstrate that Photoreceptors and Müller Glia Are Targets of AAV5. *Stem Cell Reports* **12**, 906–919 (2019).
156. Kondratova, L., Kondratov, O., Ragheb, R. & Zolotukhin, S. Removal of Endotoxin from rAAV Samples Using a Simple Detergent-Based Protocol. *Mol Ther Methods Clin Dev* **15**, 112–119 (2019).
157. Martinez-Fernandez de la Camara, C., McClements, M. & MacLaren, R. Accurate Quantification of AAV Vector Genomes by Quantitative PCR. *Genes (Basel)* **12**, 601 (2021).
158. Dobnik, D. *et al.* Accurate Quantification and Characterization of Adeno-Associated Viral Vectors. *Front Microbiol* **10**, (2019).
159. Wang, Y., Menon, N., Shen, S., Feschenko, M. & Bergelson, S. A qPCR Method for AAV Genome Titer with ddPCR-Level of Accuracy and Precision. *Mol Ther Methods Clin Dev* **19**, 341–346 (2020).
160. Wang, Y., Cooper, R., Kiladjian, A., Bergelson, S. & Feschenko, M. A Digestion-free Method for Quantification of Residual Host Cell DNA in rAAV Gene Therapy Products. *Mol Ther Methods Clin Dev* **13**, 526–531 (2019).
161. Daniels, D. M., Shen, W.-Y., Constable, I. J. & Rakoczy, P. E. Quantitative model demonstrating that recombinant adeno-associated virus and green fluorescent protein are non-toxic to the rat retina. *Clin Exp Ophthalmol* **31**, 439–444 (2003).
162. Kiser, P. D., Golczak, M., Maeda, A. & Palczewski, K. Key enzymes of the retinoid (visual) cycle in vertebrate retina. *Biochimica et Biophysica Acta (BBA) - Molecular and Cell Biology of Lipids* **1821**, 137–151 (2012).
163. Wang, J. S. & Kefalov, V. J. The Cone-specific visual cycle. *Prog Retin Eye Res* **30**, 115–128 (2011).
164. Applebury, M. L. *et al.* The Murine Cone Photoreceptor: a single cone type expresses both S and M opsins with retinal spatial patterning. *Neuron* **27**, 513–523 (2000).
165. Ortín-Martínez, A. *et al.* Number and Distribution of Mouse Retinal Cone Photoreceptors: Differences between an Albino (Swiss) and a Pigmented (C57/BL6) Strain. *PLoS One* **9**, e102392 (2014).
166. Röhlich, P., van Veen, Th. & Szél, Á. Two different visual pigments in one retinal cone cell. *Neuron* **13**, 1159–1166 (1994).
167. Carvalho, L. S. *et al.* Long-term and age-dependent restoration of visual function in a mouse model of CNGB3-associated achromatopsia following gene therapy. *Hum Mol Genet* **20**, 3161–3175 (2011).
168. Zhang, Y. *et al.* Gene-based Therapy in a Mouse Model of Blue Cone Monochromacy. *Sci Rep* **7**, 6690–6698 (2017).
169. Alexander, J. J. *et al.* Restoration of cone vision in a mouse model of achromatopsia. *Nat Med* **13**, 685–687 (2007).
170. Michalakis, S. *et al.* Gene Therapy Restores Missing Cone-Mediated Vision in the CNGA3−/− Mouse Model of Achromatopsia. in 183–189 (2012). doi:10.1007/978-1-4614-0631-0_25.
171. Doudna, J. A. & Charpentier, E. The new frontier of genome engineering with CRISPR-Cas9. *Science (1979)* **346**, (2014).
172. Akimoto, M. *et al.* Targeting of GFP to newborn rods by Nrl promoter and temporal expression profiling of flow-sorted photoreceptors. *Proceedings of the National Academy of Sciences* **103**, 3890–3895 (2006).
173. Peddle, C. F. Development of all-in-one CRISPR/Cas9 and CRISPRi AAV constructs to treat autosomal dominant retinitis pigmentosa. (University of Oxford, 2021).
174. Lopez, J., Borchert, M., Lee, T. C. & Nagiel, A. Subretinal deposits in young patients treated with voretigene neparvovec-rzyl for RPE65-mediated retinal dystrophy. *British Journal of Ophthalmology* **107**, (2023).
175. Chandler, L. C. *et al.* Characterizing the cellular immune response to subretinal AAV gene therapy in the murine retina. *Mol Ther Methods Clin Dev* **22**, 52–65 (2021).

176. Charbel Issa, P. *et al.* Optimization of In Vivo Confocal Autofluorescence Imaging of the Ocular Fundus in Mice and Its Application to Models of Human Retinal Degeneration. *Investigative Opthalmology & Visual Science* **53**, 1066 (2012).
177. Elsner, A. E., Burns, S. A., Weiter, J. J. & Delori, F. C. Infrared imaging of sub-retinal structures in the human ocular fundus. *Vision Res* **36**, 191–205 (1996).
178. Lieber, M. R. The Mechanism of Double-Strand DNA Break Repair by the Nonhomologous DNA End-Joining Pathway. *Annu Rev Biochem* **79**, 181–211 (2010).
179. Symington, L. S. & Gautier, J. Double-Strand Break End Resection and Repair Pathway Choice. *Annu Rev Genet* **45**, 247–271 (2011).
180. Xue, C. & Greene, E. C. DNA Repair Pathway Choices in CRISPR-Cas9-Mediated Genome Editing. *Trends in Genetics* **37**, 639–656 (2021).
181. Song, B., Yang, S., Hwang, G.-H., Yu, J. & Bae, S. Analysis of NHEJ-Based DNA Repair after CRISPR-Mediated DNA Cleavage. *Int J Mol Sci* **22**, 6397 (2021).
182. Conant, D. *et al.* Inference of CRISPR Edits from Sanger Trace Data. *CRISPR J* **5**, 123–130 (2022).
183. Brockman, Q. R. *et al.* Discrepancies in indel software resolution with somatic CRISPR/Cas9 tumorigenesis models. *Sci Rep* **13**, 14798 (2023).
184. Yan, Z., Zak, R., Zhang, Y. & Engelhardt, J. F. Inverted Terminal Repeat Sequences Are Important for Intermolecular Recombination and Circularization of Adeno-Associated Virus Genomes. *J Virol* **79**, 364–379 (2005).
185. Wilmott, P., Lisowski, L., Alexander, I. E. & Logan, G. J. A User's Guide to the Inverted Terminal Repeats of Adeno-Associated Virus. *Hum Gene Ther Methods* **30**, 206–213 (2019).
186. Yu, W. *et al.* Nrl knockdown by AAV-delivered CRISPR/Cas9 prevents retinal degeneration in mice. *Nat Commun* **8**, 14716 (2017).
187. Qi, Y. *et al.* Trans-Corneal Subretinal Injection in Mice and Its Effect on the Function and Morphology of the Retina. *PLoS One* **10**, e0136523 (2015).
188. Mühlfriedel, R., Michalakis, S., Garrido, M. G., Biel, M. & Seeliger, M. W. Optimized Technique for Subretinal Injections in Mice. in 343–349 (2012). doi:10.1007/978-1-62703-080-9_24.
189. Wagner, J. E. *et al. In Vivo* Potency Testing of Subretinal rAAV5.hCNGB1 Gene Therapy in the *Cngb1* Knockout Mouse Model of Retinitis Pigmentosa. *Hum Gene Ther* **32**, 1158–1170 (2021).
190. Michalakis, S. *et al.* Gene Therapy Restores Missing Cone-Mediated Vision in the CNGA3−/− Mouse Model of Achromatopsia. in 183–189 (2012). doi:10.1007/978-1-4614-0631-0_25.
191. Michalakis, S. *et al.* Restoration of Cone Vision in the CNGA3−/− Mouse Model of Congenital Complete Lack of Cone Photoreceptor Function. *Molecular Therapy* **18**, 2057–2063 (2010).
192. Ye, G.-J. *et al.* Cone-Specific Promoters for Gene Therapy of Achromatopsia and Other Retinal Diseases. *Hum Gene Ther* **27**, 72–82 (2016).
193. Siegert, S. *et al.* Genetic address book for retinal cell types. *Nat Neurosci* **12**, 1197–1204 (2009).
194. Brunet, A. A. *et al.* Validating Fluorescent Chrnb4.EGFP Mouse Models for the Study of Cone Photoreceptor Degeneration. *Transl Vis Sci Technol* **9**, 28 (2020).
195. Liu, Y. V. *et al.* Characterization and allogeneic transplantation of a novel transgenic cone-rich donor mouse line. *Exp Eye Res* **210**, 108715 (2021).
196. Mears, A. J. *et al.* Nrl is required for rod photoreceptor development. *Nat Genet* **29**, 447–452 (2001).
197. Komor, A. C., Badran, A. H. & Liu, D. R. CRISPR-Based Technologies for the Manipulation of Eukaryotic Genomes. *Cell* **168**, 20–36 (2017).
198. Gilbert, L. A. *et al.* Genome-Scale CRISPR-Mediated Control of Gene Repression and Activation. *Cell* **159**, 647–661 (2014).
199. Radzisheuskaya, A., Shlyueva, D., Müller, I. & Helin, K. Optimizing sgRNA position markedly improves the efficiency of CRISPR/dCas9-mediated transcriptional repression. *Nucleic Acids Res* **44**, e141–e141 (2016).

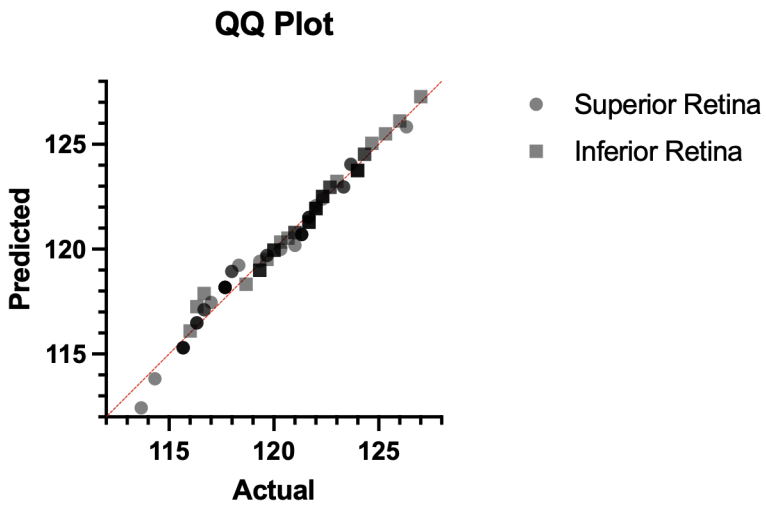
200. Xie, H. *et al.* SaCas9 Requires 5'-NNGRRT-3' PAM for Sufficient Cleavage and Possesses Higher Cleavage Activity than SpCas9 or FnCpf1 in Human Cells. *Biotechnol J* **13**, (2018).
201. Chavez, A. *et al.* Comparison of Cas9 activators in multiple species. *Nat Methods* **13**, 563–567 (2016).
202. Bajwa, K. K. *et al.* Electroporation-based CRISPR gene editing in adult buffalo fibroblast cells. *Anim Biotechnol* **34**, 5055–5066 (2023).
203. Ariel Kantor. Development of CRISPR-Cas genome and epigenome engineering tools towards retinal degenerations. (University of Oxford, 2022).
204. Moreno, A. M. *et al.* In Situ Gene Therapy via AAV-CRISPR-Cas9-Mediated Targeted Gene Regulation. *Molecular Therapy* **26**, 1818–1827 (2018).
205. Kim, S. *et al.* Generation, transcriptome profiling, and functional validation of cone-rich human retinal organoids. *Proceedings of the National Academy of Sciences* **116**, 10824–10833 (2019).
206. Kallman, A. *et al.* Investigating cone photoreceptor development using patient-derived NRL null retinal organoids. *Commun Biol* **3**, 82 (2020).
207. Li, G. *et al.* Generation of Retinal Organoids with Mature Rods and Cones from Urine-Derived Human Induced Pluripotent Stem Cells. *Stem Cells Int* **2018**, 1–12 (2018).
208. Saha, A. *et al.* Cone photoreceptors in human stem cell-derived retinal organoids demonstrate intrinsic light responses that mimic those of primate fovea. *Cell Stem Cell* **29**, 460-471.e3 (2022).
209. Hyder, I., Eghbalsaied, S. & Kues, W. A. Systematic optimization of square-wave electroporation conditions for bovine primary fibroblasts. *BMC Mol Cell Biol* **21**, 9 (2020).
210. Pierce, E. A. *et al.* Gene Editing for *CEP290* -Associated Retinal Degeneration. *New England Journal of Medicine* (2024) doi:10.1056/NEJMoa2309915.
211. Dyka, F. M. *et al.* Cone Specific Promoter for Use in Gene Therapy of Retinal Degenerative Diseases. in 695–701 (2014). doi:10.1007/978-1-4614-3209-8_87.
212. Yan, A. L., Du, S. W. & Palczewski, K. Genome editing, a superior therapy for inherited retinal diseases. *Vision Res* **206**, 108192 (2023).
213. Issa, S. S., Shaimardanova, A. A., Solovyeva, V. V. & Rizvanov, A. A. Various AAV Serotypes and Their Applications in Gene Therapy: An Overview. *Cells* **12**, 785 (2023).
214. Salman, A. *et al.* Non-Viral Delivery of CRISPR/Cas Cargo to the Retina Using Nanoparticles: Current Possibilities, Challenges, and Limitations. *Pharmaceutics* **14**, 1842 (2022).
215. Chien, Y. *et al.* Nanoparticles-mediated CRISPR-Cas9 gene therapy in inherited retinal diseases: applications, challenges, and emerging opportunities. *J Nanobiotechnology* **20**, 511 (2022).
216. Banskota, S. *et al.* Engineered virus-like particles for efficient in vivo delivery of therapeutic proteins. *Cell* **185**, 250-265.e16 (2022).
217. Li, B. *et al.* Metabolic Features of Mouse and Human Retinas: Rods versus Cones, Macula versus Periphery, Retina versus RPE. *iScience* **23**, 101672 (2020).
218. Shirley, J. L., de Jong, Y. P., Terhorst, C. & Herzog, R. W. Immune Responses to Viral Gene Therapy Vectors. *Molecular Therapy* **28**, 709–722 (2020).
219. Zhang, C.-J. *et al.* Effects of fluorescent protein tdTomato on mouse retina. *Exp Eye Res* **243**, 109910 (2024).
220. Hu, X. *et al.* The application and progression of CRISPR/Cas9 technology in ophthalmological diseases. *Eye* **37**, 607–617 (2023).
221. Zhang, X.-H., Tee, L. Y., Wang, X.-G., Huang, Q.-S. & Yang, S.-H. Off-target Effects in CRISPR/Cas9-mediated Genome Engineering. *Mol Ther Nucleic Acids* **4**, e264 (2015).
222. Lopes, R. & Prasad, M. K. Beyond the promise: evaluating and mitigating off-target effects in CRISPR gene editing for safer therapeutics. *Front Bioeng Biotechnol* **11**, (2024).
223. Guo, C., Ma, X., Gao, F. & Guo, Y. Off-target effects in CRISPR/Cas9 gene editing. *Front Bioeng Biotechnol* **11**, (2023).

224. Bao, X. R., Pan, Y., Lee, C. M., Davis, T. H. & Bao, G. Tools for experimental and computational analyses of off-target editing by programmable nucleases. *Nat Protoc* **16**, 10–26 (2021).
225. Sherkatghanad, Z., Abdar, M., Charlier, J. & Makarenkov, V. Using traditional machine learning and deep learning methods for on- and off-target prediction in CRISPR/Cas9: a review. *Brief Bioinform* **24**, (2023).
226. Zhuo, C. *et al.* Spatiotemporal control of CRISPR/Cas9 gene editing. *Signal Transduct Target Ther* **6**, 238 (2021).
227. Petris, G. *et al.* Hit and go CAS9 delivered through a lentiviral based self-limiting circuit. *Nat Commun* **8**, 15334 (2017).
228. Li, A. *et al.* A Self-Deleting AAV-CRISPR System for In Vivo Genome Editing. *Mol Ther Methods Clin Dev* **12**, 111–122 (2019).
229. Liang, S.-Q. *et al.* Genome-wide profiling of prime editor off-target sites in vitro and in vivo using PE-tag. *Nat Methods* **20**, 898–907 (2023).
230. Mingozzi, F. & High, K. A. Immune responses to AAV vectors: overcoming barriers to successful gene therapy. *Blood* **122**, 23–36 (2013).
231. Verdera, H. C., Kuranda, K. & Mingozzi, F. AAV Vector Immunogenicity in Humans: A Long Journey to Successful Gene Transfer. *Molecular Therapy* **28**, 723–746 (2020).
232. Dhungel, B. P., Bailey, C. G. & Rasko, J. E. J. Journey to the Center of the Cell: Tracing the Path of AAV Transduction. *Trends Mol Med* **27**, 172–184 (2021).
233. Charlesworth, C. T. *et al.* Identification of preexisting adaptive immunity to Cas9 proteins in humans. *Nat Med* **25**, 249–254 (2019).
234. Simhadri, V. L. *et al.* Prevalence of Pre-existing Antibodies to CRISPR-Associated Nuclease Cas9 in the USA Population. *Mol Ther Methods Clin Dev* **10**, 105–112 (2018).
235. Toral, M. A. *et al.* Investigation of Cas9 antibodies in the human eye. *Nat Commun* **13**, 1053 (2022).
236. Streilein, J. W. Ocular immune privilege: therapeutic opportunities from an experiment of nature. *Nat Rev Immunol* **3**, 879–889 (2003).
237. Bainbridge, J. W. B. *et al.* Long-Term Effect of Gene Therapy on Leber's Congenital Amaurosis. *New England Journal of Medicine* **372**, 1887–1897 (2015).
238. Dimopoulos, I. S. *et al.* Two-Year Results After AAV2-Mediated Gene Therapy for Choroideremia: The Alberta Experience. *Am J Ophthalmol* **193**, 130–142 (2018).
239. Ghoraba, H. H. *et al.* Ocular Gene Therapy: A Literature Review with Special Focus on Immune and Inflammatory Responses. *Clinical Ophthalmology* **Volume 16**, 1753–1771 (2022).
240. Chu, W. S. & Ng, J. Immunomodulation in Administration of rAAV: Preclinical and Clinical Adjuvant Pharmacotherapies. *Front Immunol* **12**, (2021).
241. Bommakanti, N. *et al.* Classification and Growth Rate of Chorioretinal Atrophy after Voretigene Neparvovec-Rzyl for RPE65-Mediated Retinal Degeneration. *Ophthalmol Retina* **8**, 42–48 (2024).
242. Picaud, S. *et al.* The primate model for understanding and restoring vision. *Proceedings of the National Academy of Sciences* **116**, 26280–26287 (2019).
243. Conlee, K. M., Hoffeld, E. H. & Stephens, M. L. A Demographic Analysis of Primate Research in the United States. *Alternatives to Laboratory Animals* **32**, 315–322 (2004).
244. Winkler, P. A., Occelli, L. M. & Petersen-Jones, S. M. Large Animal Models of Inherited Retinal Degenerations: A Review. *Cells* **9**, 882 (2020).
245. Kaya, K. D. *et al.* Transcriptome-based molecular staging of human stem cell-derived retinal organoids uncovers accelerated photoreceptor differentiation by 9-cis retinal. *Mol Vis* **25**, 663–678 (2019).
246. McClements, M. E. *et al.* Tropism of AAV Vectors in Photoreceptor-Like Cells of Human iPSC-Derived Retinal Organoids. *Transl Vis Sci Technol* **11**, 3 (2022).
247. Bremond-Gignac, D., Robert, M. P. & Daruich, A. Update on gene therapies in pediatric ophthalmology. *Archives de Pédiatrie* **30**, 8S41-8S45 (2023).

248. Leroy, B. P. *et al.* Gene Therapy for Inherited Retinal Disease: Long-Term Durability of Effect. *Ophthalmic Res* **66**, 179–196 (2023).

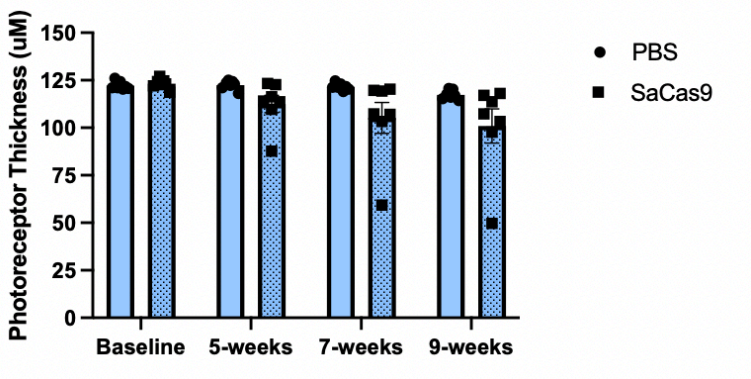
Chapter 8: Appendix

Figure 8.1 Normal Distribution of Superior and Inferior Retina PRL Thickness



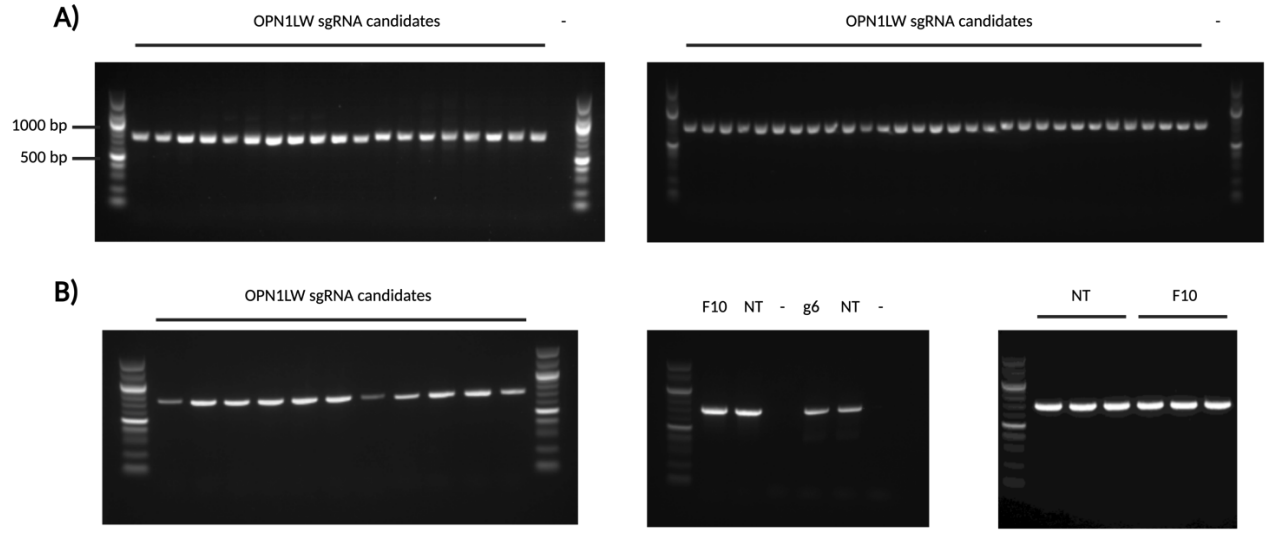
Q-Q Plot of superior and inferior PRL measurements (n=40) against expected normal distribution. Normality of data supported by D'Agonstina and Pearson test: superior *p=0.4060* inferior *p=0.6556*, Anderson-Darling test: superior *p=0.0593*, inferior *p=0.4724*, and Shapiro-Wilk test: superior *p=0.1709* inferior p=0.5702.

Figure 8.2 Inferior PRL Measurements of High-Dose AAV5-hGRK1-SaCas9-F10



Inferior PRL thickness measurements at baseline, 5-weeks, 7-weeks, and 9-weeks post-injection of AAV5-hGRK1-SaCas9-F10 at a viral dose of $1x10^{13}$ gc/mL. Two-way ANOVA analyzed effect of injection and time post-injection on inferior photoreceptor layer thickness: Injection effect F(1, 12)=3.702, p=0.0784, Time effect F(1.06, 12.71)=7.550, p=0.0158, Interaction effect F(3, 36)=3.84, p=0.0175. Sidak's multiple comparisons test showed no difference in PRL thickness between PBS and SaCas9 at any timepoint.

Figure 8.3 Gel electrophoresis of PCR products sent for sequencing



Representative UV exposure images of gel electrophoresis of PCR products sent for sequencing for TIDE analysis in Chapter 5. All ladders used are 100bp DNA ladder from NEB with reference bands at 500bp and 1000bp. A) ~700bp region amplified from HEK293T cells transfected with EFS-SaCas9-OPN1LW sgRNA candidates. B) ~700bp region amplified from CGFP fibroblasts transfected with EFS-SaCas9-OPN1LW or EFS-SaCas9-F10.

8.4: Macro for Mean Grey Fluorescence

Superior Retina

{run("Gaussian Blur...", "sigma=3");

run("Specify...", "width=1336 height=1080 x=100 y=100 oval");

{run("Sup MGF");}

run("Measure");}

Inferior Retina

{run("Gaussian Blur...", "sigma=3");

```
run("Specify...", "width=1336 height=1080 x=100 y=356 oval");
{run("Inf MGF");}
run("Measure");}

Sup MGF or Inf MGF
macro "Sup MGF" {
    if (selectionType!=1)
        exit("Elliptical selection required");
    getBoundingRect(x, y, width, height);
    midy = y + height/2;
    getSelectionCoordinates(sx, sy);
    for (i=0; i<sy.length; i++) {
        if (sy[i]>midy) sy[i] = midy;
    }
    makeSelection(3, sx, sy);
 }

macro "Inf MGF" {
    if (selectionType!=1)
        exit("Elliptical selection required");
    getBoundingRect(x, y, width, height);
    midy = y + height/2;
```

```
    getSelectionCoordinates(sx, sy);
    for (i=0; i<sy.length; i++) {
        if (sy[i]>midy) sy[i] = midy;
    }
    makeSelection(3, sx, sy);
}
```

8.5: sgRNA Sequences

Target	Name	Sequence
EGFP	F10	GCCGGTGGTGCAGATGAACTT
OPN1LW	g3	CCTTGGCTTTCCTAAGCTTA
	g4	AGCTGATGGAAGCCGTGAAA
	g5	TGGAAACTGAGGCGAGGCTA
	g6	GTCACCGCCACCTTCCTGGC
	g8	ACCTTCCTGGCGGGGATGGG
	g9	AGTCACCGCCACCTTCCTGG
	g10	GGCGGACGCAGGACAGTAGA
	g11	TCAAGAGAACCACATGAGAA
	g12	CGGACATGGCTGGCCTCGCA
	g13	TCAGTCTGCCCCCCCTACAC
	g14	GCCAAAGGACCTACAGCTCA

	g15	AAGGCTGTGAACTCAGGGCA
	g16	CTGTCTGGACACTCTGTCGA
	g17	CCTGCGAAGCGTGGGGACAC

8.6: Sequencing Primers

Plasmid/Element	**Name**	**Sequence**
hGRK1-DsRed	RFP-F1-1	CTCGGCCTCTAGAACTAGTG
	RFP-F1-2	CTCCTCCGAGGACGTCATC
	RFP-F2	CGGCCAAATGAATTCCCAAACC
	RFP-F3	CTTTAATCGGCCTCCTGTTTAGC
	RFP-F4	CCTCTCCGGCATGAATTTATCAG
	RFP-F5	CAACATTTCCGTGTCGCCC
	RFP-F6	CCCGTATCGTAGTTATCTACACG
	RFP-F7	CGGAACAGGAGAGCGCAC
	RFP-F8	CGCCATGCTACTTATCTACGTAG
	RFP-F9	GGGCAACGTGCTGGTTATTG
hGRK1-SaCas9	GRK1-Cas9 Seq1	AGCCTGGTGGTTGTTTGTCC
	GRK1-Cas9 Seq2	AGAGAGGCGCCAGAAGGCTG
	GRK1-Cas9 Seq3	ACTATGAGGGACCTGGCGAG
	GRK1-Cas9 Seq4	AGGAAGAGATCGAGCAGATC
	GRK1-Cas9 Seq5	TGGAAGATCTGCTGAACAAC

	GRK1-Cas9 Seq6	TTGCCAACGCCGATTTCATC
	GRK1-Cas9 Seq7	ACGGCAACAAACTGAACGCC
	GRK1-Cas9 Seq8	AGAAGCACCCTCAGATCATC
	GRK1-Cas9 Seq9	TGGACTATCATATGCTTACC
	GRK1-Cas9 Seq10	TCTCCTTACGCATCTGTGCG
	GRK1-Cas9 Seq11	TGCACTCTCAGTACAATCTG
	GRK1-Cas9 Seq12	ACGAGTGGGTTACATCGAAC
	GRK1-Cas9 Seq13	ACTGGATGGAGGCGGATAAAG
	GRK1-Cas9 Seq14	TTGCCGGATCAAGAGCTACC
	GRK1-Cas9 Seq15	TCTAGCTAGGTCTTGAAAGG
hGRK1 promoter	GRK1 F1	CTGAATTCGGTACCGGGCC
CAG promoter	CAG F1	CCCACGTTCTGCTTCACTCT
EFS promoter	EFS Seq	ACTCTTCCTCGCTCAGCTTC
EFS-dSaCas9	hU6-F	GAGGGCCTATTTCCCATGATT
OPSIN-LCR-EGFP	SeqF1	AATGGGAGGTTCAAGGCGAG
	SeqF2	GGGCAACAGAGTGAGACTCC
	SeqF3	CTGTGATGCCCTCCTGGATC
	SeqF4	ACGTGCCACATTCACACTCT
	SeqF5	CCGCGTGGAGTCATTTAGGA
	SeqF6	CCAGGGAAGCCTCAGAGTTG
	SeqF7	CCACCCTTCCACTGTCTGTC

	SeqF8	GCTACCATGTCCAGCCCAAT
	SeqF9	TGCTTCTACCATGTGGCCTG
	SeqF10	GAACTCAGGGCAAGGGAGAC
	SeqF11	TGGTTCCCAGCAAATCCCTC
	SeqF12	TTCTTCAAGTCCGCCATGCC
	SeqR1	TAATCTCACCCTGGCTGCTG
	SeqR2	ACATCCCAGGAAGGAGAGTG
	SeqR3	ATGAAGGGCCTAGAGTGGTC
	SeqR4	GGCTCCATCTCTGTGAAATGC
	SeqR5	GGCCCTCTCTGTGTTTATGTG
	OPN1-Reverse1	CGCATCACCTGAGGGTCAC
	OPN1-Reverse2	CTATGGAAAGCCCTGTCCC
PsiCheck2	SV40 Eurofins	TATTTATGCAGAGGCCGAGG
	PsiCheck2 R	GTGCTTCTCGGAATCATAG

8.7 – PCR Primers

Purpose	**Name**	**Sequence**
CGFP Genotyping	EGFP forward genotype	ACGTAAACGGCCACAAGTTC
	EGFP reverse genotype	AAGTCGTGCTGCTTCATGTG
OPN1 CRIPSRi	TIDE F1	AGCCCTTCATTCCCTGTTATG
	TIDE F2	TTGTGCCTGCAGCAGAAGC
	TIDE F3	TGTCTGGACACTCTGTCGAC

	TIDE R1	ACGGATGACCTGTTAGTGCC
	TIDE R2	TGGTGAAACTGCTCAGAGCCC
	TIDE R3	TTATACTGGCCTGTGGGATC
EGFP KO	EGFP F1	TGAGCAAGGGCGAGGAGC
	EGFP Reverse	TTGTACAGCTCGTCCATGCCG
	KO TIDE F2	TGACCCTCAGGTGATGCGC
	TIDE Caroline F10	GTCTTGTAGTTGCCGTCGTC
	KO TIDE R2	TGTGATCGCGCTTCTCGTTG

8.8 – qPCR Primers

Target	**Name**	**Sequence**
DsRed	RFP qPCR F1	CGACTACAAGAAGCTGTCC
	RFP qPCR R1	AAGTTCACGCCGATGAAC
	RFP qPCR F2	CCGTAATGCAGAAGAAG
	RFP qPCR R2	GTAGATGGACTTGAACTC
	RFP qPCR F3	CGTAATGCAGAAGAAGAC
	RFP qPCR R3	TAGATGGACTTGAACTCC
hGRK1 Promoter	GRK1 F1	CTGAATTCGGTACCGGGCC
	GRK1 R1	CGAAGGCAGCGCGCAGC

8.9 – OPN1LW regions for sgRNA Screening

Name	Sequence
Region 1	CAAGCTCACGCCTTGGCTTTCCTAAGCTTAAGGAATAAACCCAAAAGGA
Region 2	CTGAGGAGCTGGGAGCTGATGGAAGCCGTGAAAGGGGATGTGCTCCTGGG
Region 3	AGGGCCCGTTGGTTGGAAACTGAGGCGAGGCTACGGAGTTGGGCACTAAC
Region 4	AGGTCATCCGTGCCCCTGCGAAGCGTGGGGACACAGGGACAGCAGAGATG
Region 5	ACAGCAGAGATGGCCTGTCTGGACACTCTGTCGACGGGGGGCCTGTGGTTG
Region 6	TGGTGAAGCCCAAGGCAAGGCTGTGAACTCAGGGCAAGGGAGACGTGAGC
Region 7	ATGTGCACCCTGGCGGCCAAAGGACCTACAGCTCATGGGGGGCAAGGGGG
Region 8	AGCAGGATGTGCGCAGTCAGTCTGCCCCCCCTACACTGGAGGAGGAGCCC
Region 9	TCGCCCGTTTGGGCCCACGGACATGGCTGGCCTCGCAAGGAGGATCCGG
Region 10	TAGTCTCCCTGGGCTTTCAAGAGAACCACATGAGAAAGGAGGATTCGGGC
Region 11	TCCACCTGCCCCAAAGGCGGACGCAGGACAGTAGAAGGGAACAGAGAAC
Region 12	AGCGGCTCCCACAGTCACCGCCACCTTCCTGGCGGGGATGGGTGGGGCGTC

8.10 – Key Sequence Elements

EGFP

ATGGTGAGCAAGGGCGAGGAGCTGTTCACCGGGGTGGTGCCCATCCTGGTCGAGCTGGACGGCGACG

TAAACGGCCACAAGTTCAGCGTGTCCGGCGAGGGCGAGGGCGATGCCACCTACGGCAAGCTGACCCTG

AAGTTCATCTGCACCACCGGCAAGCTGCCCGTGCCCTGGCCCACCCTCGTGACCACCCTGACCTACGGCG

TGCAGTGCTTCAGCCGCTACCCCGACCACATGAAGCAGCACGACTTCTTCAAGTCCGCCATGCCCGAAG

GCTACGTCCAGGAGCGCACCATCTTCTTCAAGGACGACGGCAACTACAAGACCCGCGCCGAGGTGAAG

TTCGAGGGCGACACCCTGGTGAACCGCATCGAGCTGAAGGGCATCGACTTCAAGGAGGACGGCAACAT

CCTGGGGCACAAGCTGGAGTACAACTACAACAGCCACAACGTCTATATCATGGCCGACAAGCAGAAGA

ACGGCATCAAGGTGAACTTCAAGATCCGCCACAACATCGAGGACGGCAGCGTGCAGCTCGCCGACCACT

ACCAGCAGAACACCCCCATCGGCGACGGCCCCGTGCTGCTGCCCGACAACCACTACCTGAGCACCCAGT

CCGCCCTGAGCAAAGACCCCAACGAGAAGCGCGATCACATGGTCCTGCTGGAGTTCGTGACCGCCGCC

GGGATCACTCTCGGCATGGACGAGCTGTACAAGTAAAGCGGCCAGATCCTCGAGCAGAAGCTTATCTCT

GAGGAGGATCTGTGATAAGCTTATCTCTGAGGAGGATCTGTGATAGGATCTTTGTGAAGGAACCTTACT

TCTGTGGTGTGACATAATTGGACAAACTACCTACAGAGATTTAAAGCTCTAAGGTAAATATAAAATTTTT

AAGTGTATAATGTGTTAAACTACTGATTCTAATTGTTTGTGTATTTTAGATTCCAACCTATGGAACTGATG

AATGGGAGCAGTGGTGGAATGCCTTTAATGAGGAAAACCTGTTTTGCTCAGAAGAAATGCCATCTAGTG

ATGATGAGGCTACTGCTGACTCTCAACATTCTACTCCTCCAAAAAAGAAGAGGAAGGTAGAAGACCCCC

AGGACTTTCCTTCAGAATTGCTAAGTTTTTTGAGTCATGCTGTGTTTAGTAATAGAACTCTTGCTTGCTTT

GCTATTTACACCACAAAGGAAAAAGC

OPSIN-LCR

CATGGGGAGGGGAGCACAGACCCAGCAGGCAGGCTCTCAATGGGAGGTTCAAGGCGAGTCCCCCTCCC

ACCCACCTGCTCCCAGCTGAGAGTCCATCTGGGCCTCCGGTGGGCAACGACAAAAAATTCCATTAGGTT

GAGAAGACGTGACTGGCACTGGCTCAAAGCCAAACAAATACTTGGTGGGCCTGCTTGGAGTTTAGCTCA

CACTTTTTGATTTTCTATTCACTGAATTTCACTGCTGTAGGAACCTCATATAAATGGAATCAGATAGTTATT

TTTTTTTATGACAGGCTTTGGGGGATATATCTTTTTGAAGGCTCTTTATAACTAAACAGTAAATAGTTTAA

TTACAGTGGAAATTCTCTGGACTAGATTGTAAAGGTGGATCAGATTTGGAAATAAGACTTTTTTCAAGTC

AAAGAAGAAAAACCAATTTAAAAATACAAGGCAATGGCCGGGTGCGGTGGCTCACGCCTGTAATCCCA

GCACCTTGGGAGGCCAAGGCAGGTGGATCAGCTGAGGTCAGGAATTCGAGACCAGCCTAGCCATCATG

GTGAAACCCTGTCTCTACTAAAAATACAAAGAAAAAATTAGCCGGGCATGGTGGTGCATGCCTGTAGTC

CCAGCTACTCAGGACACTGAGGCTGAGGAGAATTGCTTGAACCCGGGAGGCAGAGGTTGTAGTGAGCA

AAGATCGCGCCACTGCACTCCAGCCTGGGCAACAGAGTGAGACTCCACGTCAAAAAAAAAAAAAAAAA

AAGACATGTCAGAAACAAAGAAAGAAAGACATGACAGGCTCAGAATCAATGTCAACCTGGGCAAAGGT

CAGAAACGGAACAGGGACCCTTTCTTTGTGGGCAGGTTTGACATGAAAGGTTCAGCGACTTCAACTCTT

CTGATTCTTTCTTCTTGAGCCCATTTTGGTAAGTTGTGTTTTCCTAAAAGTTTGTCCATTCCATCCAAATGT

TCACATTAGTCAGGATCTGTGAAGGATGTCAATGGCTGTGAGGCGAGGGCCCCTTGCCAGTCCCCATGT

TCGTTATTTATGGATGCCTGATGCCCACAACCTCGACTTCTCAGCTGAGGGCAACTCCTCCTGTCCTCTCG

CTGCTTCCACCTAAGCCACCAGGAAATCCTGTTGACTCCACTTACAAAAGCTCTCCAGAGTCTGCTACCTC

TTACCACCCTACTGTCGCCTCCCAGACCTGGTCTCCCCGCTTCTGCCCTGGCCCCTACAGCTCGCAGACAG

CTGCCAGAGGAGTCCATCCGAATCAACTTCAGATTGCGTCACTTTTTCTTTCAAAATCCGACAAAGCTCCT

CATTCCATTCAGAGTGAGAAGGGCCCCGCCATGCAGCCTTTCCTCCTCCTATTCACCAACCCCACTCTCGC

TCCAGCCATCTTGATATCCTTGCTGGTCCTGGAGCAGGCCAGCCACGCTCTTGCCCCAGGGCCTTTGCAC

TTGCTGCCCCTCTCCTGTGATGCCCTCCTGGATCTCTGCATGGCTCCCTCCTGCCCTCCCTCCCTCGAGTCT

TTGCTCACATGTCCCCTTCTCAGAGGGGCTCACCCTGGTGCCCTTCGAAAGTGGGCATCCACTCCCTTCCC

ACCCTGGCACCCGCACCCTCCTGTCTTCCTTTTTCTGTTCTCCATCCTACTCATCTCCCCCAACTAGAAAGG

CAGCTGCAGCTGCGGAGCACGGGATCTCCATCTGCAGCTGCATCCCGGGACCTAGAACAGGTACAAAA

GTACCTAATAAGTACCCACTGAATGAATAATTGGCTGAGTTTTCTGTACCAAAGACTGAGCTAAGACTCT

TTAAAAGGATGATCTTATTTAAGCCTTACAGCAAGTAAATGTTATCCCCATCTTCCTGATGAGGACACAG

TGACCACCACGCTCAAGGACACAGAGGGTGGACGTGCCACATTCACACTCTGTGACTTAGAGCGGCTGG

ACGGGCAGGGACTTAGGAGGCCTACAGCAGCCAGGGTGAGATTATGAGGCTGAGCTGAGAATATCAA

GACTGTACCGAGTAGGGGGCCTTGGCAAGTGTGGAGAGCCCGGCAGCTGGGGCAGAGGGCGGAGTAC

GGTGTGCGTTTACGGACCTCTTCAAACGAGGTAGGAAGGTCAGAAGTCAAAAAGGGAACAAATGATGT

TTAACCACACAAAAATGAAAATCCAATGGTTGGATATCCATTCCAAATACACAAAGGCAACGGATAAGT

GATCCGGGCCAGGCACAGAAGGCCATGCACCCGTAGGATTGCACTCAGAGCTCCCAAATGCATAGGAA

TAGAAGGGTGGGTGCAGGAGGCTGAGGGGTGGGGAAAGGGCATGGGTGTTTCATGAGGACAGAGCT

TCCGTTTCATGCAATGAAAAGAGTTTGGAGACGGATGGTGGTGACTGGACTATACACTTACACACGGTA

GCGATGGTACACTTTGTATTATGTATATTTTACCACGATCTTTTTAAAGTGTCAAAGGCAAATGGCCAAAT

GGTTCCTTGTCCTATAGCTGTAGCAGCCATCGGCTGTTAGTGACAAAGCCCCTGAGTCAAGATGACAGC

AGCCCCCATAACTCCTAATCGGCTCTCCCGCGTGGAGTCATTTAGGAGTAGTCGCATTAGAGACAAGTCC

AACATCTAATCTTCCACCCTGGCCAGGGCCCCAGCTGGCAGCGAGGGTGGGAGACTCCGGGCAGAGCA

GAGGGCGCTGACATTGGGGCCCGGCCTGGCTTGGGTCCCTCTGGCCTTTCCCCAGGGGCCCTCTTTCCTT

GGGGCTTTCTTGGGCCGCCACTGCTCCCGCTCCTCTCCCCCCATCCCACCCCCTCACCCCCTCGTTCTTCAT

ATCCTTCTCTAGTGCTCCCTCCACTTTCATCCACCCTTCTGCAAGAGTGTGGGACCACAAATGAGTTTTCA

CCTGGCCTGGGGACACACGTGCCCCCACAGGTGCTGAGTGACTTTCTAGGACAGTAATCTGCTTTAGGC

TAAAATGGGA-CTTG-ATCTTCT-GTTAGCCCT-AATCATCAATTAGCAGAGCC--GGTGAAGGTGCAGAA-

CCTACCGCCTTTCCAGGCCTCCTCCCACCTCTGCCACCTCCACTCTCCTTCCTGGGATGTGGGGGCTGGCA

CACGTGTGGCCCAGGGCATTGGTGGGATTGCACTGAGCTGGGTCATTAGCGTAATCCTGGACAAGGGC

AGACAGGGCGAGCGGAGGGCCAGCTCCGGGGCTCAGGCAAGGCTGGGGGCTTCCCCCAGACACCCCA

CTCCTCCTCTGCTGGACCCCCACTTCATAGGGCACTTCGTGTTCTCAAAGGGCTTCCAAATAGCATGGTG

GCCTTGGATGCCCAGGGAAGCCTCAGAGTTGCTTATCTCCCTCTAGACAGAAGGGGAATCTCGGTCAAG

AGGGAGAGGTCGCCCTGTTCAAGGCCACCCAGCCAGCTCATGGCGGTAATGGGACAAGGCTGGCCAGC

CATCCCACCCTCAGAAGGGACCCGGTGGGGCAGGTGATCTCAGAGGAGGCTCACTTCTGGGTCTCACAT

TCTTGGATCCTCGGATCCTCTGACTCTGGTGGGGACAGGCAGACCAAGCTCTCTTGGACCCGGGAAGAG

GGACCCTTGGAAGTCACTTGGGATTGAGTTCTAGAGTCTTGACACTGTTTCAGCAGATCTATACTTTGAA

CCCACCTCAGGCATCTCATCCACAGAACAGGGACAGTGACCATTCCATCTTGCCAAGGAGTGCGGGGCA

CACACCATGCTGCTGGCAGCCAGGGTGGAAAGTCAAGGGGTCCCAGCTGAAGCACTGCCACAGAGGCA

GGATGCAGTCCGAGAGGGGACTTCAGAGCAGGGGCCCAAGGCCAAGGCCATCAGGGAGGTCTTTCTG

CAGGAGGGACCTCTTTAGGAGTTAGGCCCTAAAAACAAATAAGAGGAAGAAAGGCACTTGGTGGTTTT

TAGTCTATTCACGGTGCTGTGCAGCCATCACCACCATCCAGCCGCAGAACTTGTTCATCTTCCCAAACTGA

AGCTCTGGCCCCGTTCAACCCCAACTCCCCACCCCCCAGCCCCTGGCACCCACCCTTCCACTGTCTGTCTC

TATGGATTTGACCACTCTAGGCCCTTCATATAAGTGGAATTTTACAGTATTTACCCTCCTGTGACTGGCTC

ATTTCACTGAGCAATGTCCTCAAGGGTCATCCATGTTGGAGCATGTGTCAAACTTCATTTCTTTTTAAGGG

TGAATCATATTCCATCGTCTGTATAGACCACAATTTGTGTAGCTAATCATCCGTTGATGTTTGTTGATTTG

TTTGTTTGTTTTGAGACAGTCTTGCCATCAGAGCTCACTGCAGGCTCAACCTCCCAGGCTCAAGAAATCCT

CCCGCCTCTCTACCTCCCAAGTAGCTGTGACTACAGGCACCTGCGACTGTGCCCTGCTAATTTTTGTATTT

TTTGTAGAGACAGGGTCTCACTATGTTGCCCAGGCTAGTCTCGAACTCCTGGGCTCAAGTGATCCTCTCA

CCTCGGCCTCCCAAAGAACTGGGATTACAGGCATGAGCTACCATGTCCAGCCCAATTGCCCATTGATGG

GCACGGGTTGCTTCCATGTTTCAGCTGTTGTGAATCACGCTGCTGTGAACATGCGTGTGCAAACAGCCCT

TCCAGACCCTGCCTTCCATTCCTCTGGGCCTATACCCAGCAGTGCGGTTGCTGGGTCCTATGGGAATTCT

ACGTTTAACTTTTGGAGGAGCTGCCAAACTGTTTTCCACAGTGGCTGCGCCATCACAATCCAATTTTAGG

ACATTTTTATCACCCATAAAGCACTCCCTGTACCCATTAAGAAGTCATCCTCCATTTCCCTCCCTCCCCTGT

CCTGGCACCCATTCCTCTGCTTTGTGTGTCTCTGGATTGCCCTATCTAAGCATTTCACAGAGATGGAGCCA

TGCGCTCCGTGGTCTTTTGTGTCTGGCTTCGCTCACTGAGCATGCTGTTCTCCAGGTCCATCCACGTTGTA

GCGTAGGTCAGCCCTTCATTCCCTGTTATGGCCAAATGATACTCCATTGTACAGACAGGCCACTTTTTACC

CACTCATCTGCTTCTGGACTTTTGGGTTGCTTCTACCATGTGGCCTGTTGGGAACAGTGCTCTGTTTGTAT

TCATGTACGGGTTTTTGTGTGGACACACATTTTCAAGTCTCTTGGGTACACAGGTGTAGAAGTGCCAGAG

TTGGGGAAAAAGCTCACCTTTCTAGGCTGTGAATGGGCCCTGGCAAGTCTGTGGCCAGGACTCGTCTTC

TCTTCCACATGGGGCCCCTAGCTTGGCACCTAGCACGTGGCAGGCAGCGACAGATGTTAAAAGCCATTC

TTGCTATGGGTAGCCAGGCTGGGGCTCCATGCAGCCCTGGCCTTCAGCTTGGCAGCCAGGGCCCCCTTG

TGCCTGCAGCAGAAGCCATGCTGCCAGGAGTGTAAGTGTGAGCCAGGAATGCTGGAGAATCGTGGCTC

TGAGAACAGGGACAAGAGGCCACAAGCTCACGCCTTGGCTTTCCTAAGCTTAAGGAATAAACCCAAAAG

GAGGTACCTGGAAGGAGCTGGATTTGGGGACTGAGGAGCTGGGAGCTGATGGAAGCCGTGAAAGGG

GATGTGCTCCTGGGGAGGCGCTGGGGCGGGTGGGCCGTGGAGGGGACAGGGCCCGTTGGTTGGAAA

CTGAGGCGAGGCTACGGAGTTGGGCACTAACAGGTCATCCGTGCCCCTGCGAAGCGTGGGGACACAGG

GACAGCAGAGATGGCCTGTCTGGACACTCTGTCGACGGGGGGCCTGTGGTTGGTGAAGCCCAAGGCAA

GGCTGTGAACTCAGGGCAAGGGAGACGTGAGCAGGCGCTGCCGTGGGCTGATGTGGGCACTGCATGT

GCACCCTGGCGGCCAAAGGACCTACAGCTCATGGGGGGCAAGGGGGAGGAGGGAAGCCAACAGCAG

GATGTGCGCAGTCAGTCTGCCCCCCCTACACTGGAGGAGGAGCCCCCCGGCACAAATCTCGCCCGTTTG

GGCCCACGGACATGGCTGGCCTCGCAAGGAGGATCCGGTTCCAGGCCTCGGCCCTAAATAGTCTCCCTG

GGCTTTCAAGAGAACCACATGAGAAAGGAGGATTCGGGCTCTGAGCAGTTTCACCACCCACCCCCCAGT

CTGCAAATCCTGACCCGTGGGTCCACCTGCCCCAAAGGCGGACGCAGGACAGTAGAAGGGAACAGAGA

ACACATAAACACAGAGAGGGCCACAGCGGCTCCCACAGTCACCGCCACCTTCCTGGCGGGGATGGGTG

GGGCGTCTGAGTTTGGTTCCCAGCAAATCCCTCTGAGCCGCCCTTGCGGGCTCGCCTCAGGAGCAGGGG

AGCAAGAGGTGGGAGGAGGAGGTCTAAGTCCCAGGCCCAATTAAGAGATCAGGTAGTGTAGGGTTTG

GGAGCTTTTAAGGTGAAGAGGCCCGGGCTGATCCCACAGGCCAGTATAAAGCGCCGTGACCCTCAGGT

GATGCGCCAGGGCCGGCTGCCGTCGGGGACAGGGCTTTCCATAGCC

DsRed

ATGGCCTCCTCCGAGGACGTCATCAAGGAGTTCATGCGCTTCAAGGTGCGCATGGAGGGCTCCGTGAAC

GGCCACGAGTTCGAGATCGAGGGCGAGGGCGAGGGCCGCCCCTACGAGGGCACCCAGACCGCCAAGC

TGAAGGTGACCAAGGGCGGCCCCCTGCCCTTCGCCTGGGACATCCTGTCCCCCCAGTTCCAGTACGGCT

CCAAGGTGTACGTGAAGCACCCCGCCGACATCCCCGACTACAAGAAGCTGTCCTTCCCCGAGGGCTTCA

AGTGGGAGCGCGTGATGAACTTCGAGGACGGCGGCGTGGTGACCGTGACCCAGGACTCCTCCCTGCAG

GACGGCTCCTTCATCTACAAGGTGAAGTTCATCGGCGTGAACTTCCCCTCCGACGGCCCCGTAATGCAGA

AGAAGACTATGGGCTGGGAGGCCTCCACCGAGCGCCTGTACCCCCGCGACGGCGTGCTGAAGGGCGA

GATCCACAAGGCCCTGAAGCTGAAGGACGGCGGCCACTACCTGGTGGAGTTCAAGTCCATCTACATGGC

CAAGAAGCCCGTGCAGCTGCCCGGCTACTACTACGTGGACTCCAAGCTGGACATCACCTCCCACAACGA

GGACTACACCATCGTGGAGCAGTACGAGCGCGCCGAGGGCCGCCACCACCTGTTCCTGTAG

hGRK1 Promoter

ATCTGAATTCGGTACCGGGCCCCAGAAGCCTGGTGGTTGTTTGTCCTTCTCAGGGGAAAAGTGAGGCGG

CCCCTTGGAGGAAGGGGCCGGGCAGAATGATCTAATCGGATTCCAAGCAGCTCAGGGGATTGTCTTTTT

CTAGCACCTTCTTGCCACTCCTAAGCGTCCTCCGTGACCCCGGCTGGGATTTAGCCTGGTGCTGTGTCAG

CCCCGGGGGAGTCGCTGCGCGCTGCCTTCG

CAG Promoter

GACATTGATTATTGACTAGTTATTAATAGTAATCAATTACGGGGTCATTAGTTCATAGCCCATATATGGA

GTTCCGCGTTACATAACTTACGGTAAATGGCCCGCCTGGCTGACCGCCCAACGACCCCCGCCCATTGACG

TCAATAATGACGTATGTTCCCATAGTAACGCCAATAGGGACTTTCCATTGACGTCAATGGGTGGAGTATT

TACGGTAAACTGCCCACTTGGCAGTACATCAAGTGTATCATATGCCAAGTACGCCCCCTATTGACGTCAA

TGACGGTAAATGGCCCGCCTGGCATTATGCCCAGTACATGACCTTATGGGACTTTCCTACTTGGCAGTAC

ATCTACGTATTAGTCATCGCTATTACCATGGTCGAGGTGAGCCCCACGTTCTGCTTCACTCTCCCCATCTC

CCCCCCCTCCCCACCCCCAATTTTGTATTTATTTATTTTTTAATTATTTTGTGCAGCGATGGGGGCGGGGG

GGGGGGGGGGGCGCGCGCCAGGCGGGGCGGGGCGGGGCGAGGGGCGGGGCGGGGCGAGGCGGAG

AGGTGCGGCGGCAGCCAATCAGAGCGGCGCGCTCCGAAAGTTTCCTTTTATGGCGAGGCGGCGGCGGC

GGCGGCCCTATAAAAAGCGAAGCGCGCGGCGGGCG

EFS Promoter

GGGCAGAGCGCACATCGCCCACAGTCCCCGAGAAGTTGGGGGGAGGGGTCGGCAATTGATCCGGTGC

CTAGAGAAGGTGGCGCGGGGTAAACTGGGAAAGTGATGTCGTGTACTGGCTCCGCCTTTTTCCCGAGG

GTGGGGGAGAACCGTATATAAGTGCAGTAGTCGCCGTGAACGTTCTTTTTCGCAACGGGTTTGCCGCCA

GAACACAG

SaCas9

AAGCGGAACTACATCCTGGGCCTGGACATCGGCATCACCAGCGTGGGCTACGGCATCATCGACTACGA

GACACGGGACGTGATCGATGCCGGCGTGCGGCTGTTCAAAGAGGCCAACGTGGAAAACAACGAGGGC

AGGCGGAGCAAGAGAGGCGCCAGAAGGCTGAAGCGGCGGAGGCGGCATAGAATCCAGAGAGTGAAG

AAGCTGCTGTTCGACTACAACCTGCTGACCGACCACAGCGAGCTGAGCGGCATCAACCCCTACGAGGCC

AGAGTGAAGGGCCTGAGCCAGAAGCTGAGCGAGGAAGAGTTCTCTGCCGCCCTGCTGCACCTGGCCAA

GAGAAGAGGCGTGCACAACGTGAACGAGGTGGAAGAGGACACCGGCAACGAGCTGTCCACCAAAGAG

CAGATCAGCCGGAACAGCAAGGCCCTGGAAGAGAAATACGTGGCCGAACTGCAGCTGGAACGGCTGA

AGAAAGACGGCGAAGTGCGGGGCAGCATCAACAGATTCAAGACCAGCGACTACGTGAAAGAAGCCAA

ACAGCTGCTGAAGGTGCAGAAGGCCTACCACCAGCTGGACCAGAGCTTCATCGACACCTACATCGACCT

GCTGGAAACCCGGCGGACCTACTATGAGGGACCTGGCGAGGGCAGCCCCTTCGGCTGGAAGGACATCA

AAGAATGGTACGAGATGCTGATGGGCCACTGCACCTACTTCCCCGAGGAACTGCGGAGCGTGAAGTAC

GCCTACAACGCCGACCTGTACAACGCCCTGAACGACCTGAACAATCTCGTGATCACCAGGGACGAGAAC

GAGAAGCTGGAATATTACGAGAAGTTCCAGATCATCGAGAACGTGTTCAAGCAGAAGAAGAAGCCCAC

CCTGAAGCAGATCGCCAAAGAAATCCTCGTGAACGAAGAGGATATTAAGGGCTACAGAGTGACCAGCA

CCGGCAAGCCCGAGTTCACCAACCTGAAGGTGTACCACGACATCAAGGACATTACCGCCCGGAAAGAG

ATTATTGAGAACGCCGAGCTGCTGGATCAGATTGCCAAGATCCTGACCATCTACCAGAGCAGCGAGGAC

ATCCAGGAAGAACTGACCAATCTGAACTCCGAGCTGACCCAGGAAGAGATCGAGCAGATCTCTAATCTG

AAGGGCTATACCGGCACCCACAACCTGAGCCTGAAGGCCATCAACCTGATCCTGGACGAGCTGTGGCAC

ACCAACGACAACCAGATCGCTATCTTCAACCGGCTGAAGCTGGTGCCCAAGAAGGTGGACCTGTCCCAG

CAGAAAGAGATCCCCACCACCCTGGTGGACGACTTCATCCTGAGCCCCGTCGTGAAGAGAAGCTTCATC

CAGAGCATCAAAGTGATCAACGCCATCATCAAGAAGTACGGCCTGCCCAACGACATCATTATCGAGCTG

GCCCGCGAGAAGAACTCCAAGGACGCCCAGAAAATGATCAACGAGATGCAGAAGCGGAACCGGCAGA

CCAACGAGCGGATCGAGGAAATCATCCGGACCACCGGCAAAGAGAACGCCAAGTACCTGATCGAGAAG

ATCAAGCTGCACGACATGCAGGAAGGCAAGTGCCTGTACAGCCTGGAAGCCATCCCTCTGGAAGATCTG

CTGAACAACCCCTTCAACTATGAGGTGGACCACATCATCCCCAGAAGCGTGTCCTTCGACAACAGCTTCA

ACAACAAGGTGCTCGTGAAGCAGGAAGAAAACAGCAAGAAGGGCAACCGGACCCCATTCCAGTACCTG

AGCAGCAGCGACAGCAAGATCAGCTACGAAACCTTCAAGAAGCACATCCTGAATCTGGCCAAGGGCAA

GGGCAGAATCAGCAAGACCAAGAAAGAGTATCTGCTGGAAGAACGGGACATCAACAGGTTCTCCGTGC

AGAAAGACTTCATCAACCGGAACCTGGTGGATACCAGATACGCCACCAGAGGCCTGATGAACCTGCTGC

GGAGCTACTTCAGAGTGAACAACCTGGACGTGAAAGTGAAGTCCATCAATGGCGGCTTCACCAGCTTTC

TGCGGCGGAAGTGGAAGTTTAAGAAAGAGCGGAACAAGGGGTACAAGCACCACGCCGAGGACGCCCT

GATCATTGCCAACGCCGATTTCATCTTCAAAGAGTGGAAGAAACTGGACAAGGCCAAAAAAGTGATGG

AAAACCAGATGTTCGAGGAAAAGCAGGCCGAGAGCATGCCCGAGATCGAAACCGAGCAGGAGTACAA

AGAGATCTTCATCACCCCCCACCAGATCAAGCACATTAAGGACTTCAAGGACTACAAGTACAGCCACCG

GGTGGACAAGAAGCCTAATAGAGAGCTGATTAACGACACCCTGTACTCCACCCGGAAGGACGACAAGG

GCAACACCCTGATCGTGAACAATCTGAACGGCCTGTACGACAAGGACAATGACAAGCTGAAAAAGCTG

ATCAACAAGAGCCCCGAAAAGCTGCTGATGTACCACCACGACCCCCAGACCTACCAGAAACTGAAGCTG

ATTATGGAACAGTACGGCGACGAGAAGAATCCCCTGTACAAGTACTACGAGGAAACCGGGAACTACCT

GACCAAGTACTCCAAAAAGGACAACGGCCCCGTGATCAAGAAGATTAAGTATTACGGCAACAAACTGA

ACGCCCATCTGGACATCACCGACGACTACCCCAACAGCAGAAACAAGGTCGTGAAGCTGTCCCTGAAGC

CCTACAGATTCGACGTGTACCTGGACAATGGCGTGTACAAGTTCGTGACCGTGAAGAATCTGGATGTGA

TCAAAAAAGAAAACTACTACGAAGTGAATAGCAAGTGCTATGAGGAAGCTAAGAAGCTGAAGAAGATC

AGCAACCAGGCCGAGTTTATCGCCTCCTTCTACAACAACGATCTGATCAAGATCAACGGCGAGCTGTATA

GAGTGATCGGCGTGAACAACGACCTGCTGAACCGGATCGAAGTGAACATGATCGACATCACCTACCGC

GAGTACCTGGAAAACATGAACGACAAGAGGCCCCCCAGGATCATTAAGACAATCGCCTCCAAGACCCA

GAGCATTAAGAAGTACAGCACAGACATTCTGGGCAACCTGTATGAAGTGAAATCTAAGAAGCACCCTCA

GATCATCAAAAAGGGC

dSaCas9

CGGAACTACATCCTGGGCCTGGCCATCGGCATCACCAGCGTGGGCTACGGCATCATCGACTACGAGACA

CGGGACGTGATCGATGCCGGCGTGCGGCTGTTCAAAGAGGCCAACGTGGAAAACAACGAGGGCAGGC

GGAGCAAGAGAGGCGCCAGAAGGCTGAAGCGGCGGAGGCGGCATAGAATCCAGAGAGTGAAGAAGC

TGCTGTTCGACTACAACCTGCTGACCGACCACAGCGAGCTGAGCGGCATCAACCCCTACGAGGCCAGAG

TGAAGGGCCTGAGCCAGAAGCTGAGCGAGGAAGAGTTCTCTGCCGCCCTGCTGCACCTGGCCAAGAGA

AGAGGCGTGCACAACGTGAACGAGGTGGAAGAGGACACCGGCAACGAGCTGTCCACCAAAGAGCAGA

TCAGCCGGAACAGCAAGGCCCTGGAAGAGAAATACGTGGCCGAACTGCAGCTGGAACGGCTGAAGAA

AGACGGCGAAGTGCGGGGCAGCATCAACAGATTCAAGACCAGCGACTACGTGAAAGAAGCCAAACAG

CTGCTGAAGGTGCAGAAGGCCTACCACCAGCTGGACCAGAGCTTCATCGACACCTACATCGACCTGCTG

GAAACCCGGCGGACCTACTATGAGGGACCTGGCGAGGGCAGCCCCTTCGGCTGGAAGGACATCAAAGA

ATGGTACGAGATGCTGATGGGCCACTGCACCTACTTCCCCGAGGAACTGCGGAGCGTGAAGTACGCCTA

CAACGCCGACCTGTACAACGCCCTGAACGACCTGAACAATCTCGTGATCACCAGGGACGAGAACGAGA

AGCTGGAATATTACGAGAAGTTCCAGATCATCGAGAACGTGTTCAAGCAGAAGAAGAAGCCCACCCTG

AAGCAGATCGCCAAAGAAATCCTCGTGAACGAAGAGGATATTAAGGGCTACAGAGTGACCAGCACCGG

CAAGCCCGAGTTCACCAACCTGAAGGTGTACCACGACATCAAGGACATTACCGCCCGGAAAGAGATTAT

TGAGAACGCCGAGCTGCTGGATCAGATTGCCAAGATCCTGACCATCTACCAGAGCAGCGAGGACATCCA

GGAAGAACTGACCAATCTGAACTCCGAGCTGACCCAGGAAGAGATCGAGCAGATCTCTAATCTGAAGG

GCTATACCGGCACCCACAACCTGAGCCTGAAGGCCATCAACCTGATCCTGGACGAGCTGTGGCACACCA

ACGACAACCAGATCGCTATCTTCAACCGGCTGAAGCTGGTGCCCAAGAAGGTGGACCTGTCCCAGCAGA

AAGAGATCCCCACCACCCTGGTGGACGACTTCATCCTGAGCCCCGTCGTGAAGAGAAGCTTCATCCAGA

GCATCAAAGTGATCAACGCCATCATCAAGAAGTACGGCCTGCCCAACGACATCATTATCGAGCTGGCCC

GCGAGAAGAACTCCAAGGACGCCCAGAAAATGATCAACGAGATGCAGAAGCGGAACCGGCAGACCAA

CGAGCGGATCGAGGAAATCATCCGGACCACCGGCAAAGAGAACGCCAAGTACCTGATCGAGAAGATCA

AGCTGCACGACATGCAGGAAGGCAAGTGCCTGTACAGCCTGGAAGCCATCCCTCTGGAAGATCTGCTG

AACAACCCCTTCAACTATGAGGTGGACCACATCATCCCCAGAAGCGTGTCCTTCGACAACAGCTTCAACA

ACAAGGTGCTCGTGAAGCAGGAAGAAGCCAGCAAGAAGGGCAACCGGACCCCATTCCAGTACCTGAGC

AGCAGCGACAGCAAGATCAGCTACGAAACCTTCAAGAAGCACATCCTGAATCTGGCCAAGGGCAAGGG

CAGAATCAGCAAGACCAAGAAAGAGTATCTGCTGGAAGAACGGGACATCAACAGGTTCTCCGTGCAGA

AAGACTTCATCAACCGGAACCTGGTGGATACCAGATACGCCACCAGAGGCCTGATGAACCTGCTGCGGA

GCTACTTCAGAGTGAACAACCTGGACGTGAAAGTGAAGTCCATCAATGGCGGCTTCACCAGCTTTCTGC

GGCGGAAGTGGAAGTTTAAGAAAGAGCGGAACAAGGGGTACAAGCACCACGCCGAGGACGCCCTGAT

CATTGCCAACGCCGATTTCATCTTCAAAGAGTGGAAGAAACTGGACAAGGCCAAAAAAGTGATGGAAA

ACCAGATGTTCGAGGAAAAGCAGGCCGAGAGCATGCCCGAGATCGAAACCGAGCAGGAGTACAAAGA

GATCTTCATCACCCCCCACCAGATCAAGCACATTAAGGACTTCAAGGACTACAAGTACAGCCACCGGGT

GGACAAGAAGCCTAATAGAGAGCTGATTAACGACACCCTGTACTCCACCCGGAAGGACGACAAGGGCA

ACACCCTGATCGTGAACAATCTGAACGGCCTGTACGACAAGGACAATGACAAGCTGAAAAAGCTGATCA

ACAAGAGCCCCGAAAAGCTGCTGATGTACCACCACGACCCCCAGACCTACCAGAAACTGAAGCTGATTA

TGGAACAGTACGGCGACGAGAAGAATCCCCTGTACAAGTACTACGAGGAAACCGGGAACTACCTGACC

AAGTACTCCAAAAAGGACAACGGCCCCGTGATCAAGAAGATTAAGTATTACGGCAACAAACTGAACGCC

CATCTGGACATCACCGACGACTACCCCAACAGCAGAAACAAGGTCGTGAAGCTGTCCCTGAAGCCCTAC

AGATTCGACGTGTACCTGGACAATGGCGTGTACAAGTTCGTGACCGTGAAGAATCTGGATGTGATCAAA

AAAGAAAACTACTACGAAGTGAATAGCAAGTGCTATGAGGAAGCTAAGAAGCTGAAGAAGATCAGCAA

CCAGGCCGAGTTTATCGCCTCCTTCTACAACAACGATCTGATCAAGATCAACGGCGAGCTGTATAGAGT

GATCGGCGTGAACAACGACCTGCTGAACCGGATCGAAGTGAACATGATCGACATCACCTACCGCGAGTA

CCTGGAAAACATGAACGACAAGAGGCCCCCCAGGATCATTAAGACAATCGCCTCCAAGACCCAGAGCAT

TAAGAAGTACAGCACAGACATTCTGGGCAACCTGTATGAAGTGAAATCTAAGAAGCACCCTCAGATCAT

CAAAAAG